



**HAL**  
open science

# Numerical characterization of point defect kinetics and sink strengths in crystalline solids using absorbing Markov chains

Savneet Kaur

► **To cite this version:**

Savneet Kaur. Numerical characterization of point defect kinetics and sink strengths in crystalline solids using absorbing Markov chains. Mechanics of materials [physics.class-ph]. Université Paris-Saclay, 2022. English. NNT: 2022UPASF007 . tel-03767531

**HAL Id: tel-03767531**

**<https://theses.hal.science/tel-03767531>**

Submitted on 2 Sep 2022

**HAL** is a multi-disciplinary open access archive for the deposit and dissemination of scientific research documents, whether they are published or not. The documents may come from teaching and research institutions in France or abroad, or from public or private research centers.

L'archive ouverte pluridisciplinaire **HAL**, est destinée au dépôt et à la diffusion de documents scientifiques de niveau recherche, publiés ou non, émanant des établissements d'enseignement et de recherche français ou étrangers, des laboratoires publics ou privés.

# Numerical characterization of point defect kinetics and sink strengths in crystalline solids using absorbing Markov chains

*Caractérisation numérique de la cinétique des défauts ponctuels et des forces de puits dans les solides cristallins à l'aide de chaînes de Markov absorbantes*

## Thèse de doctorat de l'université Paris-Saclay

École doctorale n° 571, Sciences chimiques : molécules, matériaux, instrumentation et biosystèmes (2MIB)  
Spécialité de doctorat : Chimie  
Graduate School : Chimie. Référent : Faculté des science d'Orsay

Thèse préparée à l'**Institut de chimie moléculaire et des matériaux d'Orsay** (Université Paris-Saclay, CNRS) et au **Service de Recherches de Métallurgie Physique** (Université Paris-Saclay, CEA), sous la direction de **Jérôme CREUZE**, Professeur, et la co-direction de **Manuel ATHÈNES**, Directeur de Recherche

Thèse soutenue à Paris-Saclay, le 2 février 2022, par

**Savneet KAUR**

## Composition du jury

<b>Yann LE BOUAR</b> Directeur de Recherche, CNRS - ONERA	Président
<b>Helena ZAPOLSKY</b> Professeure, Université de Rouen	Rapportrice & Examinatrice
<b>Alexandre LEGRIS</b> Professeur, Université de Lille	Rapporteur & Examineur
<b>Charlotte BECQUART</b> Professeure, Université de Lille	Examinatrice
<b>Thomas D SWINBURNE</b> Chercheur, CINaM, Marseille	Examineur
<b>Jérôme CREUZE</b> Professeur, ICMMO-Université Paris-Saclay	Directeur de thèse

**Titre :** Caractérisation numérique de la cinétique des défauts ponctuels et des forces de puits dans les solides cristallins à l'aide de chaînes de Markov absorbantes

**Mots clés :** Cinétiques sur réseau, Défauts ponctuels, Chaînes de Markov absorbantes, Algorithme de premier passage, Projection sur sous-espaces de Krylov, Force de puits, Monte Carlo cinétique

**Résumé :** L'évolution microstructurale des matériaux pour le nucléaire est pilotée par l'agglomération et la recombinaison des défauts créés sous irradiation, tels que les lacunes et les atomes interstitiels. Prédire les cinétiques des défauts d'irradiation est essentiel si l'on souhaite comprendre comment les propriétés mécaniques des matériaux vont évoluer dans le temps. De nombreux modèles physiques décrivant les cinétiques de vieillissement prennent en compte les fréquences des saut élémentaires des défauts ponctuels à l'échelle atomique et font intervenir une équation maîtresse régissant l'évolution temporelle d'un vecteur de probabilité d'état, étant donné un état initial. La théorie des états de transition et la théorie de l'élasticité sont ici utilisées pour calculer les fréquences de saut et construire la matrice des taux de transition qui est l'ingrédient crucial de l'équation maîtresse.

Dans cette thèse, nous développons des techniques numériques non-stochastiques pour caractériser le mouvement de défauts individuels migrant sur de longues distances avant de se recombinaison avec un autre défaut mobile ou d'être absorbés par un puits, généralement un défaut étendu immobile. Notre approche est fondée sur la théorie des chaînes de Markov absorbantes dans laquelle les états absorbants correspondent à des recombinaisons de défauts ou des absorptions de défauts mobiles par des puits fixes. Les mouvements des défauts sont alors entièrement déterminés par la distribution des temps de premier passage vers des sites éloignés, la distribution de non-passage, et les flux de probabilité vers les puits. Ces quantités découlent directement des propriétés spectrales de la matrice des taux de transition et définissent les lois probabilistes des événements non locaux qui

peuvent ensuite être simulés par un algorithme de Monte Carlo cinétique de premier passage. Elles permettent également de calculer les forces de puits qui sont les paramètres d'entrée cruciaux des équations de cinétique chimique considérées dans les simulations de dynamique d'amas.

En supposant que les défauts migrent suivant un processus de diffusion réversible, nous montrons que la matrice des taux de transition absorbante est diagonalement similaire à une matrice symétrique définie positive. Cette particularité facilite grandement l'extraction de ses propriétés spectrales par des solveurs itératifs creux. Nous démontrons l'efficacité de l'approche en calculant directement les propriétés d'élastodiffusion d'une lacune autour d'une cavité dans l'aluminium et en mesurant la diffusivité de petits amas de solutés dans des aciers faiblement alliés en manganèse. En outre, nous évaluons également l'efficacité de divers schémas mathématiques pour caractériser les lois d'évolution d'un défaut ponctuel près d'un puits. En particulier, nous développons un schéma combinant projection sur des sous-espaces de Krylov et déflation de modes propres. Dans le cas du système modèle décrivant l'absorption d'une lacune par une cavité dans l'aluminium, un petit sous-espace de Krylov déflaté par le mode propre unique correspondant à la distribution quasi-stationnaire est capable de capturer fidèlement la cinétique d'absorption du défaut. Enfin, nous discutons de la manière dont un algorithme de Monte Carlo cinétique peut être mis en œuvre pour calculer efficacement les forces de puits de petits amas auto-interstitiels migrant rapidement le long d'une ligne de glissement et effectuant occasionnellement des rotations.

**Title** : Numerical characterization of point defect kinetics and sink strengths in crystalline solids using absorbing Markov chains

**Keywords** : Lattice kinetics, Point defects, Absorbing Markov chains, First-Passage processes, Krylov subspace projection, Sink strengths, Kinetic Monte Carlo

**Abstract** : The microstructural evolution of nuclear materials is driven by the agglomeration and recombination of the defects that are created under irradiation, such as vacancies and interstitial atoms. Predicting the ageing kinetics of these irradiation defects is essential to understand how the mechanical properties of the materials will evolve with time. Many physical models describing the ageing kinetics account for the elementary jump frequencies of point defects at the atomic scale and involve a master equation governing the time evolution of a state probability vector given an initial state. Transition state theory and elasticity theory are used to compute the jump frequencies and construct the transition rate matrix that is the crucial ingredient of the master equation.

In this thesis, we develop non-stochastic numerical techniques to characterize the motion of individual defects migrating over long distances prior to recombining with another mobile defect or being absorbed by a sink, usually an immobile extended defect. Our approach is based on the theory of absorbing Markov chains in which the absorbing states correspond to the recombinations of two mobile defects or to the absorptions of a defect by an immobile sink. The defect motions are then entirely determined by their first-passage time distribution to distant absorbing locations, no-passage distribution, and the probability fluxes to the sinks. These quantities directly stem from the spectral

properties of the transition rate matrix and define the probabilistic laws of non-local events that can then be simulated by a first-passage kinetic Monte Carlo algorithm. They also allow computing the sink strengths that are the crucial input parameters of rate-equation cluster dynamics simulations.

Assuming that defects undergo reversible diffusion, we show that the absorbing transition rate matrix is diagonally similar to a symmetric definite positive matrix. This feature greatly facilitates the extraction of its spectral properties by using iterative sparse solvers. We demonstrate the efficiency of the approach with direct computations of elasto-diffusion properties of a vacancy around a cavity in aluminum and Monte Carlo computations of cluster diffusivity in low alloyed manganese steels. Additionally, we also assess the efficiency of various mathematical schemes to characterize the evolution laws of a point defect near a sink. In particular, we develop a scheme combining Krylov subspace projection and eigenvalue deflation. For our model system describing the absorption of a vacancy by a cavity in aluminum, a small Krylov subspace deflated by the unique eigenmode corresponding to the quasi-stationary distribution makes it possible to capture the kinetics of the defect absorption faithfully. Finally, we discuss how a first-passage kinetic Monte Carlo algorithm performing non-local moves of small self-interstitial clusters can be used to compute sink strengths efficiently.



*“Real learning comes about when the competitive spirit  
has ceased.”*

-Jiddu Krishnamurti



# Abstract

**Keywords:** *Lattice kinetics, Point defects, Absorbing Markov chains, First-Passage processes, Krylov subspace projection, Sink strengths, Kinetic Monte Carlo*

The microstructural evolution of nuclear materials is driven by the agglomeration and recombination of the defects that are created under irradiation, such as vacancies and interstitial atoms. Predicting the ageing kinetics of these irradiation defects is essential to understand how the mechanical properties of the materials will evolve with time. Many physical models describing the ageing kinetics account for the elementary jump frequencies of point defects at the atomic scale and involve a master equation governing the time evolution of a state probability vector given an initial state. Transition state theory and elasticity theory are used to compute the jump frequencies and construct the transition rate matrix that is the crucial ingredient of the master equation.

In this thesis, we develop non-stochastic numerical techniques to characterize the motion of individual defects migrating over long distances prior to recombining with another mobile defect or being absorbed by a sink, usually an immobile extended defect. Our approach is based on the theory of absorbing Markov chains in which the absorbing states correspond to the recombinations of two mobile defects or to the absorptions of a defect by an immobile sink. The defect motions are then entirely determined by their first-passage time distribution to distant absorbing locations, no-passage distribution, and the probability fluxes to the sinks. These quantities directly stem from the spectral properties of the transition rate matrix and define the probabilistic laws of non-local events that can then be simulated by a first-passage kinetic Monte Carlo algorithm. They also allow computing the sink strengths that are the crucial input parameters of rate-equation cluster dynamics simulations.

Assuming that defects undergo reversible diffusion, we show that the absorbing transition rate matrix is diagonally similar to a symmetric definite positive matrix. This feature greatly facilitates the extraction of its spectral properties by using iterative sparse solvers. We demonstrate the efficiency of the approach with direct computations of elastodiffusion properties of a vacancy around a cavity in aluminum and Monte Carlo computations of cluster diffusivity in low alloyed manganese steels. Additionally, we also assess the efficiency of various mathematical schemes to characterize the evolution

laws of a point defect near a sink. In particular, we develop a scheme combining Krylov subspace projection and eigenvalue deflation. For our model system describing the absorption of a vacancy by a cavity in aluminum, a small Krylov subspace deflated by the unique eigenmode corresponding to the quasi-stationary distribution makes it possible to capture the kinetics of the defect absorption faithfully. Finally, we discuss how a first-passage kinetic Monte Carlo algorithm performing non-local moves of small self-interstitial clusters can be used to compute sink strengths efficiently.



# Résumé

*Mots-clés: Cinétiques sur réseau, Défauts ponctuels, Chaînes de Markov absorbantes, Algorithme de premier passage, Projection sur sous-espaces de Krylov, Force de puits, Monte Carlo cinétique*

L'évolution microstructurale des matériaux pour le nucléaire est pilotée par l'agglomération et la recombinaison des défauts créés sous irradiation, tels que les lacunes et les atomes interstitiels. Prédire les cinétiques des défauts d'irradiation est essentiel si l'on souhaite comprendre comment les propriétés mécaniques des matériaux vont évoluer dans le temps. De nombreux modèles physiques décrivant les cinétiques de vieillissement prennent en compte les fréquences des saut élémentaires des défauts ponctuels à l'échelle atomique et font intervenir une équation maîtresse régissant l'évolution temporelle d'un vecteur de probabilité d'état, étant donné un état initial. La théorie des états de transition et la théorie de l'élasticité sont ici utilisées pour calculer les fréquences de saut et construire la matrice des taux de transition qui est l'ingrédient crucial de l'équation maîtresse.

Dans cette thèse, nous développons des techniques numériques non-stochastiques pour caractériser le mouvement de défauts individuels migrant sur de longues distances avant de se recombinaison avec un autre défaut mobile ou d'être absorbés par un puits, généralement un défaut étendu immobile. Notre approche est fondée sur la théorie des chaînes de Markov absorbantes dans laquelle les états absorbants correspondent à des recombinaisons de défauts ou des absorptions de défauts mobiles par des puits fixes. Les mouvements des défauts sont alors entièrement déterminés par la distribution des temps de premier passage vers des sites éloignés, la distribution de non-passage, et les flux de probabilité vers les puits. Ces quantités découlent directement des propriétés spectrales de la matrice des taux de transition et définissent les lois probabilistes des événements non locaux qui peuvent ensuite être simulés par un algorithme de Monte Carlo cinétique de premier passage. Elles permettent également de calculer les forces de puits qui sont les paramètres d'entrée cruciaux des équations de cinétique chimique considérées dans les simulations de dynamique d'amas.

En supposant que les défauts migrent suivant un processus de diffusion réversible, nous montrons que la matrice des taux de transition absorbante est diagonalement similaire à une matrice symétrique définie positive. Cette particularité facilite grandement l'extraction de ses propriétés spectrales par

des solveurs itératifs creux. Nous démontrons l'efficacité de l'approche en calculant directement les propriétés d'élastodiffusion d'une lacune autour d'une cavité dans l'aluminium et en mesurant la diffusivité de petits amas de solutés dans des aciers faiblement alliés en manganèse. En outre, nous évaluons également l'efficacité de divers schémas mathématiques pour caractériser les lois d'évolution d'un défaut ponctuel près d'un puits. En particulier, nous développons un schéma combinant projection sur des sous-espaces de Krylov et déflation de modes propres. Dans le cas du système modèle décrivant l'absorption d'une lacune par une cavité dans l'aluminium, un petit sous-espace de Krylov déflaté par le mode propre unique correspondant à la distribution quasi-stationnaire est capable de capturer fidèlement la cinétique d'absorption du défaut. Enfin, nous discutons de la manière dont un algorithme de Monte Carlo cinétique peut être mis en œuvre pour calculer efficacement les forces de puits de petits amas auto-interstitiels migrant rapidement le long d'une ligne de glissement et effectuant occasionnellement des rotations.



# Acknowledgments

I would like to thank all the people who contributed to help me achieve this research project. Firstly, I would like to extend my sincerest gratitude to Manuel Athènes, co-director, and supervisor of this thesis. I am thankful for his encouragement, patience, being welcoming, helpful, and above all, for his guidance throughout the work. Furthermore, I am grateful to Prof. Jérôme Creuze, my Ph.D. director, for his contribution and constant motivation; this work would not have been possible.

I thank Jean-Luc Béchade, head of "Service de Recherche en Métallurgie Physique (SRMP)," for allowing me to carry out research work at CEA Saclay and provide me with an opportunity with all the facilities. Thank you, Yann Le Bouar, for being an external reviewer of my thesis work and providing me with a handful of essential suggestions. I am indebted to all the jury members of my Ph.D. defense: the reviewers Helena Zapolsky and Alexandre Legris; the examiner's Charlotte Becquart, Yann LeBouar, and Thomas D Swinburne for investing time and reviewing my manuscript.

I would like to acknowledge my colleagues at SRMP. First, I greatly appreciate Orane Barbour's constant assurance, ensuring I am doing nicely, and fruitful office-room N°112 chat sessions. Second, I thank all the other amazing talented Phd students: Marié-Jose, Kajal, Xixi, Pamella, Yunhou, Shyam, Charbel, Océane, Clovis, Fabrice and Anruo.

Santhini VM, thank you for always being there for me as a sister and a true-to-your-word person. Adithya RK, thank you for always supporting me in my decisions, motivating me, and not letting me ever lose hope. Your constant efforts have made me understand to look at the brighter side of every situation.

I extend my heart full of gratitude to my family in France: Shifali Singh, Vaishnvi Tiwari, Ronit Panda, Shambhavi Nandan, Vaibhav Jaiswal, Advait Ghate, Ravi RJ, Neeraj Kumar, and Kavya Clement. I am glad never to feel lonesome because of you all, and thank you for being with me through thick and thin.

And finally, I am short of words to express my gratitude to my late grandparents, mom, dad, chachi, and chachu, who forever has been a constant source of inspiration and encouraged me with all their love and support. I am thankful for the universal power I believe in for being bestowed with everything I need, the strength, and the willpower to complete this work.



# Contents

<b>Abstract</b>	<b>iv</b>
<b>Résumé</b>	<b>vii</b>
<b>Acknowledgments</b>	<b>x</b>
<b>Contents</b>	<b>xii</b>
<b>List of Figures</b>	<b>xvi</b>
<b>List of Tables</b>	<b>xxii</b>
<b>List of Abbreviations</b>	<b>xxiv</b>
<b>Synopsis</b>	<b>2</b>
<b>1 Industrial Aspect</b>	<b>5</b>
1.1 Types of Materials . . . . .	8
1.2 Damage in reactor pressure vessels . . . . .	10
1.3 Primary damage caused by neutron irradiation . . . . .	12
1.4 Numerical modeling approach . . . . .	15
1.5 Summary . . . . .	17
<b>2 Theoretical Context and Objectives</b>	<b>19</b>
2.1 Markov Chains and first-passage events . . . . .	20
2.1.1 Discrete Time Markov chain . . . . .	20
2.1.2 Continuous Time Markov chain . . . . .	21
2.1.3 Absorbing Markov chains . . . . .	21
2.1.4 First-passage events . . . . .	23
2.1.4.1 First-passage time . . . . .	24
2.1.5 Properties of Markov chain . . . . .	24
2.1.5.1 Ergodicity . . . . .	24
2.1.5.2 Detailed Balance . . . . .	25
2.1.5.3 Residence times . . . . .	25
2.2 Numerical Algorithms . . . . .	25

2.2.1	Standard KMC method . . . . .	27
2.2.2	First-passage Kinetic Monte Carlo method (FPKMC) . . . . .	28
2.3	Construction of the transition rate matrix . . . . .	30
2.3.1	Transition state theory . . . . .	30
2.3.2	Effect of elastic field on point defects . . . . .	30
2.3.2.1	Elastic Dipole Tensor . . . . .	32
2.3.2.2	Elastic interaction energy . . . . .	34
2.4	Summary . . . . .	34
<b>3</b>	<b>Fast first-passage algorithms for reversible diffusion processes</b>	<b>36</b>
3.1	Introduction . . . . .	37
3.2	Theory and methods . . . . .	39
3.2.1	Master equation and evolution operator . . . . .	39
3.2.2	Standard Kinetic Monte Carlo . . . . .	39
3.2.3	First-passage kinetic Monte Carlo . . . . .	41
3.2.4	Application of absorbing Markov chains . . . . .	41
3.3	Mathematical derivation . . . . .	43
3.3.1	Conditional reversibility . . . . .	43
3.3.2	Spectral decomposition of the evolution operator . . . . .	45
3.3.3	No-passage and quasi-stationary distributions . . . . .	46
3.3.4	Expected values of first-passage times, residence times and exit probabilities . . . . .	47
3.3.5	Rank-one update . . . . .	48
3.3.6	Path factorization and space-time randomization . . . . .	49
3.4	Elasto-diffusion of vacancies in Aluminium . . . . .	51
3.4.1	Vacancy emission flux from cavity . . . . .	51
3.4.2	Computational complexity and stability . . . . .	55
3.4.3	Survival probabilities and spectral truncation . . . . .	58
3.5	Diffusion of Mn-V clusters in $\alpha$ -iron . . . . .	64
3.6	Summary . . . . .	68
<b>4</b>	<b>First passage algorithms based on Krylov subspace projection and eigenvalue deflation</b>	<b>71</b>
4.1	Introduction . . . . .	72
4.2	Model Order Reduction and Iterative Methods . . . . .	73
4.2.1	Eigenvector Subspace Model Projection . . . . .	73
4.2.2	Krylov Subspaces . . . . .	74
4.2.3	Krylov Subspace Model Projection . . . . .	75
4.2.4	Eigenvector and Krylov Subspace Model Projection . . . . .	76
4.3	Implementation . . . . .	77
4.4	Numerical results and analysis . . . . .	78
4.4.1	Efficiency and scalability of eigensolvers . . . . .	78
4.4.2	Survival Probabilities . . . . .	81
4.4.3	Vacancy absorption kinetics . . . . .	89
4.5	Summary . . . . .	93
<b>5</b>	<b>Characterization and computation of sink strengths</b>	<b>96</b>
5.1	Reaction rate theory . . . . .	97

5.2	Sink strengths . . . . .	98
5.2.1	Analytical solution to sink strength . . . . .	98
5.2.1.1	Laplace’s approach . . . . .	98
5.2.1.2	Poisson’s approach . . . . .	99
5.2.1.3	Wiederisch’s approach . . . . .	100
5.2.2	Numerical approaches to sink strengths computation . . . . .	101
5.3	Characterization of sink strengths: single vacancy absorption to the cavity . . . . .	103
5.4	Sink strengths for mixed mobilities . . . . .	107
5.5	Agglomeration between two interstitial clusters in $\alpha$ -Fe . . . . .	109
5.6	Summary . . . . .	113
	<b>Conclusions</b>	<b>115</b>
	<b>Perspectives</b>	<b>118</b>
<b>A</b>	<b>Algorithmic implementation</b>	<b>120</b>
A.1	Path factorization . . . . .	120
A.2	Spacetime randomization . . . . .	120
A.3	Reformulation of path factorization . . . . .	122
A.3.1	LU decomposition . . . . .	122
A.3.2	Cholesky decomposition . . . . .	126
<b>B</b>	<b>Restarted Krylov Subspace Projection</b>	<b>128</b>
<b>C</b>	<b>Cholesky preconditioning</b>	<b>131</b>
<b>D</b>	<b>Theory of Elasticity</b>	<b>135</b>
D.1	Strain Tensor . . . . .	135
D.2	Stress Tensor . . . . .	137
<b>E</b>	<b>Algorithm for 1D-1D mobility</b>	<b>140</b>
<b>F</b>	<b>Résumé du manuscrit</b>	<b>144</b>
<b>G</b>	<b>Publications and Oral presentations</b>	<b>147</b>
	<b>Bibliography</b>	<b>148</b>



# List of Figures

1.1	Schematic representation of the reactor pressure vessel from a PWR [15] . . . . .	7
1.2	Component of RJH reactor - part of core fabricated using 6061 T6 aluminum alloy. . . . .	9
1.3	Evolution of a stress-strain curve after irradiation [19]. . . . .	10
1.4	Evolution of a stress-strain curve for A533B steel for different neutron exposures [20]. . . . .	10
1.5	Representation of shift in ductile to brittle transition temperature ( $\Delta TT$ ). . . . .	12
1.6	Schematic representation of the stages of evolution of a collision cascade [35] - damage by neutron irradiation. . . . .	13
1.7	Point defects in a crystal (a) SIA, (b) vacancy, (c) substitutional impurity, and (d) interstitial impurity [38]. . . . .	15
1.8	Schematic representation of the multi-scale simulation method [44]. . . . .	16
2.1	Schematic representation of random sequence which is also an AMC with three absorbing ( $X_1, X_2, X_5$ ) and two transient states ( $X_3, X_4$ ). Red arrows represents the transitions to absorbing state with probability equal to one, and black arrows represent the transition probabilities equal to less than one. . . . .	22
2.2	Schematic representation of first passage and no passage distributions of two random diffusing particles initially at time $t = 0$ in panel (a). First-passage time is $t'$ in panel (b) and (c) [8, 75]. . . . .	28
2.3	Reaction progression for point defect going from initial state $i$ to final state $j$ [90, 91] . . . . .	31
2.4	Representation of a vacancy by the forces. $u(\mathbf{r}^q)$ is the displacement field of atoms (grey circle) induced by the vacancy (light blue square), while $\mathbf{F}^q$ is the field of forces applied to a perfect lattice in order to produce the same displacement field $\mathbf{u}$ [101]. . . . .	33

- 3.1 Schematic of FPKMC method for two vacancies evolving on a square lattice symbolizing a FeMn alloy. Fe and Mn atoms are displayed in orange and violet. Vacancies  $V^1$  and  $V^2$ , represented by the two labeled squares, are initially trapped inside Mn clusters. Exit sites for the trapped vacancies are indicated by stars. First-passage events are represented by dotted arrows. Events occurring first and second are colored in green and red, respectively. The sequence of events is as follows: (a) The two  $V$ -Mn clusters are spatially protected; First-passage times  $t_{fp}^1$  and  $t_{fp}^2$  are drawn (here  $t_{fp}^2 < t_{fp}^1$ ); (b)  $V^2$  dissociates from Mn cluster, diffuses and collides with spatial protection of  $V^1$  at time  $t_{col}^2$  (here  $t_{col}^2 < t_{fp}^1$ ); A no-passage event [8, 75, 76, 84, 86], materialized by the green solid arrow, is generated for synchronization; (c)  $V^2$  attaches to the  $V^1$ -Mn cluster (nearest neighbor interactions are assumed); (d) a diffusing entity composed of two vacancies is created and spatially protected. Vacancy locations inside the thick solid line correspond to states that are referred to as *transient* in the theory of absorbing Markov processes. *Absorbing* states are those with the vacancy located on a starred site, beyond the solid line and before the dashed line. . . . . 42
- 3.2 Emission of a single vacancy from the centered gray cavity of radius 20.7 Å to the absorbing sphere of radius 101 Å: Panels (a) and (b) display the residence times using two distinct color scales; Panels (c) and (d) display the radial and orthoradial vacancy fluxes, respectively. Coordinates of displayed sites satisfy  $\hat{\mathbf{r}}_j \cdot \hat{\mathbf{k}} = 0$  where  $\hat{\mathbf{k}}$  is the normalized basis vector orthogonal to (001). The Euclidean norm  $\|\hat{\mathbf{r}}_j\|$  corresponds to the distance to the cavity center and  $\theta(\|\hat{\mathbf{r}}_j\|)$  is the average residence time on the centered sphere of radius  $\|\hat{\mathbf{r}}_j\|$  and surface area  $4\pi\|\hat{\mathbf{r}}_j\|^2$ . Vector  $\hat{\mathbf{n}}_j = \hat{\mathbf{r}}_j/\|\hat{\mathbf{r}}_j\|$  is the normalized radial vector. The cross product  $\hat{\mathbf{n}}_j \times \hat{\mathbf{k}}$  corresponds to the orthoradial direction of the flux at  $\hat{\mathbf{r}}_j$ . . . . . 53
- 3.3 Anisotropy of peripheral site absorption for vacancies emitted from a small Aluminum cavity. Absorbing probability vector is  $\mathbf{p}^{aT} = \boldsymbol{\pi}^T \mathbf{P}^{(N)}$ . Red and blue coloration respectively indicates values larger and lower than the one average for the displayed site absorbing probabilities. The inverse mean probability corresponds to the number of peripheral sites. Cavity and protection radii are 20.7 Å and 101 Å, respectively. . . . . 54
- 3.4 Comparative cost of direct and iterative linear solvers. See text for details on the solvers. Simulations are performed on an Intel 4-Cores i5-4310U processor running at 2.00GHz with 8GB memory. OpenMP shared-memory parallelism is enabled for  $LDL^T$  factorization. . . . . 56

3.5	Effect of scaling matrix $\mathbf{B}$ on accuracy of residence and first-passage time calculations. The residual norms and condition numbers are displayed for two setups: $\mathbf{B}$ equal to $\mathbf{I}$ and $\Delta = \text{Diag}(\mathbf{A})^{-1}$ . The corresponding mean-first passage times, evaluated from $\boldsymbol{\pi}^T \boldsymbol{\tau}^{(N)}$ and $\boldsymbol{\theta}^T \vec{\mathbf{1}}$ , are displayed for comparison. Note that $\ \vec{\mathbf{1}}\ _1 = N$ and $\ \boldsymbol{\pi}\ _1 = 1$ . . . . .	57
3.6	Emission of a single vacancy from cavity (4.04 Å radius) to protective sphere (10.1 Å radius). The survival probabilities (left axis) and first-passage distributions (right axis) are evaluated from the quasi-stationary distribution (Lowest Eigenvalue), the exact distribution (Full Spectrum) and randomization (Factorization). Time is given in unit of mean first-passage time (mfpt). . . . .	59
3.7	Emission of a single vacancy from the cavity (20.7 Å radius) to the protective sphere (101 Å radius). Survival probabilities and first-passage distributions are respectively plotted in panels (a) and (b) using various truncation thresholds $k$ . . . . .	60
3.8	Absorption of a single vacancy by the cavity (20.5 Å radius). Survival probability distribution [panel (a)] and first-passage distribution [panel (b)] as a function of time. . . . .	61
3.9	Effect of retaining the $k$ lowest modes for approximating the reduced mean first-passage time $\mathcal{T}_k$ [panel (a)] and the initial survival probability [panel (b)]. . . . .	62
3.10	Absolute values of $\alpha_k$ contributing coefficients displayed as a function of the eigenvalues scaled relatively to the lowest eigenvalue $\lambda_1$ . . . . .	63
3.11	Diffusion coefficients of Mn solute atoms as a function of cluster size for various temperatures. For clarity, scaling is done relative to monomer diffusivity at $T_0$ and its high temperature activation energy $E^a = 0.646$ eV. Reference temperature is $T_0 = 600$ K and reference diffusivity is $D(1, T_0) = 6.716 \cdot 10^{-15} \text{m}^2/\text{s}$ at vacancy concentration of 5‰. . . . .	66
3.12	Relative efficiencies of the algorithms as a function of cluster size. Efficiency is evaluated as the ratio of the simulated physical time to that of F-KMC for a given wall-clock time. Filling around curves corresponds to the 68% confidence interval. . . . .	67
4.1	Comparison of CPU cost for four different iterative solvers (EPS) based on extracting the indicated number of requested eigenvalues (EV). . . . .	79
4.2	CPU times for extracting 100 eigenvalues using Krylov-Schur method without preconditioning and with Cholesky preconditioning as a function of the cell size ( $L$ ). . . . .	80
4.3	Evaluated cost for extracting 100 eigenvalues using Krylov-Schur method in sequential and parallel computations as a function of number of transient states $N = L \times L$ with varying the number of cores ( $N_c$ ). . . . .	81

4.4	Computed (a) Speedup ratio and (b) Efficiency of Krylov-Schur method for varying transient states ( $N = L \times L$ ) as a function of cores ( $N_c$ ). . . . .	82
4.5	(a) Survival probability distribution computed using ESMP (2500 and 3500 eigenvalues), and R-KSP plotted in blue, green, and red, respectively. (b) CPU cost for computing survival probability vector at a particular instant of time using R-KSP. . . . .	84
4.6	Comparison of survival probabilities and first passage distributions evaluated for the localized initial distribution using the KSMP method is presented in panels (a,b), and the EKSMP method is presented in panels (c,d). . . . .	85
4.7	Comparison of survival probabilities and first passage distributions evaluated for the uniform initial distribution using the KSMP method is presented in panels (a,b), and the EKSMP method is presented in panels (c,d). . . . .	86
4.8	Comparison of (a) survival probabilities $S_k(0)$ , (b) reduced MFPT $T_{k,\ell}$ computed for ESMP (3500 eigenvalues), KSMP (500 eigenvalues) and EKSMP (500 eigenvalues) methods. The panel (c) represents the zoomed in plot for the range of reduced MFPT $T_{k,\ell}$ from 0.92 to 1.04 for the respective methods. . . . .	88
4.9	Reduced and truncated MFPT $T_{1,\ell}$ evaluated for a localized and uniform initial distribution using EKSMP method. . . . .	88
4.10	Estimation of residence times (a,b), radial vacancy flux (c), and ortho-radial vacancy fluxes (d) starting from a localized initial distribution. Absorption of a single vacancy initially located at a distance of 57.98 Å from the cavity center in $\langle 100 \rangle$ crystalline directions. Coordinates of displayed sites satisfy $\hat{r}_j \cdot \hat{k} = 0$ where $\hat{k}$ is the normalized basis vector orthogonal to (001). . . . .	90
4.11	Estimation of residence times (a,b), radial vacancy flux (c), and ortho-radial vacancy fluxes (d) using a uniform initial distribution. The cavity center is in $\langle 100 \rangle$ crystalline directions. Coordinates of displayed sites satisfy $\hat{r}_j \cdot \hat{k} = 0$ where $\hat{k}$ is the normalized basis vector orthogonal to (001). . . . .	91
4.12	Estimated quasi-stationary distribution (a), anisotropy of quasi-stationary distribution probability (b), anisotropy of radial vacancy fluxes (c), and anisotropic ortho-radial vacancy fluxes (d) for the localized initial distribution. . . . .	92
5.1	Sink geometry with spherical symmetry. . . . .	99
5.2	Comparison of absorption efficiencies calculated for the sink absorption model using MFPT from Eq.(3.25) and uniform initial distribution to those obtained from Laplace, Poisson, and Wiedersich approaches. . . . .	104

5.3	Distances traveled by the vacancy before absorption scaled by the minimum distance separating the sinks, for uniform and localized initial distributions, and plotted as a function of the separating distance. . . . .	105
5.4	Using uniform distribution, (a) estimation of anisotropic sink strengths for the site $j$ , and (b) evolution of the sink strengths parameter over a radial distance between the cavity and the vacancy. . . . .	105
5.5	Schematic view of the geometric condition for the interaction of two non-coplanar particles with glide direction $\vec{l}_A$ and $\vec{l}_B$ respectively (from [173]). . . . .	108
5.6	Schematic view of the trajectory of two absorbing 1D random walkers (black circles with $\vec{l}_A$ and $\vec{l}_B$ jump vectors) and the 2D-random walk of their midpoint (blue solid and dashed circles for the current and past positions respectively) being absorbed by a fixed sink sitting at the intersection of their glide directions (from [173]). . . . .	108
5.7	Flowchart representing the formulation of transition rate matrix and sink strengths for two 1DR-1DR mobile interstitial clusters in super cell. . . . .	110
5.8	Schematic view of hops for cluster A in glide direction represented as a segment for $2^N - 1$ sites where $N$ is the number of transient states. . . . .	111
5.9	Comparison of mean first-passage times (MFPT) for $N$ transient states computed with KMC and kPS methods. . . . .	111
5.10	Comparison of absorption efficiencies and sink strengths calculated for the sink absorption model using algorithm 4. . . . .	112
D.1	Deformation of a solid body. . . . .	136



# List of Tables

4.1	CPU time taken by ESMP, KSMP, and EKSMP methods to compute the first passage distributions for the single vacancy absorption. Processor A is Intel(R) Xeon(R) Gold 6132 CPU, each node running at 2.60GHz with $2 \times 14$ cores. Processor B is Intel i5-8400H running at 2.5GhZ with eight cores. CP stands for Cholesky preconditioning using MUMPS package and $N_c$ is the used number of cores. . . . .	87
5.1	Analytical solution of absorption efficiency by different approaches for spherical sink geometry [14, 164]. The term $r_{cv}$ is the equal to sum of the cavity radius and the vacancy radius i.e. $r_{cv} = r_{ca} + r_V$ . We estimate $\eta$ in Wiedersich approach as $r_{cv}/R$ . . . . .	103
C.1	CPU time taken by ESMP method to extract the indicated number of eigenvalues (NEV) for the vacancy absorption model. The simulations are performed using a single core of an Intel i5-8400H processor (running at 2.5GhZ). Parameter NCV represents the maximum dimension of the working subspace to be used by the solver. In inputs, Cholesky preconditioning (CP) may be enabled or disabled. In the outputs, C and D of the result column denote whether simulations have converged or diverged, respectively. . . . .	132
C.2	CPU time taken by ESMP to extract 10 eigenvalues for the indicated number of system size ( $N$ ) using KS solver and Cholesky preconditioning from MUMPS. . . . .	133
C.3	CPU time to evaluate survival probability distributions for the indicated number of system size ( $N$ ) using EKSMP method with $(k, \ell) = (1, 50)$ and KS solver without Cholesky preconditioning. . . . .	133



# List of Abbreviations

<b>NPP</b>	<b>Nuclear Power Plant</b>
<b>RR</b>	<b>Research Reactor</b>
<b>ME</b>	<b>Master Equation</b>
<b>KMC</b>	<b>Kinetic Monte Carlo</b>
<b>IAEA</b>	<b>International Atomic Energy Agency</b>
<b>PWR</b>	<b>Pressurized Water Reactor</b>
<b>RPV</b>	<b>Reactor Pressure Vessel</b>
<b>DPA</b>	<b>Displacements Per Atom</b>
<b>MTR</b>	<b>Material Test Reactor</b>
<b>DBTT</b>	<b>Ductile Brittle Transition Temperature</b>
<b>PKA</b>	<b>Primary Knock-on Atoms</b>
<b>DFT</b>	<b>Density Functional Theory</b>
<b>MD</b>	<b>Molecular Dynamics</b>
<b>MC</b>	<b>Monte Carlo</b>
<b>OKMC</b>	<b>Object Kinetic Monte Carlo</b>
<b>AKMC</b>	<b>Atomistic Kinetic Monte Carlo</b>
<b>LKMC</b>	<b>Lattice Kinetic Monte Carlo</b>
<b>EKMC</b>	<b>Event Kinetic Monte Carlo</b>
<b>FPKMC</b>	<b>First Passage Kinetic Monte Carlo</b>
<b>AMC</b>	<b>Absorbing Markov Chain</b>
<b>DTMC</b>	<b>Discrete Time Markov Chain</b>
<b>CTMC</b>	<b>Continuous Time Markov Chain</b>
<b>TST</b>	<b>Transition State Theory</b>
<b>RT</b>	<b>Rate Theory</b>
<b>CD</b>	<b>Cluster Dynamics</b>



*Dedicated to my dad, mom, chachu, chachi who has supported me all through my life; to Baba Deep Singh ji, and Guru Nanak ...*



# Synopsis

Radiation damages in nuclear materials adversely affect their mechanical and ageing properties [1]. In order to better understand irradiation effects in materials, computer modeling has become an indispensable complement to experimental characterization. Depending on the length scale, from a few pico-meters ( $10^{-12}$  m) to meters (m), there exist different types of computation techniques. These techniques can be categorized as solving quantum mechanical models that include the information on electrons, molecular dynamics models that incorporate the propagation of atoms/lattices, and continuum levels, including diffusion processes. Often, the changes visible at the macroscopic scale are caused by phenomena occurring at the microscopic scale. The atomic mechanisms for these phenomena are studied more thoroughly via both experimental characterization techniques and computational modeling approaches [2, 3]. To understand the micro-structural evolution of the materials, it is necessary to comprehend the physical phenomenon occurring at the microscopic scale, i.e., formation, agglomeration, and propagation of defects. The Service de Recherche en Métallurgie Physique/Physical Metallurgy Research Service in CEA-Saclay provides the research study behind nuclear material's foundation science, including experiments at the Jannus facility [4] and collaborated work with computational or numerical modeling techniques [5, 6]. This thesis presents the computational modeling approach to study the short-term and long-term effects of point defects formed under irradiation using physical theories.

The stochastic processes are categorized as Markov chains, Gaussian processes, Langevin dynamics, among others. These processes and the probability theory are commonly used as mathematical models to understand dynamic systems dealing with random variables. The most common mathematical representation of these processes is a set of differential equations known as the master equation that describes the time evolution of the probability of the system. Introductory examples for processes governed by a master equation are random walk on an integer line with possible steps in forward and backward directions, Brownian motion, the path of a diffusing particle before it gets absorbed [7, 8]. The time evolution of condensed matter systems can be simulated directly using a stochastic approach like Langevin dynamics for model systems whose phase space is continuous and Kinetic Monte Carlo (KMC) methods for discrete systems. One such discrete system where KMC is widely used is in studying the dynamics of a defect

in alloys, for instance, understanding vacancy motion in general or vacancy/interstitial clustering in ion or neutron-irradiated materials of nuclear reactors [9, 10]. While pressure vessels in industrial reactors are usually made of ferritic stainless steels, aluminum alloys are also employed in some experimental/research reactors (RR). Under irradiation, these materials lose their mechanical properties over time due to the vacancies and interstitials that recombine and form vacancy cavities and interstitial loops. This gives rise to physical phenomena such as hardening and swelling. Given its complexity, the master equation (ME) associated with the microstructural evolution [11, 12] of irradiated materials is often simulated using various KMC methods [13].

The thesis is organized as follows:

- **Chapter 1** provides readers an insight on industrial aspects of primary damage caused by irradiation in nuclear power plants. A brief description of the numerical modeling has been discussed.
- **Chapter 2** details the importance of the theory, different types, and properties of Markov chains. Further, this Chapter describes the First-passage (FP) algorithm to deal with stochastic processes. Additionally, transition state theory (TST) and theory of elasticity are also discussed as they are used in constructing the transition rate matrix.
- **Chapter 3** introduces the mathematical formalism employed in the theory of absorbing Markov chains with conditionally reversible processes. It illustrates features of the approach on two realistic problems: the elasto-diffusion of vacancies in the neighborhood of cavities [14] in pure Aluminum and the diffusion of small vacancy-Mn clusters in  $\alpha$ -iron. In addition, we discuss the ability of these new features to compute transition currents over large physical volumes and to approximate the evolution operator.
- **Chapter 4** describes model order reduction (MOR) techniques based on Krylov subspace projection and eigenvalue decomposition. First, we assess the efficiency of the various sparse iterative eigensolvers. Second, we test the efficiency of developed MOR algorithms to the physical model describing the absorption of a distant single vacancy by a cavity in Aluminum [14]. In addition, we discuss the most efficient strategy to compute the probability vector at times shorter than the mean first-passage time depending on the problem.
- **Chapter 5** focuses on the reaction kinetics using rate theory (RT). Different analytical solutions and numerical approaches to determine sink strengths are presented. In this chapter, we also discuss and present numerical approach to evaluate sink strengths for mixed mobilities of defect clusters.

The manuscript finally reviews the conclusions and avenues of future research of the work done. Annexes describe well-established techniques used in or required for this work done.



# Industrial Aspect

## Contents

---

1.1	Types of Materials . . . . .	8
1.2	Damage in reactor pressure vessels . . . . .	10
1.3	Primary damage caused by neutron irradiation . . . . .	12
1.4	Numerical modeling approach . . . . .	15
1.5	Summary . . . . .	17

---

The substantial increase in urbanization and the world’s population has led to the rise in global energy consumption. Many challenges lie in front of the human-kind to fulfill the demand of world energy consumption, also taking into account the reduction of carbon footprints<sup>1</sup>. Alongside fossil fuels, which produce 64% of the total electricity, there exists low carbon emission technologies that make 36.7% of the electricity<sup>2</sup>. One of the low carbon emission technologies is nuclear energy that contributes 10.4% to global electricity production. In the early 1950s, the nuclear power industry first came into existence in the United States of America. And up to date, as per IAEA data, there are about 440 operational nuclear power reactors<sup>3</sup> producing 393,068 MWe of electricity.

The critical difference between nuclear power reactors and other operating power reactors is the process of energy production - a controlled fission chain reaction. In this, a heavy nucleus of an atom splits into lighter nuclei, neutrons, and releases some kinetic energy, known as the fission products. These newly generated neutrons can further cause more fission reactions. Hence, the self-sustaining reaction repeats. Over the years, different nuclear power reactors from Generation I to Generation IV have been introduced.

---

<sup>1</sup><https://www.world-nuclear.org/information-library/current-and-future-generation/world-energy-needs-and-nuclear-power.aspx>

<sup>2</sup><https://ourworldindata.org/electricity-mix>

<sup>3</sup><https://pris.iaea.org/pris/>

The most common type of reactors in use today is the thermal reactors. Common examples of these reactors are light water reactors (LWR), which are further categorized based on moderator and coolant materials: the pressurized water reactor (PWR), the boiling water reactor (BWR), and the supercritical water reactor (SCWR). After the USA, France is the second-largest country that produces 70% of the electricity by using its 56 pressurized water reactors (PWRs) that are part of Generation II reactor design.

A typical nuclear reactor operates on three distinct yet inter-connected circuits: primary, secondary, and tertiary. The primary circuit comprises a reactor pressure vessel (RPV) which is the source of energy generation. The inside of RPV is a complex structure with approximately 13.2m of height and 5.5m in diameter (depicted in Fig. 1.1) designed by taking into account all the safety guidelines<sup>4</sup>. It is because of the presence of nuclear fuel assemblies. These fuel assemblies consist of uranium oxide (UO<sub>2</sub>) fuel pellets encased in a zircaloy cladding. The secondary circuit consists of the coolant and the heat exchange system. The reactor coolant pump pumps the water to the primary circuit (i.e., into the RPV), transfers the generated energy out of the reactor core in the form of steam. Later, the steam of the secondary circuit drives the steam turbine and condenses in a condenser again to water to feed it back to steam generators. In the last stage, the heat released in the condenser is discharged via a cooling water system (tertiary circuit) to the river or the cooling tower.

The materials used in the construction of NPPs are thoroughly examined, both theoretically and experimentally. In case of RPV, it is important to employ material with high structural integrity such that RPV structure undergoes less of a damage due to radiation. Thus, Research reactors (RR)<sup>5</sup> are used to study primary radiation effects in materials. Different testbeds in various shapes, sizes, and types are used to evaluate the structural materials and fuel assemblies for NPP. The primary function of RR is to generate neutrons via fission reaction for nuclear education and training purposes, to analyze neutron activation and neutron scattering studies, among others [16]. One such RR used to study structural changes in materials using intense neutron irradiation is Material testing reactors (MTR). Choosing the right materials used for the construction of an RPV is vital as NPP operates at high temperatures at which structural changes such as embrittlement at macro scale are visible. One such example of MTR is the Jules Horowitz Reactor (RJH) in Cadarache, France, which will contribute to the development and qualification of materials and nuclear fuel used in the future NPP or optimization for existing NPP.

This chapter aims at giving the physical background behind the importance of the materials used in nuclear reactors and research reactors. First, a piece

<sup>4</sup>[https://www-pub.iaea.org/MTCD/publications/PDF/Pub1013e\\_web.pdf](https://www-pub.iaea.org/MTCD/publications/PDF/Pub1013e_web.pdf)

<sup>5</sup><https://www.world-nuclear.org/information-library/non-power-nuclear-applications/radioisotopes-research/research-reactors.aspx>

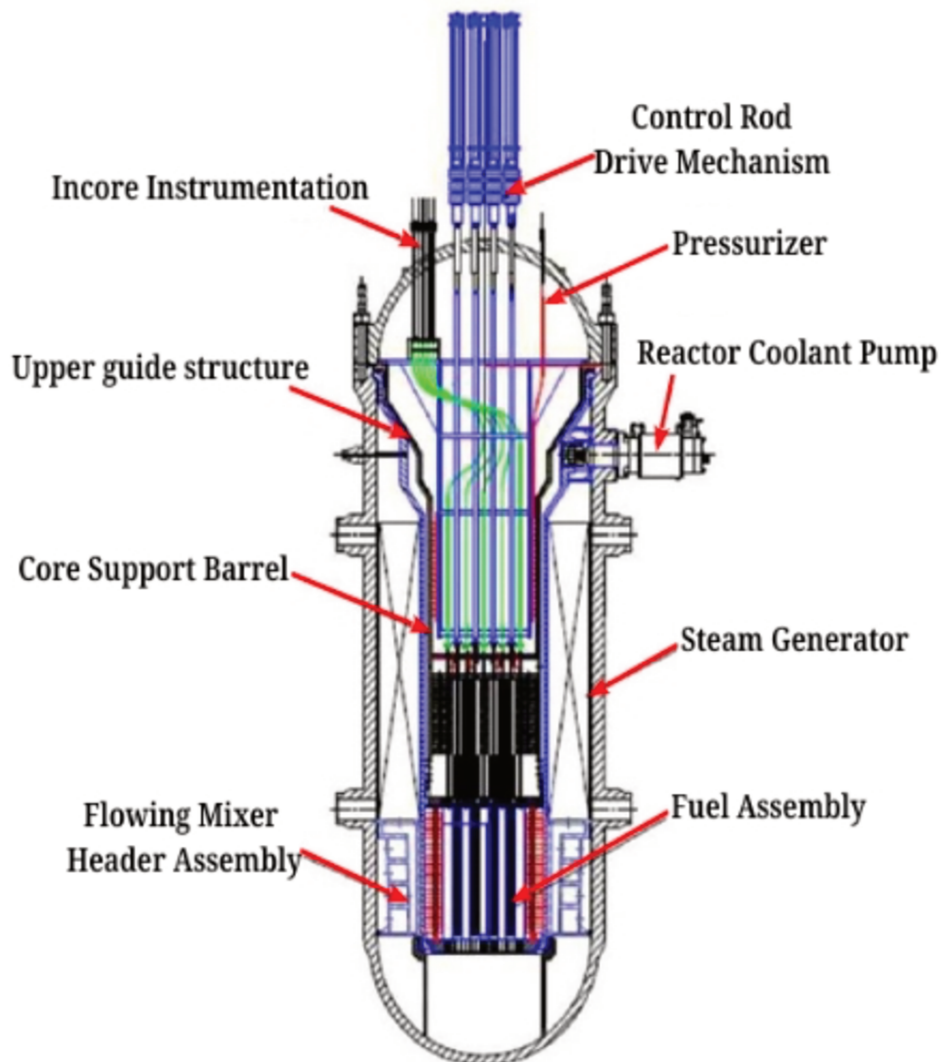


**Figure 1.1:** Schematic representation of the reactor pressure vessel from a PWR [15]

of brief information on materials used for RPV components in NPPs is presented in Section. 1.1. Then in Section. 1.2, we briefly introduce the structural evolution of materials undergoing nuclear irradiation. Finally, in Section. 1.4, we provide insight on multi-scale computational modeling of nuclear materials.

## 1.1 Types of Materials

There are numerous components in NPPs with the complex design as it operates in different circuits as discussed above. The RPV is the most difficult and expensive component to be fixed or replaced [17]. Thus, it is a limiting factor to achieve a long-term operation. The fission chain reaction occurring in the reactor core produces a high amount of energy that can lead to the fracture of the RPV's material. In PWRs, the heavy steel RPV must withstand the pressure ranging from 14 to 17 MPa, coolant temperature around 290°C, and high energy neutrons to achieve thermodynamic efficiency [2]. The structural materials employed in an RPV's internal structure, such as a reactor core, are austenitic stainless steels and nickel-based alloys in commercial NPPs to protect from corrosion. The material used for commercial RPVs fabrication is low alloy ferritic steels, including different solutes such as Ni, Si, Mn, etc. These solutes are added to enhance the mechanical properties of the steel (structural integrity) [18].

In conventional operating mode of an NPP, the energy in form of heat produced due to the fission reaction produces an electrical output. Some amount of energy stored reflects in the nuclear activation of defects. Therefore, the structural materials that resist less heat are favored. RRs perform studies to minimize the heat generation by non-fissile materials. In RR, aluminum alloy is used to construct many components, including RPV (which usually withstand coolant temperatures > 100°C). By the exact naming, it is a 6061-aluminum alloy that contains magnesium and silicon as their major alloying elements as depicted in Fig. 1.2. Different properties of aluminum alloy have been discussed in the Ref. [16].



**Figure 1.2:** *Component of RJH reactor - part of core fabricated using 6061 T6 aluminum alloy.*

## 1.2 Damage in reactor pressure vessels

The entire functioning of the nuclear reactor core provides exposure of high-energy neutrons to the internal components of RPV due to fission reaction. These high-energy neutrons damage the material and alter its mechanical properties. The RPV steels usually exhibit high fracture toughness. However, neutron irradiation increases the hardness and reduces the ductility, impeding the motion of atoms in the materials, causing dislocations. With the increase in hardening, there will be a change of the tensile properties as well (the yield stress and ultimate tensile strength increase with increased neutron fluence), as illustrated in Figs. 1.3 and 1.4.

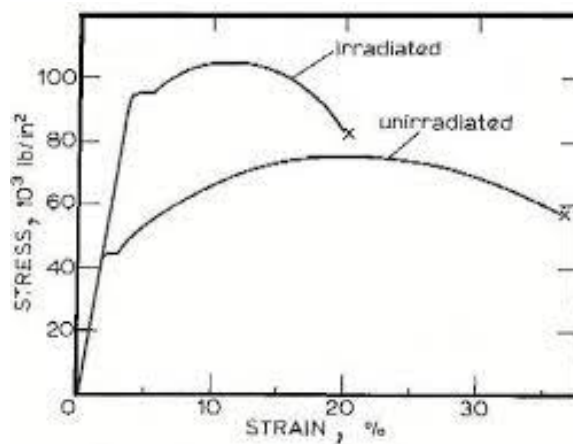


**Figure 1.3:** Evolution of a stress-strain curve after irradiation [19].

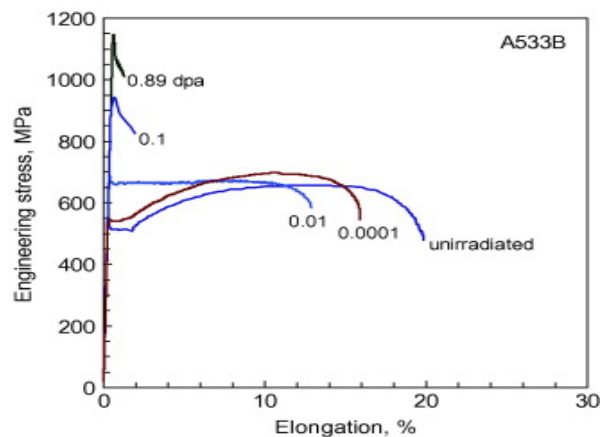


**Figure 1.4:** Evolution of a stress-strain curve for A533B steel for different neutron exposures [20].

The RPV is the component which receives least amount of neutron flux i.e.

dose rate. At end of cycle (EOC) of the reactor, it receives of total neutron fluence<sup>6,7</sup> from  $5 \times 10^{22} \text{ m}^{-2}$  to  $1.6 \times 10^{24} \text{ m}^{-2}$ , which is also equivalent to 0.0075-0.24 displacements per atom (dpa) that leads to embrittlement in the RPV steel [2, 21]. The displacements-per-atom which is a dimensionless quantity, given as

$$\text{dpa} = \frac{\text{Number of displaced atoms in the given volume}}{\text{Total number of atoms in the given volume}} \quad (1.1)$$

Further, the number of displaced atoms can be quantified by the formula

$$N_d = \frac{\mathcal{K}(E - \hat{Q})}{2E_d} = \frac{\mathcal{K}\hat{E}}{2E_d} \quad (1.2)$$

where  $\mathcal{K}$  is the displacement efficiency,  $\hat{Q}$  is the total energy lost in the cascade by electronic excitation,  $E_d$  is the displacement threshold energy,  $E$  is the primary knock-on atom (PKA) energy, and  $\hat{E}$  is the damage energy for the atom displacement [22]. This method was first proposed in 1975 [22] to analyze the total number of defects created in terms of deposited energy. If the damage energy is high enough, then it causes the displaced atoms to induce other atomic displacements as well, hence damaging the crystal lattice site [3]. The model discussed by Ref. [22] is widely used to study the displacement rates. The primary damage caused by irradiation is discussed more briefly in Sec. 1.3.

Vessel integrity analysis requires activities from in-service flaw inspections to thermal-hydraulic stress analysis. The actual issue in material damage does not lie in the toughness of the fabricated RPVs. However, it is the exposure to neutrons in the beltline region of the RPV that surrounds the reactor core. Indeed it degrades fracture toughness of RPV steels [23]. A familiar method used to investigate embrittlement caused by neutron irradiation is to estimate its ductile-brittle transition temperature (DBTT) [24]. This quantity marks the transition between low toughness brittle and high toughness ductile fracture regimes. The transition temperature can also be determined by Master curve methodology [25, 26]. Figure 1.5 represents the DBTT ( $\Delta T$ ) shift. The transition temperature in certain cases exceed  $200^\circ\text{C}$  [27].

Nuclear regulatory bodies initiated several surveillance programs to understand more about the degradation of RPV steels. In France, PSI (Programme de Surveillance à l'Irradiation) was the first monitoring program established in early 1970 [25, 28, 29]. The surveillance capsules of the steels similar to those used for the fabrication of RPV are used. The required samples of RPV steels are mounted in the reactor core and later are collected to investigate the ageing of the steels. These samples experience neutron flux higher than what a typical RPV experiences in normal operating conditions. These sample capsules are extracted periodically and tested for tensile strength, ductility, and

<sup>6</sup>Neutron fluence is defined as the flux integrated over time ( $\text{n}/\text{m}^2$ ).

<sup>7</sup>Neutron flux is defined as the number of neutrons crossing a unit area per unit time ( $\text{nm}^{-2}\text{s}^{-1}$ ).

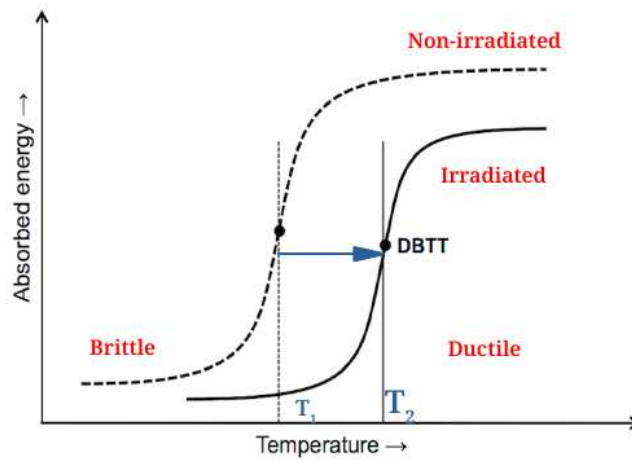


**Figure 1.5:** Representation of shift in ductile to brittle transition temperature ( $\Delta TT$ ).

fracture mechanical properties [24, 30, 31, 32]. The data obtained from this set of evaluations, combined with neutron-irradiated materials from experimental reactors, for example, MTRs, provides crucial information on irradiated materials. However, the number of test samples is limited and due to the operational life-cycle constraint, repeated extraction of the samples is not an ideal solution [3]. Thus, in addition to the experimental approach, multi-scale computational modeling approach is also necessary to complement the study of primary damage and altered mechanical properties in materials due to irradiation which is discussed in next section.

### 1.3 Primary damage caused by neutron irradiation

The radiation damages or effects seen at macroscopic levels are due to the structural modifications at the atomic level, i.e., high-energy neutrons in MeV. The whole process is known to follow three phenomena; nuclear activation, transmutation, and atomic displacement [3, 33, 34]. All these three effects are harmful, and the consequence (embrittlement) depends majorly on the neutron field (neutron flux, fluence, and energy), irradiation temperature, and impurities present in the steels. The irradiation temperature ranges between 300°C to 400°C, which plays a vital role in investigating the damage. The atomic processes such as diffusion, recombination, annihilation, and segregation of defects depend on the temperature [24]. In addition, minor alloying elements such as Copper and Phosphorus acts as additional elements that impact the irradiation effects [17].

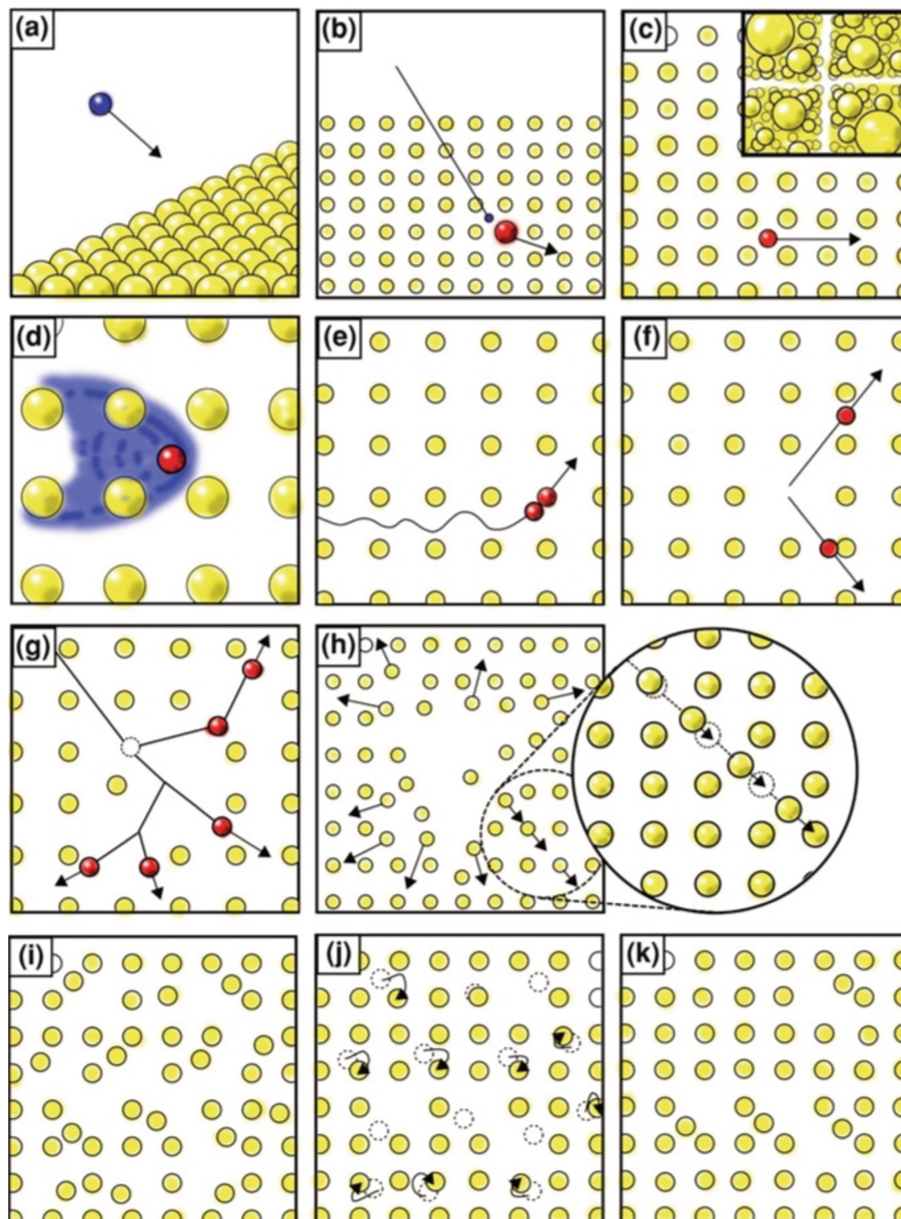


**Figure 1.6:** Schematic representation of the stages of evolution of a collision cascade [35] - damage by neutron irradiation.

High energy neutrons interact with the surrounding or target materials; if it is an elastic interaction, some energy is imparted to an atom (see Fig. 1.6 (a)). The energy, if higher than the threshold displacement energy ( $E_d$ ), then an atom is ejected from the lattice by creating a vacancy and interstitial defect (typically  $\sim 30$  eV) [11]. The point defects make nano-scale changes in the alloys that cause material hardening [36]. In the case where the neutron energy

is higher than  $2E_d$ , then the targeted atom becomes the PKA (see Fig. 1.6 (b)) and removes other atoms from the lattice sites [37]. If PKA has kinetic energy  $\sim 80$  keV, the target atom will be able to travel without any collision and be responsible for the material's damage. This process is known as channeling Fig. 1.6 (c). The mobile channeling target atom interacts with the surroundings and loses its energy to the other target material (Fig. 1.6 (d)). Eventually, the PKA will slow down and will go under another collision with another atom (Fig. 1.6 (e)). Depending on their energies from the collision, it could be possible for them to move further and cause sub-cascade branching (Fig. 1.6 (f)). Once the kinetic energies of the moving atoms get below  $\sim 30$  keV, the interactions with the surrounding will get strong, and further collisions will get frequent to cause the displacement phase of the cascade. An approximate value for the lifetime of a displacement cascade is few picoseconds ( $10^{-12}$ ). The region displaced on the lattice site by cascade of collisions forms displacement (Fig. 1.6 (g)) spike initiated from its equilibrium position and has a length of a few nano-meters ( $10^{-9}$ m). The whole displacement cascade is categorized into three phases: ballistic phase, thermal spike, and recombination phase (refer to chapter 15 from the book [3, 32]). The region of irradiation damage caused by displaced atoms constitutes point defects such as self-interstitial atoms, and vacancies [1]. Defects such as vacancies are the missing atoms from their actual lattice position, and interstitials are atoms present in non-lattice positions. Figure. 1.7 depicts the schematic of point defects. During the evolution, point defects agglomerates and form clusters. Thus, the lattice site's final configuration could be a vacancy-rich region neighboring SIAs (probably in clusters), commonly known as cascade debris. This whole process is known as the primary damage of neutron irradiation.

Usually, SIAs defects migrate faster than the vacancies. As per the natural phenomena, the defects migrate and get absorbed in sinks. Here, sinks are defined as the particular characteristic at a micro-structural level in which the defects are absorbed/annihilate through the recombination process when they encounter each other. Dislocations, grain boundaries are examples of sinks for single point defects and the clusters [3, 39, 40]. An example of a three-dimensional cavity is a cluster of point defects that act as a sink for single point defects. These clusters then grow and migrate [41]. Therefore, it is essential to know the size and the density of the sinks and the defect migration mechanism to determine the distance traveled by the defects. The vacancy clusters are usually less mobile if they grow in size, and they become voids visible through Transmission electron microscopy (TEM). Whereas small clusters or single vacancies are noticeable using Positron annihilation spectroscopy (PAS) or Small-Angle Neutron Scattering (SANS) [24, 42, 43].

All microscopic effects occurring over time due to the defects generation at nano-meters scale highly compromise the ability of a material to maintain its integrity with visible consequences at macroscopic levels. Quoting the literature, "these radiation effects are a multi-physics problem - implying the

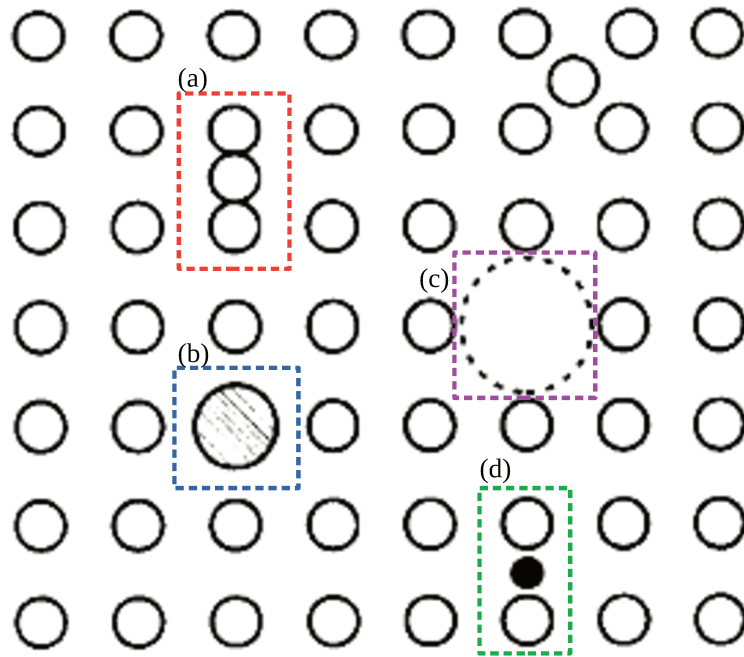


**Figure 1.7:** Point defects in a crystal (a) SIA, (b) vacancy, (c) substitutional impurity, and (d) interstitial impurity [38].

involvement of classical physics, modern physics, nuclear physics, atomic physics, thermodynamics, mechanics" [2]. Since there are many dependent factors, the convolution of the problem does require support from the numerical tools. Furthermore, various computational modeling techniques depend on the length scale, i.e., atomic-level interactions to mechanical modeling, and are presented in the following Section. 1.4.

## 1.4 Numerical modeling approach

The experimental approach is not enough to understand the evolution of the materials at the nano-scale, which results in the visible macroscopic consequences. In this case, computational simulation models are essential to support the experimental data. The multi-physics and multi-scale nature of the radiation effects make it more challenging to comprehend and develop numerical simulations. The computational approach usually requires quite a long CPU times but is relatively cheaper than experiments. However, results from experimental and theoretical modeling are complementary to each other. Usually, the simulation length scale starts from a few pico-meters ( $10^{-12}$ ) and goes up to meters (m). Thus, each stage is characterized by the modeling techniques depicted in Fig. 1.8.

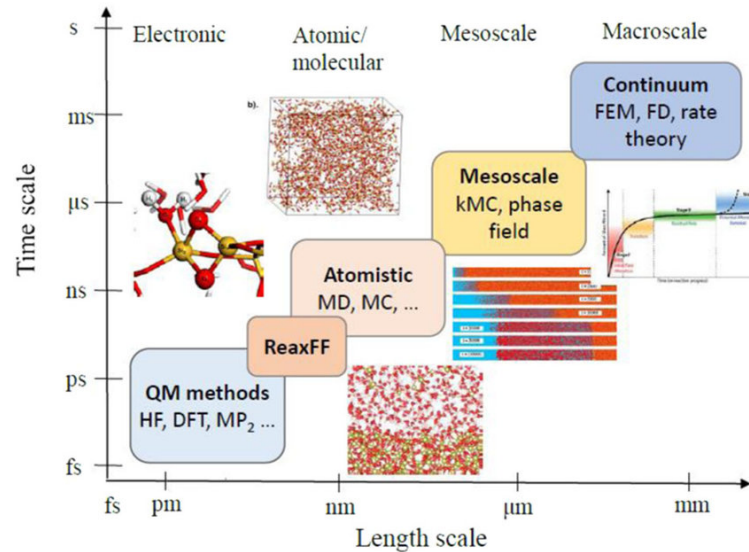


**Figure 1.8:** Schematic representation of the multi-scale simulation method [44].

Starting from the lowest scale, i.e., the atomic level interactions, ab-initio quantum mechanical (QM) calculations, often based on density functional theory (DFT) are used [5, 45]. The main aim of DFT calculations is to determine the ground state energy of the interacting particles in the given system. It is a one-body formulation of the many-body quantum mechanical problem and is governed by the Schrödinger equation. However, limitation arises in their application when the system size increases. So only clusters of a few point defects can be studied using DFT. The DFT simulations become very expensive in CPU time. To avoid the limitation of the restricted size of the system and the CPU time, two approaches based on approximate methods are Molecular dynamics (MD) and the Monte Carlo methods (MC). MD simulations are often deterministic, whereas MC is always probabilistic [3]. With the current configurations of the recent computers, system sizes of up to  $10^7$  atoms can be studied using MD simulations [46]. It is often challenging to validate the results obtained from the MD simulations via experiments because the limitation is the simulated time, which corresponds to the cascade timescale. So, the output of the MD simulations is given as an input to the MC method. The MC method encompasses a many algorithms and covers numerous families of versatile approaches based on stochastic modeling. An example is the Markov Chain Monte Carlo method. MC methods consist of drawing from a probability distribution, performing numerical integration analysis, and solving the optimization problem. The first set of simulations performed using MC methods in materials science was to study the short-term annealing of defects in fcc (face-centered cubic) and bcc (body-centered cubic) materials [47, 48]. Over the decades, many MC methods have developed [49], and nowadays, the Kinetic Monte Carlo (KMC) method is being used quite extensively in materials science [13, 50, 51]. In this thesis work, we develop an evolution laws for the point defects by implementing the theory of absorbing Markov chains.

## 1.5 Summary

In this chapter, we briefly presented the materials used in nuclear power plants and research reactors. These materials specially for reactor pressure vessel steels are deteriorated under neutron irradiation due high energy neutrons. The phenomenon that affects the mechanical properties is well known as primary damage. It is caused by the different kinds of point defects such as vacancies and interstitials that are created at microstructural level. To study the microstructural evolution experimental studies are validated with numerical approach. We have briefly discussed about different kinds of multi-scale numerical approaches. In a multi-scale modeling approach, a chain of simulation techniques is formed from highly accurate DFT calculations for the smaller scales to MC methods for approximated simulations at higher order scale. In the next chapter, we discuss the theory of Markov chains, first-passage events, and present algorithm based on first-passage events.



# Theoretical Context and Objectives

## Contents

---

<b>2.1 Markov Chains and first-passage events . . . . .</b>	<b>20</b>
2.1.1 Discrete Time Markov chain . . . . .	20
2.1.2 Continuous Time Markov chain . . . . .	21
2.1.3 Absorbing Markov chains . . . . .	21
2.1.4 First-passage events . . . . .	23
2.1.5 Properties of Markov chain . . . . .	24
<b>2.2 Numerical Algorithms . . . . .</b>	<b>25</b>
2.2.1 Standard KMC method . . . . .	27
2.2.2 First-passage Kinetic Monte Carlo method (FPKMC)	28
<b>2.3 Construction of the transition rate matrix . . . . .</b>	<b>30</b>
2.3.1 Transition state theory . . . . .	30
2.3.2 Effect of elastic field on point defects . . . . .	30
<b>2.4 Summary . . . . .</b>	<b>34</b>

---

This chapter introduces the probabilistic computational modeling technique based on stochastic processes in general and MC methods in particular. Different research studies involving stochastic methods are stock market fluctuations; speech, audio, and video signals; blood pressure. Theoretically, the KMC method is based on the theory of Markov chains and is discussed briefly in Section. 2.1. Further, the Markov chains are also categorized based on time and boundary conditions. A general introduction to KMC and the type of algorithm implemented is presented in Section. 2.2. We also demonstrate the importance of first-passage processes in Section. 2.1.4. In this thesis, we have developed the acceleration technique named first passage Kinetic Monte Carlo (FPKMC). In Section. 2.2.2, we give a brief presentation of the FPKMC methodology. Finally, in Section. 2.3, we present the various atomic-scale theories that are used for modeling the migration of point defects, such as vacancies and interstitials.

## 2.1 Markov Chains and first-passage events

Any stochastic process can be described using probability theory and the concept of random variables [52]. Markov chains are one of the stochastic tools often used in probability theory to simulate a model with random events that are described by a Chapman–Kolmogorov equation [53]. The probability of each event in Markov chains is independent of the previously visited state. Thus, the future state or value of the variable is independent of the history of the trajectories. This property is referred as Markov property. The change in system states is called transitions, and the associated probabilities are called transition probabilities. Mathematically, Markov chains are represented as state space using a transition rate matrix that defines the transition probabilities. If the Markov chain moves with given discrete time steps, it is known as discrete-time Markov Chain (DTMC). Whereas, for continuous-time, the process is called a continuous-time Markov chain (CTMC). Further in this section, we provide basic information on different types of Markov chains and properties that the Markov chain satisfies.

### 2.1.1 Discrete Time Markov chain

A discrete-time Markov chain (DTMC) is the sequence of random variables in discrete-time step  $n = 0, 1, 2, \dots$ , i.e., the time step of each jump in the system to be constant. The  $X_n$  state represents the value of state at time  $n$ . If the random variables are discrete in space, then the stochastic process is called discrete-valued. Besides, values of  $X_n$  belong to a state space, denoted as  $S$ . This is the most common type of Markov Chain. Formally, DTMC is defined as the sequence of discrete random variables with the property of conditional distribution of  $X_{n+1}$  given that  $X_0, X_1, \dots, X_{n-1}$  depends only on the value of  $X_n$  but not on  $X_{n-1}$  such that [54]

$$P(X_{n+1} = j | X_0 = i, \dots, X_n = j) = P(X_{n+1} = j | X_n = i) = P_{ij}, \quad (2.1)$$

where  $P_{ij}$  is the transition probability to move from state  $i$  to state  $j$ . The total transition probability matrix is a general stochastic matrix, written as

$$\mathbf{P} = \begin{matrix} & \begin{matrix} X_1 & X_2 & X_3 & \dots & X_m \end{matrix} \\ \begin{matrix} X_1 \\ X_2 \\ X_3 \\ \vdots \\ X_m \end{matrix} & \left( \begin{matrix} P_{11} & P_{12} & P_{13} & \dots & P_{1m} \\ P_{21} & P_{22} & P_{23} & \dots & P_{2m} \\ P_{31} & P_{32} & P_{33} & \dots & P_{3m} \\ \vdots & \vdots & \vdots & \dots & \vdots \\ P_{m1} & P_{m2} & P_{m3} & \dots & P_{mm} \end{matrix} \right) \end{matrix} \quad (2.2)$$

where  $X_m \in S$ . Let define  $\mathbf{p}$  as the state probability vector, for which components  $P_i$  stands for the probability that system is in state  $X_i$  and  $\sum P_i = 1$ . The state probability vector for DTMC governed by a master equation (ME) is given as

$$\mathbf{p}^T(n+1) = \mathbf{p}^T(n)\mathbf{P}, \quad (2.3)$$

where  $n$  represents the discrete time step and  $T$  stands for transposition. The solution to Eq. (2.3) is

$$\mathbf{p}^T(n) = \mathbf{p}^T(0)\mathbf{P}^n. \quad (2.4)$$

In the following text, we refer to a state  $X_i$  by its label  $i$ .

### 2.1.2 Continuous Time Markov chain

In a DTMC, the time spent in any state  $i$  visited by the chain is equal to the same unit value. At variance, in a continuous time Markov chains (CTMC), the time spent in any state  $i$  by the random walker is a strictly positive random variable  $t_i$  is known as hitting time [55]. The next state  $j$  in the system is attained when there is a jump with transition rate  $K_{ij}$  and the hitting time for the respective state  $i$  ends.

Formally, a CTMC is defined as the stochastic process in continuous time  $X(t) : t \geq 0$  in a discrete state space  $S$

$$P(X(s+t) = j | X(s) = i, \{X(u) : 0 \leq u \leq s\}) = P(X(s+t) = j | X(s) = i)P_{ij}, \quad (2.5)$$

where  $s \geq 0$ ,  $i \in S$ ,  $j \in S$ ,  $X(s+t)$  is the future state,  $X(s)$  is the present state, and the condition  $\{X(u) : 0 \leq u \leq s\}$  signifies no relation between the present and future state [55, 56]. Thus, CTMC satisfies the Markov property and hitting times are distributed as exponential random variables that is discussed in Section. 2.1.5.

Analogous to Eq.(2.3), the state probability vector for CTMC is given by time derivative of Chapman–Kolmogorov equation which is known as master equation (ME)

$$\dot{\mathbf{p}}^T(t) = \mathbf{p}^T(t)\mathbf{K}, \quad (2.6)$$

where  $\mathbf{K}$  is the Markov matrix. Its elements  $K_{ij}$  are the transition rates from state  $i$  to state  $j$  with the unit of  $\text{time}^{-1}$  and superscript  $T$  stands for transposition. The solution to Eq.(2.6) is given by the exponential of the Markov matrix,

$$\mathbf{p}^T(t) = \mathbf{p}^T(0) \exp[-\mathbf{K}t] \quad (2.7)$$

### 2.1.3 Absorbing Markov chains

In probability theory, a Markov chain is an absorbing Markov chain (AMC) if at least one of the states in the state space is an absorbing state. In an finite number of steps, it is possible to go from any state, i.e., transient to an absorbing state. Once the system enters an absorbing state, it never leaves. A state  $X_i$  is an absorbing state of a Markov chain if in row  $i$  of the transition probability matrix, the diagonal entry  $P_{ii}$  is equal to 1 and all the other entries  $P_{ij, j \neq i}$  are zero. That means the state with the diagonal entry equal to 1 can not be left once entered. To have better understanding of the concept, let us consider a series of Markov chain system with 5 distinctive states. The sequence of Markov chain in Fig. 2.1 is an AMC as it has three states  $X_1$ ,  $X_2$ ,

and  $X_5$  as an absorbing states, whereas state  $X_3$  and state  $X_4$  are the transient states. The random walker can transit from state  $X_3$  to all the other states with equal probability to end up in any of the absorbing states. There is a slight probability that random walker can transit through state  $X_4$  to absorbing state  $X_5$ . Once the random walker reaches either of the absorbing states, it never leaves the site.

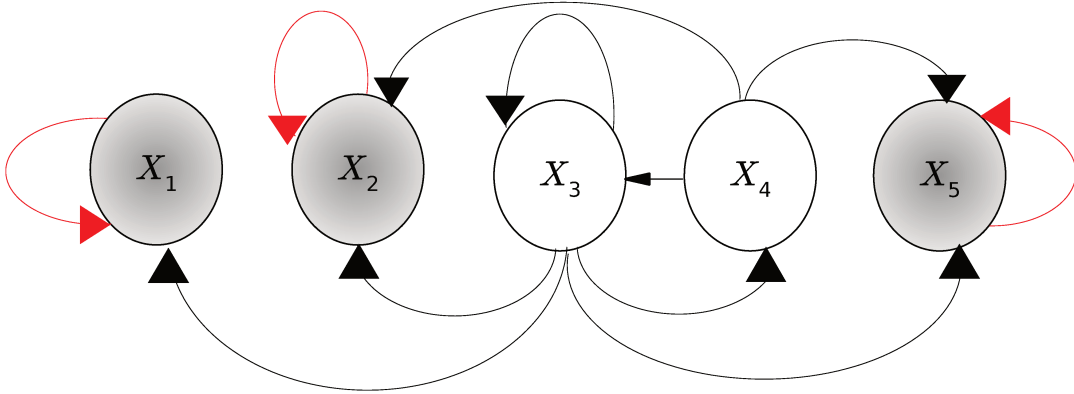


**Figure 2.1:** Schematic representation of random sequence which is also an AMC with three absorbing ( $X_1, X_2, X_5$ ) and two transient states ( $X_3, X_4$ ). Red arrows represents the transitions to absorbing state with probability equal to one, and black arrows represent the transition probabilities equal to less than one.

As the size of the system grows, the amount of transition probabilities of a walker transitioning from different states also increases. So, more convenient way to solve for AMC is to start by rearranging the matrix elements such as rows and columns of the absorbing states are enlisted last. The canonical representation transition matrix  $\mathbf{P}$  associated with the AMC is

$$\mathbf{P} = \left( \begin{array}{c|c} \mathbf{T}_{s \times s} & \mathbf{R}_{s \times r} \\ \hline \mathbf{0}_{r \times s} & \mathbf{I}_{r \times r} \end{array} \right). \quad (2.8)$$

The concept of AMC in the form of transition rate matrix was initially studied by Ref. [57]. In Eq.(2.8),  $s$  is the total transient states, and  $r$  is the absorbing states. The elements of the sub-matrix  $\mathbf{I}$  is equal to 1 as it is the identity matrix, sub-matrix  $\mathbf{T}$  is known as transient matrix consisting of transition probabilities between transient states, and the sub-matrix  $\mathbf{R}$  is the recurrent matrix with transition probabilities from transient states to absorbing states [58]. The canonical form of the matrix is subdivision of the original transition rate matrix. It is a more convenient way to solve for the absorbing states. There are two ways to solve the transition rate matrix associated to AMC

- Raise the transition rate matrix to high power  $n$ , such that  $\mathbf{P}$  remains stable and provides with the probability of ending in an absorbing state.
- Sub-divide the original transition rate matrix to its canonical form and evaluate the fundamental matrix for the AMC.

In this thesis, the notation for transition rate matrix associated with the absorbing Markov matrix is represented as [59]

$$\mathbf{K}^a = \left( \begin{array}{c|c} -\mathbf{A} & \mathbf{A}\vec{\mathbf{1}} \\ \hline \vec{\mathbf{0}}^T & 0 \end{array} \right) \quad (2.9)$$

where  $\mathbf{A}$  is a  $N \times N$  matrix such that  $A_{ij} = -K_{ij}$ ,  $\mathbf{A}\vec{\mathbf{1}} = -\mathbf{a}^0$ , and  $\vec{\mathbf{1}} = (1, \dots, 1)^T$  the  $N$ -dimensional column vector whose components all equal one. Vector  $\vec{\mathbf{0}} = (0, \dots, 0)^T$  is similarly defined.

Different random walker models can be solved using by resorting to the theory of AMC. In literature, first-passage processes are employed to characterize the evolution laws for the random walker. In the next section, we discuss the idea of the first-passage process and provide an analogy of it with AMC.

### 2.1.4 First-passage events

The concept of first-passage process (FPP) was introduced in the early 1970s by the name of first hitting times models [60, 61, 62, 63]. FPP have been constantly implemented in diverse fields of study such as medicine, economics, physics, finance, and sociology. Basic idea behind these processes is when a random walker or stochastic process is initiated from a state and encounters a set of boundary state. The boundary can be anything, naming a barrier or a different state of the system. The model consists of two basic components:

- a stochastic process  $X(t) \in \mathcal{X}$  state space at  $t \in \mathcal{T}$  time space with initial value  $X_0 = i$ ,
- a boundary condition  $\mathcal{B} \subset \mathcal{X}$ .

Consider an initial state  $X_0 = i \in \mathcal{X}$ , and a different set of states that corresponds to  $\mathcal{B}$ . Here we can define a random variable  $\mathcal{N}$  as first passage time at which the system jumps from state  $i$  to states in  $\mathcal{B}$  [62],

$$\mathcal{N} = \inf\{t : X_0 \in \mathcal{B}\}. \quad (2.10)$$

The overall time required for the entire process, starting from one initial state  $i$  to encounter a boundary condition is termed as the first passage time. The probability distribution of the times when the process reaches site or enters boundary for the first time is termed as first passage probability distribution. And the process is defined as the first passage process.

### 2.1.4.1 First-passage time

Time taken by the Markov chains to start from one state  $i$  and reach another state  $j$  for the first time is known as first-passage time. In literature, this time is also called hitting time. The exponential distribution law gives the time when a random walker enters a state and remains there for a while before it transit to another state. The exponential distribution provides the distribution of elapsed time. Note, in the case of AMC, the exponential distribution is known as a phase-type distribution constructed from a stochastic process with transient and absorbing states. All the states of AMC represent individual phases. For AMC, the transition rate matrix is written as Eq.(2.9). The probability density function for the distribution is given as  $\mathbf{P}^a(t) = \exp(\mathbf{K}^a t)$ . The mathematical derivation is presented in Section. 3.2 of Chapter 3.

A model describing a stochastic process can be solved using FPP and AMC by considering the set of boundary states as absorbing states. Once the random walker satisfies the boundary condition, it remains inside forever. In this thesis, we employ AMC as a tool to characterize first-passage events by evaluating first passage times. This method is termed as the first passage kinetic monte carlo (FPKMC) discussed in Section. 2.2.2. In the next section, we present important properties associated to Markov chains.

## 2.1.5 Properties of Markov chain

In this section, we will present some basic Markov chain properties without going in to detailed mathematical descriptions [64]. These properties have been taken into account in this PhD work to mathematically formalize the computational modeling method.

### 2.1.5.1 Ergodicity

Markov chains are said to be *irreducible* when the probability is always positive, and it is possible to reach any state to any other state. This is known as the accessibility property. A state  $i$  in the Markov chain is ergodic if it is aperiodic and positive recurrent. This property is known as irreducibility in mathematics. In physics, this property is related to the concept of periodicity and possible return length. Besides, if all the states in the Markov chain are aperiodic and irreducible, then the Markov chain is *ergodic* in nature.

For any state  $i$ ,

$$P_{ij} = P(X_n = i, n \geq 1 | X_0 = i). \quad (2.11)$$

Besides, a state is said to be recurrent; if a random walker leaves that state, it will return to that state in the future with probability one i.e.  $P_{ij} = 1$ . All the absorbing states are recurrent states. If the probability of return is less than one  $P_{ij} \leq 1$ , the state is called transient.

### 2.1.5.2 Detailed Balance

The detailed balanced condition writes

$$\pi_i P_{ij} = \pi_j P_{ji} \quad (2.12)$$

where  $P_{ij}$  is the transition probability from state  $i$  to state  $j$ ,  $P_{ji}$  is the transition probability from state  $j$  to state  $i$ ,  $\pi_i$  and  $\pi_j$  are the stationary probabilities of states  $i$  and  $j$ . If a Markov chain satisfies the detailed balance condition, then it is called reversible Markov chain.

### 2.1.5.3 Residence times

The first-passage times are known as the residence times. As mentioned in Section. 2.1.4.1, the time is exponentially distributed. Here, we present an example of a single state  $i$  having  $n$  transitions, reaching to an absorbing state that is labeled as  $n + 1$ . Using complementary cumulative distribution function<sup>1</sup> (CCDF), the transition probability of this system is given as

$$P(\min\{t_1, \dots, t_n\} > t) = \exp\left(-t \sum_{j=1}^n \kappa_j\right), \quad (2.13)$$

where  $\{t_1, \dots, t_n\}$  are random variables that are distributed exponentially with  $\kappa_1, \dots, \kappa_n$  rate parameters. CCDF is usually implemented to study the survival function  $S(t)$  which evaluates the survival of the phase after specified time  $t$  which corresponds to the residence time. The mathematical derivation of residence times is detailed in Section. 3.3.4 of Chapter. 3.

## 2.2 Numerical Algorithms

As mentioned before, the stochastic processes are extensively used in engineering, medicine, finance, and many science fields. A basic example is the random walker that perform steps in the forward or backward direction. These stochastic processes are simulated using the so-called Monte Carlo (MC) methods which samples the possible outcomes of the micro-states of a system according to the known multi-dimensional energy surface. In physical sciences, the Kinetic Monte Carlo (KMC) method is a particular branch of MC methods that focuses on the dynamical properties of many-body systems. A series of physical events are considered in the KMC method, for which probability of occurrence is known; hence its name is "Kinetic Monte Carlo." The main principle of this method is to assign transition rate or probability to each event and test whether the event has occurred or not depending on the generation of random numbers.

The potential energy surfaces exhibits high activation energy barriers (usually more significant than the value of  $k_B T$ ) which define thermally activated

<sup>1</sup>[https://en.wikipedia.org/wiki/Cumulative\\_distribution\\_function#Complementary\\_cumulative\\_distribution\\_function\\_\(tail\\_distribution\)](https://en.wikipedia.org/wiki/Cumulative_distribution_function#Complementary_cumulative_distribution_function_(tail_distribution))

events [51]. These kinds of events are classified as rare events. Typically it takes few picoseconds for individual atoms to reach a transition state, i.e., to cross a barrier and reach another system's state. The system's time evolution is provided by the hops between different states, commonly known as metastable states or basins. As the system tends to spend more time in one potential basin, it loses its initial memory. Before entering the next basin, each possible way of escaping from the basin becomes utterly independent of its preceding history. The escape time of a system from a state is usually larger than the time that it takes to cross the saddle region separating two stable states. This process gives rise to the exponential decay of the survival probability before the escape. These types of state-to-state jumps satisfy the Markov property discussed in Section. 2.1. The KMC method is a tool that is based on Markov chains. Thus, the system evolution is characterized by the evolution operator:

$$\mathbf{P}(t, t') = \exp((t' - t)\mathbf{K}), \quad (2.14)$$

which is the formal solution to the CTMC ME as given in Eq.(2.6). Recalling, matrix element  $P_{ij}(t, t')$  are the probability to find a system in state  $j$  at time  $t'$  given that it was previously in state  $i$  at time  $t$ .  $\mathbf{K}$  is the Markov matrix with elements  $K_{ij}$  which are the transition rates from state  $i$  to state  $j$  with the unit of time<sup>-1</sup> and  $K_{ii} = -\sum_{j \neq i} K_{ij}$ .

It is unfeasible to solve a system with a huge number of transitions tabulated in the matrix form. Thus, a comprehensive way to study the evolution of the system using KMC is to generate stochastic trajectories using random number generators at random times. In principle, correct time evolution of the system can then be calculated by averaging over these trajectories. The first KMC application to the lattice dynamics was proposed by A. Bortz, et al. [65]. A system generates a trajectory with an average time of  $\Delta t$ , depending on the hops from the visited states along the trajectory. The time depends on the total escape rate and is estimated using

$$\Delta t = \frac{\ln \mathcal{R}}{K_{ii}}, \quad (2.15)$$

where  $\mathcal{R} \propto \mathcal{U}_{[0,1]}$  is a uniformly distributed random number in  $[0, 1[$ . The random number is completely dependent on the total rate  $\mathbf{K}$  with no memory of its primary trajectory. This rate determines to which state the system will propagate. In simple terms, the new state becomes the starting point for the next KMC step. In practice, different types of algorithms are being implemented depending on the investigated time and space scales. They are selected or implemented on the movements of the atoms in the lattice space state in Lattice Kinetic Monte Carlo (LKMC). In Atomistic Kinetic Monte Carlo (AKMC), the position of all atoms on the lattice [65, 66, 67] or over the space [68, 69]. In this method, position tracking of all the atoms is considered. It is based on the atomic interaction model of a rigid or non rigid lattice type. Hence, this method accounts for hopping frequencies, and their influence on the surroundings [70]. This type of method requires taking into

account all the atoms present in the system (jumps of the point defects). Another method, commonly known as OKMC, rather simulates diffusing entities like defect-solute clusters [71]. In this method, the system consists of clusters that altogether are treated as objects [72]. All events that can occur are atomic jumps, the creation of point defects by irradiation, the annihilation of defects sinks and clusters (dislocations, grain boundaries, etc.). The main issue in this approach is to determine the rates of the activated mechanisms. The most frequent atomic jump limits the physical time that can be simulated. The class of OKMC methods encompasses event Kinetic Monte Carlo (EKMC) methods [60, 73, 74] and first-passage kinetic Monte Carlo (FPKMC) methods [75, 76]. The former assumes that all events are possible at any time independently of each other. Simultaneously, the latter approach introduces spatial protections and enforces the synchronization of the diffusing entities rigorously based on the exact first-passage and no-passage distributions defined hereafter. In EKMC, the total event is considered for modeling i.e. the sequence of atomic hops which cause the sinks or cluster to evolve. This method usually accounts for the macro time step, in which all the events occurring during that time step are considered [77]. The notation and implementation of KMC is discussed in Section. 3.2.2 and Section. 3.2.2 of Chapter 3, respectively.

### 2.2.1 Standard KMC method

A common KMC algorithm named as BKL algorithm or residence time algorithm follows simple few steps, which also includes the random number generation [78, 79].

1. Set the clock at time,  $t = 0$ .
2. Choose the initial state  $i$ .
3. Tabulate all the transition rates  $\kappa_l$  from state  $i$  to state  $j$  for all the possible  $n$  transitions in the system .
4. Calculate the total cumulative frequencies.
5. Estimate random number  $\mathcal{R}_1 \propto \mathcal{U}_{[0,1[}$
6. Find the event  $j$  to carry out such that  $\sum_{l=1}^{\ell-1} \kappa_l \leq \mathcal{R}_1 \kappa_l \leq \sum_{l=1}^{\ell} \kappa_l$ , where  $j(l)$  denotes the ending state associated with the l-th listed transition.
7. Propagate the event.
8. Update the clock  $t = t + \Delta t$  where  $\Delta t = \frac{-\ln \mathcal{R}_2}{\kappa_l}$  where  $\mathcal{R}_2 \propto \mathcal{U}_{[0,1[}$
9. Repeat from step 2, until the total target time or number of events is achieved.

All transitions are associated with probabilities and are evaluated. Hereafter, the cumulative frequencies  $\kappa_l$  are denoted as frequency  $K_{ij(l)}$ .

### 2.2.2 First-passage Kinetic Monte Carlo method (FPKMC)

The FPKMC method is based on the principle of first passage processes [80] discussed in Section. 2.1.4. The essential idea behind this method is to independently propagate the spatially protected walkers and to simulate the small sequence hops by replacing them with long sequences of hops [76]. This method aims to solve the exact solution of the multi-walker problem by converting it into one or two-walker problems. This method is based on events (EKMC) and belongs to asynchronous event-driven algorithms [81]. A detailed description of this method is presented in Refs. [8, 75].

The FPKMC algorithms entail sampling by estimating two probability distribution functions. As depicted in Fig. 2.2 (a), the walkers  $p_1$  and  $p_2$  are separated by their respected protective regions of lengths  $x_1$  and  $x_2$  at time  $t = 0$ . As long as both walkers are inside their protective region, their motion is independent and propagated by single walker propagators [8]. The probability distribution functions are estimated by selecting one of the events. In Fig. 2.2 (b), the particle  $p_1$  propagates to the end of its protected region, where particle  $p_2$  propagates and remains inside its region. The first-passage time

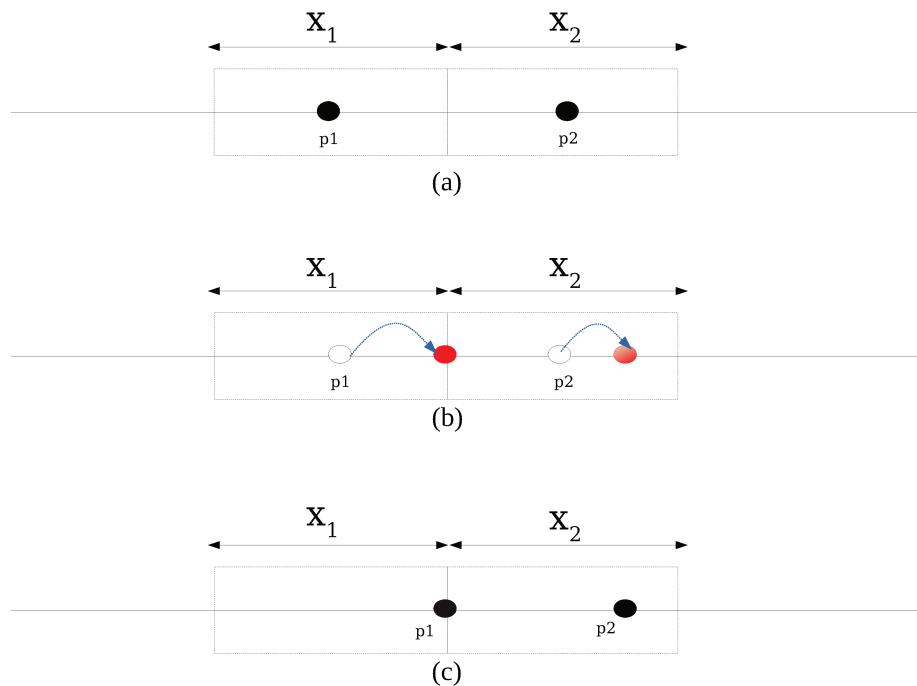


**Figure 2.2:** Schematic representation of first passage and no passage distributions of two random diffusing particles initially at time  $t = 0$  in panel (a). First-passage time is  $t'$  in panel (b) and (c) [8, 75].

$t'$  is when the particle leaves reaches at the end of its protective region. The no-passage conditional probability at a given time  $t$  corresponds to the probability that the particle propagate in its protective region and never left. In

practice, the first-passage time of both the particles are generated randomly from the first-passage distribution. All the samples event times are put into an event queue, and the shortest time is identified for corresponding particle. The global clock of the simulation time is updated at each step by the least first-passage time.

Historically, FPKMC algorithms have been developed to speed up KMC simulations. Indeed, the conventional KMC method may become inefficient when employed to simulate all the hops of defects on a lattice [82] and when the transition rate matrix equation exhibits a broad spectrum of frequencies. The causes of inefficiency may be energetic or entropic in origin. In the former situation, a diffusing defect performs many transitions between a few atomic configurations connected by small energy barriers, typically a vacancy binding to a solute cluster, before escaping elsewhere [83]. These connected configurations form trapping basins. The typical escape time of a defect is much higher than the typical time to cross into the small barriers. Subsequently, the freed vacancy may perform a considerable number of hops in bulk before recombining with another defect or being absorbed: the entropic origin for simulation inefficiency refers to this situation. The statistically exact approach to mitigate the inefficiency of the KMC methods is to draw sequences of events and first-passage times based on the theory of absorbing Markov chains [57, 75, 76, 80, 84, 85, 86]. Mathematically, the first passage times are the sum of the residence times spent by the walker in connected states before getting absorbed by the boundary such as an artificial or physical sink. The absorbing sink is artificial when it corresponds to the peripheral states of an energetic trap, while a physical absorbing sink usually corresponds to an energetic trapping basin, like solute clusters and dislocations. Furthermore, once the system has reached an absorbing state in absorbing Markov chains, it stays there infinitely. Because the probability of being absorbed tends to one as time tends to infinity, the connected states of the trapping basin are commonly known as transient states. Besides, a defect initially located in any transient state can reach any absorbing state, typically in many steps. This entails that the defect can also reach any transient state.

## 2.3 Construction of the transition rate matrix

The reactive events associated with radiation defects can be characterized with the help of AMC. It is achieved by computing the first-passage and no-passage distributions numerically. The first function represents the distribution of first passage times for a defect to reach the absorbing sink. The second function represents the distribution of the defect at a given time knowing that it did not reach the absorbing sink yet. To achieve these tasks, one implements one of the two following randomization procedures: kinetic path sampling or reverse sampling that is based on the factorization [59, 85, 87] or the eigenvalue decomposition [57, 59] of the absorbing transition rate matrix, respectively. A detailed explanation of the eigenvalue decomposition method is presented in Chapter. 3. Here, we will address the two crucial physical theories employed to construct the transition rate matrix.

### 2.3.1 Transition state theory

In diffusion processes, the point defects transition from state  $i$  to state  $j$  through a saddle point<sup>2</sup> on the potential energy surface. The energy of the system reaches its maximum value at the saddle points. The difference between the saddle energy and energy at the initial configuration is called as migration energy of the involved defect. A theory developed by Refs. [88, 89], named as Transition state theory (TST) studies the rate at which the atoms propagate from the initial state  $i$  to the final state  $j$ . In this thesis work, we employ TST to model the thermally-activated frequency  $K_{ij}$  for a point defect

$$K_{ij} = \nu_0 \exp\left(-\frac{E_{i \rightarrow s}^{\text{mig}}}{k_B T}\right), \quad (2.16)$$

where  $\nu_0$  is the attempt jump frequency,  $k_B$  is the Boltzmann constant,  $T$  is the temperature, and  $E_{i \rightarrow s}^{\text{mig}} = E(s) - E(i)$  is the migration energy of the point defect to go from initial state  $i$  to final state  $j$ .

A lower value of the migration energy means that reaction will be faster, since the transition rate will be greater. This value of the migration energy may be calculated using ab-initio calculations [92] or empirical inter-atomic potentials.

### 2.3.2 Effect of elastic field on point defects

The material properties are altered when point defects such as vacancy or self interstitial atoms are introduced or created in the lattice. There are long-range disturbances in the lattices due to the presence of elastic fields [93]. In practice, it is not feasible to take into account the distortion of every lattice point for the calculations explicitly in a crystal of any size. Instead, the crystal must be treated as a continuum. The continuum for lattice imperfections

<sup>2</sup>The state with the highest energy along with the reaction coordinate. The saddle state corresponds to a path on the energy landscape or surface.

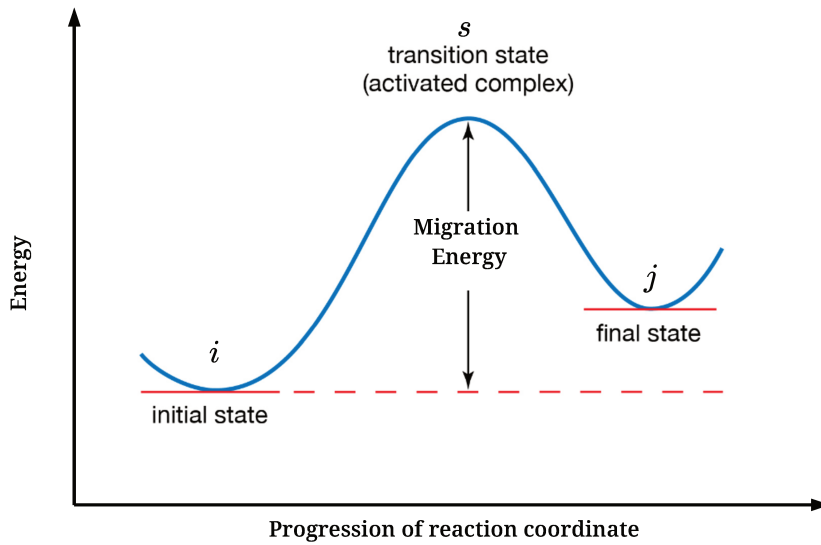


**Figure 2.3:** Reaction progression for point defect going from initial state  $i$  to final state  $j$  [90, 91]

is an elastic model. The theory of elasticity in such models, incorporates the internal stresses [94]. The fundamental elastic model has been studied by Eshelby in which a spherical inclusion of a system into a spherical hole, both being of different sizes in an infinite elastic medium [95]. The theory of elasticity is basically a relationship between a deformed structure and the energy content of the system. First, we recall the basic principles underlying the theory of elasticity [96]. Any solid body under stress gets deformed. If applied stress is below a threshold value, i.e. elastic limit, then the body tries to attain its original equilibrium or shape when the stress is removed. Hooke's law states that at equilibrium the magnitude of applied stress  $\sigma_{ij}$  is directly proportional to the amount of strain  $\varepsilon_{ij}$  is given as

$$\sigma_{ij} = C_{ijkl}\varepsilon_{kl} \quad (2.17)$$

where  $\varepsilon_{ij} = \left[ \frac{u_{i,j} + u_{j,i}}{2} \right]$  (refer to Appendix D). Indexes  $i, j$  refers to the three space dimensions<sup>3</sup>.

As an alternate, it can be written as

$$\varepsilon_{ij} = S_{ijkl}\sigma_{kl}, \quad (2.18)$$

where  $S_{ijkl}$  and  $C_{ijkl}$  are known as the elastic compliance tensor and elastic stiffness tensor [97]. Since,  $\varepsilon$  and  $\sigma$  are symmetric second rank tensors,  $S$  and  $C$  are rank four tensors with 36 independent coefficients out of 81 coefficients. The two four-rank tensors are the inverse of each other.

<sup>3</sup>Einstein convention over indices.

### 2.3.2.1 Elastic Dipole Tensor

The elastic equilibrium attained by a deformed body is given by the solution under certain boundary conditions. Using Eq.(2.18), the conditions for equilibrium in an infinite elastic medium are

$$\mathcal{C}_{ijkl} \frac{\partial^2 u_k(\mathbf{r})}{\partial r_j \partial r_k} + f_i(\mathbf{r}) = 0 \Rightarrow \sigma_{ij} + f_i(\mathbf{r}) = 0, \quad (2.19)$$

where  $\mathbf{u}(\mathbf{r})$  is the elastic displacement field and  $\mathbf{f}$  is the external body forces [93, 98]. Refer Appendix D for notations.

The elastic Green's function can be used to solve for the equilibrium equation Eq.(2.19). The Green's function  $G(\mathbf{r}, \mathbf{r}')$  is defined as

$$\mathcal{C}_{ijkl} G_{km,l}(\mathbf{r}, \mathbf{r}') + \delta_{im} \delta(\mathbf{r}' - \mathbf{r}) = 0, \quad (2.20)$$

where  $\delta(\mathbf{r}' - \mathbf{r})$  is the Dirac delta function i.e.  $\delta = 0$  if  $\mathbf{r}' \neq \mathbf{r}$  and otherwise. For isotropic materials, the Green's function is written as [98]

$$G_{km}(\mathbf{r}) = \frac{1}{16\pi\mu(1-\nu)r} \left[ (3-4\nu)\delta_{km} + \frac{r_k r_m}{\|\mathbf{r}^2\|} \right], \quad (2.21)$$

where  $r_k$  and  $r_m$  are the cartesian components of  $\mathbf{r}$ ;  $\mathbf{r} = \mathbf{r}' - \mathbf{r}$ .  $\mu$  is the shear modulus, and  $\nu$  is the Poisson ratio, both corresponding to Lamé coefficients.

A point defect is described as the distribution of equilibrated point forces on a continuous solid body. The force denoted by  $\mathbf{F}^q$ , is exerted to the neighboring atoms  $q$  at position  $\mathbf{r}^q$  illustrated in Fig. 2.4. The net force distribution when atoms are displaced from the equilibrium position is

$$\mathbf{f}(\mathbf{r}) = \sum_{q=1}^N \mathbf{F}^q \delta(\mathbf{r} - \mathbf{r}^q), \quad (2.22)$$

which are also known as defect forces [93, 99, 100].

According to elasticity theory, the displacements produced and the body force are related by the Green's function  $G_{ij}$

$$u_i(\mathbf{r}) = \sum_{q=1}^N G_{ij}(\mathbf{r} - \mathbf{r}^q) F_j^q, \quad (2.23)$$

where  $N$  is the total number of neighboring atoms at the position  $\mathbf{r}^q$  of the point defect. When the force is distributed using Taylor series expansion and Einstein convention, the displacement Eq.(2.23) can be written as

$$u_i(\mathbf{r}) = G_{ij}(\mathbf{r}) \sum_{q=1}^N F_j^q - G_{ij,k}(\mathbf{r}) \sum_{q=1}^N F_j^q r_k^q + o(|\mathbf{r}^q|), \quad (2.24)$$

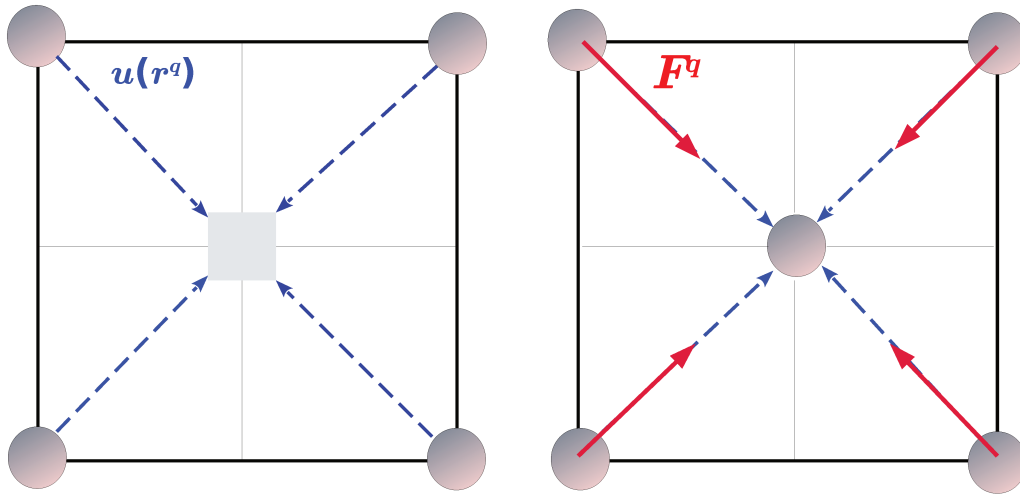


**Figure 2.4:** Representation of a vacancy by the forces.  $u(\mathbf{r}^q)$  is the displacement field of atoms (grey circle) induced by the vacancy (light blue square), while  $\mathbf{F}^q$  is the field of forces applied to a perfect lattice in order to produce the same displacement field  $\mathbf{u}$  [101].

if  $\|\mathbf{r}\| \gg \|\mathbf{r}^q\|$ , and  $G_{ij,k} = \partial G_{ij}/\partial r_k$ . At equilibrium,  $\sum_q \mathbf{F}^q$  are equivalent to zero, and Eq.(2.24) is written as

$$u_i(\mathbf{r}) = -G_{ij,k}(\mathbf{r})\mathcal{P}_{jk}, \quad (2.25)$$

where the term  $\mathcal{P}_{jk}$  is the second rank elastic dipole tensor. For the point defect sources, the elastic dipole tensor is

$$\mathcal{P}_{jk} = \sum_{q=1}^N F_j^q r_k^q. \quad (2.26)$$

It captures the symmetry, and is often used to study the point defects at lower symmetry [93, 102]. Because the torque  $\sum_q \mathbf{F}^q \times \mathbf{r}^q = 0$ , the elastic dipole tensor has a property of being symmetric. There are different methods discussed in literature [100] to evaluate elastic dipole tensor, based on different assumptions.

### 2.3.2.2 Elastic interaction energy

Here, we provide the derivation of elastic interaction energy  $E^{int}$  of the point defect with an external elastic field  $\mathbf{u}^{ext}$  adapted from Ref. [93]. The elastic energy can be written as:

$$E^{int} = - \sum_{q=1}^N \mathbf{F}^q \cdot \mathbf{u}^{ext}(\mathbf{r}^q). \quad (2.27)$$

Assuming the external field is changing very slowly near point defects, then Eq. (2.27) can be written as by series expansion of displacement in first order

$$E^{int} = -\mathbf{u}_i^{ext}(\mathbf{0}) \sum_{q=1}^N F_i^q - \mathbf{u}_{i,j}^{ext}(\mathbf{0}) \sum_{q=1}^N F_i^q r_j^q, \quad (2.28)$$

where by using Einstein convention over indices  $i$  and  $j$ ,  $\mathbf{u}_{i,j}^{ext} = \partial \mathbf{u}_i^{ext} / \partial a_j$ . Due to the equilibrium properties of force distribution,

$$E^{int} = -P_{ij} \mathbf{u}_{i,j}^{ext}. \quad (2.29)$$

Since,  $P$  is a symmetric tensor, we deduce an expression of elastic interaction energy as a function of the symmetric strain tensor

$$E^{int} = -P_{ij} \varepsilon_{ij}. \quad (2.30)$$

The study of elastic interactions between point defects is important as it affects the migration energy between the saddle position and stable points [101]. In this thesis, point defects are represented by their elastic dipole tensors and are computed by DFT calculations [14].

## 2.4 Summary

This chapter briefly discusses how the migration of point defects under irradiation can be fully understood using the computational mathematical technique based on Markov chains. The key point here to be noticed is the analogy between the absorbing Markov chains and first-passage processes. Then, we present a basic algorithm for the KMC method and introduce the concept of first-passage Kinetic Monte Carlo. Additionally, we have shown two essential theories such as transition state theory and theory of elasticity, used in constructing the transition rate matrix. In the following chapter, we will focus on the techniques to draw first passage times to simulate the behavior of point defects. We provide the mathematical derivation employing the theory of absorbing Markov chains for reversible diffusion processes using different assumptions.



# Fast first-passage algorithms for reversible diffusion processes

This chapter is based on the article "Elastodiffusion and cluster mobilities using kinetic Monte Carlo simulations: Fast first-passage algorithms for reversible diffusion processes", Physical Review Materials **3**, 103802 (2019).

## Contents

---

<b>3.1</b>	<b>Introduction . . . . .</b>	<b>37</b>
<b>3.2</b>	<b>Theory and methods . . . . .</b>	<b>39</b>
3.2.1	Master equation and evolution operator . . . . .	39
3.2.2	Standard Kinetic Monte Carlo . . . . .	39
3.2.3	First-passage kinetic Monte Carlo . . . . .	41
3.2.4	Application of absorbing Markov chains . . . . .	41
<b>3.3</b>	<b>Mathematical derivation . . . . .</b>	<b>43</b>
3.3.1	Conditional reversibility . . . . .	43
3.3.2	Spectral decomposition of the evolution operator . . . . .	45
3.3.3	No-passage and quasi-stationary distributions . . . . .	46
3.3.4	Expected values of first-passage times, residence times and exit probabilities . . . . .	47
3.3.5	Rank-one update . . . . .	48
3.3.6	Path factorization and space-time randomization . . . . .	49
<b>3.4</b>	<b>Elasto-diffusion of vacancies in Aluminium . . . . .</b>	<b>51</b>
3.4.1	Vacancy emission flux from cavity . . . . .	51
3.4.2	Computational complexity and stability . . . . .	55
3.4.3	Survival probabilities and spectral truncation . . . . .	58
<b>3.5</b>	<b>Diffusion of Mn-V clusters in <math>\alpha</math>-iron . . . . .</b>	<b>64</b>
<b>3.6</b>	<b>Summary . . . . .</b>	<b>68</b>

---

In this chapter, we introduce mathematical derivation for AMC theory for conditionally reversible processes in Section. 3.2. Then, we illustrate several features of the AMC theory on two realistic problems: the elasto-diffusion of vacancies in the neighborhood of cavities [14] in pure Aluminum and the diffusion of small vacancy-Mn clusters in  $\alpha$ -iron. In Section. 3.3, we present new features involving the ability to compute transition currents over large physical volumes and to approximate the evolution operator through projection on reduced subspaces. These two aspects are discussed little in the literature on lattice-based Markov processes, to our knowledge.

## 3.1 Introduction

We recall here that KMC method can be used for analysing a physical system with a model governed by a ME. But efficiency of the KMC reduces whenever the transition rate matrix describing the rate of the system exhibits a wide spectrum of frequencies. In this situation, the system transits a huge number of times between configurations separated by small energy barriers. These connected configurations form trapping basins from which the average escape time is much larger than the characteristic time for crossing the small barriers inside the basins. This issue is recurrent in KMC simulations. Cavities may form under irradiation and remain stable over a long period of time due to the low vacancy emission rate resulting from the strong attraction between cavities and neighboring vacancies. Kinetic trapping may also be caused by the formation of dynamically stable clusters of Manganese or Copper substitutional atoms and vacancies in  $\alpha$ -iron. These solute clusters migrate slowly without dissociating owing to numerous atomic rearrangements.

Different ways of enhancing the efficiency of the KMC method are available in the literature. First, the encountered events may be tabulated for later reuse [68, 103, 104, 105, 106, 107, 108, 109, 110], which avoids repeatedly evaluating the same transition rates. This way of proceeding is particularly relevant whenever stable and saddle point energies are costly to evaluate as in off-lattice simulations [111]. Transition rates associated to tabulated events are then retrieved on the fly.

Spatial protection of defects and exact time synchronization is considered to separate out the propagation of each point defect. As mentioned in Section. 2.4, this Spatial protection helps to prevent from collision of two point defects or enables two neighboring defects to recombine. For the time synchronization, we use the theory of AMC (refer to Section. 2.1.3) to draw first-passage times and paths to distant states located on the periphery of the protection, which acts as an absorbing sink [57, 80, 85, 86]. These first-passage times are achieved via two randomization methods which are:

1. **Direct factorization of the absorbing transition rate matrix [85]:** This method is based on the probabilistic interpretation of the factorization

in term of paths [112, 113, 114]. This interpretation is implicitly invoked in the matrix method [115, 116, 117] to compute correlation factors associated with vacancy-solute exchanges in dilute alloy models for any crystallographic structure. These correlation factors are crucial quantities giving access to diffusion coefficients. They are obtained by inverting a matrix, which amounts to summing over all paths between two consecutive vacancy-solute exchanges. Green functions used in atomic transport theory [118, 119] also appear as pseudo-inverses of transition rate matrices and may also be interpreted as geometric sums of path probabilities.

2. **Eigenvalue decomposition** [57, 58, 84, 86, 120]: This method consists of entirely computing the evolution operator for transient states, a matrix exponential. The approach was extended to Gaussian random walks in continuous three dimensional spaces using a Green function formalism [8, 75, 76]. In this framework, the probability that the walker is still in its protected volume appears as a series of decaying (real) exponential functions. At times large enough, the infinite sum can be safely truncated retaining only a limited number of the slowest eigen-modes because the contributions of the fastest eigen-modes rapidly decay with time. In these studies [8, 75, 76], the spectral decomposition is analytically tractable for the considered symmetric diffusion operators.

The symmetry property assumed in Ref. [8, 75, 76] entails that atomic transport is mediated by defects whose diffusion is reversible at equilibrium, i.e. the involved diffusion processes obey detailed balance even though the defect concentration may be out of equilibrium, as for instance after a quench or an irradiation cascade. This assumption is satisfied in many materials of practical interest. Even the state-to-state evolution of far from equilibrium glasses can be well approximated by a Markov chain that does obey detailed balance. A noticeable exception involves alloy systems subjected to steady irradiation, temperature gradients or chemical potential gradients. At the atomic scale, a consequence of reversibility is that the discrete transition rate matrix can be symmetrized by similarity transformation [118, 121]. For absorbing Markov processes, reversibility of diffusion is conditional upon the fact that the system is still located in a transient state. This guarantees that the transition rate matrix restricted to transient states is similar to a symmetric definite negative and that the transient evolution operator is the sum of decaying exponential functions. In this chapter, we investigate the computational implications of the conditional reversibility of the diffusion processes involved.

## 3.2 Theory and methods

### 3.2.1 Master equation and evolution operator

The phase space is considered to be discrete and is denoted by  $\Omega$ . States describing the system correspond to the locations of atoms and defects (such as vacancies) on a crystalline lattice. Our knowledge about the current state of the system is materialized by a probability vector, i.e. a probability distribution over  $\Omega$ . The time evolution of the probability vector  $\mathbf{p}_t \equiv \mathbf{p}(t)$  is governed by the following master equation

$$\dot{\mathbf{p}}_t^T = \mathbf{p}_t^T \mathbf{K}, \quad (3.1)$$

where  $\mathbf{K}$  stands for the Markov matrix of transition rates, assumed here to be time-independent:  $K_{ij}$  is the rate of transition from state  $i$  to state  $j$  (off-diagonal elements only). The standard convention is used to define the diagonal elements as  $K_{ii} = -\sum_{\ell \neq i} K_{i\ell}$ . Superscript  $T$  stands for transpose. The evolution operator, obtained formally from solutions of the ME, can be expressed as an exponential of the Markov matrix of transition rates ( $t_1 > t_0$ )

$$\mathbf{P}(t_0, t_1) = \exp \left[ \int_{t_0}^{t_1} \mathbf{K} dt \right] = \exp [(t_1 - t_0)\mathbf{K}]. \quad (3.2)$$

Matrix element  $P_{ij}(t_0, t_1)$  is the probability to find the system in state  $j$  at  $t_1$  given that it was in state  $i$  at time  $t_0$ . This operator fully characterizes the time evolution of the probability vector:  $\mathbf{p}^T(t_1) = \mathbf{p}^T(t_0)\mathbf{P}(t_0, t_1)$ . As defined, the evolution operator belongs to the class of stochastic matrices such that  $\sum_{\ell} P_{i\ell} = 1$  and  $P_{ij} \geq 0$  for any  $i, j, t_0$  and  $t_1$ . This property entails conservation of the total probability. Besides, the stationary distribution satisfies  $\boldsymbol{\rho}^T \mathbf{P}(t_1, t_0) = \boldsymbol{\rho}^T$ , it is a left-eigenvector of the evolution operator associated with eigenvalue one.

If known, the evolution operator can be used to sample transitions between any two states and over arbitrary time intervals  $\tau = t_1 - t_0$ . In practice, the evolution operator can only be solved for small subspaces delimited by artificial absorbing boundaries. Substantial simulation speed-ups can be achieved by sampling transitions to distant states located on the absorbing perimeters of encountered trapping basins [57, 84, 85, 86, 112].

Prior to explaining how the theory of absorbing Markov chains, can be used to formulate such accelerated KMC algorithms, we recall the standard KMC method.

### 3.2.2 Standard Kinetic Monte Carlo

Standard KMC methods avoid exponentiating the transition rate matrix. The evolution operator is instead linearized to get a simple stochastic matrix and a randomization procedure is invoked to draw the time at which the event

occurred. The simplest form of such matrix is

$$\mathbf{P}^{\text{lin}} = \mathcal{I} + \tau \mathbf{K} \quad (3.3)$$

where  $\mathcal{I}$  is the identity operator and  $\tau$  is a positive time step that must be lower or equal to  $-1/K_{ii}$  for all states  $S_i \in \Omega$ . Time randomization then consists in drawing a time in the exponentially decaying distribution of rate  $\tau^{-1}$ . Since  $P_{ii}^{\text{lin}} \geq 0$ , it is possible that no transition has occurred after time incrementation. In practice, a different stochastic matrix is implemented, so as to guarantee a KMC transition at each step. Letting  $\text{Diag}(\mathbf{K})$  denote the diagonal matrix composed of the diagonal elements of  $\mathbf{K}$ , the following stochastic matrix is rather used

$$\mathbf{P}^{\text{std}} = \mathcal{I} - \text{Diag}(\mathbf{K})^{-1} \mathbf{K}. \quad (3.4)$$

If system is currently located in state  $i$ , the exponentially decaying distribution of rate  $-K_{ii}$  must instead be used to sample the residence time, i.e a stochastic variable yielding the elapsed time. The mean residence time on  $i$  is then  $-1/K_{ii}$ , compensating for the fact that the stationary distribution of  $\mathbf{P}^{\text{std}}$  is proportional to  $-\text{Diag}(\mathbf{K})\boldsymbol{\rho}$ , a left eigenvector associated with the eigenvalue equal to 1. In the following we consider the generic stochastic matrix of the form

$$\mathbf{P}^{(0)} = \mathcal{I} + \text{diag}(\boldsymbol{\tau}^{(0)}) \mathbf{K} \quad (3.5)$$

where  $\boldsymbol{\tau}^{(0)}$  stands for an effective residence time vector such that  $\tau_i^{(0)} \leq -1/K_{ii}$  for all  $i$  and  $\text{diag}(\boldsymbol{\tau}^{(0)})$  denotes the diagonal matrix composed of the elements of  $\boldsymbol{\tau}^{(0)}$ .

### KMC implementation

The natural way of implementing KMC algorithm does not involve explicitly forming the transition matrices appearing in Eq. (3.5). At each cycle, the possible transition events are tabulated and two random numbers  $r_1$  and  $r_2$  are drawn uniformly in  $]0, 1]$  interval. The selected transition  $\ell$  satisfies the following double inequality

$$\sum_{l=1}^{\ell-1} K_{i,j(l)} < -r_1 K_{ii} \leq \sum_{l=1}^{\ell} K_{i,j(l)},$$

where  $i$  and  $j(l)$  denote the current state and the ending state associated with the  $l$ -th listed transition, while the elapsed time is simulated from  $K_{ii} \ln r_2$ .

An alternative algorithm consists in assigning an independent Markov process and time clock to each diffusing or reacting entity, while keeping a time ordered list of events up to date. Let  $\kappa_i^d$  stand for the total transition rate of the  $d$ -th diffusing entity from state  $i$ . At each KMC cycle, the time of the

master clock is incremented to the time of the next event and the corresponding transition is performed. After an event occurred, a limited number of events needs being annihilated, created or re-sampled. This way of proceeding is statistically equivalent because the distribution of the minimum of exponential random variables is exponential with rate  $\sum_d \kappa_i^d = -K_{ii}$  (refer to Sec. 2.2.1). This alternative algorithm is easier to implement on a parallel computer architecture [67, 122]. It is currently implemented in EKMC methods [60, 73], wherein distant binary collisions can easily be simulated using simplified laws assumed to be mutually independent.

### 3.2.3 First-passage kinetic Monte Carlo

The FPKMC algorithm briefly described in Sec. 2.2.2, is a statistically exact EKMC algorithm in which spatial protections is introduced to ensure that binary collisions are handled rigorously [8, 75, 76, 84, 86]. Figure 3.1 depicts the principle of the first-passage approach applied to the diffusion and collision of two vacancies in presence of trapping precipitates. FPKMC computations of the mobilities of vacancy-Manganese clusters in Iron are reported in Sec. 3.5. FPKMC technique requires forming the transition rate matrices appearing in Eq. (3.5).

### 3.2.4 Application of absorbing Markov chains

For the ease of exposition, trapping states are labeled from 1 to  $N$  and are called *transient*. Perimeter states connected to the transient states are pooled together into a single absorbing state labeled by index  $N+1$ . Transitions from a transient state to any perimeter states are thus replaced by a single transition to the absorbing macro-state with an overall transition rate cumulating the transition rates towards pooled peripheral states. Transitions from the macro-state to transient states or any other states are no more permitted. As defined, the absorbing Markov process coincides with the original Markov process as long as it remains located inside the trapping basin. As a result, the  $N$  trapping states become transient and the absorbing macro-state, acting like an artificial sink trapping the system infinitely, remains the only *recurrent* state of the system. The system being initially in a transient state, states beyond the perimeter states can not be reached and need not being considered. Recalling from Eq.(2.9), the Markov matrix for the absorbing process is thus defined as

$$\mathbf{K}^a = \left( \begin{array}{c|c} -\mathbf{A} & \mathbf{A}\vec{\mathbf{1}} \\ \hline \vec{\mathbf{0}}^T & 0 \end{array} \right) \quad (3.6)$$

where  $\mathbf{A}$  is a  $N \times N$  matrix such that  $A_{ij} = -K_{ij}$  and  $\vec{\mathbf{1}} = (1, \dots, 1)^T$  the  $N$ -dimensional column vector whose components all equal one. Vector  $\vec{\mathbf{0}} = (0, \dots, 0)^T$  is similarly defined and  $\mathbf{I}$  will stand for the  $N \times N$  identity matrix. The associated evolution operator reads

$$\mathbf{P}^a(t) = \exp[\mathbf{K}^a t]. \quad (3.7)$$

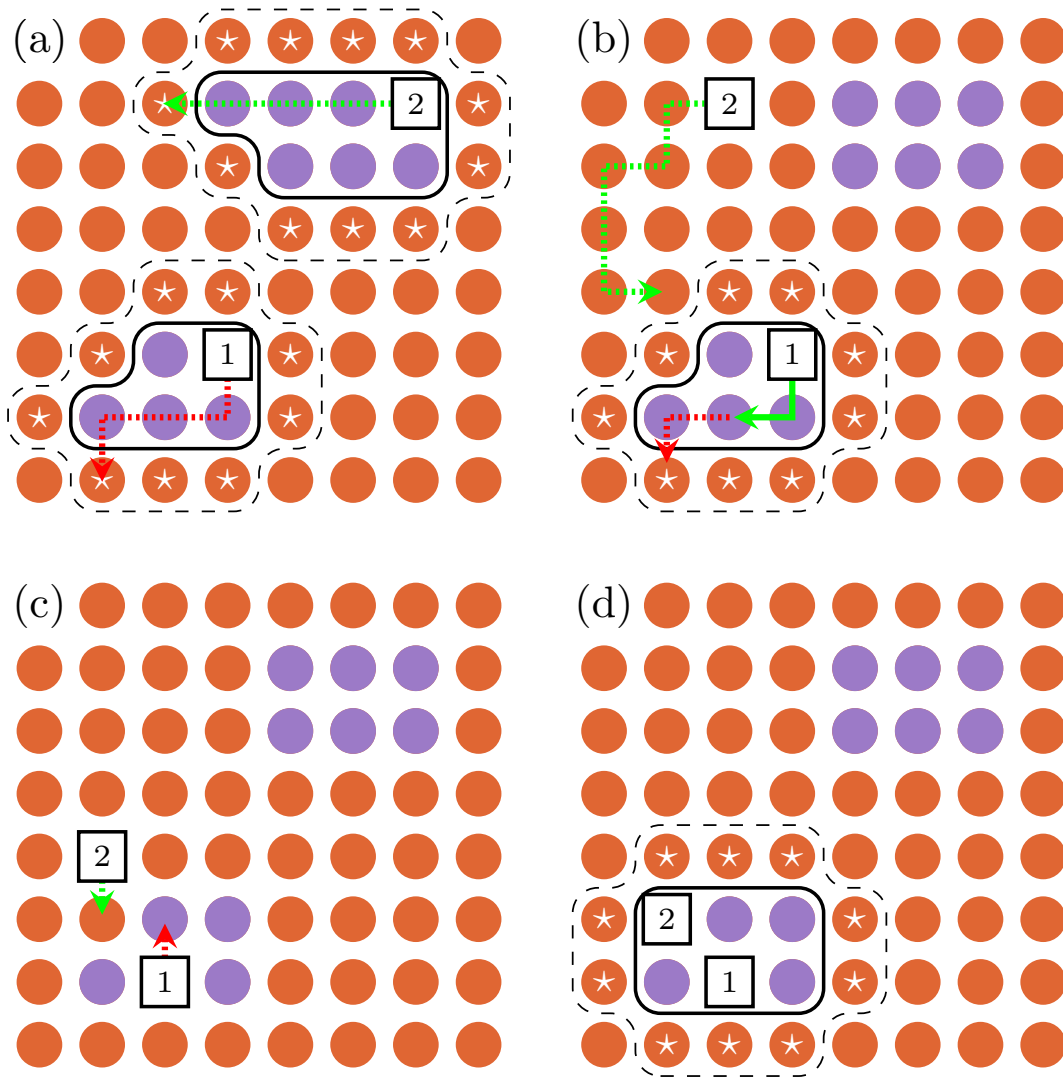


**Figure 3.1:** Schematic of FPKMC method for two vacancies evolving on a square lattice symbolizing a FeMn alloy. Fe and Mn atoms are displayed in orange and violet. Vacancies  $V^1$  and  $V^2$ , represented by the two labeled squares, are initially trapped inside Mn clusters. Exit sites for the trapped vacancies are indicated by stars. First-passage events are represented by dotted arrows. Events occurring first and second are colored in green and red, respectively. The sequence of events is as follows: (a) The two  $V$ -Mn clusters are spatially protected; First-passage times  $t_{\text{fp}}^1$  and  $t_{\text{fp}}^2$  are drawn (here  $t_{\text{fp}}^2 < t_{\text{fp}}^1$ ); (b)  $V^2$  dissociates from Mn cluster, diffuses and collides with spatial protection of  $V^1$  at time  $t_{\text{col}}^2$  (here  $t_{\text{col}}^2 < t_{\text{fp}}^1$ ); A no-passage event [8, 75, 76, 84, 86], materialized by the green solid arrow, is generated for synchronization; (c)  $V^2$  attaches to the  $V^1$ -Mn cluster (nearest neighbor interactions are assumed); (d) a diffusing entity composed of two vacancies is created and spatially protected. Vacancy locations inside the thick solid line correspond to states that are referred to as **transient** in the theory of absorbing Markov processes. **Absorbing** states are those with the vacancy located on a starred site, beyond the solid line and before the dashed line.

With these definitions,  $\mathbf{K}^a$  is a proper transition rate matrix and likewise  $\mathbf{P}^a$  is a proper stochastic matrix, their components in each row summing to zero and one respectively:

$$\mathbf{K}^a \begin{pmatrix} \vec{1} \\ 1 \end{pmatrix} = \begin{pmatrix} \vec{0} \\ 0 \end{pmatrix} \quad \text{and} \quad \mathbf{P}^a \begin{pmatrix} \vec{1} \\ 1 \end{pmatrix} = \begin{pmatrix} \vec{1} \\ 1 \end{pmatrix}. \quad (3.8)$$

Consequently, for any probability vector  $\boldsymbol{\pi}_t \equiv \boldsymbol{\pi}(t)$  evolving according to the ME  $\dot{\boldsymbol{\pi}}_t^T = \boldsymbol{\pi}_t^T \mathbf{K}^a$  the probability to find the walker in one of the  $N + 1$  states is conserved over time and we have  $\boldsymbol{\pi}_t^T = \boldsymbol{\pi}_0^T \exp[\mathbf{K}^a t]$ . We are now going to express the evolution operator Eq. (3.7) as a function of the exponential of  $\mathbf{A}$ . We first notice that the powers of minus the absorbing transition rate matrix writes for  $h \geq 1$

$$(-\mathbf{K}^a)^h = \left( \begin{array}{c|c} \mathbf{A} & -\mathbf{A}\vec{1} \\ \hline \mathbf{0}^T & 0 \end{array} \right)^h = \left( \begin{array}{c|c} \mathbf{A}^h & -\mathbf{A}^h\vec{1} \\ \hline \mathbf{0}^T & 0 \end{array} \right). \quad (3.9)$$

This relation enables us to rearrange the matrix exponential as:

$$\begin{aligned} \exp[\mathbf{K}^a t] &= \left( \begin{array}{c|c} \mathbf{I} & \mathbf{0} \\ \hline \mathbf{0}^T & 1 \end{array} \right) + \sum_{h=1}^{+\infty} \left( \begin{array}{c|c} \mathbf{A}^h & -\mathbf{A}^h\vec{1} \\ \hline \mathbf{0}^T & 0 \end{array} \right) \frac{(-t)^h}{h!} \\ &= \left( \begin{array}{c|c} \exp[-\mathbf{A}t] & (\mathbf{I} - \exp[-\mathbf{A}t])\vec{1} \\ \hline \mathbf{0}^T & 1 \end{array} \right), \end{aligned} \quad (3.10)$$

where we substituted back the two matrix exponentials for the series in the two upper blocks of Eq. (3.10). The probability of being in state  $j \leq N$  at time  $t$  starting from state  $i \leq N$  is

$$P_{ij}^a(t) = \mathbf{e}_i^T \exp(-\mathbf{A}t) \mathbf{e}_j \quad (3.11)$$

where  $\mathbf{e}_i$  denotes the  $i$ th standard basis vector.

## 3.3 Mathematical derivation

### 3.3.1 Conditional reversibility

We assume here that the original Markov process obeys detailed balance, which implies that the probability flux from state  $i$  to state  $j$  is equal to the reverse flux. The  $i$ -to- $j$  probability flux is defined as the product of the stationary probability  $\rho_i$  to be in state  $i$  and the rate  $K_{ij}$  of transitioning to state  $j$ . The equation of detailed balance thus writes

$$\rho_i K_{ij} = \rho_j K_{ji}. \quad (3.12)$$

When condition in Eq. (3.12) is satisfied, the stationary probability vector  $\boldsymbol{\rho}$  of the reference Markov process is usually associated with an equilibrium

Gibbs-Boltzmann distribution. It corresponds to the left eigenvector of the Markov rate matrix for eigenvalue 0, since we have  $\boldsymbol{\rho}^T \mathbf{K} = \mathbf{0}^T$ .

The detailed balance condition in Eq. (3.12) can be recast with respect to the absorbing Markov process considering the allowed transitions between the  $N$  transient states ( $1 \leq i, j \leq N$ ):

$$\sqrt{\rho_i} A_{ij} / \sqrt{\rho_j} = \sqrt{\rho_j} A_{ji} / \sqrt{\rho_i}. \quad (3.13)$$

The following symmetric matrix is defined from Eq. (3.13),

$$A_{ij}^B = s_i s_j \sqrt{\rho_i} A_{ij} / \sqrt{\rho_j} = A_{ji}^B, \quad (3.14)$$

where the scaling factors  $s_i$  are strictly positive. They are numerical parameters reflecting the degree of freedom in the construction of stochastic matrices for KMC simulations based on Eq. (3.5). To specify this statement, we cast transformation Eq. (3.14) into matrix form resorting to the  $N \times N$  diagonal matrices

$$\mathbf{S} = \sum_{i=1}^N s_i \mathbf{e}_i \mathbf{e}_i^T, \quad \mathbf{R} = \sum_{i=1}^N \frac{1}{\sqrt{\rho_i}} \mathbf{e}_i \mathbf{e}_i^T, \quad (3.15)$$

which are both diagonal definite positive. Hence matrices  $\mathbf{S}$ ,  $\mathbf{R}$  and  $\mathbf{B} = \mathbf{S}^2$  commute and are invertible, enabling one to define

$$\mathbf{A}^B = \mathbf{S} \mathbf{R}^{-1} \mathbf{A} \mathbf{R} \mathbf{S} = (\mathbf{S} \mathbf{R})^{-1} \mathbf{B} \mathbf{A} (\mathbf{S} \mathbf{R}). \quad (3.16)$$

Scaling matrix  $\mathbf{B}$  acts like a preconditioner. Its aim is to decrease the condition number of  $\mathbf{A}^B$ , which will be the main matrix in the first-passage problems investigated in the following.  $\mathbf{B}$ -scaling is introduced in the formalism for the sake of generality. Setting  $\mathbf{B}$  to identity amounts to disabling the explicit preconditioning, as done in most literature studies and in Ref. [85] in particular. This setup also arises in the linearized KMC method based on Eq. (3.3), up to the  $\tau$  limiting factor. In other works [112, 113, 114, 123],  $\mathbf{B}$  is set to  $\text{Diag}(\mathbf{A})^{-1}$ . This setup arises in the standard KMC method based on Eq. (3.4). Noticeably, it entails that  $s_i = 1/\sqrt{A_{ii}}$  and  $A_{ii}^B = 1$  for all  $i$ . We carry out a comparative study between the two mentioned setups in Sec. 3.4.2.

Matrix  $\mathbf{S} \mathbf{R}$  serves to make a diagonal similarity transformation and to formulate a generalized symmetric eigenvalue problem. Setting  $\mathbf{B}$  to identity allows us to conclude that  $\mathbf{A}$  is similar to a symmetric matrix  $\mathbf{A}^I$ . Similarity transformations preserving spectral properties and the spectrum of symmetric matrices being real, we conclude that the eigenvalues of  $\mathbf{A}$  are real. By applying Gershgorin circle theorem to  $\mathbf{A}$ , we also conclude that they are positive. Eventually none of the eigenvalues are equal to zero, otherwise a stationary distribution over transient states would possibly be established, which is excluded.

### 3.3.2 Spectral decomposition of the evolution operator

Matrices  $\mathbf{A}$  and  $\mathbf{B}^{-1}\mathbf{A}^B$  being similar, we deduce that the spectrum of  $\mathbf{A}$  can be obtained by solving the generalized symmetric eigenvalue problem (GSEP)

$$\mathbf{A}^B \boldsymbol{\varphi}_k = \mathbf{B} \boldsymbol{\varphi}_k \lambda_k. \quad (3.17)$$

Sorting the eigenvalues  $(\lambda_1, \dots, \lambda_N)$  of Eq. (3.17) in ascending order and letting  $\boldsymbol{\Phi} = (\boldsymbol{\varphi}_1, \boldsymbol{\varphi}_2, \dots, \boldsymbol{\varphi}_N)$  be a  $B$ -orthonormal basis of eigenvectors, the GSEP can be cast in the following matrix form

$$\mathbf{A}^B \boldsymbol{\Phi} = \mathbf{B} \boldsymbol{\Phi} \boldsymbol{\Lambda}. \quad (3.18)$$

where  $\boldsymbol{\Lambda}$  is a diagonal matrix with diagonal elements  $\Lambda_{ii}$  equal to  $\lambda_i$ . Left multiplying both sides of Eq. (3.18) by  $\boldsymbol{\Phi}^T$  and then right-multiplying Eq. (3.18) again by  $\boldsymbol{\Phi}^T$  yields the two relations

$$\boldsymbol{\Phi}^T \mathbf{A}^B \boldsymbol{\Phi} = \boldsymbol{\Lambda}, \quad \mathbf{A}^B = \mathbf{B} \boldsymbol{\Phi} \boldsymbol{\Lambda} \boldsymbol{\Phi}^T \mathbf{B} \quad (3.19)$$

where we simplified resorting to  $B$ -orthogonality of  $\boldsymbol{\Phi}$ :

$$\boldsymbol{\Phi}^T \mathbf{B} \boldsymbol{\Phi} = \mathbf{I}, \quad \boldsymbol{\Phi} \boldsymbol{\Phi}^T = \mathbf{B}^{-1}. \quad (3.20)$$

Using the generalized spectral theorem Eq. (3.19) and reverting relation Eq. (3.16), the absorbing matrix may therefore be decomposed as  $\mathbf{A} = \mathbf{R} \mathbf{S} \boldsymbol{\Phi} \boldsymbol{\Lambda} \boldsymbol{\Phi}^T \mathbf{S} \mathbf{R}^{-1}$ . Expanding the matrix exponential of  $\mathbf{A}$  in series, substituting  $\mathbf{B}$  for  $\mathbf{S}^2$  and invoking  $B$ -orthogonality in Eq. (3.20) eventually yield

$$\exp[-\mathbf{A}t] = \mathbf{R} \mathbf{S} \boldsymbol{\Phi} \exp[-\boldsymbol{\Lambda}t] \boldsymbol{\Phi}^T \mathbf{S} \mathbf{R}^{-1}. \quad (3.21)$$

To express components of the matrix exponential, it is practically convenient to introduce a few additional notations. We denote the scaling and rescaling vectors composed of the diagonal elements of  $\mathbf{S}$  and  $\mathbf{R}$  by  $\mathbf{s}$  and  $\mathbf{r}$ , respectively. We have  $\mathbf{s} = \mathbf{S} \vec{\mathbf{1}}$  and  $\mathbf{r} = \mathbf{R} \vec{\mathbf{1}}$ . Letting  $\odot$  and  $\oslash$  symbols stand for element-wise multiplication and division, we also define two sets of rescaled basis vectors  $\mathbf{g}_i = \mathbf{e}_i \odot \mathbf{s} \odot \mathbf{r}$  and  $\mathbf{d}_j = \mathbf{e}_j \odot \mathbf{s} \oslash \mathbf{r}$ . Then, resorting to the scalar products  $g_i^h = \boldsymbol{\varphi}_h^T \mathbf{g}_i$  and  $d_j^h = \boldsymbol{\varphi}_h^T \mathbf{d}_j$ , the evolution operator in Eq. (3.11) reads

$$P_{ij}^a(t) = \sum_{h=1}^N g_i^h d_j^h \exp(-\lambda_h t), \quad (3.22)$$

where  $(i, j) \leq N$ . The survival probability after duration  $t$  given that the system was prepared in state  $i \leq N$  at  $t_0 = 0$  corresponds to the probability of not having been absorbed during the elapsed time, i.e. the probability of

remaining in one of the  $N$  transient states,

$$\begin{aligned}
 p_i^s(t) &\triangleq \sum_{j=1}^N P_{i,j}^a(t) \\
 &= (\mathbf{e}_i^T, 0) \exp[\mathbf{K}^a t] \begin{pmatrix} \vec{\mathbf{1}} \\ 0 \end{pmatrix} \\
 &= \mathbf{e}_i^T \exp[-\mathbf{A}t] \vec{\mathbf{1}} \\
 &= \sum_{h=1}^N a_i^h \exp(-\lambda_h t), \tag{3.23}
 \end{aligned}$$

where the weighing coefficients read

$$a_i^h = g_i^h \sum_{j=1}^N d_j^h. \tag{3.24}$$

Since matrix  $\Phi^T$  is  $B$ -orthogonal, the  $a_i^h$  coefficients sum to one:

$$\sum_{h=1}^N a_i^h = \sum_{j,h=1}^N \frac{r_i}{r_j} \Phi_{ih} s_h^2 \Phi_{jh} = \sum_{j=1}^N \frac{r_i}{r_j} I_{ij} = 1.$$

This feature is consistent with the fact that initially the survival probability of the absorbing process is one :  $p_i^s(0) = 1$ .

KMC simulations require drawing first-passage times with the appropriate statistics. This may be achieved by sampling a random number  $r_2 \propto \mathcal{U}_{(0,1]}$  that is uniformly distributed in  $(0, 1]$  and looking for  $t_{\text{fp}}$  satisfying  $p_i^s(t_{\text{fp}}) = R$ . This way of proceeding requires evaluating the survival distribution through the spectral decomposition of  $\mathbf{A}$ . To avoid collision with another absorbing process interacting with the transient states, it is sometimes necessary to stop the simulation at a given time  $t_{\text{col}}$  for synchronizing the Markov processes. This task, depicted in Fig. 3.1.b, involves the ability to sample the so-called *no-passage* distribution [8, 75, 76, 84, 86].

### 3.3.3 No-passage and quasi-stationary distributions

The no-passage distribution is the conditional probability to find the system in transient state  $j$  at time  $t$  given that it was initially in transient state  $i$  and that the process has not been absorbed yet. It is obtained by dividing the probability of being in  $j$  by the survival probability  $p_i^s(t)$ :

$$P_{ij}^{\text{np}}(t) = \frac{\mathbf{e}_i^T \exp[-\mathbf{A}t] \mathbf{e}_j}{\mathbf{e}_i^T \exp[-\mathbf{A}t] \vec{\mathbf{1}}}.$$

The quasi-stationary distribution over transient states corresponds to the probability vector  $\mathbf{q}$  that is reached asymptotically in time by the no-passage distribution [124]. This asymptotic distribution is independent of the initial

distribution, arbitrarily set equal to state  $i$  in the limit below

$$q_j = \lim_{t \rightarrow \infty} P_{ij}^{\text{np}}(t) = \frac{d_j^1}{\sum_{\ell=1}^N d_\ell^1}$$

The quasi-stationary distribution being proportional to  $\varphi_1 \odot \mathbf{s} \otimes \mathbf{r}$ , is also a left eigenvector of the lowest eigenvalue of the transition rate matrix  $\mathbf{A}$ .

### 3.3.4 Expected values of first-passage times, residence times and exit probabilities

The complementary of the survival probability,  $p_i^{\text{a}}(t) = 1 - p_i^{\text{s}}(t)$ , corresponds to the probability of having been absorbed. Its time derivative at  $t$  is positive and equal to the probability density of exiting at  $t$ . Since  $p_i^{\text{a}}(0) = 0$  and  $p_i^{\text{a}}(\infty) = 1$ , the absorbing probability  $p_i^{\text{a}}(t)$  coincides with the cumulative distribution of the time probability of first passage. The mean first-passage time from  $i$  is the time expected with respect to the first-passage probability distribution. It can be formally obtained through integration by part:

$$\begin{aligned} \tau_i^{(N)} &= \int_0^\infty t \frac{d}{dt} p_i^{\text{a}}(t) dt \\ &= [t p_i^{\text{a}}(t) - t]_0^\infty - \int_0^\infty \{p_i^{\text{a}}(t) - 1\} dt \\ &= \int_0^\infty \mathbf{e}_i^T \exp(-\mathbf{A}t) \vec{\mathbf{1}} dt = \mathbf{e}_i^T \mathbf{A}^{-1} \vec{\mathbf{1}}. \end{aligned} \quad (3.25)$$

The mean-first passage time satisfies  $\mathbf{A} \boldsymbol{\tau}^{(N)} = \vec{\mathbf{1}}$  and is always more rapidly obtained by solving the linear system of equations involving the definite symmetric matrix  $\mathbf{A}^B$ :

$$\mathbf{A}^B \mathbf{x}^B = \mathbf{b}^B. \quad (3.26)$$

Symmetrizing the linear system entails scaling the right-hand side vector  $\mathbf{b}^B$  and rescaling back the obtained solution. This is done by resorting to relation Eq. (3.16) between  $\mathbf{A}$  and  $\mathbf{A}^B$ . Setting  $\mathbf{b}^B$  to  $\mathbf{s} \otimes \mathbf{r}$  yields the mean first-passage times as  $\boldsymbol{\tau}^{(N)} = \mathbf{x}^B \odot \mathbf{s} \odot \mathbf{r}$ .

The mean residence time in transient state  $j$  knowing that the system started from state  $i$  is given by the time integral

$$\begin{aligned} \int_0^\infty dt P_{ij}(t) &= \int_0^\infty \mathbf{e}_i^T \exp(-\mathbf{A}t) \mathbf{e}_j dt \\ &= \mathbf{e}_i^T \mathbf{A}^{-1} \mathbf{e}_j. \end{aligned} \quad (3.27)$$

The residence time vector associated with initial distribution  $\boldsymbol{\pi}$  reads  $\boldsymbol{\theta}^{(N)T} = \boldsymbol{\pi}^T \mathbf{A}^{-1}$  or, after taking the transpose,  $\boldsymbol{\theta}^{(N)} = \mathbf{A}^{-T} \boldsymbol{\pi}$ . As for the mean first-passage problem, the symmetric linear system Eq. (3.26) is invoked. However, it is solved using a different right-hand side vector and with transposed

scalings. Setting  $\mathbf{b}^B$  to  $\boldsymbol{\pi} \odot \mathbf{s} \odot \mathbf{r}$  eventually provides us with mean residence times via  $\boldsymbol{\theta}^{(N)} = \mathbf{x}^B \odot \mathbf{s} \odot \mathbf{r}$ .

The absorbing probability at state  $\ell$  is the sum of the probability flux from neighboring connected states and of the initial source contribution, reflected by the identity matrix  $I_{i\ell}$  below:

$$\begin{aligned} P_{i\ell}^{(N)} &= I_{i\ell} + \sum_{j=1}^N \int_0^{\infty} dt P_{ij}^a(t) K_{j\ell} \\ &= I_{i\ell} + \sum_{j=1}^N \mathbf{e}_i^T \mathbf{A}^{-1} \mathbf{e}_j K_{j\ell} \end{aligned} \quad (3.28)$$

The probability  $P_{i\ell}^{(N)}$  is equal to 0 if state  $\ell$  is transient ( $\ell < N$ ) or not connected to any transient state. It is non-zero for transitions to the peripheral states pooled in the absorbing macro-state.

The stochastic matrix  $P_{i\ell}^{(N)}$  yields the transition probabilities used in first-passage or mean first-passage KMC methods. The latter variant method, implemented in Sec. 3.5 and referred to as factorized KMC, increments the elapsed time by the mean first-passage time. The mean of the first-passage times can be used when a simulated walker (defect) never collides with another walker. In this case, the Markov process needs not being interrupted and synchronization is not required. Note that the stochastic matrix and residence time vector can be extended so as to encompass transitions from non-transient states  $i > N$ :

$$P_{ij}^{(N)} = P_{ij}^{(0)} + \sum_{\ell=1}^N P_{i\ell}^{(0)} P_{\ell j}^{(N)} \quad (3.29)$$

$$\tau_i^{(N)} = \tau_i^{(0)} + \sum_{\ell=1}^N P_{i\ell}^{(0)} \tau_{\ell}^{(N)} \quad (3.30)$$

where  $\mathbf{P}^{(0)}$  and  $\boldsymbol{\tau}^{(0)}$  are defined in Eq. (3.5).

### 3.3.5 Rank-one update

Let us assume that we have already identified  $n - 1$  trapping states, turned them transient by computing the transition probabilities  $\mathbf{P}^{(n-1)}$  together with the mean times  $\boldsymbol{\tau}^{(n-1)}$  and  $\boldsymbol{\theta}^{(n-1)}$ , and eventually performed a distant move. In practice, it may happen that the selected peripheral state is also a trapping state, in the sense that the system will later return to this peripheral state with a high probability. Fortunately, stochastic matrix  $\mathbf{P}^{(n)}$  needs not being computed again from scratch. It is possible to perform a rank-one update of the stochastic matrix  $\mathbf{P}^{(n-1)}$  by directly adding the selected peripheral state to the list of transient state. Based on  $\mathbf{P}^{(n-1)}$ , the probability of a transition

from  $i$  to  $j$  via the new transient state labeled  $n$  is

$$P_{ij}^{(n)} = P_{ij}^{(n-1)} + P_{in}^{(n-1)} \sum_{f=0}^{+\infty} \left[ P_{nn}^{(n-1)} \right]^f P_{nj}^{(n-1)}, \quad j > n,$$

$$P_{ij}^{(n)} = 0 \quad j \leq n,$$

where the sum accounts for the probabilities of all possible round-trips from  $n$ . Note that the updating rule involves both transient and peripheral states as starting states  $i$ . It is also possible to update the mean time vectors directly to get  $\tau^{(n)}$  and  $\theta^{(n)}$ . The mean first-passage time to make a non-local transition starting from state  $n$  to any state  $j > n$  is updated by accounting for the mean time spent performing flickers from  $n$

$$\begin{aligned} \tau_n^{(n)} &= \sum_{f=0}^{+\infty} \left[ P_{nn}^{(n-1)} \right]^f \left[ 1 - P_{nn}^{(n-1)} \right] (f+1) \tau_n^{(n-1)} \\ &= \tau_n^{(n-1)} / \left( 1 - P_{nn}^{(n-1)} \right). \end{aligned} \quad (3.32)$$

Concerning the mean first-passage time to make the non-local transitions from any state  $i$  to any state  $j > n$ , one must account for a possible transition to state  $n$ , which eventually leads to

$$\tau_i^{(n)} = \tau_i^{(n-1)} + P_{in}^{(n-1)} \tau_n^{(n)}. \quad (3.33)$$

The updating rule obviously covers the case  $i$  equal to  $n$ .

### 3.3.6 Path factorization and space-time randomization

Path factorization [85] consists of directly constructing stochastic matrix  $\mathbf{P}^{(N)}$  by repeatedly applying rank-one updates starting from stochastic matrix  $\mathbf{P}^{(0)}$  defined in Eq. (3.5). The factorization may involve on-the-fly re-indexing. The mean first-passage time vector needs to be initialized. For all relevant states  $i$ ,  $\tau_i^{(0)}$  may be set to either  $\tau = \min_{i \in \Omega} (-1/K_{ii})$  or  $-1/K_{ii}$ . The repeated updates can also be performed on the mean residence time vector  $\theta^{(n-1)}$ . The starting vector  $\theta^{(0)}$  is initially set to  $\tau^{(0)} \odot \pi$  and the updating rule Eq. (3.33) becomes:

$$\theta_j^{(n)} = \theta_j^{(n-1)} + \tilde{P}_{nj}^{(n-1)} \theta_n^{(n)}, \quad (3.34)$$

where the involved probability is defined from detailed balance and reads

$$\tilde{P}_{nj}^{(n-1)} = \frac{\rho_j \tau_n^{(0)}}{\rho_n \tau_j^{(0)}} P_{jn}^{(n-1)}. \quad (3.35)$$

This quantity corresponds to the canceled probability to eliminated states  $j < n$ , otherwise it is  $P_{nj}^{(n-1)}$ , the usual absorbing probability to the states  $j \geq n$  that are not yet eliminated. Hence, setting  $j$  equal to  $n$  in Eq. (3.34)

yields

$$\theta_n^{(n)} = \theta_n^{(n-1)} / (1 - P_{nn}^{(n-1)}). \quad (3.36)$$

Note that updating rules Eq. (3.32) and Eq. (3.36) exhibit a similar form.

The usefulness of path factorization is that it can be used not only to compute the expected values of the first-passage and residence times, but also to draw these two random variables from their exact distributions. Such randomization thus obviates the need to perform an eigenvalue decomposition. Algorithm 3 described in Appendix A and illustrated in Sec. 3.4.3 implements time randomization based on the probabilistic interpretation of the factorization.

Path factorization amounts to constructing the triangular matrices involved in  $LU$  or  $LDL^T$  decomposition as well as their inverses, as shown in Appendix A.3. It is shown that the repeated application of updating rules Eq. (3.33) and Eq. (3.34) to obtain  $\tau^{(N)}$  and  $\theta^{(N)}$  from  $\tau^{(0)}$  and  $\theta^{(0)}$  amounts to directly applying the inverted triangular factors on  $\tau^{(0)}$  and  $\theta^{(0)}$ . Noticeably, transitions to new transient states are removed within path factorization in the same way as matrix elements are canceled through Gaussian elimination. The latter technique is the crucial ingredient for direct solvers. A direct sparse solver is implemented in Sec. 3.4.2 to investigate the algorithmic complexity on the vacancy elastodiffusion problem. The solver computes the solutions  $\tau^{(N)}$  and  $\theta^{(N)}$  of Eq. (3.26) through forward and backward substitutions based on the symmetric triangular factor without its explicit inversion. The advantage of programming the rank-one updates is that the transition rate property of the transformed matrices can be preserved, as explained by Wales *et al.* in Ref. [114, 123]. Hence, the approach is more robust, albeit much slower, than available direct solvers. Preservation of probability fluxes is achieved by imposing that the flicker probability  $P_{nn}^{(n-1)}$  from  $n$  and the corresponding escape probability,  $D_{nn} = \sum_{j>n} P_{nj}^{(n-1)}$ , exactly sum to one after each elimination. Path factorization is found more appropriate for studying trapping of vacancies in small Mn clusters in iron. It is used to accelerate KMC measurements of Mn-cluster diffusion coefficients in Sec. 3.5.

## 3.4 Elasto-diffusion of vacancies in Aluminium

In the first application, we consider the diffusion of a single vacancy around a cavity in Aluminium. The crystalline structure is face-centered cubic. The coordination number is  $Z = 12$ . The vacancy formation energy is  $E_V^f = 0.67$  eV. It corresponds to the energy difference for displacing a vacancy from a free surface to the bulk. In our model, it determines the interaction energy of two neighboring vacancies. We consider nearest-neighbor pair interactions only and set  $E_{VV}^{\text{nn}} = -2E_V^f/Z$ . We also set  $E_{V\text{Fe}}^{\text{nn}} = 0$  and  $E_{\text{FeFe}}^{\text{nn}} = 0$ . These interaction energies entail that nearest-neighbor vacancy pairs are energetically favored. The model describing thermally activated jumps of Aluminum atoms into next nearest-neighbor vacancy accounts for the elastic field created by the cavity [14]. The dipole tensor associated with the vacancy has been computed using electronic structure calculations. It is assumed to be independent of the induced elastic strain, i.e., higher order terms in the fast-multiple expansion of elastic interactions are neglected.

### 3.4.1 Vacancy emission flux from cavity

We focus on the emission of a single vacancy from a cavity. In this set-up, we neglect some dynamical effects and assume that only a single vacancy can migrate and be emitted from a static cavity. The vacancy emission rate could conceivably be impacted by a dynamically evolving cavity. The cavity is composed first of 2243 vacancies. Cavity sites are located inside a sphere of radius 20.7 Å. The mobile vacancy is considered to be initially equilibrated at temperature  $T = 600$  K on the sites of the first shell of the cavity. Trapping results from the fast intra-shell vacancy jumps and from the immediate re-connection of the vacancy after it just disconnected from it. A total of  $N = 259320$  transient states are used to characterize the vacancy emission properties, which correspond to the vacancy sites located inside the protective sphere of radius 101 Å and centered on the cavity center.

We first resorted to algorithm 1 to construct matrix  $\mathbf{A}^B$ . We next solved equation Eq. (3.26) by implementing a direct solver (see Sec. 3.4.2) to obtain the mean residence time vector  $\boldsymbol{\theta}^{(N)}$  associated with the imposed initial distribution  $\pi$  and through appropriate rescaling (see Sec. 3.3.4). We next define the mean probability currents  $\theta_j K_{j\ell} - \theta_\ell K_{\ell j}$  between both transient and absorbing states, where  $\boldsymbol{\theta}$  stands for an extended mean residence time vector coinciding with  $\boldsymbol{\theta}^{(N)}$  on transient states and canceling elsewhere. Probability currents are a practical tool serving to characterize not only nonequilibrium steady states [121, 125], but also transient nonequilibrium regimes as presently. Letting  $\hat{\mathbf{r}}_i$  denote the three-dimensional lattice coordinates of the vacancy associated with state  $i$ , the vacancy flux at  $\hat{\mathbf{r}}_i$  is defined as the three-dimensional vacancy current density:

$$\hat{\phi}_j = \frac{1}{2v} \sum_{\ell} (\theta_j K_{j\ell} - \theta_\ell K_{\ell j}) (\hat{\mathbf{r}}_\ell - \hat{\mathbf{r}}_j). \quad (3.37)$$

The site volume  $v$  is uniform and the half factor stems from the fact that adjacent transitions are counted twice and entails an average of the fluxes entering and leaving lattice site  $\hat{r}_j$ . Note that for reversible dynamics obeying detailed balance, probability currents and vacancy fluxes vanish at equilibrium. The absorbing probability to state  $\ell > N$  given initial distribution  $\pi$  is eventually computed by plugging the residence time vector into relation Eq. (3.28), which yields

$$\pi_\ell^a = \sum_{i \leq N} \pi_i P_{i\ell}^{(N)} = \sum_{i \leq N} \theta_i^{(N)} K_{i\ell}. \quad (3.38)$$

Residence times and vacancy fluxes are displayed in Fig. 3.2 for sites  $j$  located in the (001) plane intercepting the cavity center. Vacancy fluxes along [001] direction inside this particular (001) plane cancel due to the reflective system symmetry. The absorbing probabilities to the peripheral states are displayed in Fig. 3.3 for the emission of a single vacancy from the (hidden) cavity located at the center. In Fig 3.2.a, we have scaled the residence times with respect to the corresponding equilibrium distribution for comparison. We observe that residence time distribution coincides with the equilibrium distribution on trapping sites located on the first two shells of the cavity. However, the former distribution becomes considerably smaller than the latter one as the vacancy moves away from the cavity. The emission anisotropy is clearly evidenced in Fig 3.2.b wherein the residence times have been rescaled with respect to their spherical averages. The vacancy preferentially resides along  $\langle 100 \rangle$  crystalline directions. This trend induces an identical anisotropy of the radial flux observed in Fig. 3.2.c. Preferential emission paths along  $\langle 110 \rangle$  crystalline directions may result from the orthoradial components of the flux that move the vacancy away from  $\langle 110 \rangle$  or towards  $\langle 100 \rangle$  directions beyond the first outer shells as evidenced in Fig. 3.2.d. The emission anisotropy is not due to the nearest-neighbor chemical interactions between the vacancy and the cavity but to the elastic interactions. This property is confirmed by the fact that isotropic fluxes are obtained when elastic interactions are switched off.

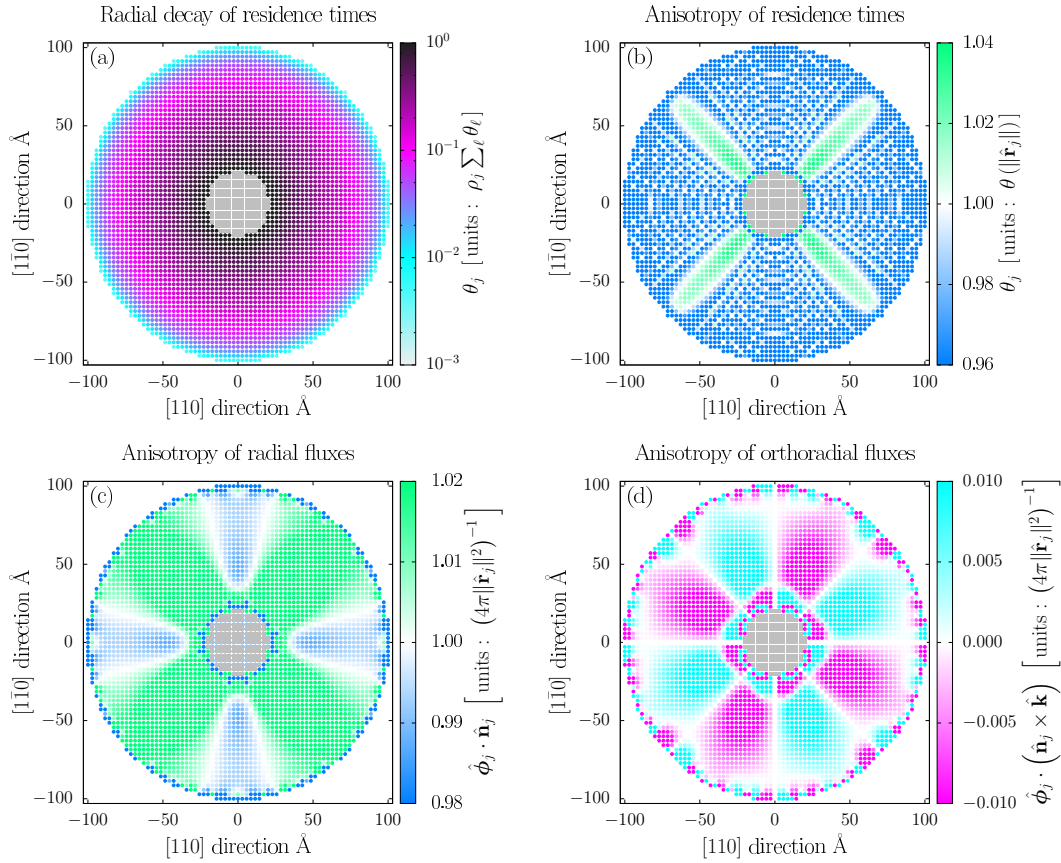


**Figure 3.2:** Emission of a single vacancy from the centered gray cavity of radius  $20.7 \text{\AA}$  to the absorbing sphere of radius  $101 \text{\AA}$ : Panels (a) and (b) display the residence times using two distinct color scales; Panels (c) and (d) display the radial and orthoradial vacancy fluxes, respectively. Coordinates of displayed sites satisfy  $\hat{\mathbf{r}}_j \cdot \hat{\mathbf{k}} = 0$  where  $\hat{\mathbf{k}}$  is the normalized basis vector orthogonal to (001). The Euclidean norm  $\|\hat{\mathbf{r}}_j\|$  corresponds to the distance to the cavity center and  $\theta(\|\hat{\mathbf{r}}_j\|)$  is the average residence time on the centered sphere of radius  $\|\hat{\mathbf{r}}_j\|$  and surface area  $4\pi\|\hat{\mathbf{r}}_j\|^2$ . Vector  $\hat{\mathbf{n}}_j = \hat{\mathbf{r}}_j/\|\hat{\mathbf{r}}_j\|$  is the normalized radial vector. The cross product  $\hat{\mathbf{n}}_j \times \hat{\mathbf{k}}$  corresponds to the orthoradial direction of the flux at  $\hat{\mathbf{r}}_j$ .

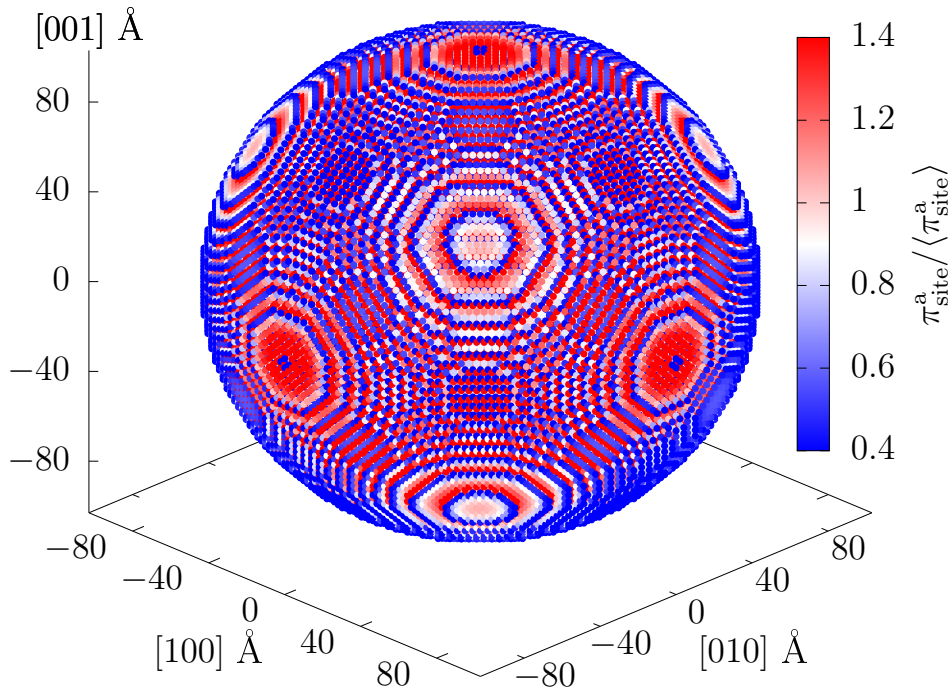


**Figure 3.3:** Anisotropy of peripheral site absorption for vacancies emitted from a small Aluminum cavity. Absorbing probability vector is  $\mathbf{p}^{aT} = \boldsymbol{\pi}^T \mathbf{P}^{(N)}$ . Red and blue coloration respectively indicates values larger and lower than the one average for the displayed site absorbing probabilities. The inverse mean probability corresponds to the number of peripheral sites. Cavity and protection radii are 20.7 Å and 101 Å, respectively.

The strong local heterogeneity observed in Fig. 3.3 for the absorbing probabilities is attributed to the varying numbers of interconnections between transient and absorbing states. However, smaller modulations are clearly visible at larger scale indicating that absorption is more important along  $\langle 100 \rangle$  directions and smaller along  $\langle 110 \rangle$  directions, in agreement with the measured vacancy fluxes. Further, we discuss about the computational aspects of the sparse linear solvers tested in the vacancy emission problem.

### 3.4.2 Computational complexity and stability

For problems involving the hopping of a defect on a lattice, the absorbing transition rate matrix is sparse and contains a maximum of  $Z + 1$  nonzero elements per rows ( $Z = 12$ ), while its size may exceed several millions in practice. Such linear systems are efficiently solved using either a multi-frontal sparse direct solver based on  $LDL^T$  decomposition [126, 127] or sparse iterative solvers based on Krylov subspace projection (KSP) methods [128, Chapter 6 and 7] based on PETSc software [129]. We first compare the costs of solving the linear system using iterative solvers to those of using direct solvers.

As for sparse iterative solvers, conjugate gradient (CG) is the appropriate method when the matrix is symmetric definite positive, however we also tested the minimum residual (MinRes) method that is adapted to general symmetric matrices. Three preconditioners were tested: the additive Schwarz method (ASM), the Jacobi and Block-Jacobi methods (B and BJ, respectively).

As for the multi-frontal sparse  $LDL^T$  factorization, we installed Version 5.2 of MUMPS [126, 127], which enables OpenMP threading and implements several ordering packages to construct the elimination tree. Among them, we selected METIS for its efficiency. The block-low rank (BLR) compression of the factors was also tested. Enabling this option reduces both storage and number of operations by an amount inversely proportional to the tolerance on the solution. The tolerance control parameter was set to  $10^{-5}$  which yielded a good trade-off between performance and accuracy. Simulations are performed for the emission problem in which the emitted vacancy reaches a protective sphere of increasing radii. The largest matrix size is nearly  $2.10^6$  (number of transient states). Results are displayed in Fig. 3.4. Scaling matrix  $B$  is first set to identity.

We observe that the iterative solver performs better than the direct solver, by a factor of 10-20. We obtain a square complexity for the standard direct solver, as expected for a sparse matrix describing transitions or connections within a 3-dimensional space. BLR becomes more beneficial the larger the matrices. For  $10^6$  transient states, BLR is 2.5 times faster and requires 15 times less operations than the standard factorization. The observed complexity of the iterative solvers is between square and linear with the combination of conjugate gradient and Jacobi preconditioning being the most efficient.

CPU costs for computing the transition rates and assembling  $A^B$  matrix are also reported in Fig. 3.4. They are represented by the dotted line referred to as "Assembly". Asymptotically, the overhead cost grows linearly with system size. It however remains larger than the one taken by any iterative solver for all simulated sizes. The preliminary calculation of transition rates is in fact substantial and should certainly be optimized in future KMC applications.

KSP methods for sparse symmetric linear system [128, Chapter 6 and 7] allow to solve first-passage problems over large volume, with matrix sizes that could not be investigated before. Note that implementing iterative KSP

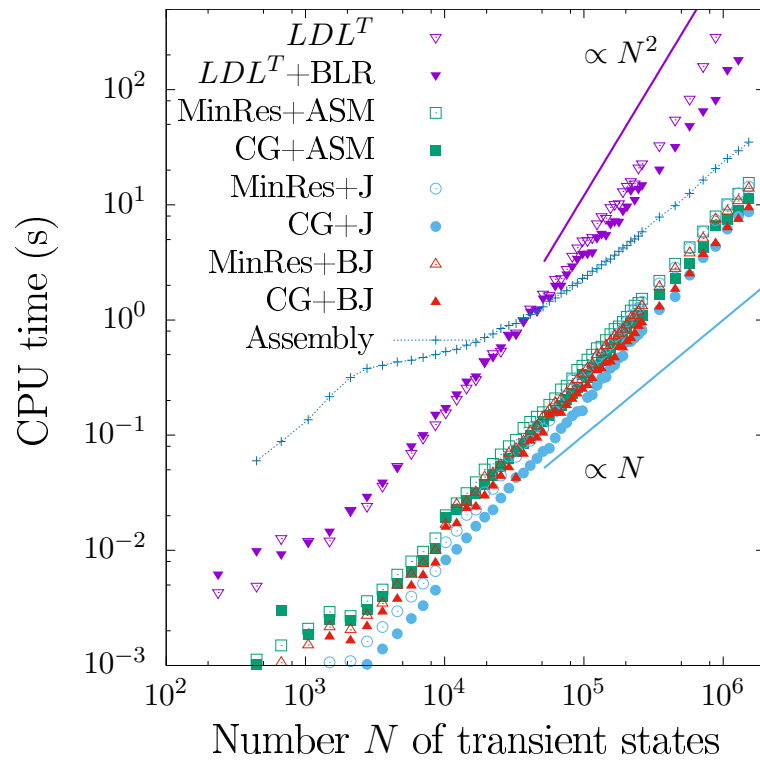


**Figure 3.4:** Comparative cost of direct and iterative linear solvers. See text for details on the solvers. Simulations are performed on an Intel 4-Cores i5-4310U processor running at 2.00GHz with 8GB memory. OpenMP shared-memory parallelism is enabled for  $LDL^T$  factorization.

methods with the original non symmetric matrix, for instance resorting to generalized minimal residual method, increases the computational cost by one-to-two orders of magnitude and requires more memory by the same amount. The deterioration of efficiency results from the orthogonalization procedure that must be performed with respect to all Krylov basis vectors. At variance, with symmetric matrices orthogonalization is performed with respect to the two last vectors, omitting occasional re-orthogonalizations aiming at preserving accuracy.

Further, we investigate the effect of scaling matrix  $\mathbf{B}$  on the condition number of  $\mathbf{A}^B$ , denoted by  $\kappa(\mathbf{A}^B)$ , and on the accuracy of the direct solver ( $LDL^T$  factorization with MUMPS). The 1-norm of the obtained residual vectors with respect to the absorbing rate matrix serves as a measure of accuracy. The 1-norms and condition numbers are evaluated for a series of temperatures ranging from 160 K to 600 K and are displayed in Fig. 3.5 wherein  $\Delta$  stands for  $\text{Diag}(\mathbf{A})^{-1}$  and  $\mathbf{B}$  is set to  $\mathbf{I}$  or  $\Delta$ .

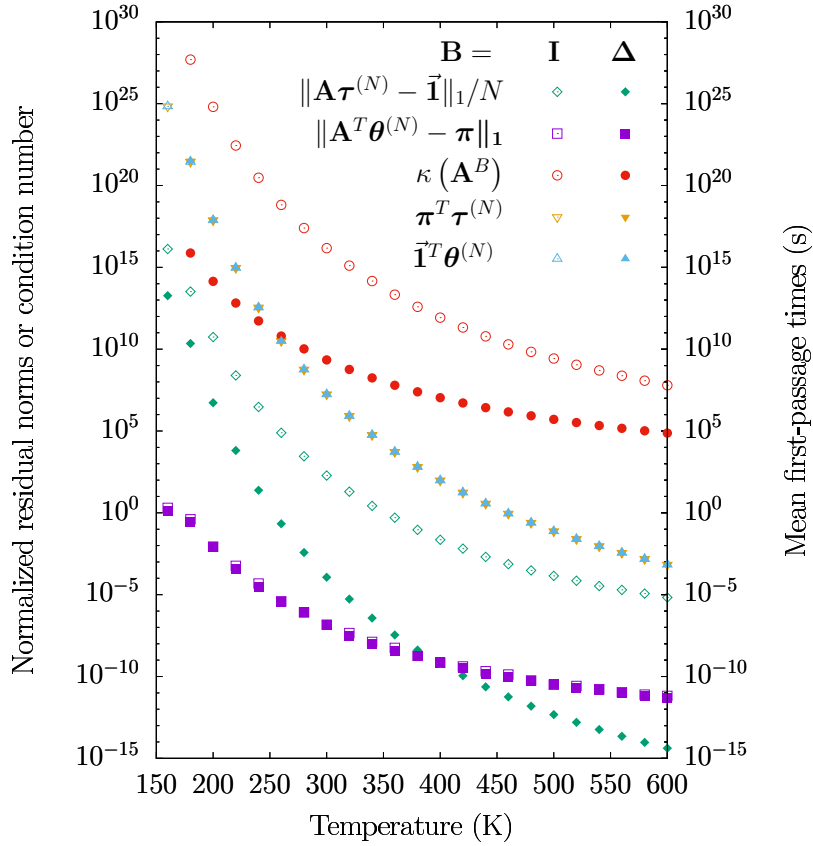


**Figure 3.5:** Effect of scaling matrix  $\mathbf{B}$  on accuracy of residence and first-passage time calculations. The residual norms and condition numbers are displayed for two setups:  $\mathbf{B}$  equal to  $\mathbf{I}$  and  $\Delta = \text{Diag}(\mathbf{A})^{-1}$ . The corresponding mean-first passage times, evaluated from  $\boldsymbol{\pi}^T\boldsymbol{\tau}^{(N)}$  and  $\boldsymbol{\theta}^T\vec{\mathbf{1}}$ , are displayed for comparison. Note that  $\|\vec{\mathbf{1}}\|_1 = N$  and  $\|\boldsymbol{\pi}\|_1 = 1$ .

We notice that the latter scaling variant improves mainly the numerical accuracy for mean first-passage time calculations. Besides, it systematically yields

the lowest condition numbers  $\kappa(\mathbf{A}^B)$ . Note that the direct solver fails below 180 K, compared to 250 K for the best iterative solver (conjugate gradient). When the solvers fail to converge, the probability flux is not preserved and negative times may even be returned. As Wales *et al.* [114, 123], we believe that this issue is due to round-off errors and too large differences between the diagonal and non-diagonal elements. For stiff problems, like the one involving the diffusivity of Mn-clusters in 3.5, path factorization is to be implemented to guarantee that the special structure of the transition matrix is preserved during eliminations.

Another advantage of performing the factorization is that additional solutions can be obtained at a much smaller cost using forward/backward substitution. The factorization can be reused to compute mean residence times over each site given any new initial conditions or to generate first-passage times directly from the exact distribution through randomization. To validate the latter time randomization procedure, we show that it is possible to reconstruct the survival probability distribution from a sample of first-passage times.

### 3.4.3 Survival probabilities and spectral truncation

Equation (3.22) yields the survival probabilities at time  $t$  with respect to the set of initial distributions  $\{\mathbf{e}_i\}_{i \leq N}$ . For the particular initial distribution  $\boldsymbol{\pi}$ , the probability becomes  $S(t) = \boldsymbol{\pi}^T \mathbf{p}^s(t)$ . Defining and plugging the scalar product  $\alpha_h = \sum_{i \leq N} \pi_i a_i^h$  into the survival probability yields

$$S(t) = \sum_{h=1}^N \alpha_h \exp[-\lambda_h t]. \quad (3.39)$$

Considering the vacancy emission problem again, we entirely solved the eigenvalue problem for a small system containing 236 transient states and 13 immobile vacancies in the central cavity of radius 4.04 Å. The protective sphere radius is 10.1 Å. The default dense solver from Lapack library was used. The survival probability and the distribution of first-passage log-times are reported in Fig. 3.6 for reference. We next run Algorithm 1 and 2 of Appendix A to make the factorization of BA and Algorithm 3 to generate a sample of  $10^5$  first-passage time to the protective sphere. The survival probability distribution reconstructed from the generated sample of first-passage times is reported in Fig. 3.6. It perfectly matches with the reference distribution obtained from Eq.(3.39), which validates the time randomization approach.

Interestingly, a perfect agreement is also observed when the survival probability is evaluated retaining only the lowest eigenvalue associated with the quasi-stationary distribution. This suggests that it is possible to truncate the

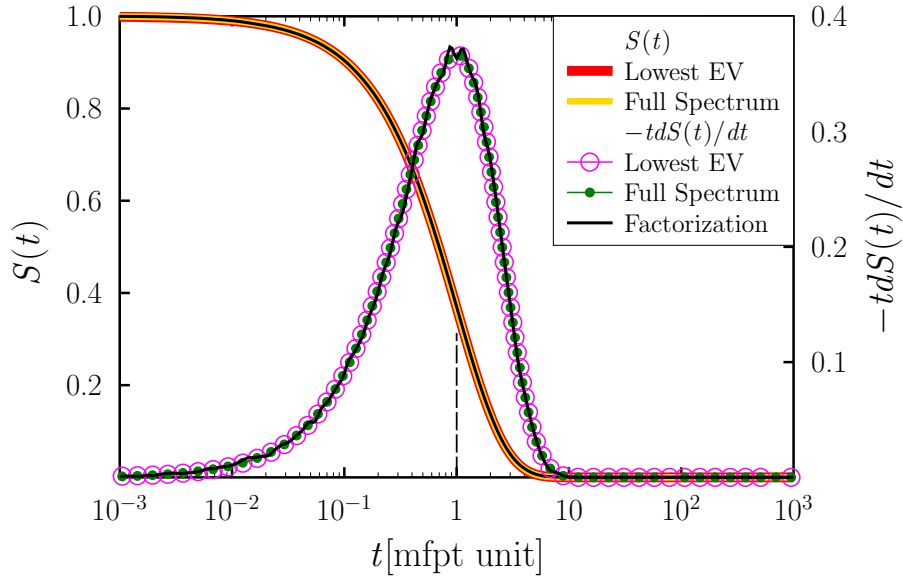


**Figure 3.6:** Emission of a single vacancy from cavity (4.04 Å radius) to protective sphere (10.1 Å radius). The survival probabilities (left axis) and first-passage distributions (right axis) are evaluated from the quasi-stationary distribution (Lowest Eigenvalue), the exact distribution (Full Spectrum) and randomization (Factorization). Time is given in unit of mean first-passage time (mfpt).

spectral decomposition above a certain threshold and approximate the survival probability retaining the  $k$  first terms:

$$S_k(t) = \sum_{h=1}^k \alpha_h \exp[-\lambda_h t]. \quad (3.40)$$

The truncation error can be directly quantified at time  $t = 0$  since we know that  $S(0) = 1$ . The time-integral of the error can also be quantified from the ratio

$$\mathcal{T}_k = \frac{\sum_{h=1}^k \alpha_h / \lambda_h}{\sum_{h=1}^N \alpha_h / \lambda_h}, \quad (3.41)$$

where the denominator formally corresponds to the mean first-passage time  $\boldsymbol{\pi}^T \boldsymbol{\tau}^{(N)}$  and is thus rather computed from a linear solve.

For the large considered systems, the  $k$  lowest eigenvalues and their associated eigenvectors are efficiently extracted by performing reverse iterations using the KrylovSchur method [130, 131] and the factored matrix. This amounts to extracting the largest eigenvalues of the inverse matrix. Calculations are performed using SLEPc software [132, 133]. We investigate the effect of truncating the spectral decomposition on two computational setups: (i) the emission of a single vacancy from a cavity of radius 20.7 Å to a protective sphere of radius 101 Å (same conditions as in Fig. 3.2 and 3.3) and

(ii) the absorption by the cavity of a single vacancy initially located at a distance of  $57.13 \text{ \AA}$  from cavity center in  $[110]$  direction. In setup (ii), there is no protective sphere and the cell is periodically replicated along  $\langle 100 \rangle$  directions with periodicity length  $80.8 \text{ \AA}$ . The absorbing macro-state is reached whenever the hopping vacancy becomes connected to the cavity. Setup (ii) entails 34801 transient states compared to 259320 for setup (i).

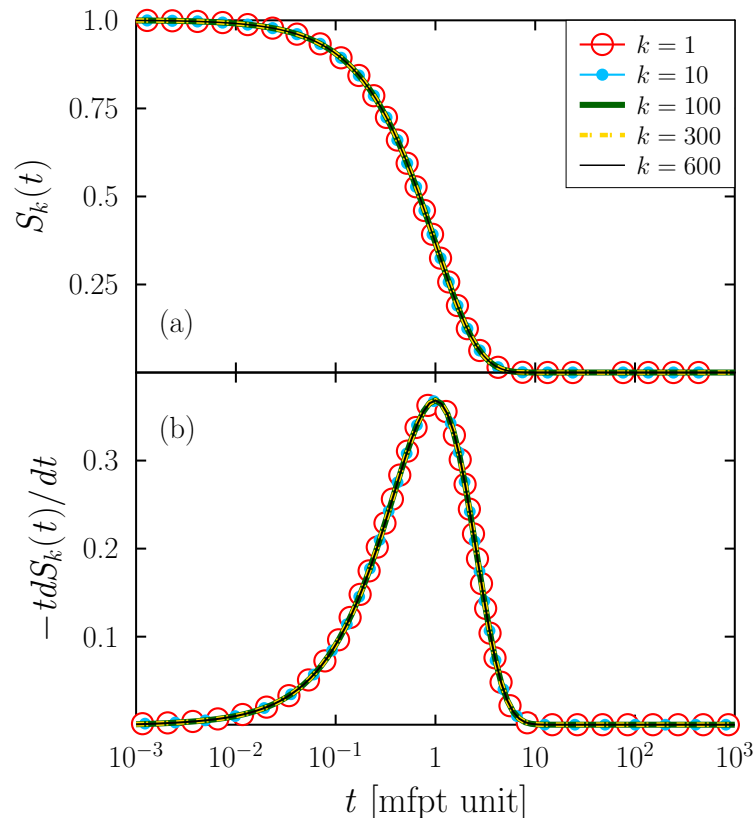


**Figure 3.7:** Emission of a single vacancy from the cavity ( $20.7 \text{ \AA}$  radius) to the protective sphere ( $101 \text{ \AA}$  radius). Survival probabilities and first-passage distributions are respectively plotted in panels (a) and (b) using various truncation thresholds  $k$ .

The survival probabilities and first-passage distributions are reported for various truncation threshold in Figs. 3.7 and 3.8. We observe that the trapping kinetics is governed by the quasi-stationary distribution [124] for the vacancy emission process at all times, and for the vacancy absorption only at times larger than the mean first-passage time. At short times, a substantial portion of 10% of the decaying exponentials needs to be included to faithfully reproduce the early stages of the absorption kinetics.

To rationalize this trend, the convergence of the truncated and reduced quantities  $\mathcal{T}_k$  and  $S_k(0)$  are displayed in panel (a) and (b) of Fig. 3.9, respectively. We observe that truncation errors are lower in the estimation of the mean

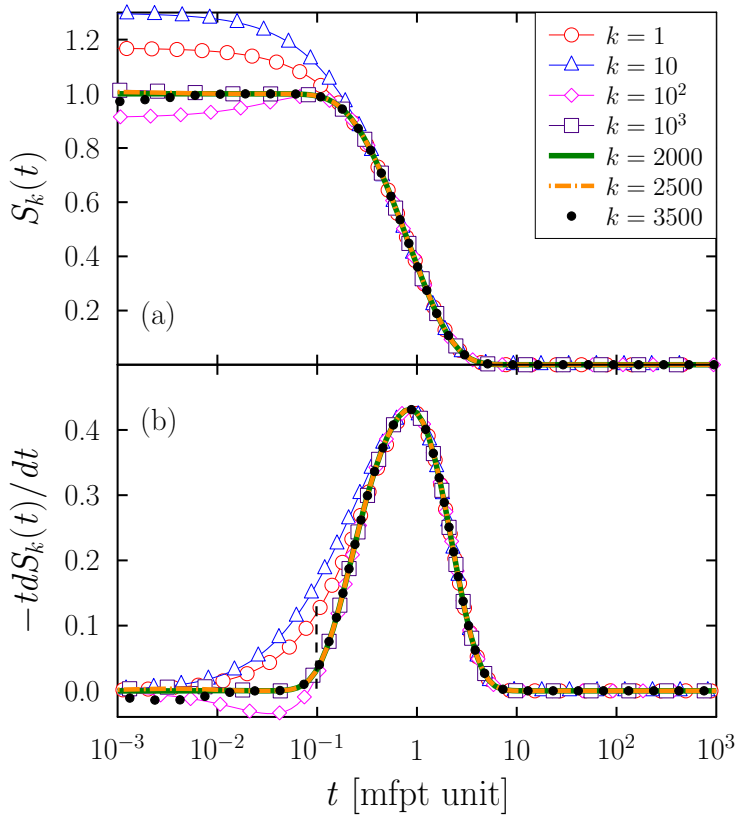


**Figure 3.8:** Absorption of a single vacancy by the cavity ( $20.5 \text{ \AA}$  radius). Survival probability distribution [panel (a)] and first-passage distribution [panel (b)] as a function of time.

first-passage time than of the initial survival probability. Convergence is non monotonous and proceeds by plateaus, suggesting the predominance of specific modes. To evidence them, scatter plots of computed eigenvalues and associated  $\alpha_k$  factors are shown in Fig. 3.10. We indeed observe that many more modes with large eigenvalues contribute in the absorption problem compared to the emission one. Furthermore, the large spectral gap between  $\lambda_1$  and  $\lambda_2$  explains the fast time-decay of the truncation error on the survival probability. At times larger than the mean-first passage time, the quasi-stationary distribution is reached. The early stage absorption kinetics is the most problematic to compute from spectral decomposition because many modes contribute.

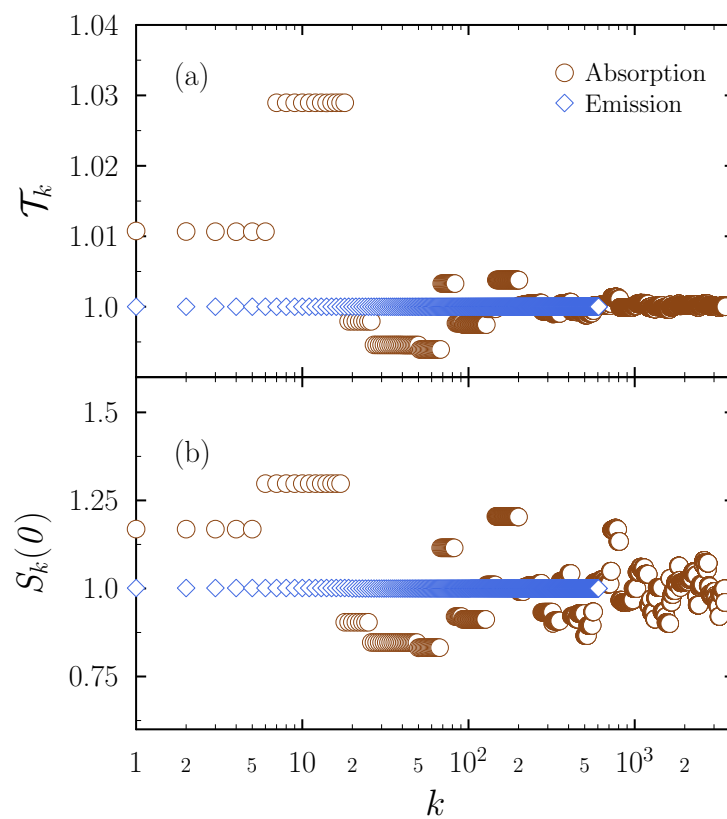


**Figure 3.9:** Effect of retaining the  $k$  lowest modes for approximating the reduced mean first-passage time  $\mathcal{T}_k$  [panel (a)] and the initial survival probability [panel (b)].

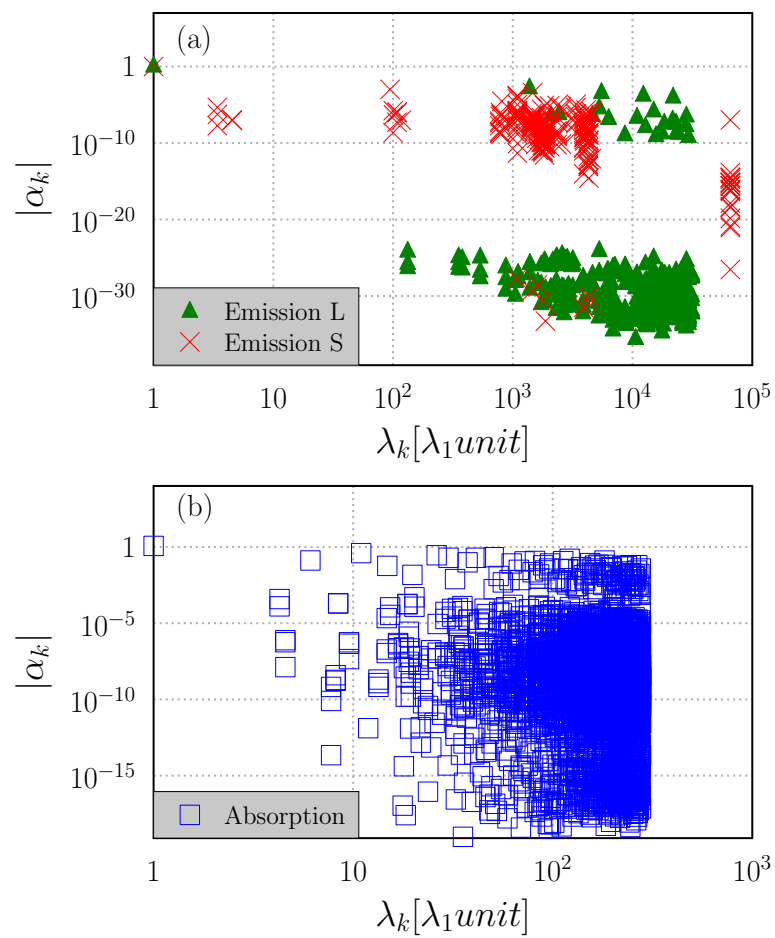


**Figure 3.10:** Absolute values of  $\alpha_k$  contributing coefficients displayed as a function of the eigenvalues scaled relatively to the lowest eigenvalue  $\lambda_1$ .

In this situation, we observe that it is far more efficient to compute the probability vector  $\boldsymbol{\pi}_t^T = \boldsymbol{\pi}_0^T \exp[-\mathbf{A}t]$  at a given time  $t$  using a krylov subspace method [134] for evaluating the application of a vector on a matrix function. Here, we applied the scaled initial probability to the exponential of  $-t\mathbf{A}^I$  and then reverted the scaling as follows:

$$\boldsymbol{\pi}_t = \{ \exp[-t\mathbf{A}^I] (\boldsymbol{\pi}_0 \odot \mathbf{r}) \} \oslash \mathbf{r} \quad (3.42)$$

This method however becomes less efficient than the truncated eigenvalue decomposition method as time increases. At half the mean first-passage time of the absorption kinetics, the QSD already yields an excellent approximation. This one is less efficiently extracted using the forward iterations of Ref. [134] than reverse iterations within Krylov-Schur method. The open question to address is how to combine both approaches optimally. Note that the absorption kinetics is paradoxically easier to simulate using KMC simulations because the energetic basin of attraction is precisely the absorbing sink. Extensive KMC simulations have been performed for the present absorption problem in Ref [14] for calculating sink strengths of various cavities and dislocations.

### 3.5 Diffusion of Mn-V clusters in $\alpha$ -iron

In this second application, we illustrate how path factorization can be implemented in kinetic Monte Carlo simulations to compute diffusion coefficients in FeMn system and how additional simulation speedups can be obtained by storing and efficiently retrieving the factorizations in hash tables. Simulation aims at computing the diffusivity of small Mn clusters. The enhanced mobility of solute clusters impacts the early stage of phase separation kinetics in quenched alloys [135], and is also suspected to be responsible for the anomalous incubation times observed in some Aluminium commercial alloys [136].

The simulation box contains  $10^3$  unit cells with two nodes per cell. The crystalline structure is body centered cubic and periodic boundary conditions are used. Interaction energies of Fe and Mn atoms and vacancies have been deduced from electronic structure calculations and are given in Ref. [137, 138]. Below 700 K, Mn atoms tend to form a single cluster that rarely dissociates during the simulations. This is due to their thermodynamic stability and to the high emission barriers. The two following algorithms are implemented and tested:

- The standard kinetic Monte Carlo algorithm denoted by KMC: At each cycle, a single vacancy transits to one of its nearest neighbour sites, i.e. exchanges with a nearest neighbour atom. Time is incremented by the mean residence time on the previously occupied site;
- The factorized KMC algorithm denoted by F-KMC: The vacancy makes a non-local transition and escapes the trapping basin based on the

path factorization algorithm. The set of transient states (the trap) encompasses the initial vacancy state and all states that can be reached via vacancy-Mn exchanges exclusively. The physical time is increased by the mean first passage time associated with the non-local escaping transition. It corresponds to the kinetic path sampling algorithm of Ref. [85].

Because a single vacancy is used in simulations, the time for performing a transition does not need to be drawn in its first-passage distribution and its expected value is used. This amounts to performing conditioning over time [139] and aims at reducing the statistical variance of the estimated diffusion coefficients. We consider here the diffusion coefficient of solute Mn atoms, defined as the three-dimensional average of half the time derivative of the mean square displacement (MSD)

$$D(X, T) = \frac{1}{6} \lim_{t \rightarrow \infty} \frac{d}{dt} \langle \|\hat{\mathbf{x}}(t) - \hat{\mathbf{x}}(0)\|^2 \rangle \quad (3.43)$$

where  $X$  is the number of Mn atoms,  $T$  is temperature and  $\hat{\mathbf{x}}(t)$  is the solute displacement vector at time  $t$ . With non-local events and conditioning performed over time, the time variable is replaced by the product of  $\ell$ , the number of involved jumps, and  $\hat{\tau}^L = \frac{1}{L} \sum_{h=1}^L \tau_h$ , the mean first-passage time averaged over a sample of size  $L$  generated using KMC or F-KMC. The solute diffusion coefficient is then estimated resorting to the following estimator

$$\hat{D}_\ell^L = \frac{\frac{1}{L-\ell} \sum_{h=1}^{L-\ell} \|\hat{\mathbf{x}}_{h+\ell} - \hat{\mathbf{x}}_h\|^2}{6\ell\hat{\tau}^L} \quad (3.44)$$

where  $\hat{\mathbf{x}}_{\ell+h}$  is the solute displacement vector after  $\ell + h$  jumps.

Simulations are carried out for temperatures  $T$  ranging from 300 K to 1200 K and numbers  $X$  of Mn atoms increasing from 1 to 60. For each  $(X, T)$  pair, a series of ten runs of eight hours are performed using a Gold-6140 Intel Xeon processor running at 2.30 GHz. The computed diffusion coefficients and their average over the 10 runs are displayed in Fig. 3.11. For better visualization, a rescaling has been done using the high temperature activation energy for Mn monomer diffusion ( $X = 1$ ) at 600 K. The diffusivity of  $V\text{-Mn}_X$  clusters increases with increasing  $X$  before tapering off for all temperatures lower than 800 K. Furthermore, the diffusivity maximum increases with temperature, suggesting the presence of a maximum at Mn content that could not be simulated.

A similar increase trend has been reported in FeCu system using standard KMC simulations (see Fig.9 in Ref. [140]), although the temperature dependence of the maximum could not be investigated due to a severe vacancy trapping in Cu clusters.

With increasing Mn content, F-KMC simulations failed to converge. This is

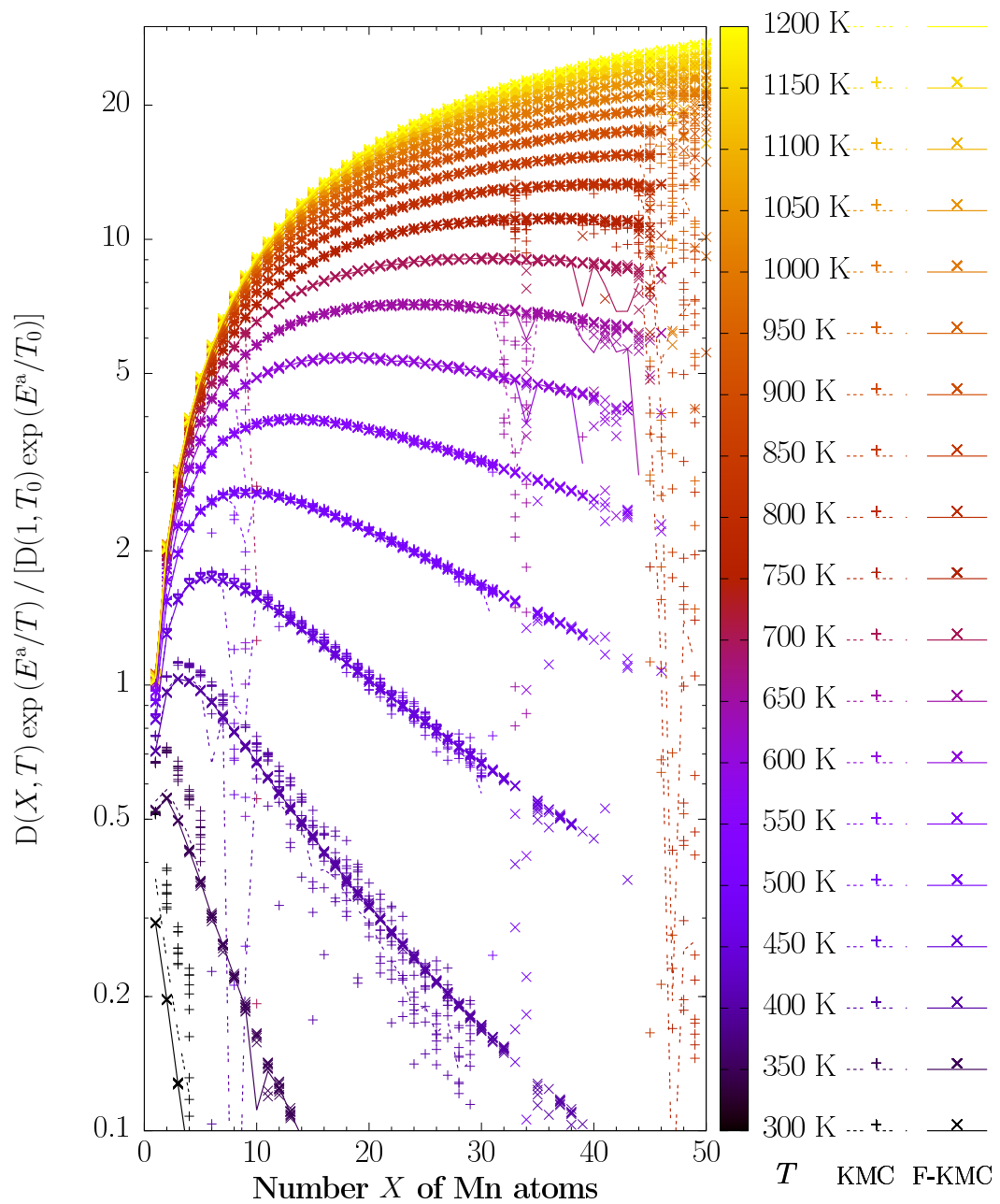


**Figure 3.11:** Diffusion coefficients of Mn solute atoms as a function of cluster size for various temperatures. For clarity, scaling is done relative to monomer diffusivity at  $T_0$  and its high temperature activation energy  $E^a = 0.646$  eV. Reference temperature is  $T_0 = 600$  K and reference diffusivity is  $D(1, T_0) = 6.716 \cdot 10^{-15} \text{m}^2/\text{s}$  at vacancy concentration of 5‰.

because path factorization becomes too costly. Besides, at the lower temperatures, the system gets trapped in super-basins containing several vacancy-cluster shapes. To understand the limitations of the current F-KMC algorithm and quantify the potential speedups of future developments, we tested two additional features in F-KMC algorithm, namely

1. A dictionary-enhanced version denoted by FD-KMC: Hash tables are used to store computed data about cluster shapes and factorizations. The goal is to retrieve the stored information when needed to avoid performing the same factorizations many times. This algorithm is described in chapters 5 and 6 of Ref. [141].
2. A graph-enhanced version denoted by FDG-KMC: The nodes of the graph correspond to the cluster keys that have been added to the dictionary. The edges of the graph correspond to the previously encountered non-local transitions. The goal is to save computational resources by making transitions from one cluster shape to another one in the graph without recalculating the cluster key. This algorithm is described in chapter 7 of Ref. [141].

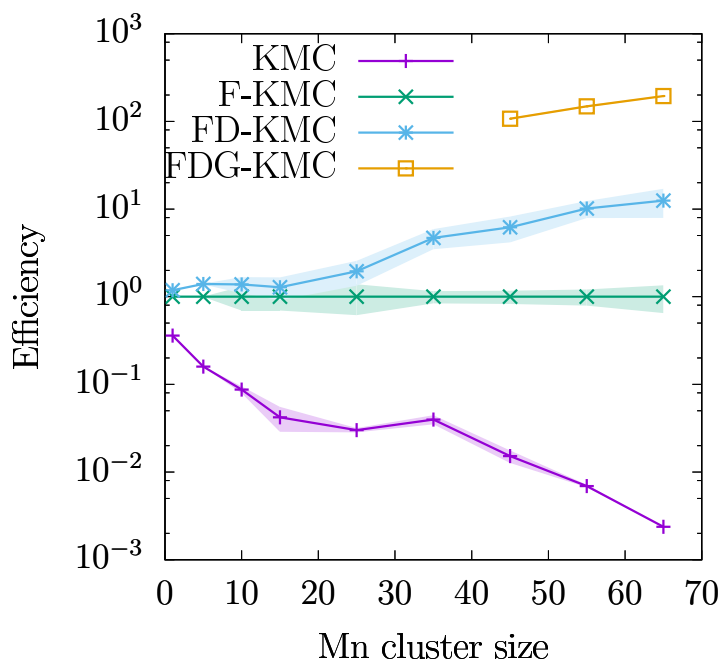


**Figure 3.12:** Relative efficiencies of the algorithms as a function of cluster size. Efficiency is evaluated as the ratio of the simulated physical time to that of F-KMC for a given wall-clock time. Filling around curves corresponds to the 68% confidence interval.

Simulations at 600 K with increasing Mn cluster sizes have been performed using the four algorithms and their relative efficiencies are displayed in Fig. 3.12. The efficiency of KMC algorithm relative to F-KMC is observed

to decrease with increasing Mn content. This trend already reported in [85] for FeCu is attributed to the increase of vacancy trapping with cluster size. The observed increase of FD-KMC efficiency with increasing Mn content is explained by the concomitant increase in factorization costs: it is more and more advantageous to store and retrieve the factored matrices, as their sizes and computational costs increase. When cluster sizes exceed 40, it is also beneficial to connect the various clusters resorting to a graph using FGD-KMC algorithm. This trend results from the fact that the kinetics repeatedly visit a few cluster shapes, as observed in FeCu system [85]. These simulations show that the use of hash tables and graphs are also beneficial for KMC simulations on a rigid lattices. A point left for future developments involves the optimal deallocation of entries rarely looked up whenever the dictionary memory reaches a given threshold.

### 3.6 Summary

In this chapter, the theory of AMC is applied to characterize rare events occurring when the diffusion process is trapped within a finite set of states. The initial probability distribution are considered to be emitting source while the peripheral states of the trap become an artificial absorbing sink. For the reversible non-absorbing diffusion process, we show that the associated first-passage problem can be simplified. The absorbing process then inherits a reversibility property that is conditional on that the dynamics has not reached the absorbing state. It transiently satisfies Kolmogorov's criterion: the probability of any circular sequence of transient states is equal to that of the time-reversed sequence, even though probability currents are nonzero. This conditional reversibility entails in particular that the absorbing transition rate matrix is similar to a symmetric definite negative matrix and that the transformation matrix exhibits a simple diagonal form.

We implement the path factorization technique to compute mean first-passage times, exit probabilities, and source-to-sink probability flux for small system. This method also corresponds to a direct and robust method for solving linear problems based on Gaussian elimination. Using path factorization approach, we formulated randomization procedure that enables first-passage times and exits to be drawn directly from the exact distributions. Furthermore, it has been shown that the acceleration in KMC simulations employing path factorization is substantial and makes it possible to compute the mobility of kinetically stable Mn clusters in iron down to the operating temperatures of pressurized reactors/vessels.

Evaluating the distributions requires the knowledge of both eigenvalues and eigenvectors of a symmetric positive definite matrix. In practical applications, we observe that the evolution of the transient state is governed only by a fraction of the eigenspectrum. The most contributing mode is the one possessing the lowest eigenvalue, and its eigenvector corresponds to the quasi-stationary distribution. We studied the single vacancy emission problem, which exhibits strong, energetic trapping; the quasi-stationary distribution

overwhelmingly predominates and correctly describes the transient evolution. In the case of the vacancy absorption problem, where trapping is essentially entropic, a small but substantial fraction of the slow modes are observed to contribute to the no-passage distribution and to govern the slow decay of the survival probability. For problems with more than  $10^4$  transient states, the transition rate matrix becomes sparse and iterative solvers are used to evaluate the eigenvalues and their contributions to no-passage distributions on the fly. We advocate to perform reverse iterations for extracting eigenvalues in ascending order. This can be achieved by iteratively applying the inverted matrix resorting to the  $LDL^T$  factorization, which amounts to extracting the largest eigenvalues of the inverted matrix.

For very large trap sizes, we show that resorting to a direct multi-frontal  $LDL^T$  solver (possibly combined with block low-rank compression) makes it possible to perform sink strength calculations for the absorption of a vacancy from a cavity and also to compute vacancy emission rates from the cavity. Computations can be done using millions of transient states per processor, allowing us to investigate realistic cavity concentrations in irradiated or quenched Aluminum.

In the next chapter, we present a new algorithm based on eigenvector deflation and Krylov subspace projection. It will be shown that the new algorithm is able to correctly characterize the transient evolution with high efficiency and low computation cost for the vacancy absorption problem. In Chapter. 5, we show how to apply the developed approaches to compute sink strengths.



# First passage algorithms based on Krylov subspace projection and eigenvalue deflation

This chapter is based on the article "Absorption kinetics of vacancies by cavities in aluminum: Numerical characterization of sink strengths and first-passage statistics through Krylov subspace projection and eigenvalue deflation", Journal of Computational Physics, 454, 110987 (2022).

## Contents

---

<b>4.1</b>	<b>Introduction</b>	<b>72</b>
<b>4.2</b>	<b>Model Order Reduction and Iterative Methods</b>	<b>73</b>
4.2.1	Eigenvector Subspace Model Projection	73
4.2.2	Krylov Subspaces	74
4.2.3	Krylov Subspace Model Projection	75
4.2.4	Eigenvector and Krylov Subspace Model Projection	76
<b>4.3</b>	<b>Implementation</b>	<b>77</b>
<b>4.4</b>	<b>Numerical results and analysis</b>	<b>78</b>
4.4.1	Efficiency and scalability of eigensolvers	78
4.4.2	Survival Probabilities	81
4.4.3	Vacancy absorption kinetics	89
<b>4.5</b>	<b>Summary</b>	<b>93</b>

---

The chapter is organized as follows. In Section. 4.2, we describe model order reduction techniques combining Krylov subspace projection and eigenvalue deflation. In Section. 4.4, we assess the efficiency of the developed methods by applying them on two problems, a laplacian model for two dimensional defect absorption and a realistic model describing the absorption of a distant single vacancy by a cavity in Aluminum [14]. We discuss the most efficient strategy to compute the probability vector at times shorter than the mean first-passage time depending on the problem. We conclude in Section. 4.5.

## 4.1 Introduction

As before mentioned, FPKMC method is used to accelerate the conventional KMC simulations. Indeed, the conventional KMC method may become inefficient when employed to simulate all the hops of defects on a lattice [82] and when the transition rate matrix equation exhibits a broad spectrum of frequencies as discussed previously. The causes of inefficiency may be energetic or entropic in origin. The statistically exact approach to mitigate the inefficiency of the KMC methods is to draw sequences of events and first-passage times based on the theory of absorbing Markov chains [57, 75, 80, 84, 85, 86]. Mathematically, the first passage times are the sum of the residence times spent by the walker in connected states prior to getting absorbed by an artificial or physical sink. The absorbing sink is artificial when it corresponds to the peripheral states of an energetic trap, while a physical absorbing sink usually correspond to an energetic trapping basin, like solute clusters and dislocations. Furthermore, in absorbing Markov chains, once the system has reached an absorbing state, it stays there infinitely. Because the probability of being absorbed tends to one as time tends to infinity, the connected states of the trapping basin are commonly known as transient states. Besides, a defect initially located in any transient state can possibly reach any absorbing state, but not necessarily in one step. The no-passage distribution is the conditional probability distribution of the defect on the transient states knowing that it has not been absorbed yet: the sum of probabilities over the transient states is one.

There exist several ways to characterize absorbing Markov chains numerically. The essential goal is to compute the first-passage and no-passage distributions. These two distributions serve to draw the first passage times and moves for a defect to reach the absorbing sink. To achieve these tasks, one implements one of the two following randomization procedures: kinetic path sampling or reverse sampling, based on the factorization [59, 85, 87] or the eigenvalue decomposition [57, 59] of the absorbing transition rate matrix, respectively. When eigenvalue decomposition is performed [57, 59, 84, 86], the survival probability of the defect on the transient state is computed directly, making it possible to draw the desired first-passage or no-passage times through reverse sampling. The original Markov chain describing the defect evolution is assumed to be reversible. This means that the transport of defects obeys detailed balance; the transition probability flux between any

two states is invariant under Markov chain reversal. The transition rate matrix of the Markov chain can therefore be symmetrized using similarity transformation, which ensures the matrix to be symmetric negative semi-definite. The survival probability of the defect before getting absorbed is obtained from the transient evolution operator, a matrix exponential, which is the sum of decaying exponentials. The eigenspectrum of the matrix is real and strictly negative. In this work, the survival probability distribution is estimated using the eigenvalue decomposition method.

In practice, it is difficult to entirely factorize or diagonalize large sparse matrices using dense solvers based on Gaussian elimination, Givens rotations or Householder reflections due to memory limitations. Krylov subspace projection (KSP) methods are commonly used to obtain solutions for sparse high dimensional linear systems. The approximations to these solutions are estimated by minimizing the residual over the subspace formed. A well known KSP method is conjugate gradient (CG) [142], which is used for solving linear systems involving symmetric and positive definite matrices. For symmetric and possibly indefinite system, iterative method like minimum residual (MINRES) method is rather used [143]. In case of non-symmetric matrices, the biconjugate gradient stabilized (BiCGSTAB) method [128, 144] that is a generalized CG method, and also a generalized minimum residual (GMRES) method [144] are available. KSP methods can also be employed to extract a few pairs of eigenvectors and eigenvalues iteratively, like for instance the Krylov-Schur method [131, 145].

The eigenvector associated with the smallest eigenvalue is proportional to the quasi-stationary distribution (QSD). It corresponds to the eigenmode exhibiting the slowest decay and thus to the limit of the no-passage distribution in the asymptotic time limit [146]. The QSD is observed to considerably contribute to the first-passage and no-passage distributions in applications in Chapter 3. It completely characterizes them when trapping is severe and has an energetic origin. However, for purely entropic traps, it is observed that many additional eigenmodes are necessary to correctly capture the early stage absorption kinetics in Chapter 3. Consequently, the computational cost increases with the number of significant eigenmodes. In this work, we investigate the ability of model order reduction techniques based on Krylov subspace projection and eigenvalue deflation to faithfully characterize the early-stage kinetics at a reduced cost, given an initial probability vector.

## 4.2 Model Order Reduction and Iterative Methods

### 4.2.1 Eigenvector Subspace Model Projection

As mentioned in the introduction and observed in Chapter 3, it is not possible to compute the entire eigenspectrum of huge sparse matrices using standard dense solvers. For the mathematical formalism, refer the reader to Section 3.3. Instead, sparse and iterative eigenvalue solvers [129, 133, 147] are to be implemented to extract a limited portion of the eigenspectrum and to

approximate the evolution operator by its projection on the reduced eigenbasis [59]. In practice, the basis encompasses the  $k$  eigenvectors with smallest eigenvalues. By doing so, a reduction of the model is performed and the symmetric transition rate matrix  $\mathbf{A}$  in Eq.(3.21) is approximated by

$$\mathbf{A}^{(k)} = \mathbf{S}\mathbf{R} \left[ \sum_{h=0}^k \varphi_h \varphi_h^T \lambda_h \right] \mathbf{S}\mathbf{R}^{-1}, \quad (4.1)$$

where  $\mathbf{S}$  and  $\mathbf{R}$  are discussed in Section. 3.3.1. The evolution operator is approximated by

$$P_{ij}^{(k)}(t) = \sum_{h=1}^k g_i^h d_j^h \exp(-\lambda_h t), \quad (4.2)$$

where  $g_i^h$  and  $d_j^h$  are discussed in Section.3.3.2.

In the following, we will refer to this approach as the Eigenvector Subspace Model Projection (ESMP) method. Assessing the convergence as a function of the eigenvalue number  $k$  can be done by calculating the survival probability on the reduced eigenvector space and comparing the result with the one obtained using a standard solver computing the matrix exponential function with a built-in convergence criteria [134]. An additional verification can be performed by comparing the truncated MFPT

$$\tau_i^{(k)} = \sum_{h=1}^k \alpha_i^h / \lambda_h \quad (4.3)$$

to the exact one, i.e., to the value  $\tau_i^{(N)}$  defined in Eq. (3.25) and computed using two well-established and robust methods: conjugate gradient and multi-frontal Cholesky [126] algorithms.

In the following subsections, we present additional model reduction approaches based on Krylov subspace projection methods: refer to [128, Ch. 7] for a textbook. Notice that  $\mathcal{A} \in \mathbb{R}^{N \times N}$  will stand for  $\mathcal{A}^I$ , i.e. for the sake of generality will always be equal to the identity to restrict our investigation.

## 4.2.2 Krylov Subspaces

Evaluating matrix functions via eigenvalue decomposition becomes extremely costly for large sparse matrices whenever many eigenpairs are needed. A solution to this problem is to restrict the computation to the product of a vector  $\mathbf{b} \in \mathbb{R}^N$  on the matrix  $\mathcal{A} \in \mathbb{R}^{N \times N}$  function

$$\mathbf{x} = f(\mathcal{A})\mathbf{b}. \quad (4.4)$$

This task is efficiently accomplished using a Krylov subspace projection (KSP) method [148]. In particular, KSP methods are among the most efficient algorithms for estimating the solution of huge sparse linear systems. As examples of Krylov subspace solvers, one mentioned in the introduction,

the conjugate gradient and minimal residual methods aim at computing the quantity

$$\mathbf{x} = \mathcal{A}^{-1}\mathbf{b}, \quad (4.5)$$

which amounts to setting  $f(\mathcal{A}) = \mathcal{A}^{-1}$  [128, Ch. 9]. The Krylov subspace is characterized by its dimension  $\ell$ , matrix  $\mathcal{A}$ , and vector  $\mathbf{b}$  and is denoted by  $\mathcal{K}_\ell(\mathcal{A}, \mathbf{b})$ . Its construction proceeds as follows: vector  $\mathbf{b}$  is left multiplied by  $\mathcal{A}$ , which results in a new vector  $\mathcal{A}\mathbf{b}$ . The new vector is multiplied again with matrix  $\mathcal{A}$  to find  $\mathcal{A}^2\mathbf{b}$ , and this goes on  $\ell - 1$  times, vector  $\mathbf{b}$  being included in the subspace:

$$\mathcal{K}_\ell(\mathcal{A}, \mathbf{b}) = \text{span}\{\mathbf{b}, \mathcal{A}\mathbf{b}, \mathcal{A}^2\mathbf{b}, \dots, \mathcal{A}^{\ell-1}\mathbf{b}\}. \quad (4.6)$$

Gram-Schmidt algorithm is also used on the fly to construct an orthogonal basis of  $\mathcal{K}_\ell(\mathcal{A}, \mathbf{b})$  whose dimension is always equal to  $\ell$ . If it happens that  $\mathcal{A}^\ell \in \mathcal{K}_\ell(\mathcal{A}, \mathbf{b})$ , the subspace construction is resumed and  $\ell$  is set to  $l$ . The basis of  $\mathcal{K}_\ell(\mathcal{A}, \mathbf{b})$  is denoted by  $\mathbf{V}_\ell$ .

### 4.2.3 Krylov Subspace Model Projection

In this section, using the definition of Krylov subspace from Section. 4.2.2, the standard scheme involving matrix-vector multiplications is recalled. In practice, the problem of computing the exponential of a huge sparse matrix  $\mathcal{A} \in \mathbb{R}^{N,N}$  is reduced to the one of computing the exponential of a small matrix  $\mathbf{T}_\ell$  of dimension  $\ell$

$$\mathcal{A}\mathbf{V}_\ell = \mathbf{V}_\ell\mathbf{T}_\ell + T_{\ell+1,\ell}\mathbf{v}_{\ell+1}\mathbf{e}_\ell^T, \quad (4.7)$$

where  $\mathbf{V}_\ell = [\mathbf{v}_1, \mathbf{v}_2, \dots, \mathbf{v}_\ell]$  consists of  $\ell$  orthonormal column vectors and  $\mathbf{T}_\ell \in \mathbb{R}^{\ell,\ell}$  is a symmetric tri-diagonal matrix. Since the vectors from  $\mathbf{V}_\ell$  basis are orthonormal, we have  $\mathbf{V}_\ell^T\mathbf{V}_\ell = \mathbf{I}_\ell$  where  $\mathbf{I}_\ell \in \mathbb{R}^{\ell,\ell}$  is the identity matrix.  $\mathbf{T}_\ell$  corresponds to the projection of  $\mathcal{A}$  onto  $\mathbf{V}_\ell$ , and  $\mathbf{e}_\ell^T$  denotes the  $\ell$ th unit coordinate vector of  $\mathbb{R}^\ell$ . The reduced tridiagonal matrix is obtained by left-multiplying both sides of Eq.(4.7) by  $\mathbf{V}_\ell^T$ :

$$\mathbf{V}_\ell^T\mathcal{A}\mathbf{V}_\ell = \mathbf{V}_\ell^T\mathbf{V}_\ell\mathbf{T}_\ell = \mathbf{T}_\ell, \quad (4.8)$$

while the Arnoldi approximation of  $\mathcal{A}$  is  $\mathbf{V}_\ell\mathbf{T}_\ell\mathbf{V}_\ell^T$ . This last matrix is then used to approximate  $f(\mathcal{A})\mathbf{b}$  using the following vector

$$\mathbf{f}_\ell = f(\mathbf{V}_\ell\mathbf{T}_\ell\mathbf{V}_\ell^T)\mathbf{b} = \beta\mathbf{V}_\ell f(\mathbf{T}_\ell)\mathbf{e}_1, \quad (4.9)$$

where  $\mathbf{e}_1$  stands for the first unit coordinate vector of  $\mathbb{R}^\ell$ ,  $\beta$  for  $\|\mathbf{b}\|$ , the Euclidean norm of  $\mathbf{b}$ , and where we plugged the relation  $\mathbf{b} = \beta\mathbf{V}_\ell\mathbf{e}_1$ .

This approach is another example of model order reduction. For a sparse matrix, the complexity is  $\mathcal{O}(N\ell)$  for storage and  $\mathcal{O}(N^2\ell)$  for the  $\ell$  steps of iteration [149, 150]. Krylov subspaces  $\mathcal{K}_\ell(\mathcal{A}, \mathbf{b})$  of low dimensions are used

in practice, hence this approach is considerably faster than exact full diagonalization techniques that exhibit  $\mathcal{O}(N^3)$  complexity in number of operations and  $\mathcal{O}(N^2)$  in storage.

#### 4.2.4 Eigenvector and Krylov Subspace Model Projection

In this section, we describe a third approach, referred to as eigenvector and Krylov subspace projection method (EKSMP), consisting in projecting the model both on eigenvector and Krylov subspaces. It is based on the standard deflation technique of linear algebra [151, 152, 153]. In deflation, the approximated subspace is divided into two complementary subspaces, so that the two parts of the solution are easier to find using an exact method in the first subspace and an iterative method in the second deflated subspace.

The deflation approach is usually implemented for solving linear systems but we consider it here for evaluating the application of any matrix function on a vector, i.e.  $f(\mathcal{A})\mathbf{b}$ . As previously, function  $f$  will be either the inverse or scaled exponential functions. The main objective of this scheme is to obtain a deflated matrix  $\mathcal{A}^\perp$  whose condition number will be smaller than that of  $\mathcal{A}$ . This is done by discarding the contribution of a few smallest eigenvalues from the system, and focusing on a deflated matrix. Hence, the first subspace is generated by the  $k$  eigenvectors of  $\mathcal{A}$  associated with the lowest eigenvalues as in Section 4.2.1 and is denoted by  $\mathcal{E}_k(\mathcal{A})$ . The deflated subspace is the orthogonal component of the eigenvector subspace and is denoted by  $\mathcal{E}_k(\mathcal{A})^\perp$ . The Krylov subspace is then constructed in the deflated space. The goal is to accelerate the convergence of the projected dynamics towards the exact solution as the dimension  $\ell$  of the Krylov subspace increases.

An orthogonal basis of  $\mathcal{E}_k(\mathcal{A})$  writes  $\Phi_k = [\varphi_1, \varphi_2, \dots, \varphi_k]$ , entailing that  $\mathbf{P} = \Phi_k \Phi_k^T$  and  $\mathbf{I} - \mathbf{P}$  are the orthogonal projection operators on  $\mathcal{E}_k(\mathcal{A})$  and  $\mathcal{E}_k(\mathcal{A})^\perp$ . A general property of projection operators is that they are involution, i.e.  $\mathbf{P}^n = \mathbf{P}$ . A particular property of  $\mathbf{P}$  and  $\mathbf{I} - \mathbf{P}$  is that they commute with  $\mathcal{A}$ , as a result of the spectral theorem. Hence, any power of  $\mathcal{A}$  can be decomposed as

$$\mathcal{A}^n = (\mathbf{P}\mathcal{A})^n\mathbf{P} + ((\mathbf{I} - \mathbf{P})\mathcal{A})^n(\mathbf{I} - \mathbf{P}) = \left(\mathcal{A}^\parallel\right)^n \mathbf{P} + \left(\mathcal{A}^\perp\right)^n (\mathbf{I} - \mathbf{P}), \quad (4.10)$$

where  $\mathcal{A}^\parallel = \mathbf{P}\mathcal{A}$ ,  $\mathcal{A}^\perp = \mathcal{A} - \mathcal{A}^\parallel$ . Consequently, the desired quantity can be decomposed as the sum of the following two terms:

$$f(\mathcal{A})\mathbf{b} = f\left(\mathcal{A}^\parallel\right) \mathbf{b}^\parallel + f\left(\mathcal{A}^\perp\right) \mathbf{b}^\perp, \quad (4.11)$$

where  $\mathbf{b}^\parallel$  and  $\mathbf{b}^\perp$  stands for  $\mathbf{P}\mathbf{b}$  and  $(\mathbf{I} - \mathbf{P})\mathbf{b}$ , respectively. Note that the Krylov subspace in the deflated space can be simply generated from the projected initial vector  $(\mathbf{I} - \mathbf{P})\mathbf{b}$ , which is formally stated by

$$\mathcal{K}_\ell(\mathcal{A}^\perp, \mathbf{b}^\perp) = \mathcal{K}_\ell(\mathcal{A}, \mathbf{b} - \mathbf{P}\mathbf{b}). \quad (4.12)$$

As a result, the approximation subspace is the sum of two subspaces:

$$\mathcal{G}_{k,\ell}(\mathcal{A}, \mathbf{b}) = \mathcal{E}_k(\mathcal{A}) \oplus \mathcal{K}_\ell(\mathcal{A}, \mathbf{b} - \mathbf{P}\mathbf{b}), \quad (4.13)$$

which are orthogonal to each other. Note that ESMP method considers the first subspace only [Section. 4.2.1], while KSMP method the second one only [Section. 4.2.3]. The second term in Eq.(4.11) is projected onto the orthogonal Krylov subspace  $\mathcal{K}_\ell(\mathcal{A}^\perp, \mathbf{b}^\perp)$  and evaluated using full eigenvalue decomposition. The matrix that must be diagonalized is

$$\mathbf{T}_\ell^\perp = (\mathbf{V}_\ell^\perp)^T \mathcal{A} \mathbf{V}_\ell^\perp, \quad (4.14)$$

where  $\mathbf{V}_\ell^\perp$  is the standard orthogonal basis of  $\mathcal{K}_\ell(\mathcal{A}^\perp, \mathbf{b}^\perp)$ . The accuracy of the model order reduction method can be verified by checking the convergence of survival probability distribution and estimation of MFPTs as a function of  $\ell$  given  $k$ . The survival probability of a system that has evolved from initial probability vector  $\boldsymbol{\pi}$  at time  $t = 0$  evaluated using EKSMP method is

$$S_{k,\ell}(t) = \sum_{i=1}^N \sum_{h=1}^k \pi_i \alpha_i^h \exp(-\lambda_h t) + \sum_{i=1}^N \sum_{h=1}^\ell \pi_i \hat{\alpha}_i^h \exp(-\lambda_h^\perp t) \quad (4.15)$$

where  $\lambda_h^\perp$  is the  $h$ th eigenvalue of  $\mathbf{T}_\ell$  and the weighting coefficient  $\hat{\alpha}_i^h$  involves the corresponding  $h$ th eigenvector  $\hat{\boldsymbol{\varphi}}_h$  in the Krylov subspace. After projecting with operator  $\hat{\boldsymbol{\varphi}}_h^T \mathbf{V}_\ell^T$ , we obtain  $\hat{\alpha}_i^h = \hat{g}_i^h \hat{d}^h$  with  $\hat{g}_i^h = \hat{\boldsymbol{\varphi}}_h^T \mathbf{V}_\ell^T \mathbf{s} \odot \mathbf{r} \odot \mathbf{e}_i$  and  $\hat{d}^h = \hat{\boldsymbol{\varphi}}_h^T \mathbf{V}_\ell^T \mathbf{s} \oslash \mathbf{r}$ . Note that assuming exact arithmetic, the survival probability  $S(t) = \boldsymbol{\pi}^T \mathbf{p}^s(t)$  defined from Eq.(3.23) is equal to  $S_{N-\ell,\ell}(t)$  in Eq.(4.15),  $\forall \ell \in \llbracket 0, N \rrbracket$ , since the approximation space  $\mathcal{G}_{N-\ell,\ell}(\mathcal{A}, \boldsymbol{\pi})$  spans the entire phase space.

To later monitor the convergence of the methods as a function of  $k$  and  $\ell$ , we will first inspect the estimated survival probability at  $t = 0$  and additionally evaluate the following reduced MFPT:

$$T_{k,\ell} = \frac{\sum_{i=1}^N \pi_i \left[ \sum_{h=1}^k \alpha_i^h / \lambda_h + \sum_{h=1}^\ell \hat{\alpha}_i^h / \lambda_h^\perp \right]}{\sum_{i=1}^N \pi_i \tau_i^N}, \quad (4.16)$$

where the denominator in Eq.(4.16) corresponds to the MFPT from initial distribution  $\boldsymbol{\pi}$ . This is computed using two linear solvers (sparse Cholesky and CG).

### 4.3 Implementation

The methods described above have been coded in PETSc/SLEPc environments resorting to the matrix function (MFN) object [129, 132, 133, 147, 154, 155]. MFN object also provides the restarted Krylov subspace projection method (R-KSP) [134] to compute the product of common matrix functions

and a vector. R-KSP was used to compute reference values to check the correctness of the faster methods described above. R-KSP is a robust and well-established KSP solver with built-in convergence criteria [134, 154] wherein the Krylov basis is restarted until a convergence criterion is fulfilled. We refer the reader to refer to Appendix B for details. In our case, the application of vector  $\mathbf{b}$  on the matrix exponential is computed for a predetermined set of times  $\{t_n\}_{0 \leq n \leq L}$ :

$$\mathbf{x} = \exp(-\mathcal{A}t_n)\mathbf{b}. \quad (4.17)$$

The operation must be repeated at each considered time. For this purpose, R-KSP method is much more expensive than EKSMF method, because it is not able to provide the entire first-passage law at once.

## 4.4 Numerical results and analysis

In this section, we first discuss the scalability and efficiency of the four different solvers used to extract eigenvalues. We set up a simple absorption model in two dimensions in Section. 4.4.1. Next, we illustrate the three computational methods discussed in Section. 4.2 by applying them to a realistic problem, the absorption of a single vacancy in a cavity in aluminum in Section. 4.4.2. The model describing thermally activated jumps of aluminum atoms into a next nearest-neighbor vacancy is detailed in Ref. [59]. It accounts in particular for the dipole-dipole elastic interactions between the vacancy and the cavity [14]. We characterize the absorption kinetics of the vacancy around the cavity and quantify the effect of the elastic interactions on the vacancy flux towards the cavity in Section. 4.4.3, and on sink strengths (Section. 5.3).

### 4.4.1 Efficiency and scalability of eigensolvers

The simple absorption model describes the motion of a defect on a periodically replicated square lattice of size  $L$  and coordination number  $Z = 4$ . The defect hops from any site to any of its four nearest neighboring sites with reduced frequency of 1. The number of transient states is  $N = L^2$ . The defect can also reach the absorbing sink from a singularized site with an absorbing frequency equal to  $10^{-2}$ . In this particular application, the considered transition rate matrix  $\mathcal{A}$  is thus a modified Laplacian matrix: diagonal elements are equal to 4, but one element is set to value 4.01, while the  $4N$  off-diagonal elements corresponding to transitions are all equal to -1. The matrix  $\mathcal{A}$  is thus symmetric positive definite by construction. We herein evaluate the cost of extracting the linear system using the various sparse iterative solvers from SLEPc library [133] in PETSc environment [129] and with varying the number of cores in the computations. This enables one to deduce the speedup and efficiency resulting from implementing the solvers on a parallel computer architecture.

We use an in-house cluster composed of 36 processing nodes, each node consisting of a dual-processor Intel(R) Xeon(R) Gold 6132 CPU running at 2.60GHz with  $2 \times 14$  cores. As for the sparse iterative solvers, we tested methods like Krylov-Schur (KS), locally optimal block preconditioned conjugate gradient (LOBPCG), generalized Davidson (GD), and Jacobi Davidson (JD). In this first series of computations, the lattice size  $L$  is set to the value of  $10^2$ , so the number of transient states is  $N = 10^4$ . The eigenvalues to be sufficiently accurate and converged, the tolerance value is set up to  $10^{-10}$ . The maximum number of iterations was set to  $6 \times 10^4$ . KS and LOBPCG solvers are implemented without preconditioning, while block Jacobi preconditioning is used by GD solver and also JD solver within its built-in MINRES routine. Figure 4.1 displays the CPU time required to compute the indicated number of eigenvalues using the four iterative solvers. We observe that the Krylov-Schur solver takes less time to extract the eigenvalues than LOBPCG, JD, and GD solvers do.

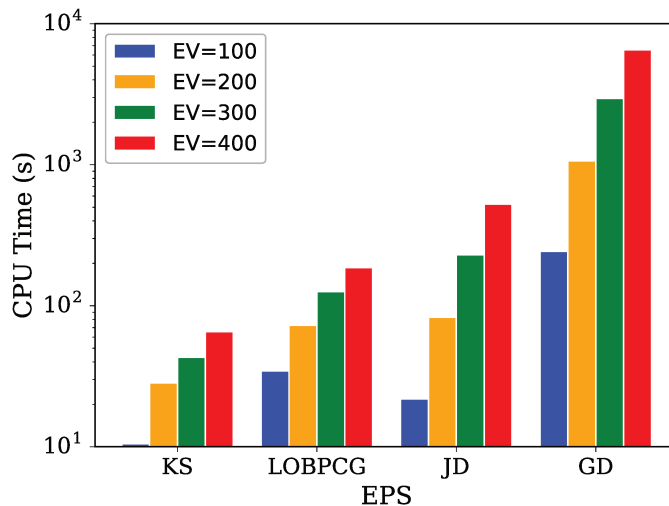


**Figure 4.1:** Comparison of CPU cost for four different iterative solvers (EPS) based on extracting the indicated number of requested eigenvalues (EV).

The performance of KS, LOBPCG, JD, and GD solvers are all expected to be positively impacted through preconditioning. We study the impact of preconditioning resorting to the very efficient sparse Cholesky solver from MUMPS, and report results for KS solver only in the following. Unfortunately, MUMPS preconditioner could not be enabled within LOBPCG in SLEPc, or sub-performed with JD and GD solvers.

For extracting the lowest eigenvalues using the preconditioned KS solver, the inverse spectral transform is enabled and the linear system arising at each reversed iteration is solved using the Cholesky method of MUMPS. Cholesky factorization [156, 157] is done once using the MUMPS package [126]. We

check the performance of Krylov-Schur with sparse Cholesky preconditioning by extracting 100 eigenvalues with varying the lattice size  $L$ . The tolerance parameter to extract converged eigenvalues is set to be  $10^{-10}$ . A linear speedup can be seen in Fig. 4.2 for the performance of Krylov-Schur if implemented with Cholesky preconditioning.

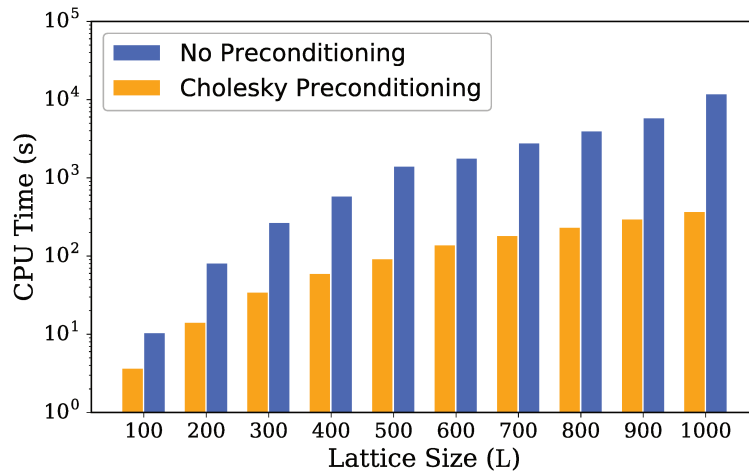


**Figure 4.2:** CPU times for extracting 100 eigenvalues using Krylov-Schur method without preconditioning and with Cholesky preconditioning as a function of the cell size ( $L$ )

As the number of transient states  $N$  increases, it gets computationally more expensive to perform a sequential simulation to extract the eigenvalues. To check the scalability of the Krylov-Schur method, we performed parallel computations with 28 cores to extract the first smallest 100 eigenvectors and corresponding eigenvalues for the transient states  $N$  increasing from  $10^2$  to  $10^6$ . In Fig. 4.3, we observe a linear decrement in the cost of extracting eigenvalues as the number of cores and the number of transient states  $N$  are increased. It can be observed the complexity of the Krylov-Schur method is between square and linear.

In addition to this, we also calculated the speedup ratio and efficiency, defined respectively by

$$S(N_c) = \frac{T(1)}{T(N_c)}, \quad \eta = \frac{S(N_c)}{N_c}, \quad (4.18)$$

where  $N_c$  corresponds to the number of cores. Again, the tolerance parameter was set to  $10^{-10}$  to provide a reasonable trade-off between accuracy and performance. We display in Fig. 4.4 the speedup ratio and efficiency for the following set of transient states numbers:  $N = 10^2, 9 \times 10^4, 36 \times 10^4$  and  $10^6$ . The scalability efficiency  $\eta(N_c)$  decreases as the number of cores increases. However, as the number of transient states increases, the efficiency increases.

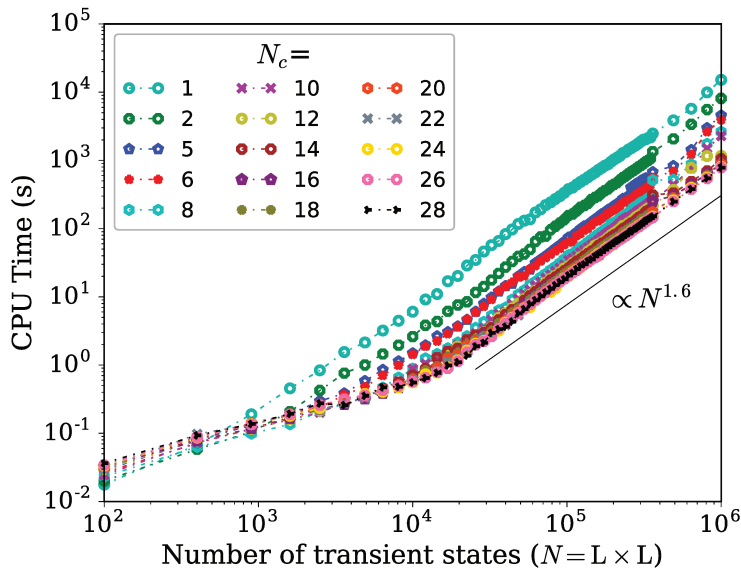


**Figure 4.3:** Evaluated cost for extracting 100 eigenvalues using Krylov-Schur method in sequential and parallel computations as a function of number of transient states  $N = L \times L$  with varying the number of cores ( $N_c$ ).

As shown in Fig. 4.4, we observe that there is a deviation from the ideal linear speedup for  $N_c$  greater than 15. This results from the loss of communication between the processors. In the following, we found a similar scalability for the more realistic model discussed next and that a sequential implementation of the preconditioned KS solver was sufficient to solve our eigenvalue problems.

#### 4.4.2 Survival Probabilities

We further assess the efficiency of the various subspace projection algorithms in computations involving the absorption of a vacancy by a cavity in aluminum. This second model is more realistic as it accounts for the deformation field created by the spherical cavity whose radius is 20.7 Å. The evolution operator given by Eq.(3.22) provides us with the survival probability distribution Eq.(3.23) at time  $t$ . The goal is to characterize the absorption kinetics of a single vacancy around a cavity at 600 K. The coordination number ( $Z = 12$ ) for the FCC lattice indicates the degree of matrix sparsity, i.e., a maximum of  $Z + 1$  elements per row are non zero. This model consists of 34801 transient states. We consider that the initial probability distribution of the vacancy is either localized or uniform: in the first setup, the vacancy is located at a distance of 57.98 Å from the cavity centered along the  $[110]$  direction. The second setup reflects the homogeneous creation of vacancies under irradiation, neglecting spatial correlations originating from cascades. In KMC simulations, the defect position would be drawn from the uniform multinomial law.

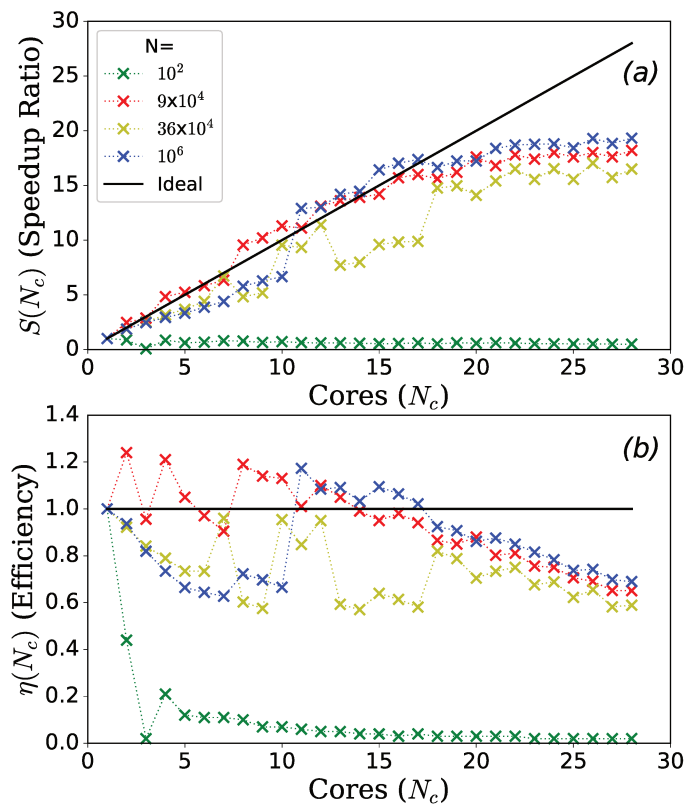


**Figure 4.4:** Computed (a) Speedup ratio and (b) Efficiency of Krylov-Schur method for varying transient states ( $N = L \times L$ ) as a function of cores ( $N_c$ ).

The survival probability distribution are computed using both setups of initial distributions, resorting to Eq.(3.23). The tolerance parameter was set to  $10^{-12}$  and computations are performed using SLEPc and PETSc softwares [132, 133, 154, 155].

We display in Fig. 4.5(a) the survival probability distribution computed using the R-KSP method (refer to Appendix B) as well as the ESMP method (Section. 4.2.1) for up to the 3500 eigenvalues. For the ESMP method, we extracted the lowest eigenvalues by implementing the Krylov-Schur method with the tolerance parameter set to  $10^{-12}$ . For the R-KSP method, the tolerance parameter set was to  $10^{-10}$  for better convergence. We extracted these lowest eigenvalues by implementing the Krylov-Schur method. The displayed distributions are scaled using the MFPT, estimated independently using the two standard linear solvers (sparse Cholesky and conjugate gradient). As it is observed from Fig. 4.5(a), the initial survival probability obtained from the ESMP method is not equal to one. This discrepancy is attributed to the fact that a substantial number of eigenmodes, higher than 3500, significantly contributes to the short time kinetics. The cost of extracting a huge portion of the eigen spectrum limits the applicability of the ESMP method. As for the R-KSP method, the survival probability is equal to one, but one needs to specify the Krylov subspace dimension. Typically, the value for the dimension of the Krylov subspace should not be less than 100. The number of restarted iterations to converge depends on the subspace dimension.

We display in Fig. 4.5(b) CPU times versus physical times for the R-KSP method. We observe that the simulation requires only 0.9 seconds for short time kinetics. However, this method becomes less efficient as time increases. It requires four more orders of magnitude of CPU time to converge at times larger than MFPT. It entails that R-KSP can be practically implemented for the evaluation of survival probabilities at short times only. We now investigate the range of applicability of KSMP and EKSMP methods and check whether they exhibit the same limitations as the ESMP method. The R-KSP method provides the reference data to support the EKSMP and KSMP algorithms.

The survival probability distributions estimated using KSMP and EKSMP methods for localized initial distribution are displayed in Fig. 4.6. The full eigenvalue decomposition of the reduced matrix  $\mathbf{T}_\ell$  was performed using a dense solver from LAPACK library. The Krylov subspace dimension  $\ell$  is varying. We observe a fast convergence with respect to the Krylov subspace dimension for EKSMP and KSMP methods. Interestingly, the EKSMP method with  $k = 1$  requires a substantially smaller Krylov subspace, about 50 to 100, than the KSMP method does, about 500. This implies that the extra dimension required by the KSMP method aims at capturing the long-term kinetics of the QSD mode. This trend is more pronounced when the initial distribution is uniform, as observed in Fig. 4.7 wherein the survival probability and first passage distribution are displayed using KSMP and EKSMP methods and the same setups. This feature is attributed to the higher overlap between the initial distribution and the QSD. The dependence on initial

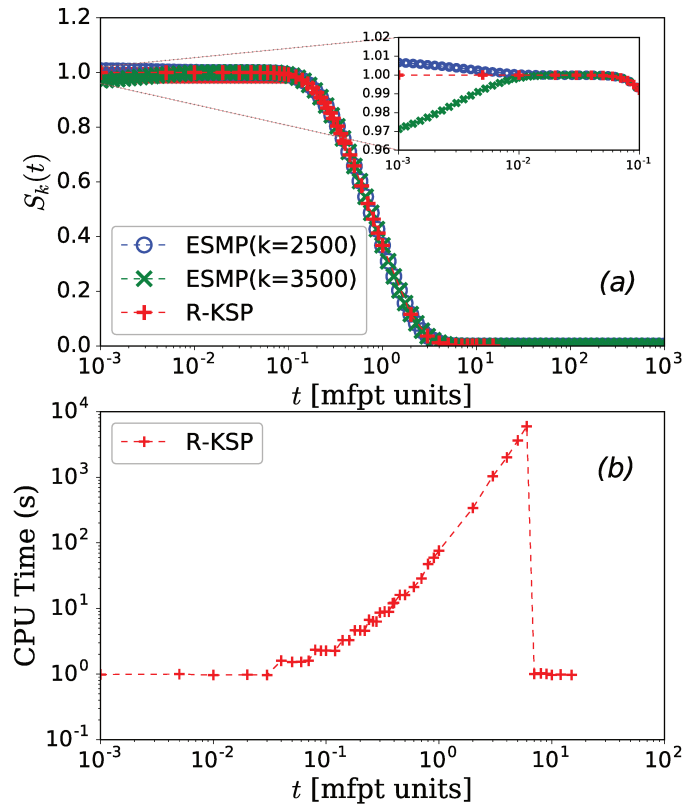


**Figure 4.5:** (a) Survival probability distribution computed using ESMP (2500 and 3500 eigenvalues), and R-KSP plotted in blue, green, and red, respectively. (b) CPU cost for computing survival probability vector at a particular instant of time using R-KSP.

conditions is the main limitation of EKSMP and KSMP methods, compared with the ESMP method that is less sensitive to the initial probability distribution. The significant number of non-local eigenmodes that must be computed contribute to the short time kinetics for a whole range of initial conditions. ESMP is, however, much more costly in terms of memory and CPU, as shown hereafter.

The CPU time taken by the three methods to calculate the survival probability distributions for the absorption problem are reported in Table 4.1. We used two different processors for the simulation of the ESMP method. The sequential run on processors A and B gave the same result. For the parallel run on processor A, a speedup by a factor of 15 was observed, similar the one reported in Fig. 4.4 for the parallel simulations of the two-dimensional model. The ESMP method is computationally more expensive than EKSMP and KSMP methods. Furthermore, it is observed that EKSMP takes more CPU time than KSMP method does. It is because EKSMP method must extract the slowest eigenmode corresponding to the QSD, which requires 153

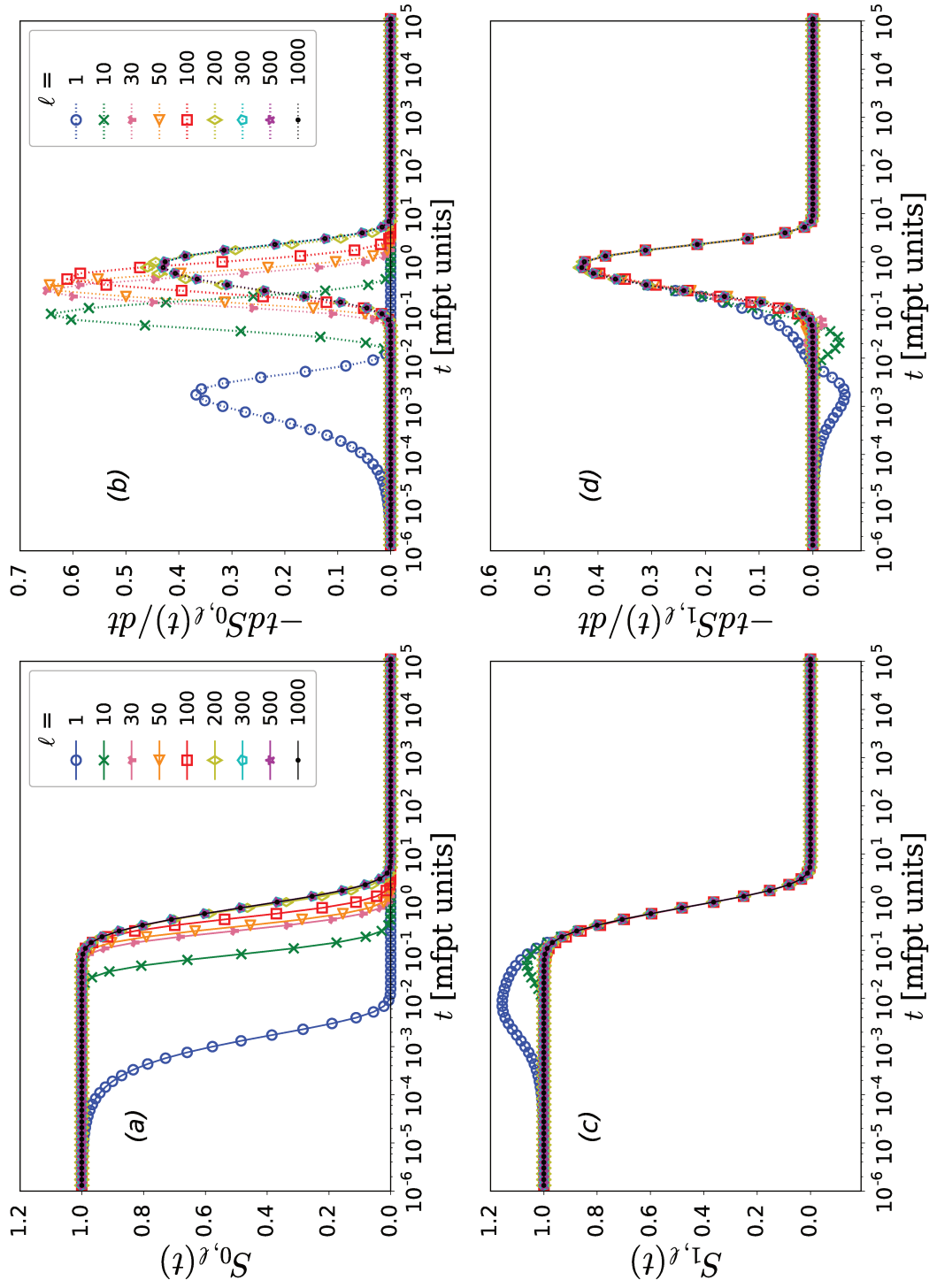


**Figure 4.6:** Comparison of survival probabilities and first passage distributions evaluated for the localized initial distribution using the KSMP method is presented in panels (a,b), and the EKSMMP method is presented in panels (c,d).

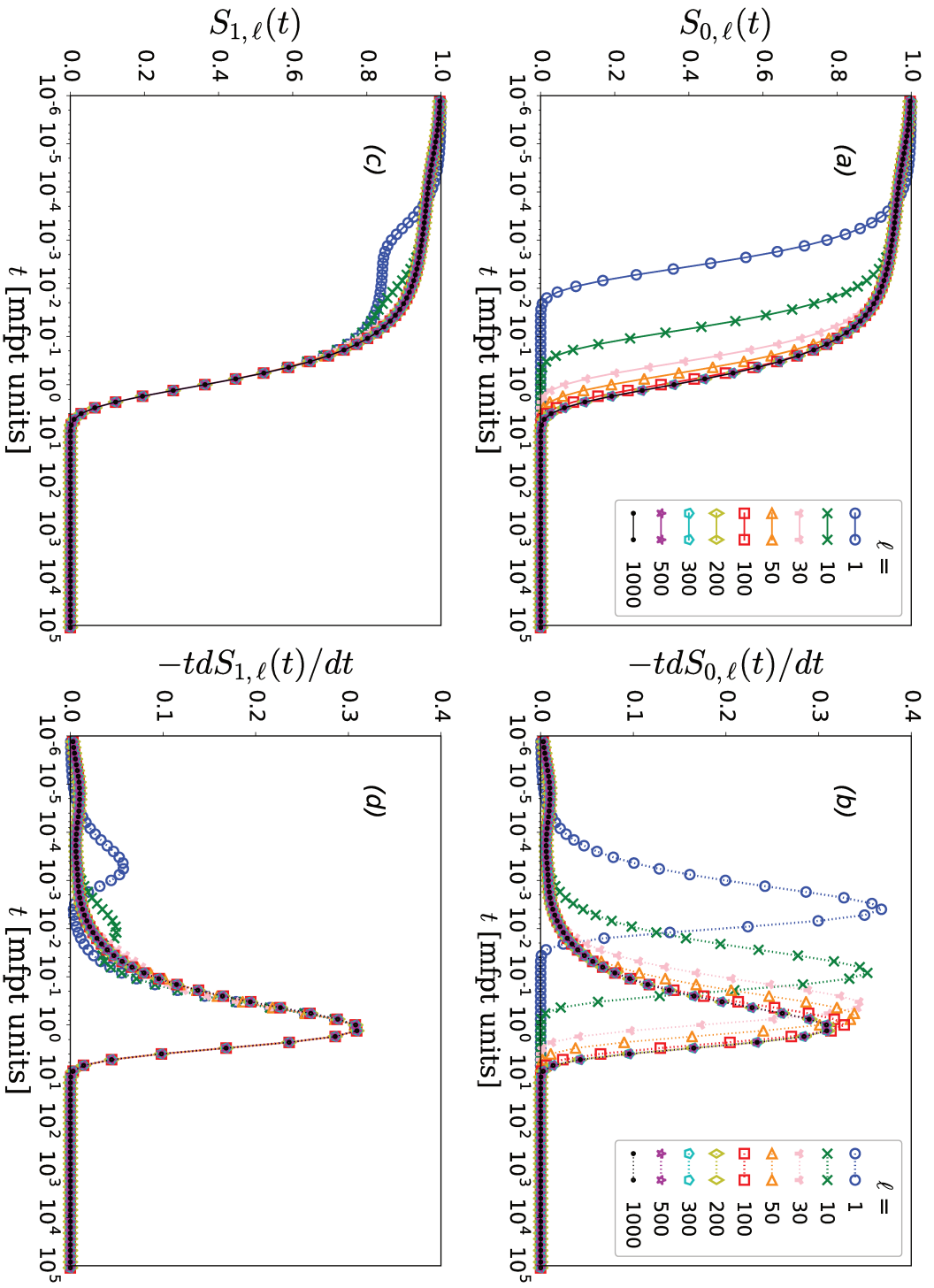


Figure 4.7: Comparison of survival probabilities and first passage distributions evaluated for the uniform initial distribution using the KSMP method is presented in panels (a,b), and the EKSMMP method is presented in panels (c,d).

Processor	Methods	Condition	CPU Time (s)	Cores ( $N_c$ )
Proc-A	ESMP	$k = 3500, \ell=0$	$3.02 \cdot 10^4$	1
		$k = 3500, \ell=0$	$2.13 \cdot 10^3$	28
Proc-B	ESMP	$k = 1, \ell=0$	$8.93 \cdot 10^1$	1
		$k = 3500, \ell=0$	$2.96 \cdot 10^4$	1
	KSMP	$k = 0, \ell=50$	$1.10 \cdot 10^1$	1
		$k = 0, \ell=500$	$8.60 \cdot 10^1$	1
	EKSMP	$k = 1, \ell=50$	$9.83 \cdot 10^1$	1
		$k = 1, \ell=500$	$2.35 \cdot 10^2$	1
ESMP-CP	$k = 3500, \ell=0$	$4.66 \cdot 10^3$	1	
EKSMP-CP	$k = 1, \ell=500$	$1.70 \cdot 10^2$	1	

**Table 4.1:** CPU time taken by ESMP, KSMP, and EKSMP methods to compute the first passage distributions for the single vacancy absorption. Processor A is Intel(R) Xeon(R) Gold 6132 CPU, each node running at 2.60GHz with  $2 \times 14$  cores. Processor B is Intel i5-8400H running at 2.5GhZ with eight cores. CP stands for Cholesky preconditioning using MUMPS package and  $N_c$  is the used number of cores.

seconds of computational time. However, if one is interested in the absorption kinetics from a set of initial vacancy positions, then the EKSMP method will be more efficient because the QSD is computed once.

We quantified the reduced MFPT  $T_{k,\ell}$  and survival probability  $S_{k,\ell}(0)$  estimated using the different methods to monitor the convergence as a function of  $k$  and  $\ell$ . The results are displayed in Fig. 4.8. The blue curve corresponds to the ESMP method. The 3500 eigenvalues evaluated previously have been used. The green and red curves correspond to EKSMP and KSMP for  $\ell = 500$ , respectively. The reduced MFPT converges within  $2 \cdot 10^{-3}$  after  $\ell = 200$  for EKSMP. Truncation errors for estimating the MFPTs are lower with a monotonous behavior and a fast convergence for the KSMP and EKSMP methods as compared to the ESMP method. In panel (c) of Fig. 4.8, we clearly distinguish the convergence rates of the three methods.

To sample the MFPT starting from a uniform initial distribution, we used the EKSMP method. The quantity  $T_{k,\ell}$  was computed with  $k = 1$ , and the results are displayed in Fig. 4.9. Convergence is clearly much faster when the initial distribution is uniform than when it is localized. Hence, a smaller Krylov subspace is required to evaluate the first passage distributions with accuracy and at a low computational cost. The main argument for using both Krylov subspace and eigenvector subspace projections is to reduce the dimension of the former subspace and to reuse the second subspace in other calculations. In Appendix C, additional results are reported concerning the use of Cholesky preconditioning (CP) and about the relevance of increasing the eigenvalue subspace  $k$  in EKSMP method. It is shown that CP decreases the overall CPU cost and facilitates the extraction of additional eigenpairs. It should therefore be enabled whenever possible.

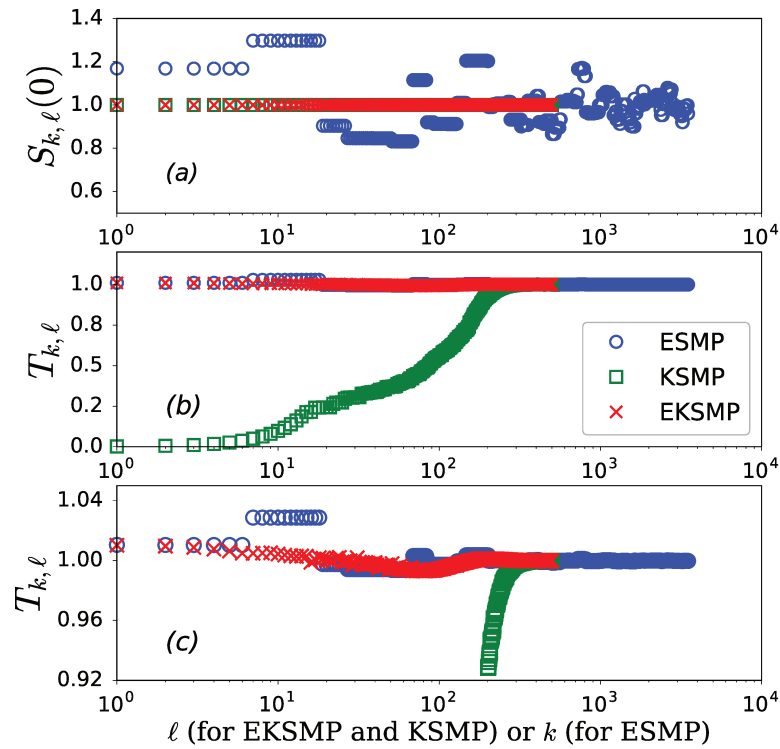


**Figure 4.8:** Comparison of (a) survival probabilities  $S_k(0)$ , (b) reduced MFPT  $T_{k,\ell}$  computed for ESMP (3500 eigenvalues), KSMP (500 eigenvalues) and EKSMP (500 eigenvalues) methods. The panel (c) represents the zoomed in plot for the range of reduced MFPT  $T_{k,\ell}$  from 0.92 to 1.04 for the respective methods.

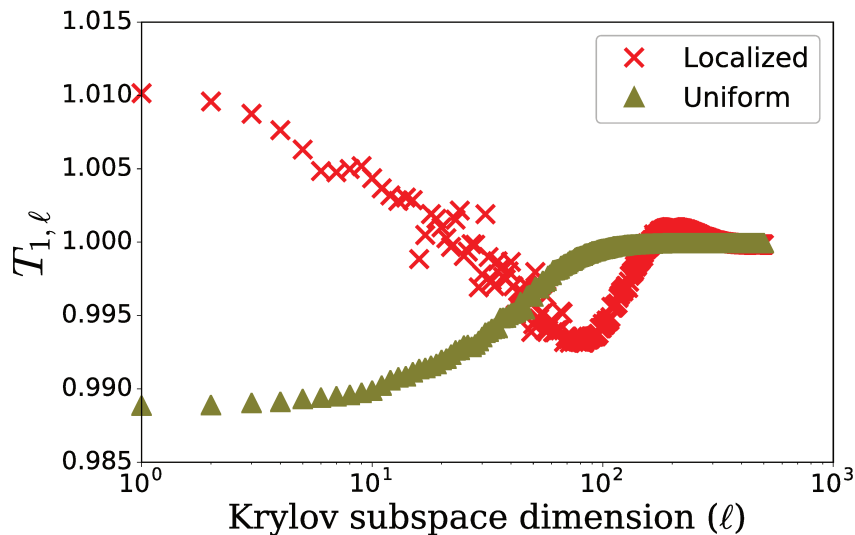


**Figure 4.9:** Reduced and truncated MFPT  $T_{1,\ell}$  evaluated for a localized and uniform initial distribution using EKSMP method.

### 4.4.3 Vacancy absorption kinetics

To visualize the absorption kinetics, we compute and display the probability fluxes to the cavity and the sink strengths from the initial sites of the mobile vacancy. The goal is to investigate the effect of the elastic deformation on the vacancy pathway to cavity.

#### Vacancy flux to cavity

We computed the mean residence time vector  $\theta$  defined by

$$\theta^T = \pi^T \mathbf{A}^{-1}, \quad (4.19)$$

for initial distribution  $\pi$  by casting this equation in the form of Eq. (4.5) and using both the sparse Cholesky and CG solvers (to check that results were matching). Then, introducing the three dimensional lattice coordinates  $\hat{\mathbf{r}}_j$  of the vacancy for state  $j$  [59], the vacancy flux was computed from the relation

$$\hat{\phi}_j = \frac{1}{2v} \sum_{\ell} (\theta_j K_{j\ell} - \theta_{\ell} K_{\ell j}) (\hat{\mathbf{r}}_{\ell} - \hat{\mathbf{r}}_j) \quad (4.20)$$

where  $\theta_j K_{j\ell} - \theta_{\ell} K_{\ell j}$  are the mean probability currents between both the transient and absorbing states,  $\theta$  is the mean residence time vector and  $v$  represents the unit cell volume assumed to be uniform over the simulation box. All panels in Fig. 4.10 represents a quarter of the (001) plane containing the center of the cavity. The vacancy resides on the (100, 100, 0) Cartesian coordinates in Fig. 4.10, along  $\langle 110 \rangle$  direction. We computed residence times Eq.(4.19) and vacancy fluxes Eq.(4.20) for the localized initial distribution for sites  $j$  using linear solver. The algorithm used to compute these quantities are detailed in [59]. Figure 4.10.(a) represents the scaled residence times. We observe that the residence time is high at the periphery and low near the center, where the vacancy is more easily absorbed. Besides, anisotropy in the residence times can be observed as the vacancy evolves through the system and stays for shorter times along [100] and [010] directions, as observed in Fig. 4.10(b). The anisotropy in radial fluxes can also be observed in Fig. 4.10(c). Absorption path along the crystalline direction [110] depicts the anisotropic behavior.

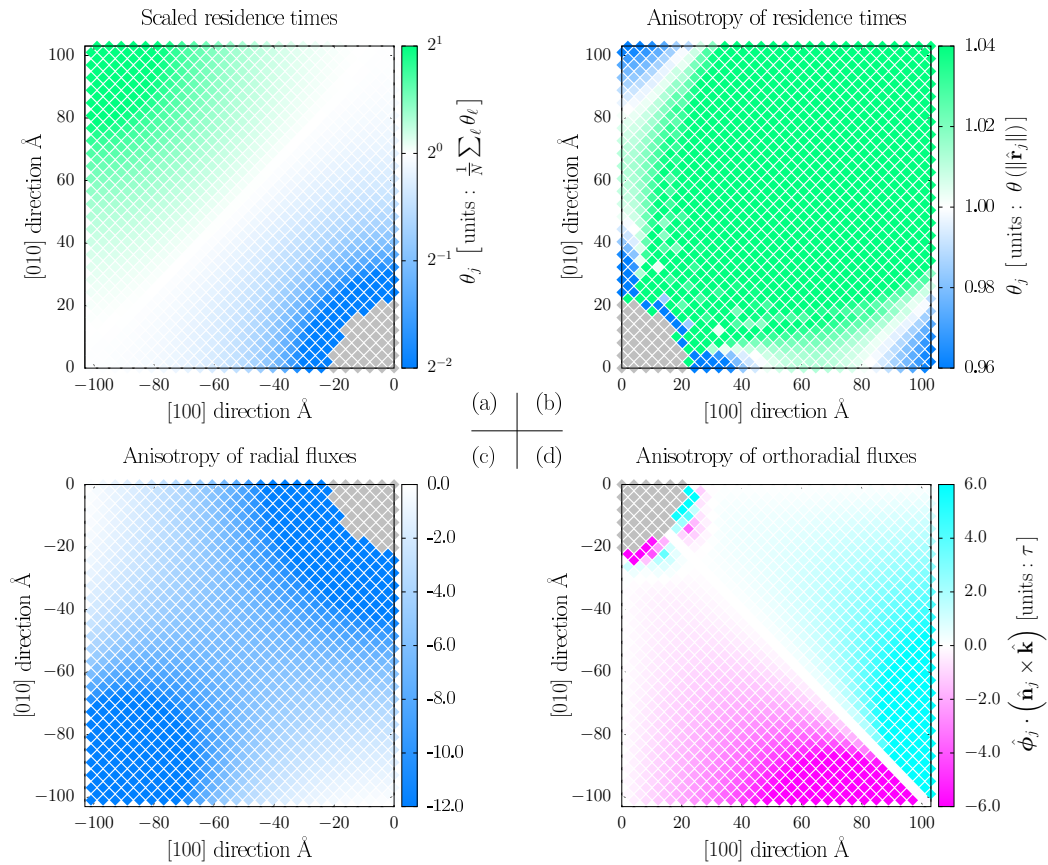


**Figure 4.10:** Estimation of residence times (a,b), radial vacancy flux (c), and ortho-radial vacancy fluxes (d) starting from a localized initial distribution. Absorption of a single vacancy initially located at a distance of 57.98 Å from the cavity center in  $\langle 100 \rangle$  crystalline directions. Coordinates of displayed sites satisfy  $\hat{\mathbf{r}}_j \cdot \hat{\mathbf{k}} = 0$  where  $\hat{\mathbf{k}}$  is the normalized basis vector orthogonal to (001).

The computed vacancy fluxes and residence times for the uniform distribution are displayed in Fig. 4.11. The trends are qualitatively similar to those observed when the initial distribution was localized, but not quantitatively. In this setup, the residence times for vacancy at each site are less, implying that vacancy absorption happens faster.

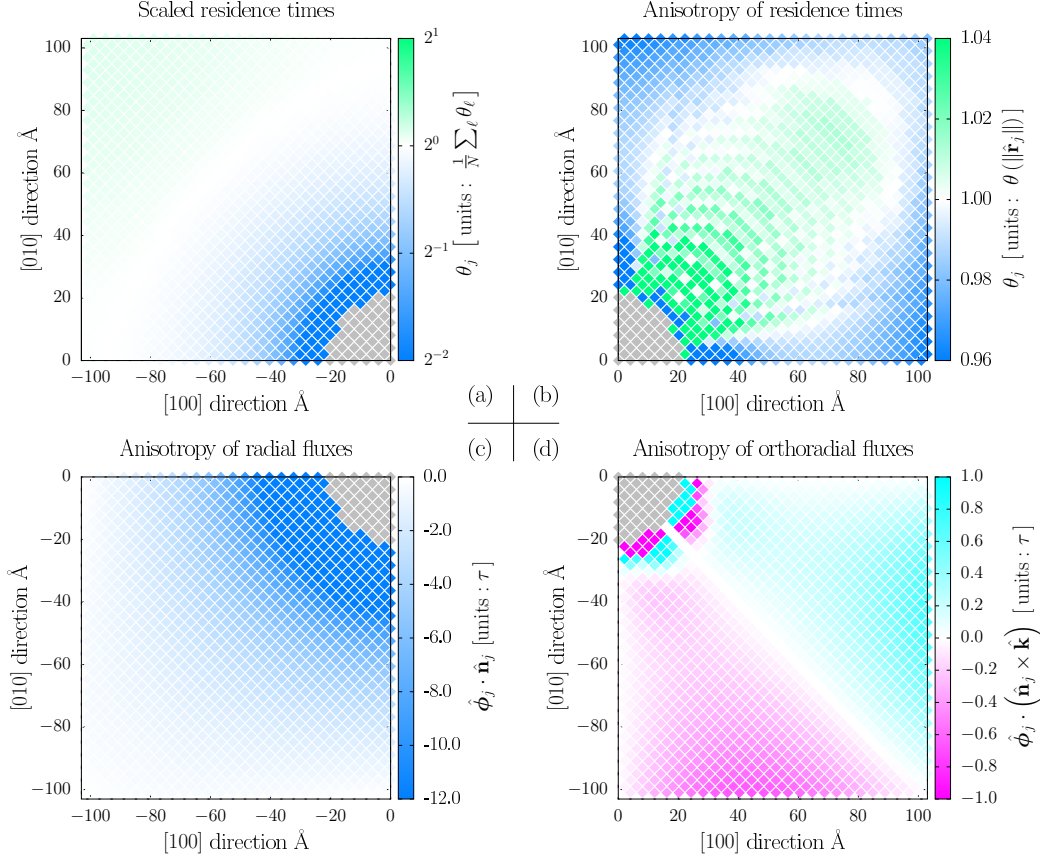


**Figure 4.11:** Estimation of residence times (a,b), radial vacancy flux (c), and ortho-radial vacancy fluxes (d) using a uniform initial distribution. The cavity center is in  $\langle 100 \rangle$  crystalline directions. Coordinates of displayed sites satisfy  $\hat{\mathbf{r}}_j \cdot \hat{\mathbf{k}} = 0$  where  $\hat{\mathbf{k}}$  is the normalized basis vector orthogonal to (001).

Replacing the reduced residence time vector  $\boldsymbol{\theta}/\boldsymbol{\theta}^T \vec{\mathbf{1}}$  with the quasi-stationary probability vector  $\mathbf{q}$  in Eq.(4.20), provides the fluxes in the asymptotic time limit. The results are displayed in Fig. 4.12. The radial dependence of the QSD is shown in Fig. 4.12(a). The reduced probability decreases from 2 far from the cavity to 0.25 at the cavity periphery where the vacancy is about to get absorbed. The anisotropic nature of the radial and ortho-radial fluxes can also be observed in Fig. 4.12 (c,d). The more pronounced anisotropic behavior observed in Fig. 4.10 is due to the localized initial distribution, whereas anisotropy is less critical in Fig. 4.11 and Fig. 4.12. The residual anisotropy associated with the QSD is entirely due to the presence of the elastic field created by the cavity.

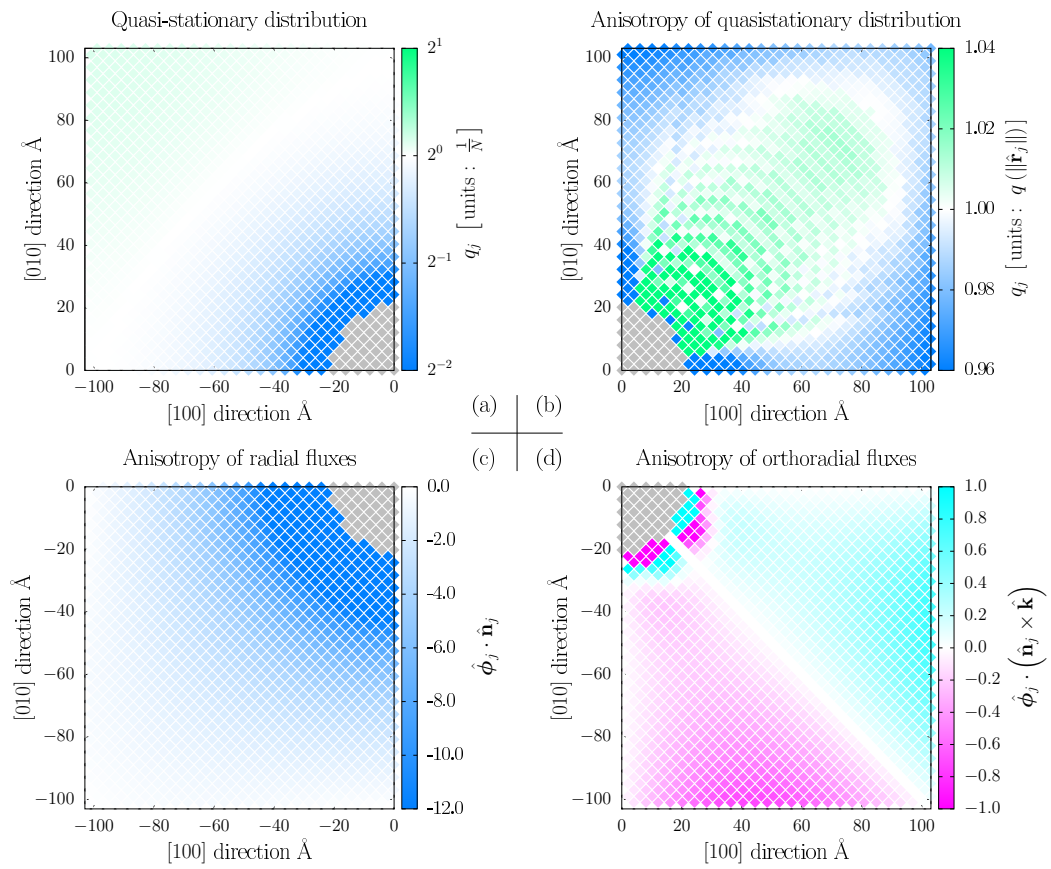


**Figure 4.12:** Estimated quasi-stationary distribution (a), anisotropy of quasi-stationary distribution probability (b), anisotropy of radial vacancy fluxes (c), and anisotropic ortho-radial vacancy fluxes (d) for the localized initial distribution.

## 4.5 Summary

The transition matrices involved in diffusion problems are considered sparse. The usual approach for sparse high-dimensional matrices is similar by repeatedly extracting portions of the eigenspectrum using iterative solvers based on deflation techniques. However, this still requires substantial computational time, restricting the range of applicability of this technique for simulating aging kinetics and microstructural evolution. We succeeded in overcoming this issue by applying Krylov subspace projection techniques. This approach involves vector-matrix multiplications only and reduces the computational complexity by calculating the exponential of a much lower-dimensional transition rate matrix. Two algorithms have been developed dubbed KSMP and EKSMP. KSMP aims at constructing a Krylov basis that starts from the initial probability vector and capturing its subsequent evolution. As the KSMP approach introduces a dependence on the initial vector, we have also developed and tested the additional EKSMP method to deflate the Krylov subspace using the slowest eigenmodes. EKSMP and KSMP methods were implemented to study the absorption kinetics of a vacancy by a cavity in Aluminium. The correctness of the two algorithms was assessed by comparing the results obtained for a subset of times using the R-KSP method as a reference: survival probabilities and first-passage distributions could be accurately reproduced using EKSMP and KSMP methods. Noticeably, an important simplification of the problem to solve stems from the fact that the diffusion process is reversible [59] entailing that all transition rate matrices can be symmetrized through diagonal similarity transformations. The reversibility condition is fulfilled in most applications involving the diffusion of defects even though these defects are created by an irreversible process like neutron, ion, or electron irradiation.

The important parameter controlling the convergence of KSMP and EKSMP methods is the dimension of the Krylov subspace. We found that the KSMP method yields accurate results with a Krylov basis (KB) whose dimension is five times the cubic root of the matrix dimension (the size of the three-dimensional lattice). Such a dimension for the KB makes it possible to capture long sequences of defect hops through the entire cell until absorption, and hence to account for the contribution of the QSD mode. We also observed that for our typical sink problem using the EKSMP method, the KB dimension is considerably reduced, by a factor of 10, even when only the QSD mode is included. This trend results from the fact that the QSD regime is reached very quickly and only involves the local diffusion of the defect. Besides, the extra cost associated with the QSD calculation being less or similar to the cost that is spared by reducing the Krylov subspace dimension, the EKSMP method is more advantageous than the KSMP method. This is especially true when more than one initial defect distribution is considered, a typical situation occurring in KMC and mean-field applications. Because

the eigenvalues are often degenerate and eigenmodes occur in bundles, it was practically inconvenient and computationally expensive to include additional eigenmodes in the EKSMP method. The working space dimension must be determined in the Krylov-Schur solver previously selected in our applications for its superior performance compared to other iterative solvers.

To conclude this Chapter, we show that it is unnecessary to extract several eigenmodes to characterize the absorbing kinetics fully. In the next chapter, we apply the developed numerical methods to compute sink strengths which are crucial input parameters in rate-equation cluster dynamic simulations.



# Characterization and computation of sink strengths

## Contents

---

5.1	Reaction rate theory . . . . .	97
5.2	Sink strengths . . . . .	98
5.2.1	Analytical solution to sink strength . . . . .	98
5.2.2	Numerical approaches to sink strengths computation . . . . .	101
5.3	Characterization of sink strengths: single vacancy absorption to the cavity . . . . .	103
5.4	Sink strengths for mixed mobilities . . . . .	107
5.5	Agglomeration between two interstitial clusters in $\alpha$ -Fe . . . . .	109
5.6	Summary . . . . .	113

---

Under irradiation, microstructures contain many types of defects. The defects are classified here into two subsets. The first subset contains defects that are mobile like vacancy, self-interstitial atoms, and small vacancy or interstitial clusters. The second subset contains defects that are considered immobile, like voids, dislocations, etc. Mobile defects can be annihilated by mutual recombination (for example, vacancy encounters an interstitial) or radiation-induced segregation (RIS) to grain boundaries, dislocations, or precipitates. Point defects can also agglomerate together to form clusters of defects. To study the microstructure evolution, various computational approaches exist, as reviewed in Section. 1.2. At the coarse-grained level, rate equation cluster dynamics (RECD) is performed to analyze the defect's behavior [158]. In RECD, rate equations derived from rate theory (RT) are employed to study the reaction between mobile and immobile defects. In this chapter, we briefly discuss RT in Section. 5.1. Further, in Sec 5.2, we introduce the concept of sink strengths [159] which are the crucial parameters for RECD. Besides, we show how these quantities can be approximated using various analytical theories or estimated using KMC simulations. Finally, in the last Section. 5.4, we show

how to quantify sink strengths restoring to the theory of absorbing Markov chains.

## 5.1 Reaction rate theory

Modern reaction kinetics involves the study of the rate of chemical processes or transformations of reactants to products. The rate of the chemical reaction is expressed in terms of the change in concentration with respect to time [160]. The reactions involving defects whether they are created under irradiation or not can be described thoroughly by transition state theory (TST) [90] (refer Section. 2.3.1). It provides well-established ways of formulating the transition rates. In addition to this, an important approximation that is used in RT is the mean-field approximation (MFA) which provides the average concentration of the defect population instead of the detailed population.

Defects created under irradiation represent the microstructure that evolves through time. At coarse-grained level, RT and MFA are the most appropriate and straightforward methods used to simplify the complexity in microstructure and to perform cluster dynamic simulations [158]. In its simplest form, the rate equations with the concentration of vacancies ( $C_V$ ) and interstitial ( $C_I$ ) in the presence of a sink are two nonlinear coupled differential equations [161]:

$$\begin{aligned}\frac{dC_I}{dt} &= K_p - K_r C_V C_I - k_I^2 D_I C_I, \\ \frac{dC_V}{dt} &= K_p - K_r C_V C_I - k_V^2 D_V (C_V - C_V^e),\end{aligned}\tag{5.1}$$

where  $K_p$  is the rate of defect production in  $\text{dpa}\cdot\text{sec}^{-1}$ . Note that the production rate is same for vacancies and interstitials. The quantities  $D_V$  and  $D_I$  are vacancy and interstitial diffusion coefficients, and  $C_V^e$  is the vacancy concentration at equilibrium. The diffusion coefficients are considered to be homogeneous in space. The second term of the right hand sides of Eq. (5.1) represents the rate of loss of defects due to the recombination [162] with the rate constant which is mathematically represented as  $K_r = 4\pi r_{rec}(D_{vc} + D_{in})V^{-1}$  [161];  $r_{rec}$  is the recombination radius and  $V$  is the atomic volume. The terms  $k_V^2$  and  $k_I^2$  are called sink strengths of defects  $V$  and  $I$ , respectively. Their derivation is discussed in Sec. 5.2. These rates completely depend on the nature of the mobile and immobile defects. The presence of elastic interactions between point defects and sinks causes an absorption bias that was initially described in Ref. [163].

## 5.2 Sink strengths

As mentioned earlier, the mobile defects annihilate to immobile defects, mutually recombine or agglomerate to form larger or smaller clusters of defects, respectively. Accordingly, rate theory predicts the point defect concentrations in space by considering a crystal lattice as an average medium containing an absorbing sinks [160]. The absorption rate of the defects to the sink depends on various factors such as type of defects, concentration, distribution of the defects. This rate is usually given by the term sink strengths  $k^2$  or absorption efficiency  $\kappa$  by normalizing with the sink concentration. Here, in this section, we discuss the theoretical methods proposed in the literature and used to estimate sink strengths Sec. 5.2.1.

### 5.2.1 Analytical solution to sink strength

Analytical formulae for sink strengths were first proposed by F. A. Nicolas [164]. The spatially independent rate equations in Eq. (5.1) are written in terms of currents of point defects towards the sink

$$\begin{aligned}\frac{dC_I}{dt} &= K_p - K_r C_V C_I - I_I, \\ \frac{dC_V}{dt} &= K_p - K_r C_V C_I - I_V,\end{aligned}\tag{5.2}$$

where  $I_V$  and  $I_I$  are the vacancy and interstitial currents entering sink, respectively. Also, known as sink strengths. Initial assumptions made in analytical derivations are: zero rate of defect production ( $K_p = 0$ ) and steady state ( $\frac{dC_V}{dt} = \frac{dC_I}{dt} = 0$ ).

The possible solutions of Eq.(5.2) to obtain sink strengths are provided by solving Laplace's equation or Poisson's equation, and by Wiederisch's approach depending on the different geometries of the sink [164, 165, 166]. Here we present the simplest spherical sink model with radius  $r_{cv}$  that is enclosed in a spherical shell of radius  $R$  depicted in Fig. 5.1. The term  $r_{cv}$  is the sum of the cavity radius and the vacancy radius i.e.  $r_{cv} = r_{ca} + r_V$ .

#### 5.2.1.1 Laplace's approach

The defect concentration is obtained by solving the Laplace equation

$$\nabla^2 C = 0,\tag{5.3}$$

where  $C$  is the concentration of either vacancies or interstitials. The boundary conditions are such that  $C_i$  and  $C_o$  are the fixed concentrations at  $r_{cv}$  and  $R$ . Let us focus on the vacancy case. So, the vacancy current on the inner sink surface at  $r = r_{cv}$  is given as

$$I_V = 4\pi r_{cv}(C_o - C_i)D_V \frac{R}{R - r_{cv}}.\tag{5.4}$$

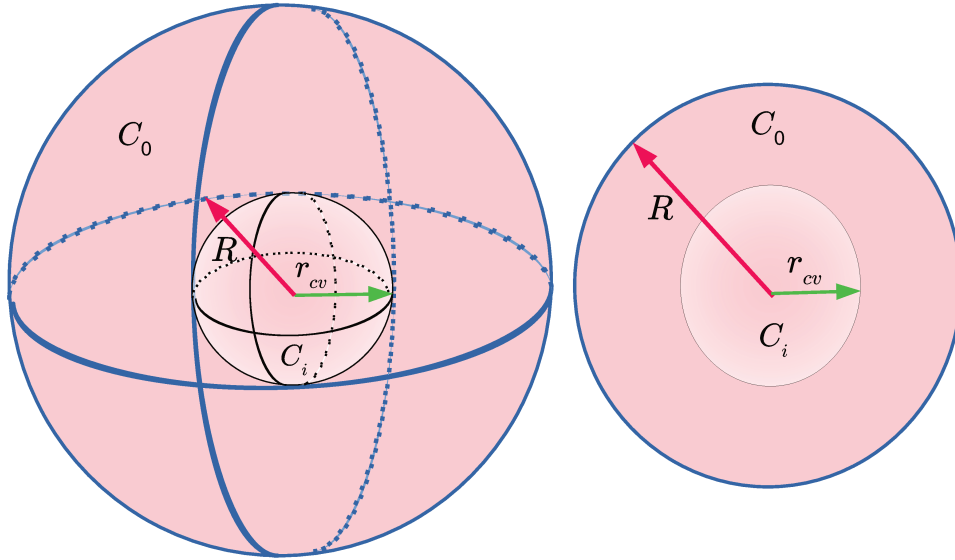


**Figure 5.1:** Sink geometry with spherical symmetry.

For the assumption of low volume fraction of sinks i.e.  $R \gg r_{cv}$ , then

$$I_V = 4\pi r_{cv}(C_o - C_i)D_V. \quad (5.5)$$

Eq. (5.5) gives the sink annihilation term used in Laplace's approach. The total amount of vacancy entering those sinks per unit time is equivalent to sink strengths  $I_v$ . The absorption efficiency is then given as

$$\kappa = \frac{I_V}{D_V(C_o - C_i)} = 4\pi r_{cv}. \quad (5.6)$$

For interstitials, the sink strength formula for the spherical geometry using Laplace's equation is similar. Therefore, the value of vacancy current and diffusion coefficient for the vacancy will be replaced by the value for the interstitial.

### 5.2.1.2 Poisson's approach

In this case, a realistic assumption of uniform rate of production of defects is employed. Thus, the equation to be solved is

$$D_V \nabla^2 C + K_p = 0. \quad (5.7)$$

Here, the sink strengths are evaluated from the concentration on the outer surface. The boundary conditions impose that the vacancy flux at outer region of the sink is null i.e.  $(\frac{dC}{dr})_R = 0$ , and at  $r = r_{cv}$ , we have the equality  $C_{r=r_{cv}} = C_i$ . We obtain the vacancy current at  $r = r_{cv}$

$$I_V = \frac{4}{3}\pi(R^3 - r_{cv}^3)K_p. \quad (5.8)$$

The vacancy current estimated by Poisson's approach in Eq. (5.8) is independent of the diffusion coefficient in comparison to Laplace's approach Eq.(5.4). However, it depends on the defects that will be produced in the spherical region between  $r_{cv}$  to  $R$ . The concentration at  $r = R$  depends on  $D_V$ , and the total vacancy current or sink strengths in this case is given as

$$I_V = 4\pi r_{cv}(C_o - C_i)D_V \frac{1 - (\frac{r_{cv}}{R})^3}{1 - \frac{3}{2}(\frac{r_{cv}}{R}) + \frac{1}{2}(\frac{r_{cv}}{R})^3}. \quad (5.9)$$

If considered the assumption of low volume fraction  $R \gg r_{cv}$ , then sink strengths is given as

$$I_V = 4\pi r_{cv}(C_o - C_i)D_V. \quad (5.10)$$

The absorption efficiency for this case is given as

$$\kappa = \frac{I_v}{D(C_o - C_i)} = 4\pi r_{cv}. \quad (5.11)$$

The formulation of sink strengths using Laplace's approach in Eq. (5.5) is similar to Poisson's approach Eq. (5.10) [164].

### 5.2.1.3 Wiederisch's approach

Wiederisch [164, 165] proposed an additional method to determine the sink strengths. The same boundary condition is assumed as in the case of Poisson's approach. The total vacancy current is estimated by averaging out the vacancy concentration at the outer sink. This implies spatial integration of the vacancy concentration over the sink surfaces in the volume between  $r_{cv}$  and  $R$  using Gauss's theorem. Thus, the vacancy current to this particular case is given as

$$I_V = \frac{6}{b^2}D_V P_k \Delta C, \quad (5.12)$$

where  $b$  is the defect hop distance,  $\Delta C = C_V - C_V^e$  with  $C_V^e$  being the thermal concentration of the vacancies,  $P_k$  is the probability of each defect being absorbed at sink. In Wiederisch formulation, concentration  $C_V^e$  is similar to concentration  $\bar{C}$  at the sink surface. Therefore, the vacancy current or sink strength at  $r = r_{cv}$  is written as

$$I_V = 4\pi r_{cv}(\bar{C} - C_i)D_V \frac{1 - (\frac{r_{cv}}{R})^3}{1 - 1.8\frac{r_{cv}}{R} + (\frac{r_{cv}}{R})^3 - 0.2(\frac{r_{cv}}{R})^6}. \quad (5.13)$$

The absorption efficiency for this analytical approach is given as

$$\kappa = 4\pi r_{cv} \frac{1 - \left(\frac{r_{cv}}{R}\right)^3}{1 - 1.8\frac{r_{cv}}{R} + \left(\frac{r_{cv}}{R}\right)^3 - 0.2\left(\frac{r_{cv}}{R}\right)^6} \quad (5.14)$$

Expressions in Eq. (5.13) yields the same sink strengths as in Eq. (5.5) and Eq. (5.10) at low sink densities, i.e.  $R \rightarrow \infty$ . Besides, the three approaches given by formulas Eq. (5.5), Eq. (5.9) and Eq. (5.13) discussed in this section do not account for the elasticity in their assumptions. In fact, it is difficult to derive analytical expressions for anisotropic sink strengths and account for effect of elastic interactions. This is because of the spherical symmetry that is assumed in the analytical derivations and that is broken by the elastic interactions. Wiedersich's approach based on averaging the defect concentration is considered more realistic by F. A. Nichols [164]. In Ref. [160], the author do not recommend Laplace's approach as it is equivalent to the assumption of having infinite sink strength in the medium as it is less accurate than Wiedersich's approach. In this thesis work, we do not discuss the effective medium approach, which is recommended and described briefly in Ref. [77, 160].

### 5.2.2 Numerical approaches to sink strengths computation

The analytical calculations of sink strengths are impossible whenever the sink geometries are complex and the elastic fields generated by the sinks are an important factor. There are numerical modeling approaches based on partial differential equations such as diffusion equation and a recently formulated phase-field equation [167] employed to quantify sink strengths. The stationary regime is extracted using finite-difference methods [101, 168, 169] or finite-element methods [77, 170, 171, 172] which belongs to partial differential equations (PDE). In the finite-difference or finite-element methods, the studies are performed on finite-size volume, including the sink. Further, the boundary conditions are applied to the point defects concentrations, which makes it similar to Laplace's or Poisson's approaches.

At variance, in the phase-field approach, the complex defects of the microstructure may be included in the model, which allows accounting for the migration of point defects in dislocations. Such models are more realistic but can be inappropriate for the sink strength calculations [77, 101]. Recently, the diffusion equation approach using the finite-element method has been used in Ref. [101] to study the microstructural heterogeneities evolution. This numerical scheme is quite extensive and requires a huge amount of CPU time. They do not consider the lattice structure while modeling the problem. In BCC steels, the motion of small SIA clusters is able to propagate along a particular glide direction and to change its gliding direction by rotating [173] occasionally. Unfortunately, it is difficult to model the rotation events using partial differential equations (PDE) method.

Another important computational approach to determine sink strengths is to simulate the diffusion of point defects towards the sink using the KMC

method. In this method, migration of defects is considered in a simulation box that contains one or several sinks. This migration of the defects depends on the various properties of the medium and sink. Periodic boundary conditions are usually applied. Recombination of vacancy and SIA is usually not considered. The sink is assumed to be immobile, and sink strength for a given volume and sink concentration is estimated depending on the concentration of the mobile defect and on its production rate of the involved defect. The sink strength is then deduced from the average point defect concentration at the stationary state [174, 175]

$$k^2 = \frac{2N}{d^2 \langle n \rangle} \quad (5.15)$$

where  $N$  is the space dimension ( $N = 3$  for three-dimensional migration) and  $\langle n \rangle$  is the average number of jumps made by a defect before absorption,  $d$  is the average jump distance. The value of  $d$  is  $a_0\sqrt{3\nu}/2$  for BCC lattice and  $a_0\sqrt{\nu}/2$  for FCC lattice, where  $a_0$  is the lattice parameter. Another KMC method employed to evaluate sink strengths is using equation [176]

$$k^2 = \frac{K_p}{DC}, \quad (5.16)$$

where  $K_p$  is the production rate per unit time of point defects in the simulation box,  $D$  is the respective diffusion coefficient, and  $\bar{C}$  is the average concentration of defects. The Eq. (5.15) and Eq. (5.16) are similar to each other as they are both equal to the inverse of the time spent by one defect before absorption multiplied by the inverse of the diffusion coefficient. This approach is more similar to the Wiederisch approach. Both approaches in Eq. (5.15) and Eq. (5.16) are valid in presence or absence of elastic interactions.

In summary, numerical approaches to the sink strength problems allows us to consider the elastic interactions naturally. The numerical solution of the diffusion equation by finite-difference and finite-element allows taking into account the elastic interactions [77]. The KMC calculations also allow taking into account the interaction energy, with the precise consideration of the properties of point defects [176].

### 5.3 Characterization of sink strengths: single vacancy absorption to the cavity

In this section, we quantify sink strength parameters for two physical models of point defects. We assess the efficiency of the numerical approaches by comparing the results obtained in absence of elastic interactions with those obtained from the analytical methods. The numerical approaches considered here are based on the theory of absorbing Markov chains introduced in Chapter. 3.

We quantify the sink strengths defined by

$$k_V^2 = \frac{1}{\tau D_V} = \frac{N}{\sum_{j=1}^N \tau_j^{(N)} D_V} \quad (5.17)$$

where  $\tau$  denotes the MFPT associated with the uniform distribution is calculated using expression Eq.(3.25),  $D_v$  the diffusion coefficient of the vacancy. Letting  $\nu$  denote the vacancy-atom exchange frequency, we have  $D_v = \alpha a^2 \nu$  and  $\nu = \nu_0 e^{-E^m/(k_B T)}$  with  $E^m$  the migration energy,  $\nu_0$  the Debye frequency of aluminum,  $k_B$  Boltzmann's constant, and  $T$  the temperature (600 K),  $\alpha = 1$  for FCC lattice [14]. To compare between simulations and theory, it is convenient to define absorption efficiencies  $\kappa$  by re-normalizing the sink strengths by the cavity concentration:

$$\kappa = k_V^2 / C_c, \quad (5.18)$$

where the cavity concentration  $C_c = (2R)^{-3}$  and  $R$  is the average half distance between sinks (cavity) [177]. For each theoretical approaches reviewed in Sec. 5.2.1 we compiled the absorption efficiencies in Table.5.1. We consider a

Approach	Absorption Efficiency
Laplace	$4\pi r_{cv}$
Poisson	$4\pi r_{cv} \frac{1-\eta^3}{1-\frac{3}{2}\eta+\frac{1}{2}\eta^3}$
Wiedersich	$4\pi r_{cv} \frac{1-\eta^3}{1-\frac{9}{5}\eta+\eta^3-\frac{1}{5}\eta^6}$

**Table 5.1:** Analytical solution of absorption efficiency by different approaches for spherical sink geometry [14, 164]. The term  $r_{cv}$  is the equal to sum of the cavity radius and the vacancy radius i.e.  $r_{cv} = r_{ca} + r_V$ . We estimate  $\eta$  in Wiedersich approach as  $r_{cv}/R$ .

model describes the absorption of a single vacancy by a cavity, here in FCC lattice of aluminum.

The computed absorption efficiencies are displayed in Fig. 5.2. The curve provided by Wiedersich model ( Table.5.1) has an almost perfect match with

the simulation results. The constant value given by Laplace's model in Table 5.1 corresponds to absorbing efficiency in the limit of zero concentration of sinks. The absorption efficiencies are obtained by solving the linear system. The absorption efficiencies obtained in the computations seem to converge to this value as concentration decreases. Another striking feature obtained by the algebraic computations is the negligible dependence of sink strengths on elastic interactions even for high concentration of the cavity, at least for the uniform initial distribution used in this numerical set-up.

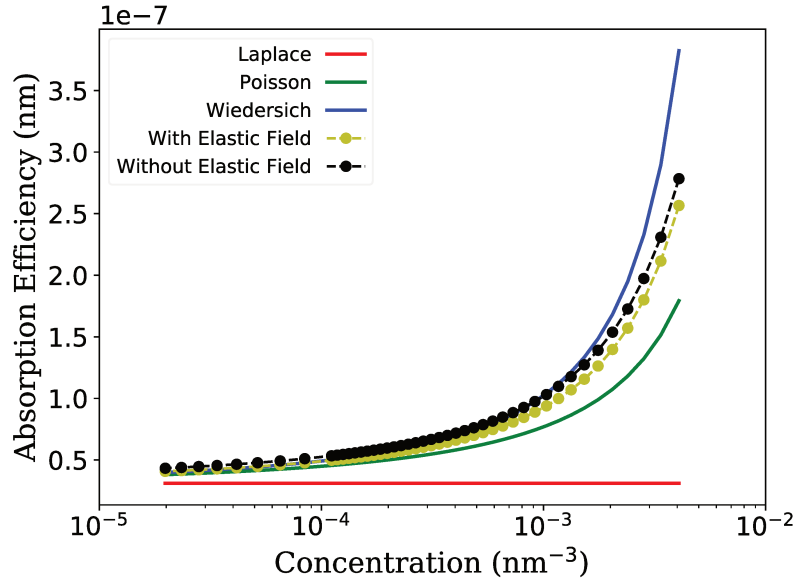


**Figure 5.2:** Comparison of absorption efficiencies calculated for the sink absorption model using MFPT from Eq.(3.25) and uniform initial distribution to those obtained from Laplace, Poisson, and Wiedersich approaches.

We note that the proposed numerical algebraic approach to sink strength computations possibly gives access to a lot of additional information, such as the total number of vacancy jumps and the distance traveled by the vacancy before absorption by the cavity, and also the dependence of the sink strengths on the initial probability distribution. The transient number of vacancy jumps is deduced from the residence time vector  $\vartheta^T = \pi^T \mathbf{A}^{-1}$ , a quantity depending on the initial probability vector  $\pi$ . The number of transient jumps from any state being equal to the product of the residence time and the jump frequency, the total number of jumps is obtained by summing over all transitions and writes  $\sum_i \vartheta_i A_{ii}$ . Multiplying by  $a\sqrt{2}/2$ , the nearest neighbour distance between lattice site yields the distance traveled by the vacancy prior absorption. The later distance scaled by minimum distance separating the cavities, i.e. the period length, has been displayed in Fig. 5.3 for a range of cavity concentrations. We observe that the traveled distance increases much faster than the separating distance. The distance ratio follows a parabolic law, entailing that the traveled distance grows as the cube of the separating distance.

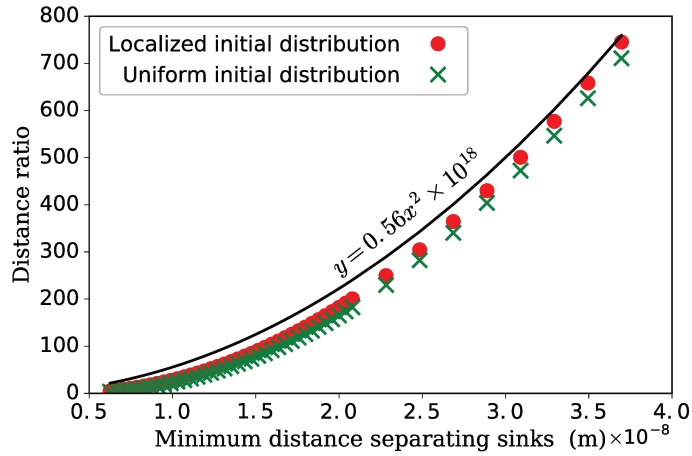


**Figure 5.3:** Distances traveled by the vacancy before absorption scaled by the minimum distance separating the sinks, for uniform and localized initial distributions, and plotted as a function of the separating distance.

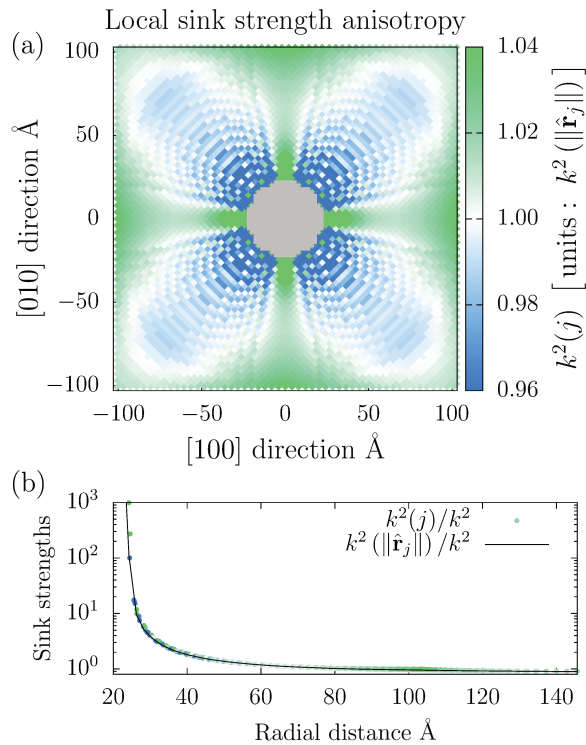


**Figure 5.4:** Using uniform distribution, (a) estimation of anisotropic sink strengths for the site  $j$ , and (b) evolution of the sink strengths parameter over a radial distance between the cavity and the vacancy.

We eventually quantify the anisotropy of the sink strengths associated with the localized initial distributions  $e_j$ . Local sink strengths are defined by

$k^2(j) = 1/(\tau_j D_v)$  where  $\tau_j$  is the MFPT from site  $j$ . Their anisotropy, clearly visible in Fig. 5.4.a, is very moderate, in contrast to the radial dependence shown in Fig. 5.4.b.

This means that there is no need to account for elasticity to compute sink strengths of small cavities with respect to vacancies in aluminium under irradiation. Note that the size of the simulation box is restricted to  $3 \times 10^6$  sites due to memory constraints, and that the cavity sizes is also modest. We however expect a higher effect of the elastic field created by interstitial loops on the absorbing/emitting fluxes of point defects in aluminum [14]. The anisotropy of these fluxes may introduce a substantial angular dispersion of sink strengths which should ideally be taken into account in cluster dynamics simulations. This can be achieved by implementing the approach developed in a recent work [177] in which the dispersion effect of the distances between the sinks is correctly accounted for in hybrid cluster dynamics simulations [178].

## 5.4 Sink strengths for mixed mobilities

Analytical solutions to sink strengths for the two mobile defect clusters migrating isotropically in the three-dimensional space (3D-3D) are available in the literature [173]. They can be deduced from the particular case where one of the defects is immobile (3D-0) and by considering that the diffusion coefficient of the hybrid defect is the sum of the diffusion coefficients of the two original defects. In Ref [40], the authors have considered small defect clusters with mixed mobility, involving a migration mechanism between pure 3D-mobility and pure 1D-mobility [173]. The migration mechanism associated with 1D/3D mixed mobility consists of random hops of defect clusters along its 1D glide direction. We refer to the mixed 1D/3D mobility as 1DR mobility, hereafter. Occasionally, these defect clusters rotate and migrate along new glide direction. The rotation mechanism is thermally activated or may result from a collision with another defect [174]. It is challenging to derive the analytical expressions of absorption rates or cluster sink strengths (CSS) for mixed mobilities that depend on defect geometry, interaction energies, migration paths, and spatial properties. This type of mixed mobility has not been implemented in the RECD method so far. We will focus here on the 1DR-1DR migration mechanism of two defect clusters with non-zero rotation frequency. This set-up has been sparsely studied in the literature so far. The limiting case where the rotation frequencies go to zero corresponds to the so-called 1D-1D mobility [173].

The schematic representation of 1D-1D mobility is displayed in Fig. 5.5 with two defect clusters A and B gliding in non-coplanar and distinct directions in a 3D system. The cluster radii are denoted by  $R_A$  and  $R_B$ . The quantity  $h$  is the distance separating the two planes. It is also the minimum distance separating the two defects. The value of  $h$  determines whether the two gliding clusters can agglomerate [173]. If the value of  $h$  distance is large enough, the clusters glide in their respective directions without and possibility to agglomerate. The condition for any two defect clusters to agglomerate before rotation is to be in an agglomeration slab, i.e., when  $h \leq R_A + R_B$ . The mixed mobility of 1D-1D was first considered by Gösele [179] and co-authors. They showed that it is analogous to the case of a 2D mobile defect with respect to an immobile sink (1D-1D  $\leftrightarrow$  2D-0). The migration of two non-coplanar defect clusters, A and B, with coplanar glide directions is illustrated in Fig. 5.6. This model is described geometrically as a 2D random walk with its midpoint in the plane. The minimum distance between two defect clusters is reached at the intersection of the two glide directions. Agglomeration occurs when the distance between the origin and the midpoint becomes equal to the  $\frac{R_A+R_B}{2}$  and  $h = 0$ .

In the following section, we further detail the case of two self-interstitial defect clusters with 1DR-1DR mobility that can agglomerate and explain how to estimate sink strengths associated with this model. Two algorithms are used to evaluate sink strengths discussed in Appendix E. The first algorithm aims at computing the mean first-passage times by solving a linear system of

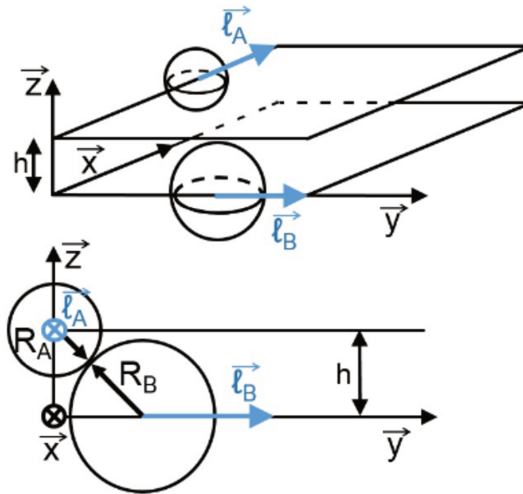


**Figure 5.5:** Schematic view of the geometric condition for the interaction of two non-coplanar particles with glide direction  $\vec{l}_A$  and  $\vec{l}_B$  respectively (from [173]).

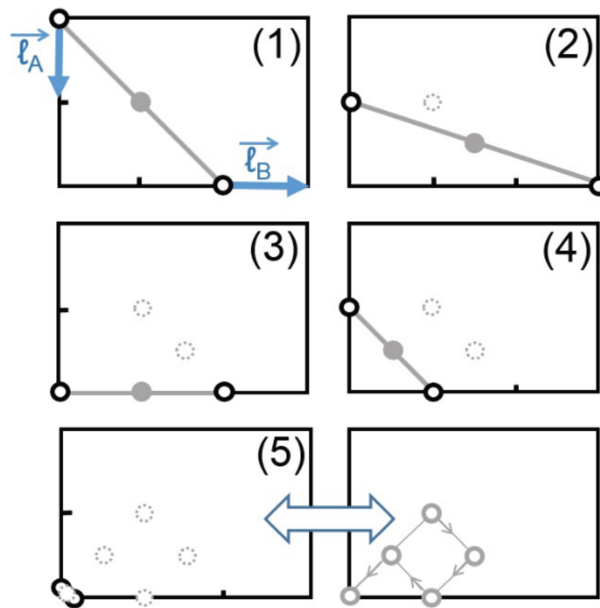


**Figure 5.6:** Schematic view of the trajectory of two absorbing 1D random walkers (black circles with  $\vec{l}_A$  and  $\vec{l}_B$  jump vectors) and the 2D-random walk of their midpoint (blue solid and dashed circles for the current and past positions respectively) being absorbed by a fixed sink sitting at the intersection of their glide directions (from [173]).

equation, as discussed in Chapter 3. This approach involves constructing the transition rate matrix. The second algorithm implements a simplified version of kinetic path sampling [85] also discussed in Chapter 3.

## 5.5 Agglomeration between two interstitial clusters in $\alpha$ -Fe

This section presents the model to study the agglomeration kinetics of two mobile interstitial defect clusters, both evolving with mixed 1DR mobility. The two clusters  $A$  and  $B$  are of different radii  $R_A$  and  $R_B$  and glide along with their respective directions with different non-zero rotation frequencies. The clusters are considered to propagate, and agglomerate, which can be conceptualized by considering an artificial absorbing sink—the geometrical representation of the 1DR-1DR mobility as discussed in Sec. 5.4 is applicable here as well. The crystal lattice considered here is  $\alpha$ -Fe BCC cubic lattice with 48 symmetries, i.e., 24 rotational and 24 reflections. The transition rate matrix of the 1DR-1DR mobility represents the transition frequencies associated with the hops.

We implement two different algorithms to estimate sink strengths for this model. Figure 5.7 represents the general steps followed by both algorithms. As a first step, we reduce the transition rate matrix by taking into account of the cubic symmetries. We introduce a descriptor over the space of configuration, that is here an integer value. For any two distinct configuration, the two associated descriptor values are different. This allows distinguishing configurations. We also construct classes of configuration as follow.

Configuration classes are generated by applying the 48 cubic symmetries to all the configuration and retaining the distinct configurations in each class. The configuration descriptors are then sorted out in ascending order, and the smallest one corresponds to the class descriptor. The transition rate matrix is then constructed with respect to the set of classes. A reduction of the dimension of the transition rate matrix by a factor of almost 48 is achieved for systems large enough.

Algorithm 4 in appendix E describes the compression of the transition rate matrix and the reduction of the linear system of equations yielding the mean first-passage times. Subsequently, sink strengths are computed using Eq. (5.2) where  $D = D_A + D_B$ . Algorithm 5 in appendix E details a kinetic path sampling algorithm for computing the sink strengths when the defect concentration is so low that the linear system cannot be solved numerically. Algorithm 5 is based on the factorization and randomization procedure which allows drawing first-passage times and displacement along the gliding directions.

Figure 5.8 represents the sequence of hops made by cluster A along the glide segment before reaching the artificial sink, a process corresponding to lines 14 and 23 in algorithm 5. To assess the efficiency of the developed algorithms, first-passage time distributions are evaluated using both KMC and kPS algorithms. The results are displayed in Fig. 5.9. It takes few seconds on Intel i5-8400H processor (running at 2.5GhZ with eight cores) to generate the distribution with kPS algorithm but few hours with the conventional KMC algorithm. In the example of Fig. 5.9, the line segment consists of 2001 sites

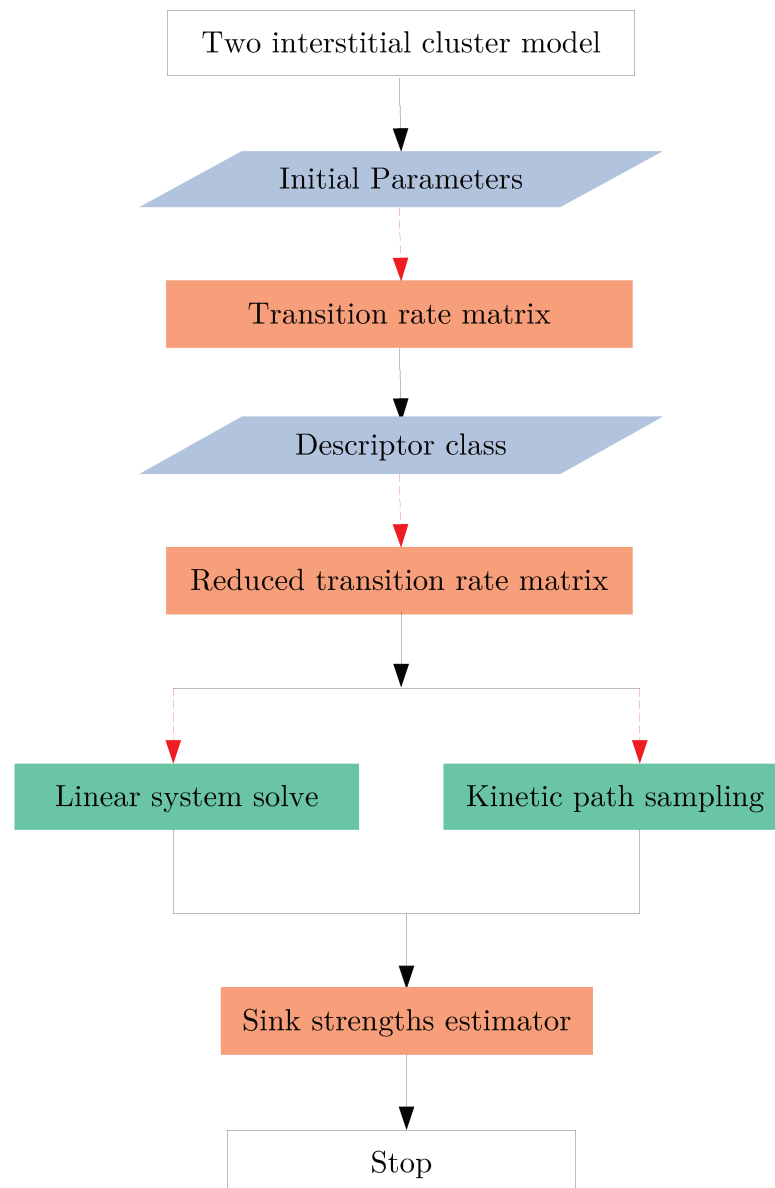


**Figure 5.7:** Flowchart representing the formulation of transition rate matrix and sink strengths for two 1DR-1DR mobile interstitial clusters in super cell.

and the mobile cluster starts at site 1251. The exit probability on the right is thus higher, as observed from the histograms displayed in Fig. 5.9. The histograms have been constructed using  $10^6$  first-passage events for both kPS and kMC algorithms. The kPS algorithm takes into account the recursive structure of the first-passage problem. This makes it possible to formulate a kPS algorithm whose computational complexity is  $\mathcal{O}(\log N)$ , where  $N$  is the

number of transient states. As a comparison, the complexity of the conventional KMC algorithm is  $\mathcal{O}(N^2)$ . Thus, the kPS algorithm will be expected to be much more efficient and cheaper than the KMC algorithm for this particular sink strength problem.

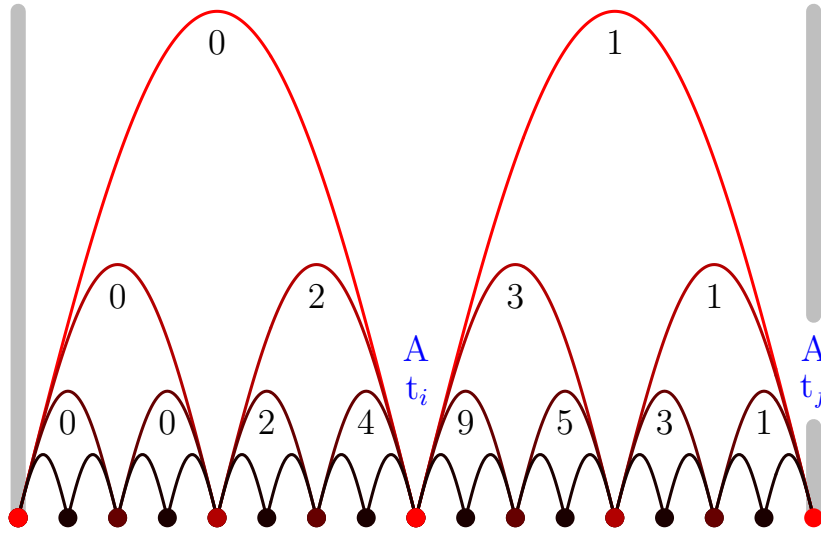


**Figure 5.8:** Schematic view of hops for cluster A in glide direction represented as a segment for  $2^N - 1$  sites where  $N$  is the number of transient states.

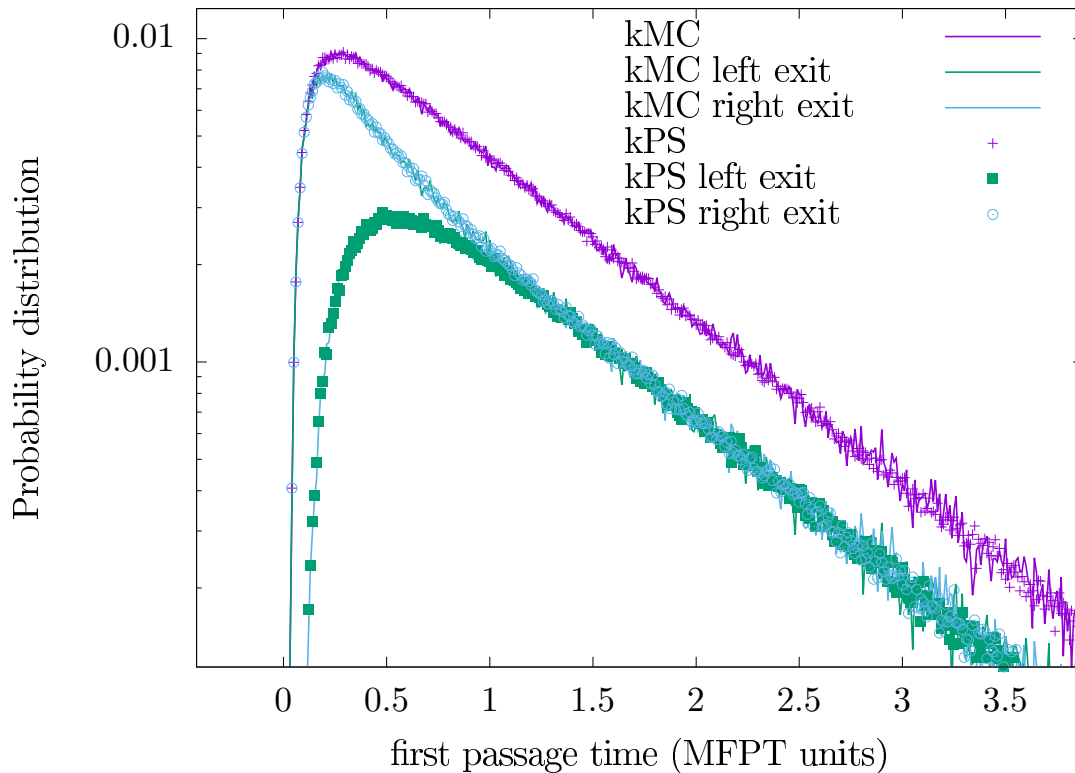


**Figure 5.9:** Comparison of mean first-passage times (MFPT) for  $N$  transient states computed with KMC and kPS methods.

We finally displayed in Fig. 5.10 the sink strengths estimated directly using algorithm 4 for three rotation-to-translation frequency ratios ( $10^{-6}$ ,  $10^{-3}$  and 1) and with varying the supercell sizes  $L$ . We observe that the absorbing efficiencies may either increase or decrease with  $L^{-1}$ , depending on the value of the rotation-to-translation frequency ratio. Capturing these two opposite trends in an analytical model will be highly challenging. This shows the relevance of developing efficient computational approaches to directly compute the sink strengths for defects with mixed mobilities.

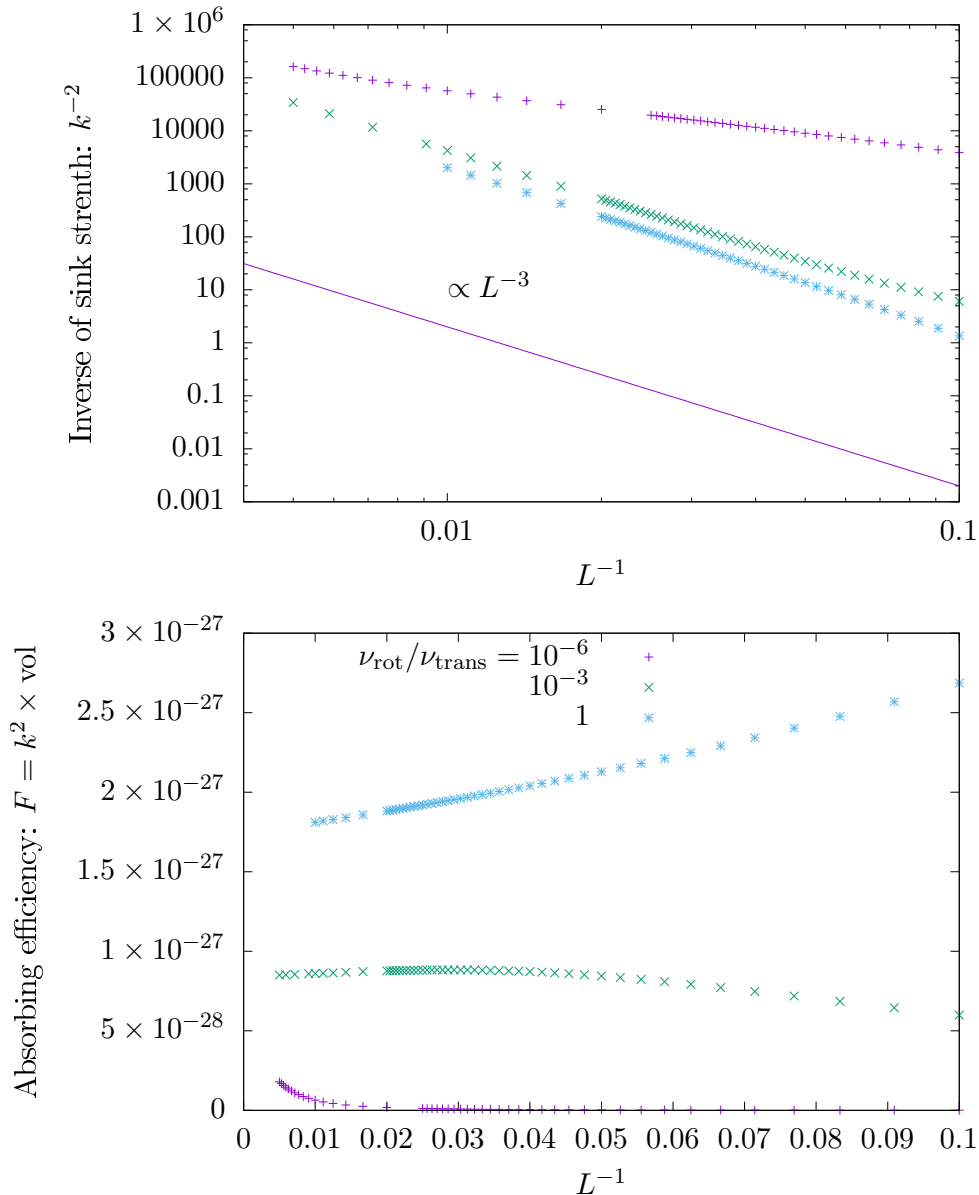


**Figure 5.10:** Comparison of absorption efficiencies and sink strengths calculated for the sink absorption model using algorithm 4.

## 5.6 Summary

In this chapter, we presented the analytical expressions to compute sink strengths. We then quantify sink strengths by considering the initial point-defect distribution homogeneous in space and compared the results obtained using the numerical approach with those obtained using analytical formulae. Overall, we show that numerical linear algebra methods enable us to study the diffusion of a mobile defect around a sink in model system accounting for elastic dipole interactions and comprising up to million lattice sites. If linear system becomes too vast, it cannot be solved numerically due to memory constraints. We briefly describe kinetic path sampling algorithms, implementing the concept of conditioning techniques [139] and able to directly generate first passage events. We tested algorithm 4 in appendix E, by generating first-passage times on a segment line and compared it with conventional KMC algorithm. Second approach algorithm 5 is still under progress. We firmly believe that it may allow computing sink strengths relative to any kind of defect clusters exhibiting mixed mobilities efficiently [173, 180]. This is an open-end to this thesis work; we present other avenues of future in perspectives.



# Conclusions

The research work presented in this thesis concerns the modeling of microstructural evolution in materials under irradiation. The damages created under irradiation by neutron or charged particles can be point defects like vacancies and self interstitial atoms (SIAs) or extended defects such as cavities and dislocation loops. The evolution in materials is governed by the migration of point defects, which affects the mechanical properties of the materials. This study aims to characterize the evolution laws of defects near sinks or recombination to other defects. The primary objective of the thesis was to develop first-passage algorithms that can characterize the evolution law for the point defects based on auxiliary absorbing Markov chains (AMC). These evolutions laws can be used in KMC and to compute sink strengths. This kind of approach was initially proposed by M. A. Novotny [57], using evolution laws to draw first-passage events in KMC, resorting to AMC. To our knowledge, only dense solvers have been used in practice so far. In this thesis, we aim to use advanced iterative sparse solvers. Furthermore, we chose the numerical linear algebra approach to study the point defect evolution.

We recall the structure of the thesis and summarize most relevant results obtained in this work:

- In **Chapter 1**, we briefly discussed the primary damages caused by the irradiation and reviewed the different modeling methods to study the defect evolution.
- In **Chapter 2**, we detail the theory of Markov chains, the traditional KMC method and the concept of first-passage processes. We recall the theory of transition state theory and elastic interaction energies to calculate the transition frequencies for atomic-scale modeling of point defects.
- In **Chapter 3**, the approach of AMC is applied to characterize rare events occurring when the diffusion process is trapped within a finite set of states. The AMC theory yields formal expressions for the transient evolution operator, the source-to-sink probability fluxes, and the mean residence times on transient states. Furthermore, we show the reversible property of an absorbing process. Besides this, we present mathematical solution to characterize the transient distribution using eigenvalues and eigenvectors.

Using iterative sparse solvers, we observe that the evolution of the transient state is governed only by a fraction of the eigenspectrum. The most contributing mode is the one possessing the lowest eigenvalue, and its eigenvector corresponds to the quasi-stationary distribution. We test the efficiency of the first-passage KMC to the vacancy emission problem, which exhibits strong energetic trapping. We observe the quasi-stationary distribution fairly describing the transient evolution. For the vacancy absorption problem, where trapping is essentially entropic, small but substantial fraction of the slow modes were observed to contribute to the no-passage distribution and govern the slow decay of the survival probability.

- In **Chapter 4**, we developed several algorithms based on the deflation technique to characterize mobile defect absorption kinetics by a sink. We used Krylov subspace projection techniques that only involve vector-matrix multiplications and reduce the computational complexity by calculating the exponential of a much lower dimensional transition rate matrix. Two algorithms Krylov Subspace Model Projection (KSMP) and Eigenvalue and Krylov Subspace Model Projection (EKSMP) were developed. The efficiency of these two algorithms was assessed by comparing the results obtained from the Restarted Krylov Subspace Projection (R-KSP) method as a reference: survival probabilities and first-passage distributions. The crucial parameter controlling the convergence of KSMP and EKSMP methods is the dimension of the Krylov subspace. Overall, we show that it is unnecessary to extract several eigenmodes to characterize the absorbing kinetics fully.
- In **Chapter 5**, we illustrate a way to estimate sink strengths parameter; with the help of matrix formulation algorithms. The correctness of the numerical modeling results are compared with the analytical Wiederisch and Laplace approaches. Additionally, we introduce a new hybrid algorithm based on Krylov subspace projection and the kPS method discussed in Chapter 3. We present an algorithm that quantifies the sink strength for two mobile defects and characterizes their evolution law before recombination or their absorption to a physical sink.

To conclude, we show that symmetrizing the transition rate matrix associated with reversible diffusion processes enables one to apply efficient linear and eigenvalue solvers. We illustrate a rigorous approach to characterize the essential rare events governing the long-term microstructural evolution of alloys, such as cluster mobilities, sink strengths, and associated first-passage distributions. All these physical quantities are crucial input parameters for larger-scale simulations employing object/event KMC methods or Rate Equation Cluster Dynamics (RECD). The dependence of cluster mobilities on their size and temperature can possibly be included in larger-scale models.



# Perspectives

The work presented in this thesis is subjected to further improvements and investigations. Following are the points that are an open-end question of this thesis:

- In KMC stochastic approach, the master equation provides jump probabilities of the transitioning defects. The irradiation causes long-time phenomenon such as dislocation and dislocation loops in which one plane is usually missing. The stochastic approaches are not efficient enough to study the evolution laws for the long times. With the help of developed first-passage laws (as discussed in Chapter 3 & Chapter 4, we can characterize the long-term evolution of the defects. It can be achieved by resorting the first-passage laws to the traditional OKMC method with spatial protection for a non-rigid crystal lattice. The entire evolution law from one state to the other will result in the macro jump.
- The hybrid algorithm with KMC method and conditioning techniques [139] discussed in Chapter 5 is under development. Thus, there are no supporting results concerning its applications. Nevertheless, we firmly believe that the algorithm could be more efficient and accurate to study the recombination kinetics for the point defects.
- Concerning the computation of sink strengths at lower sink densities, algorithm 5 discussed in appendix E consisting of Krylov subspace projection technique and KMC method as conditioning techniques [139] can be implemented to circumvent the curse of dimensionality and memory constraints.
- We point out that the proposed approach is based on the actual transition rate matrix on the crystal lattice. It may then straightforwardly be applied to investigate the anisotropic migration of interstitial clusters, whose diffusion mechanism mixes fast translations and slow rotations. The approach may allow computing sink strengths relative to any different kind of defect clusters exhibiting mixed mobilities efficiently such as 1DR as discussed in Ref. [173, 180].
- Later the computed value of sink strength in mixed mobilities can be used as an input parameter in CRESCENDO code [158] which is based on the Rate Equation Cluster Dynamics (RECD). This has never been included in RECD so far.



# Algorithmic implementation

Adapted from the article "Elastodiffusion and cluster mobilities using kinetic Monte Carlo simulations: Fast first-passage algorithms for reversible diffusion processes", Physical Review Materials **3**, 103802 (2019).

## A.1 Path factorization

Algorithm 1 is used to compute transition rates, to discriminate transient and absorbing states and to assemble the associated transition sub-matrices. Then, algorithm 2 is used to make the path factorization. Note that the characterization of transition rates and transient states can be done on the fly in algorithm 2. This requires a selection rule for next transient state based on the transformed transition probabilities, as done in Ref. [85] for simulating the anomalous diffusion of a defect on a disordered substrate.

## A.2 Spacetime randomization

At the  $N$ th rank-one update, stochastic probability matrix  $\mathbf{P}^{(N)}$  subsumes all possible transitions involving the deleted states in the trapping basin  $\mathbb{E} = \{1, \dots, N\}$ . Although any intermediate matrix  $\mathbf{P}^{(n)}$  with  $n \in \mathbb{E}$  can be used to randomly generate escapes from any state  $i \in \mathbb{E}$ , a trajectory generated using  $\mathbf{P}^{(N)}$  is the simplest containing a single transition. On the other end, reverting back to a standard KMC simulation based on  $\mathbf{P}^{(0)}$ , a detailed escape trajectory that accounts for all transitions within  $\mathbb{E}$  can be generated. Remarkably, it is possible to efficiently construct statistically correct escape trajectories without ever performing any detailed (and inefficient) KMC simulation. Space-time randomization is based from the set of conditional probabilities defined for all  $i$  and for  $j > n$

$$R_{ij}^{(n)} = P_{ij}^{(n-1)} / P_{ij}^{(n)}. \quad (\text{A.1})$$

**Algorithm 1** Assembly of transition sub-matrices.

---

```

1:  $N \leftarrow 1; N^{\text{tot}} \leftarrow 1;$ 
2: initial transient state is indexed 1;  $i \leftarrow N;$ 
3: while  $i \leq N$  do
4:   list the  $Z_i$  possible transitions of  $S_i;$ 
5:   for  $\ell = 1, \dots, Z_i$  do
6:     evaluate key for final state associated with  $\ell$ -th transition;
7:     if new key then
8:        $N^{\text{tot}} \leftarrow N^{\text{tot}} + 1; j \leftarrow N^{\text{tot}};$ 
9:       add key and its state index  $j$  to dictionary;
10:      if state transient then
11:         $N \leftarrow N + 1;$ 
12:      end if
13:      else ▷ key exists
14:        retrieve state index  $j$  of existing key;
15:      end if
16:      evaluate  $K_{ij}$ , transition rate from  $S_i$  to  $S_j;$  ▷ for  $\ell$ -th listed
17:      transition
18:    end for
19:     $i \leftarrow i + 1$ 
20: end while
21: re-order transient states from 1 to  $N$  and absorbing states from  $N + 1$  to  $N^{\text{tot}};$ 
22: construct  $\tau^{(0)}, \mathbf{P}^{(0)}$  and absorbing transient rate matrix  $\mathbf{A}^B$  from  $\mathbf{K};$ 

```

---

**Algorithm 2** path factorization [85] adapted from graph transformation [114] and an early version [112].

---

```

1: construct  $\mathbf{P}^{(0)}$  and  $\tau^{(0)};$ 
2: if flux enabled then
3:    $\theta^{(0)} = \tau^{(0)} \odot \pi;$ 
4: end if
5: for  $n$  from 1 to  $N$  do
6:   if adaptation enabled then
7:     select new transient state and label it  $n$ 
8:     re-order  $\mathbf{P}^{(n)}, \tau^{(n)}$  and possibly  $\theta^{(n)};$ 
9:   end if
10:  compute  $\mathbf{P}^{(n)}$  by performing rank-one update of  $\mathbf{P}^{(n-1)};$ 
11:  compute  $\tau^{(n)}$  by performing rank-one update of  $\tau^{(n-1)};$ 
12:  if flux enable then
13:    compute  $\theta^{(n)}$  by performing rank-one update of  $\theta^{(n-1)};$ 
14:  end if
15: end for
16: if flux calculation enabled then
17:  compute fluxes from  $\theta^{(n)}$ 
18: end if

```

---

A particular  $R_{ij}^{(n)}$  yields the probability that an  $n$ th order transition from  $i$  to  $j > n$  avoids site  $n$  when decomposed in term of  $(n - 1)$ th order transitions. Prior to describing space-time randomization, the following preliminary definitions are required. The binomial law of trial number  $h \in \mathbb{N}$  and success probability  $r$  is denoted by  $B(h, r)$ . The probability of  $s$  successes is  $\binom{h}{s} r^s (1 - r)^{h-s}$ . The negative binomial law of success number  $h$  and success (escape) probability  $1 - p$  is denoted by  $NB(h, 1 - p)$ . The probability of  $f$  failures before the  $h$ -th success is  $\binom{f+h-1}{f} p^f (1 - p)^h$  where  $p$  is the failure or flicker probability (flickers will correspond to round-trips from a given state). The gamma law of shape parameter  $h$  and time-scale  $\tau$  is denoted by  $j(h, \tau)$ .  $C_\alpha$  denotes the categorical laws whose probability vector is the  $\alpha$ -th row of  $\mathbf{P}^{(N)}$  if  $\alpha \leq N$  or of the stochastic matrix obtained from  $\mathbf{P}^{(0)}$ . The symbol  $\sim$  means “is a random variate distributed according to the law that follows”. Let  $\mathbb{A}$  denote the set of absorbing peripheral states. The set of states beyond the peripheral states (that are non transient and non absorbing) is  $\overline{\mathbb{A} \cup \mathbb{E}}$ , the complementary of the union of  $\mathbb{A}$  and  $\mathbb{E}$ . State  $\alpha$  denote the current state of the system.

After implementation of Algorithm 3, the system has moved beyond the peripheral set and is disconnected to the trapping basin reached: the current state  $\alpha$  belongs to  $\overline{\mathbb{E} \cup \mathbb{A}}$  in item (6). The gamma law  $j(T_n, \tau_n^{(0)})$  in (23) simulates the time elapsed after performing  $T_n$  consecutive Poisson processes of rate  $1/\tau_n^{(0)}$ . Indeed, after any hop or flicker performed with  $\mathbf{P}^{(0)}$ , the physical time must be incremented by a residence time drawn in the exponential distribution of time-scale  $\tau_n^{(0)}$ . Note that algorithm (3) generalizes the time randomization procedure proposed by Mason and coworkers [181] for the second-order residence time algorithm [112].

In practice, several transitions exiting  $\mathbb{E}$  are typically recorded in the hopping matrix. As a result, the elapsed physical time is generated for several escaping trajectories simultaneously. The generated path may also return to the same trap several times prior to reaching another trap. In practice, the current path factorization is re-used as many times as necessary.

## A.3 Reformulation of path factorization

### A.3.1 LU decomposition

We herein establish the connection between rank-one updates of Sec. 3.3.5 and the Gauss-Jordan elimination method on the scaled transition rate matrix  $\mathbf{BA}$ . Scaling matrix  $\mathbf{B}$  is set to  $\tau \mathbf{I}$  or  $\text{Diag}(\mathbf{A})^{-1}$  where  $\tau = \min(1/A_{ii} : 1 \leq i \leq N)$ .

More precisely, we show that path factorization entails decomposition  $\mathbf{BA} = \mathbf{L}^+ \mathbf{DU}^+$  when the initial stochastic matrix  $\mathbf{P}^{(0)}$  is set to  $\mathbf{I} - \mathbf{BA}$ . Matrix  $\mathbf{D}$  is diagonal and its diagonal elements  $D_{nn}$  are equal to  $1 - P_{nn}^{(n-1)}$ , the escape probability from state  $n$ . The quantity  $P_{nn}^{(n-1)}$  is the probability of a round-trip

---

**Algorithm 3** Kinetic path sampling [85]: subset  $\mathbb{E} = \{1, \dots, N\}$  encompasses the transient states and subset  $\mathbb{A} = \{N + 1, \dots, N_{\text{tot}}\}$  includes absorbing peripheral states; system is initially in state  $\alpha \in \mathbb{E} \cup \mathbb{A}$

---

```

1: define  $N_c \times N_c$  hopping matrix  $\mathbf{H}^{(N)}$  and set its entries to zero;
2: while  $\alpha \in \mathbb{A} \cup \mathbb{E}$  do
3:   draw  $j \propto C_{\alpha j}$ ;
4:   increment  $H_{\alpha, j}^{(N)}$  by one;
5:    $\alpha \leftarrow j$ ; ▷ move current state  $\alpha$  to  $j$ 
6: end while ▷  $\alpha \in \overline{\mathbb{A} \cup \mathbb{E}}$ 
7: for  $n = N$  to 1: do
8:   evaluate  $\mathbf{P}^{(n-1)}$ ;
9:   deallocate  $\mathbf{P}^{(n)}$ ;
10:  for  $i \in \{\mathbb{E} \cup \mathbb{A}\} \setminus \{n\}$  and  $j \in \{n + 1, \dots, N_c\}$  do
11:    evaluate  $R_{ij}^{(n)} = P_{ij}^{(n-1)} / P_{ij}^{(n)}$ 
12:    draw  $H_{ij}^{(n-1)} \sim \text{B}(H_{ij}^{(n)}, R_{ij}^{(n)})$ 
13:  end for
14:  for  $i \in \{\mathbb{E} \cup \mathbb{A}\} \setminus \{n\}$  do ▷ count new hops from  $i$  to  $n$ :
15:     $H_{in}^{(n-1)} = \sum_{j \in \{n+1, \dots, N_c\}} H_{ij}^{(n)} - H_{ij}^{(n-1)}$ 
16:  end for
17:  for  $j \in \{n + 1, \dots, N_c\}$  do ▷ count hops from  $n$  to  $j$ 
18:     $H_{nj}^{(n-1)} = H_{nj}^{(n)} + \sum_{i \in \mathbb{E} \setminus \{n\}} H_{ij}^{(n)} - H_{ij}^{(n-1)}$ 
19:  end for
20:   $h_n = \sum_{j \in \{n+1, \dots, N_c\}} H_{nj}^{(n-1)}$  ▷ count hop number from  $n$ ,
21:   $H_{nn}^{(n-1)} \sim \text{NB}(h_n, 1 - P_{nn}^{(n-1)})$  ▷ draw flicker number
22:   $T_n = h_n + H_{nn}^{(n-1)}$  ▷ evaluate hop number from  $n$ ,
23:   $\tilde{\theta}_n \sim j(T_n, \tau_n^{(0)})$  ▷ convert to residence time in  $n$ ,
24:  deallocate  $\mathbf{H}^{(n)}$  and  $\mathbf{R}^{(n)}$ ;
25: end for
26: evaluate first-passage time  $\tilde{\tau}^{(N)} = \sum_{\ell \in \mathbb{E} \cup \mathbb{A}} \tilde{\theta}_\ell$  associated with the path
    generated in (2);
27: increment the physical time  $t$  by  $\tilde{\tau}^{(N)}$ .

```

---

from the same state. We next define three matrices  $L_{ij}^+$ ,  $U_{ij}^-$  and  $U_{ij}^+$  whose entries are initially set to zero. At the  $n$ th update, the  $n$ th columns  $L_{in}^+$  and  $U_{in}^-$  are filled by setting

$$L_{in}^+ = \begin{cases} \frac{P_{in}^{(n-1)} - I_{in}}{P_{nn}^{(n-1)} - 1} & \text{if } i \geq n, \\ 0, & \text{if } i < n \end{cases}, \quad (\text{A.2})$$

$$U_{in}^- = \begin{cases} I_{in} & \text{if } i \geq n \\ P_{in}^{(n-1)} & \text{if } i < n \end{cases} \quad (\text{A.3})$$

The  $n$ th row  $U_{nj}^+$  is filled as

$$U_{nj}^+ = \frac{P_{nj}^{(n-1)} - I_{nj}}{P_{nn}^{(n-1)} - 1}. \quad (\text{A.4})$$

We have

$$L_{in}^+ - U_{in}^- D_{nn}^{-1} = -\frac{P_{in}^{(n-1)}}{1 - P_{nn}^{(n-1)}}, \quad (\text{A.5})$$

$$D_{nn} U_{nj}^+ = P_{nj}^{(n-1)} - I_{nj}. \quad (\text{A.6})$$

Since  $P_{ij}^{(n-1)} = 0$  for  $j \leq n-1$ , matrix  $\mathbf{U}^+$  remains upper triangular after the  $n$ th row addition. The  $n$ th rank-one update of Sec. 3.3.5 amounts to constructing  $\mathbf{P}^{(n)}$  as follows:

$$P_{ij}^{(n)} = P_{ij}^{(n-1)} + (L_{in}^+ - U_{in}^- D_{nn}^{-1}) D_{nn} U_{nj}^+, \quad (\text{A.7})$$

where  $P_{ij}^{(n)} = 0$  for  $j \leq n$ , as required. This property holds by induction up to  $n = N$ . Recall that the probabilities of transitions from  $i$  to  $j$  ( $j > n$ ) subsume the canceled probability of all possible transitions from  $i$  to  $n$ . This ensures that the transformed matrices  $\mathbf{P}^{(n)}$  remain stochastic.

Summing relation (A.7) from  $n = i$  to  $n = N$  when  $i \leq N$  yields the relation

$$P_{ij}^{(N)} = P_{ij}^{(i-1)} + L_{ii}^+ D_{ii} U_{ij}^+ - \sum_{n=i}^N U_{in}^- U_{nj}^+, \quad (\text{A.8})$$

$$= I_{ij} - \sum_{n=i}^N U_{in}^- U_{nj}^+, \quad (\text{A.9})$$

where we substituted  $I_{ij}$  for  $P_{ij}^{(i-1)} + L_{ii}^+ D_{ii} U_{ij}^+$ . Let  $\mathbf{U}^+$  and  $\mathbf{U}^-$  denote the  $N \times N$  upper triangular submatrices obtained by restricting  $U_{ij}^+$  and  $U_{ij}^-$  to the trapping states  $i, j \leq N$ . Since  $P_{ij}^{(N)} = 0$  for  $i, j \leq N$ , we obtain

$$\mathbf{I} = \mathbf{U}^- \mathbf{U}^+, \quad (\text{A.10})$$

recalling that  $\mathbf{I}$  is the  $N \times N$  identity matrix. Relation (A.10) entails that  $\mathbf{U}^-$  is the inverse of  $\mathbf{U}^+$ . Summing relation (A.7) from  $\ell = 1$  to  $\ell = i - 1$  yields the relation

$$P_{ij}^{(i)} = P_{ij}^{(0)} + \sum_{n=1}^i L_{in}^+ D_{nn} U_{nj}^+ - U_{ii}^- U_{ij}^+.$$

Since  $P_{ij}^{(i)} = I_{ij} - U_{ii}^- U_{ij}^+$ , we obtain the following factorization

$$\sum_{n=1}^i L_{in}^+ D_{nn} U_{nj}^+ = I_{ij} - P_{ij}^{(0)} = B_{ii} A_{ij}.$$

We eventually obtain the decomposition of the  $N \times N$  scaled rate matrix  $\mathbf{BA}$  into the product of a lower triangular matrix, a diagonal matrix  $\mathbf{D} = \text{diag}(D_{11}, D_{22}, \dots, D_{NN})$  and an upper triangular matrix:

$$\mathbf{BA} = \mathbf{L}^+ \mathbf{D} \mathbf{U}^+. \quad (\text{A.11})$$

Matrix  $\mathbf{U}^-$  being the inverse of  $\mathbf{U}^+$ , inverting  $\mathbf{A}$  from the factorization still requires inverting the lower triangular matrix  $\mathbf{L}^+$ . Let  $\mathbf{L}^-$  denote the inverse of  $\mathbf{L}^+$ .  $\mathbf{D}$  being diagonal and positive definite, its inverse, denoted below by  $\mathbf{D}^{-1}$ , exists. Matrices  $\mathbf{L}^\pm$  can be written as products involving the following elementary matrices

$$\mathbf{L}_n^\pm = \mathbf{I} \pm \sum_{i \neq n} \mathbf{e}_i L_{in} \mathbf{e}_n. \quad (\text{A.12})$$

We have in particular  $\mathbf{L}^+ = \mathbf{L}_1^+ \mathbf{L}_2^+ \dots \mathbf{L}_N^+$  and  $\mathbf{L}^- = \mathbf{L}_N^- \mathbf{L}_{N-1}^- \dots \mathbf{L}_1^-$ . From the matrix products above and property  $\mathbf{L}_n^+ \mathbf{L}_n^- = \mathbf{I}$ , we deduce that  $\mathbf{L}^+ \mathbf{L}^- = \mathbf{I}$ , hence  $\mathbf{L}^-$  corresponds to the inverse of  $\mathbf{L}^+$ . The decomposition of  $\mathbf{L}^-$  and  $\mathbf{U}^-$  into product of triangular elemental matrices are used in the updating rule (3.33) to compute  $\vec{\tau}^{(N)}$ , the vector of mean first-passage times. The sequential procedure (3.33) amounts to applying vector  $\mathbf{b} = \mathbf{B}\vec{\mathbf{1}}$  on matrices  $\mathbf{L}^-$ ,  $\mathbf{D}^{-1}$  and  $\mathbf{U}^-$ , successively:

$$\begin{aligned} \mathbf{b} &= \left( \tau_1^{(0)}, \tau_2^{(0)} \dots, \tau_N^{(0)} \right)^T \\ \mathbf{L}^- \mathbf{b} &= \left( \tau_1^{(0)}, \tau_2^{(1)} \dots, \tau_N^{(N-1)} \right)^T \\ \mathbf{D}^{-1} \mathbf{L}^- \mathbf{b} &= \left( \tau_1^{(1)}, \tau_2^{(2)} \dots, \tau_N^{(N)} \right)^T \\ \mathbf{U}^- \mathbf{D}^{-1} \mathbf{L}^- \mathbf{b} &= \left( \tau_1^{(N)}, \tau_2^{(N)} \dots, \tau_N^{(N)} \right)^T. \end{aligned}$$

Replacing the product  $\mathbf{U}^- \mathbf{D}^{-1} \mathbf{L}^-$  by  $\mathbf{A}^{-1} \mathbf{B}^{-1}$  in the last equation yields the expected expression for the mean first-passage time:

$$\mathbf{A}^{-1} \vec{\mathbf{1}} = \vec{\tau}^{(N)}.$$

As for time randomization (algorithm 3), the information processed to evaluate the conditional probabilities  $R_{ij}^{(n)}$  defined in (A.1) can easily be retrieved by resorting to (A.7) and the stored entries of  $\mathbf{L}^+$ ,  $\mathbf{D}$ ,  $\mathbf{U}^+$  and  $\mathbf{U}^-$ .

### A.3.2 Cholesky decomposition

Whenever the underlying Markov process is reversible, the symmetric positive definite matrix  $\mathbf{A}^B = \mathbf{S}\mathbf{R}^{-1}\mathbf{A}\mathbf{R}\mathbf{S}$  can be defined, where diagonal matrix  $\mathbf{R}$  is defined in (3.15) from the equilibrium distribution  $\rho$ . Cholesky decomposition can then be applied, yielding

$$\mathbf{A}^B = \mathbf{L}^B \mathbf{D} \mathbf{L}^{BT} \quad (\text{A.13})$$

where  $\mathbf{L}^B$  is a  $N \times N$  lower triangular matrix with ones on the diagonal. Since  $\mathbf{D}$ ,  $\mathbf{R}$  and  $\mathbf{S}$  commute, the absorbing transition rate matrix writes

$$\mathbf{B}\mathbf{A} = (\mathbf{S}\mathbf{R})\mathbf{L}^B(\mathbf{S}\mathbf{R})^{-1}\mathbf{D}(\mathbf{S}\mathbf{R})\mathbf{L}^{BT}(\mathbf{S}\mathbf{R})^{-1} \quad (\text{A.14})$$

Comparing to  $\mathbf{L}^+\mathbf{D}\mathbf{U}^+$  decomposition enables one to identify the following relations

$$\begin{aligned} \mathbf{L}^+ &= (\mathbf{S}\mathbf{R})\mathbf{L}^B(\mathbf{S}\mathbf{R})^{-1} \\ \mathbf{U}^+ &= (\mathbf{S}\mathbf{R})\mathbf{L}^{BT}(\mathbf{S}\mathbf{R})^{-1} \end{aligned}$$

We deduce that  $\mathbf{U}^+ = (\mathbf{S}\mathbf{R})^2\mathbf{L}^{+T}(\mathbf{S}\mathbf{R})^{-2}$  and that the inverse of  $\mathbf{L}^+$  is  $\mathbf{L}^- = (\mathbf{S}\mathbf{R})^2\mathbf{U}^{-T}(\mathbf{S}\mathbf{R})^{-2}$ .



## Restarted Krylov Subspace Projection

The restarted Krylov subspace algorithm proposed in ref.[134], generates Krylov basis of dimension  $\ell$ . In later step, that algorithm updates the approximation to  $f(\mathbf{A})\mathbf{b}$  and discards the basis vectors except the one which serves as an initial vector of the next Krylov subspace [182]. The following derivation is to recall the restarted setup using two Lanczos decomposition

$$\mathbf{A}\mathbf{V}_\ell^1 = \mathbf{V}_\ell^1\mathbf{T}_\ell^1 + T_{\ell+1,\ell}^1\mathbf{v}_{\ell+1}^1\mathbf{e}_\ell^T \quad (\text{B.1})$$

$$\mathbf{A}\mathbf{V}_\ell^2 = \mathbf{V}_\ell^2\mathbf{T}_\ell^2 + T_{\ell+1,\ell}^2\mathbf{v}_{\ell+1}^2\mathbf{e}_\ell^T \quad (\text{B.2})$$

where  $\mathbf{V}^1$  and  $\mathbf{V}^2$  are the orthonormal bases of  $\mathcal{K}_\ell(\mathbf{A}, \mathbf{v}_1)$  and  $\mathcal{K}_\ell(\mathbf{A}, \mathbf{v}_{\ell+1})$ .  $\mathbf{T}_\ell^1$  and  $\mathbf{T}_\ell^2$  are two tridiagonal matrices.  $\mathbf{e}_\ell^T$  denotes the  $\ell$ th unit coordinate vector  $\in \mathbb{R}^\ell$ . Together the columns of  $\mathbf{W}_{2\ell} := [\mathbf{V}_\ell^1, \mathbf{V}_\ell^2]$  forms a basis of  $\mathcal{K}_{2\ell}(\mathbf{A}, \mathbf{b})$ . On combining the two Lanczos decomposition Eq.(B.1) and Eq.(B.2) to Lanczos-like decomposition we get,

$$\mathbf{A}\mathbf{W}_{2\ell} = \mathbf{W}_{2\ell}\mathbf{T}_{2\ell} + T_{\ell+1,\ell}^2\mathbf{v}_{\ell+1}^2\mathbf{e}_{2\ell}^T \quad (\text{B.3})$$

where  $\mathbf{T}_{2\ell}$  is the tridiagonal block Matrix represented as,

$$\mathbf{T}_{2\ell} := \begin{bmatrix} \mathbf{T}_\ell^1 & \mathcal{O} \\ T_{\ell+1,\ell}^1\mathbf{e}_1\mathbf{e}_\ell^T & \mathbf{T}_\ell^2 \end{bmatrix}. \quad (\text{B.4})$$

The restarted method of Krylov subspace approximation associated to Eq.(B.3) is given as,

$$\mathbf{f}_{2\ell} = \beta\mathbf{W}_{2\ell}f(\mathbf{T}_{2\ell})\mathbf{e}_1. \quad (\text{B.5})$$

The  $f(\mathbf{T}_{2\ell})$  term exhibits the following block lower triangular structure,

$$f(\mathbf{T}_{2\ell}) = \begin{bmatrix} f(\mathbf{T}_\ell^1) & \mathcal{O} \\ \mathbf{X}_{2,1} & f(\mathbf{T}_\ell^2) \end{bmatrix}. \quad (\text{B.6})$$

Hence, the approximation Eq.(B.5) has the form,

$$\mathbf{f}_{2\ell} = \beta \mathbf{V}_\ell^1 f(\mathbf{T}_\ell^1) \mathbf{e}_1 + \beta \mathbf{V}_\ell^2 \mathbf{X}_{2,1} \mathbf{e}_1 \quad (\text{B.7})$$

where the first term of Eq.(B.7) is evaluated using Arnoldi approximation for the basis  $\mathcal{K}_\ell(\mathbf{A}, \mathbf{b})$ . Once the  $\mathbf{X}_{2,1} \mathbf{e}_1$  term is estimated, the basis vectors of  $\mathbf{V}_\ell^1$  are discarded and Eq.(B.7) yields the basis of restarting method by updating the Arnoldi approximation. The approximation after  $m$  restart cycles is given as

$$\mathbf{f}^m = \beta \mathbf{W}_{m\ell} f(\mathbf{T}_{m\ell}) \mathbf{e}_1 = \mathbf{f}^{(m-1)} + \beta \mathbf{V}_\ell^m [f(\mathbf{T}_{m\ell}) \mathbf{e}_1]_{(m-1)\ell+1:m\ell} \quad (\text{B.8})$$

where the subscript of the last term in Eq.(B.8) represents the vector with the last  $\ell$  components of  $f(\mathbf{T}_{m\ell}) \mathbf{e}_1$  [134].



## Cholesky preconditioning

CPU times for performing ESMP or EKSMP simulations are compiled in Tables C.1, C.2 and C.3. From data reported in Table C.1, we observe that Cholesky preconditioning (CP) should be performed whenever possible because it reduces the overall CPU times and improves the convergence of the KS solver. Eigenvalues being pooled in bundles for symmetry reasons, eigenvectors appears simultaneously in the extraction algorithm. Handling the eigenvalue degeneracy is facilitated by the inverted iterations within CP. CP is limited in memory because the computed Cholesky factor is a denser matrix. The largest system CP can solve contains 217245 transient state, as shown in table C.2. For the larger systems reported in Table C.3, the QSD eigenvector was successively computed using KS solver without preconditioning up to 905681 transient states.

Input		Output				
CP	NEV	CP Time (s)	EPS Time (s)	Converged Eigenpairs	NCV	Result
Disabled	1	-	$8.93 \cdot 10^1$	1	16	C
	5	-	$1.23 \cdot 10^2$	1	20	D
	10	-	$1.30 \cdot 10^2$	2	25	D
	30	-	$1.91 \cdot 10^2$	21	60	D
	40	-	$2.25 \cdot 10^2$	31	80	D
	50	-	$2.35 \cdot 10^2$	53	100	C
	60	-	$1.91 \cdot 10^2$	60	120	C
	70	-	$1.94 \cdot 10^2$	70	140	C
	80	-	$2.34 \cdot 10^2$	82	160	C
	90	-	$2.45 \cdot 10^2$	90	180	C
	100	-	$2.89 \cdot 10^2$	102	200	C
Enabled	1	$1.58 \cdot 10^0$	$1.55 \cdot 10^1$	1	1	C
	5	$5.53 \cdot 10^0$	$1.98 \cdot 10^1$	7	7	C
	10	$5.92 \cdot 10^0$	$1.99 \cdot 10^1$	11	11	C
	30	$1.54 \cdot 10^1$	$3.13 \cdot 10^1$	37	60	C
	40	$1.94 \cdot 10^1$	$3.55 \cdot 10^1$	42	80	C
	50	$2.06 \cdot 10^1$	$3.52 \cdot 10^1$	60	100	C
	60	$2.20 \cdot 10^1$	$3.70 \cdot 10^1$	64	120	C
	70	$2.33 \cdot 10^1$	$3.99 \cdot 10^1$	73	140	C
	80	$2.66 \cdot 10^1$	$4.37 \cdot 10^1$	81	160	C
	90	$3.05 \cdot 10^1$	$4.71 \cdot 10^1$	90	180	C
	100	$3.75 \cdot 10^1$	$5.69 \cdot 10^1$	114	200	C
	3500	$1.52 \cdot 10^3$	$4.73 \cdot 10^3$	3539	4000	C

**Table C.1:** CPU time taken by ESMP method to extract the indicated number of eigenvalues (NEV) for the vacancy absorption model. The simulations are performed using a single core of an Intel i5-8400H processor (running at 2.5GHz). Parameter NCV represents the maximum dimension of the working subspace to be used by the solver. In inputs, Cholesky preconditioning (CP) may be enabled or disabled. In the outputs, C and D of the result column denote whether simulations have converged or diverged, respectively.

Cell size (Å)	Number of Transient States ( $N$ )	Time (s)
66.66	14141	$3.55 \cdot 10^0$
74.74	21085	$7.83 \cdot 10^0$
86.16	34801	$2.13 \cdot 10^1$
98.98	53053	$4.36 \cdot 10^1$
107.06	68061	$7.06 \cdot 10^1$
127.26	116921	$2.36 \cdot 10^2$
139.38	154973	$4.83 \cdot 10^2$
147.46	184381	$6.31 \cdot 10^2$
151.5	200369	$7.91 \cdot 10^2$
159.58	217245	$9.80 \cdot 10^2$

**Table C.2:** CPU time taken by ESMP to extract 10 eigenvalues for the indicated number of system size ( $N$ ) using KS solver and Cholesky preconditioning from MUMPS.

Cell size (Å)	Number of Transient States ( $N$ )	Time (s)
74.74	21085	$4.42 \cdot 10^1$
86.86	34801	$1.11 \cdot 10^2$
98.98	53053	$2.33 \cdot 10^2$
107.06	68061	$4.10 \cdot 10^2$
119.18	95313	$5.23 \cdot 10^2$
127.26	116921	$7.47 \cdot 10^2$
139.38	154973	$1.20 \cdot 10^3$
147.46	184381	$1.57 \cdot 10^3$
151.50	200369	$1.80 \cdot 10^3$
159.58	235033	$2.62 \cdot 10^3$
167.66	273441	$3.26 \cdot 10^3$
187.86	387101	$5.66 \cdot 10^3$
208.06	497757	$9.33 \cdot 10^3$
248.46	905681	$2.38 \cdot 10^4$

**Table C.3:** CPU time to evaluate survival probability distributions for the indicated number of system size ( $N$ ) using EKSMP method with  $(k, \ell) = (1, 50)$  and KS solver without Cholesky preconditioning.



# Theory of Elasticity

## D.1 Strain Tensor

The theory of elasticity describes the mechanics of solid bodies. The solid-body tends to deform under applied forces, i.e., there is a change in shape and volume. When the body is deformed, every point in the structure is displaced. Let us consider a particular point whose radius vector before deformation is denoted by  $\mathbf{r}$ , and after deformation by  $\mathbf{r}'$ . The displacement due to deformation is given by

$$\mathbf{u} = \mathbf{r}' - \mathbf{r} \tag{D.1}$$

called the displacement vector. The coordinates  $r'_i$  of the displaced point are the function of coordinate  $r_i$  before the displacement as represented in Fig. D.1. So, the displacement vector  $u_i$  as a function of coordinates

$$u_i = r'_i - r_i \tag{D.2}$$

We define the measure of distortion tensor  $\partial u_i / \partial r_j$  in terms of vector  $d\mathbf{r}$  before deformation that has been transformed as vector  $d\mathbf{r}'$  after deformation. As represented Fig. D.1, a small cube becomes parallelepiped after deformation such that

$$dr'_i = \left( \delta_{ij} + \frac{\partial u_i}{\partial r_j} \right) dr_j \tag{D.3}$$

where  $\delta_{ij}$  is the Kronecker delta which holds the values 1 or 0 according to whether  $i$  and  $j$  are or are not equal, and the summation over all the repeated indices are implicit<sup>1</sup>. The distortion tensor is made free from any reference of

---

<sup>1</sup>Einstien summation convention

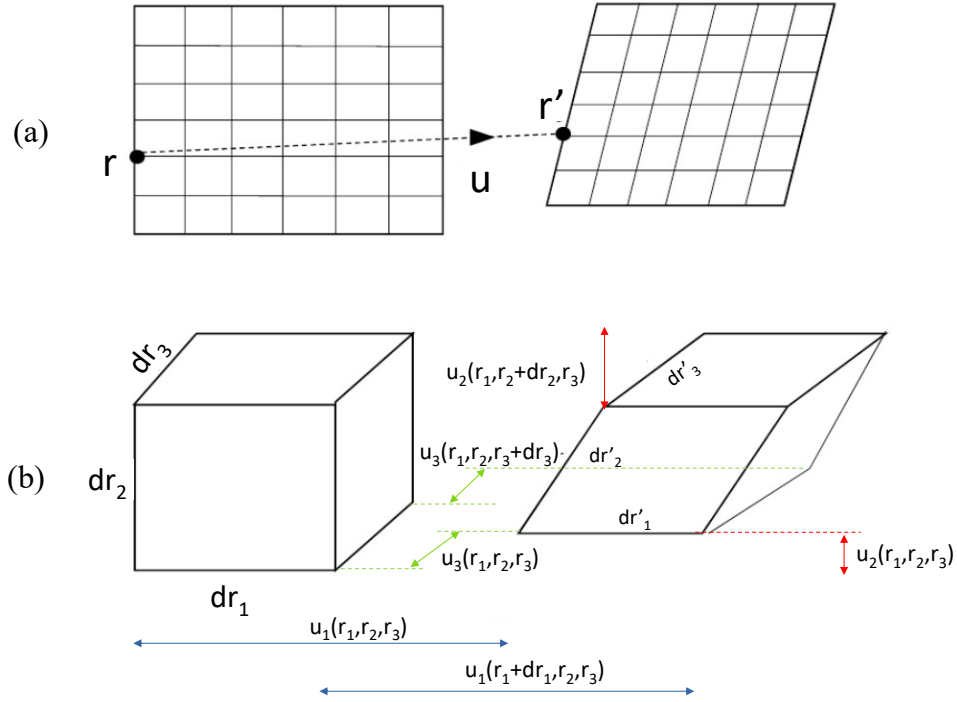


**Figure D.1:** Deformation of a solid body.

oriental of an elementary mesh and the strain tensor is defined by

$$\begin{aligned}\varepsilon_{ij}(\mathbf{r}') &= \frac{1}{2} \left[ \left( \delta_{in} + \frac{\partial u_n}{\partial r_i} \right) \left( \delta_{nj} + \frac{\partial u_n}{\partial r_j} \right) - \delta_{ij} \right] \\ &= \frac{1}{2} \left( \frac{\partial u_i}{\partial r_j} + \frac{\partial u_j}{\partial r_i} + \frac{\partial u_n}{\partial r_i} \frac{\partial u_n}{\partial r_j} \right)\end{aligned}\quad (\text{D.4})$$

The expression represented in Eq.(D.4) provides the change in the shape and volume when a body is deformed. From its definition, we can see that it is symmetrical, such that

$$\varepsilon_{ij} = \varepsilon_{ji} \quad (\text{D.5})$$

When a body is deformed, the radius vector between any two points change by the factor of the displacement vector. Let us consider two points, whose radius vector joining before deformation is  $dr_i$ . After deformation, this radius vector joining the same two points after the deformations is  $dr'_i = dr_i + du_i$ . The distance between the points is given as  $dl = \sqrt{(dr_1^2 + dr_2^2 + dr_3^2)}$  before deformation, and  $dl' = \sqrt{(dr_1'^2 + dr_2'^2 + dr_3'^2)}$  after deformation. Applying the general summation rule, we have  $dl^2 = dr_i^2$ ,  $dl'^2 = dr_i'^2 = (dr_i + du_i)^2$ .

The length element after the deformation can also be written as

$$dl'^2 = dl^2 + 2\varepsilon_{ij}dr_i dr_j. \quad (\text{D.6})$$

For the small deformations, the strain tensor corresponds to the symmetric part of the the distortion tensor given as

$$\varepsilon_{ij}(\mathbf{r}) = \frac{1}{2} \left( \frac{\partial u_i}{\partial r_j} + \frac{\partial u_j}{\partial r_i} \right). \quad (\text{D.7})$$

Due to the absence of internal torque, there are no energetic contributions and the anti-symmetric part of the distortion tensor.

## D.2 Stress Tensor

A solid body is said to be in thermal equilibrium if it is not deformed by means of any force. If the deformation occurs, the molecules in the body tends to arrange and try attain the equilibrium. This happens due to the presence of internal forces, commonly known as internal stresses. These forces are present due to the force of interaction between the molecules. However, these forces are short range in action, and are considered negligible in the macroscopic theory of elasticity. So, the forces which causes internal stresses are the forces act only on the surface of the solid body. Let us consider the total force  $\mathbf{F}$  acting on some portion of the unstrained solid body. The total force is equivalent to the summation of all the forces  $\delta\vec{F}$  on all the volume element  $\delta V$  of the strained body. Mathematically, the resultant total force can be considered as the sum of the forces exerted on the surface of the body i.e. as an integral over the surface<sup>2</sup>. Thus, for any part of the body, the three components of the resultant internal stresses  $\int F_i dV$  can be written as integral over surface<sup>3</sup> The vector  $F_i$  must be the divergence rank two tensor.

$$\delta F_i = \int_{\delta V} f_i dV + \oint_{\delta S} \sigma_{ij} dS_j \quad (\text{D.8})$$

where  $\sigma_{ij}$  is the stress tensor that defines the internal stresses [93]. If there is mechanical equilibrium, then total resultant force is written as

$$F_i = \frac{\partial \sigma_{ij}}{\partial r_j} \quad (\text{D.9})$$

The total force on any volume can also be written as

$$\int F_i dV = \int \frac{\partial \sigma_{ij}}{\partial r_j} dV = \oint \sigma_{ij} dS_j \quad (\text{D.10})$$

<sup>2</sup>As per Newton's third law, the forces on some part of the solid body considered act on one another provide zero resultant force.

<sup>3</sup>Applying Divergence theorem

where  $df_j$  are the surface element  $d\mathbf{f}$  components along the outward normal [96].

The torque  $\mathbf{T}$  of the force  $\mathbf{F}$  is defined as an anti-symmetrical rank two tensor which has components such as  $F_i r_j - F_j r_i$ , where  $r_i$  are the coordinated of the point where force is exerted<sup>4</sup>. As total force on any volume, the moment can also be expressed as integral over surface

$$\mathbf{T}_{ij} = \int \left( \frac{\partial \sigma_{ik}}{\partial r_k} r_j - \frac{\partial \sigma_{jk}}{\partial r_k} r_i \right) dV \quad (\text{D.11})$$

$$= \int \frac{\partial (\sigma_{ik} r_j - \sigma_{jk} r_i)}{\partial r_k} dV - \int \left( \sigma_{ik} \frac{\partial r_j}{\partial r_k} - \sigma_{jk} \frac{\partial r_i}{\partial r_k} \right) dV \quad (\text{D.12})$$

where the first term can be written as the divergence of a well defined vector field and is thus identified as the only torque contribution. The second integral in Eq.(D.12) is therefore equal to zero. Since  $\partial r_j / \partial r_k$  is the unit tensor  $\delta_{jk}$ , we have  $\sigma_{ik} \delta_{jk} = \sigma_{ij}$  and similarly  $\sigma_{jk} \delta_{ik} = \sigma_{ji}$ . The stress tensor must therefore be symmetrical

$$\sigma_{ij} = \sigma_{ji}. \quad (\text{D.13})$$

---

<sup>4</sup>The torque is defined as the vector product of  $\mathbf{F} \times \mathbf{r}$ .



# Appendix E

## Algorithm for 1D-1D mobility

Algorithm 4 details the computational steps for evaluating the sink strength associated with the agglomeration kinetics of two mobile defects. The algorithm can possibly applied to any combination of migration mechanisms: 1DR-1DR, 1D-1D , 1DR-3D, 1DR-0, 3D-3D or 3D-0 (refer to Section. 5.4 for an explanation of the notations) in cubic lattices. The algorithm is applied to the agglomeration of two interstitial clusters both migrating through the 1DR mechanism in BCC crystal structure corresponding to  $\alpha$ -iron. The state space comprises all the possible positions and orientations of two interstitial clusters in a periodically replicated supercell. The supercell here is a BCC lattice. Note that the algorithm involves solving a linear system whose dimension is greatly reduced by accounting of the 48 cubic symmetries of BCC lattice.

---

**Algorithm 4** Numerical computation of sink strengths by solving a reduced linear system involving the compressed transition rate matrix.

---

- 1: Construct the linear transformations  $\mathcal{T}_s$  with  $s \in \mathbb{N}_{48}^*$  associated with the 48 cubic symmetries;
  - 2: Assign a descriptor  $\mathcal{D}(S)$  to each supercell state  $S$ ;
  - 3: Determine the  $N$  transient states and the  $N^a$  absorbing states;
  - 4: Index the transient states as  $S_n$  with  $1 \leq n \leq N$  ;
  - 5: Set class index  $i$  to 0 ;
  - 6: **for**  $n = 1, \dots, N$  **do** ▷ Construct classes
  - 7:     Evaluate class descriptor as  $\mathcal{D}^c(S_n) = \min \mathcal{D}(\mathcal{T}_s(S_n))$  among  $s \in \mathbb{N}_{48}^*$ ;
  - 8:     **if** new class **then**
  - 9:          $i \leftarrow i + 1$  ;
  - 10:         Determine  $\sigma = \arg \min \mathcal{D}(\mathcal{T}_s(S_n))$  among  $s \in \mathbb{N}_{48}^*$  ;
  - 11:         Define class-representative state as  $S_i^c = \mathcal{T}_\sigma(S_n)$ ;
  - 12:     **end if**
  - 13: **end for**
  - 14: Define the number of classes by setting  $N^c = i$  ;
  - 15: **for**  $i = 1, \dots, N^c$  **do** ▷ Compute class cardinal  $c_i$
  - 16:     Set  $c_i$  to the number of distinct states in  $\{\mathcal{T}_s(S^c)/s \in \mathbb{N}_{48}^*\}$
  - 17: **end for**
  - 18: Check that  $N = \sum_{i=1}^{N^c} c_i$
  - 19: Set compressed transition rate matrix  $\mathbf{A}^c$  to zero
  - 20: **for**  $n, m = 1, \dots, N$  **do** ▷ Construct  $\mathbf{A}^c$
  - 21:     **if**  $A_{n,m}$  is non zero **then**
  - 22:         Determine class index  $i$  (resp.  $j$ ) of state  $S_n$  (resp.  $S_m$ );
  - 23:         **if** new pair  $(i, j)$  **then**
  - 24:             Set  $A_{ij}^c$  to  $A_{nm}$ ;
  - 25:         **end if**
  - 26:     **end if**
  - 27: **end for**
  - 28: Solve compressed linear system  $\sum_{j=1}^{N^c} A_{ij}^c c_j \tau_j = 1$  with unknown  $\tau = (\tau_1, \dots, \tau_{N^c})^T$  representing MFPT vector with respect to the classes;
  - 29: Compute MFPT from uniform distribution  $\bar{\tau} = \frac{1}{N} \sum_{i=1}^{N^c} c_i \tau_i$  ;
  - 30: Compute sink strength as :  $k^2 = \frac{1}{\bar{\tau}(D_A + D_B)}$ ;
-

---

**Algorithm 5** Computation of sink strengths associated with the agglomeration of two interstitial clusters with mixed 1DR mobility. The first-intersection times are drawn using the recursive kPS algorithm described in Chapter 5. Its algorithmic complexity is logarithm in the number of transient states.

---

- 1: Construct supercell and transition rate matrix;      ▷ Call of Algorithm 4
  - 2: Draw initial cluster configuration from uniform distribution;
  - 3: **for**  $m = 1, \dots, M$  **do**
  - 4:     **while** configuration **not** in agglomeration slab **do**   ▷ free propagation
  - 5:         Draw total number of hops prior next rotation from geometric distribution;
  - 6:         Dispatch hops between  $A$  and  $B$  defects using binomial law;
  - 7:         Dispatch hops between backward and forward hops using binomial law for both defects;
  - 8:         Draw defect that will rotate using binomial law;
  - 9:         Draw elapsed time from total hop number using Gamma law;
  - 10:        Check whether new configuration in agglomeration slab by computing the distance between the two glide lines;
  - 11:     **end while**    ▷ Configuration in agglomeration slab
  - 12:     Read agglomeration probability  $\pi^{\text{agg}}$  from table;
  - 13:     Draw first-rotation time ;
  - 14:     Draw first-intersection time for both defects
  - 15:     **if** first-intersection time **lower than** first-rotation time **then**
  - 16:         Synchronize defects to first-intersection time ;
  - 17:     **else**
  - 18:         Synchronize defects to first-rotation time ;
  - 19:     **end if**
  - 20:     **while** physical time **lower than** first-rotation time **do**
  - 21:         Draw first-intersection time for defect away intersection
  - 22:         **if** first-intersection time lower than first-rotation time **then**
  - 23:             Move defects away intersection to intersection
  - 24:             Synchronize other defect at intersection by free propagation;
  - 25:         **else**
  - 26:             Synchronize both defects to rotation-time;
  - 27:             Exit **while loop**;
  - 28:         **end if**
  - 29:         **if** Agglomeration **then**
  - 30:             Update number of agglomeration  $\nu^{\text{ag}}$ ;
  - 31:             Draw new configuration from uniform distribution;
  - 32:             Exit **while loop**;
  - 33:         **end if**
  - 34:     **end while**
  - 35:     Monitor elapsed physical time in  $\theta_m$ ;
  - 36: **end for**
  - 37: Evaluate overall diffusion coefficient  $D = D_A + D_B$ ;
  - 38: Evaluate the standard estimate of sink strengths as  $k^2 = \frac{\nu^{\text{ag}}}{\theta_M D}$ ;
  - 39: Evaluate the conditioned estimate of sink strengths as  $k^2 = \frac{1}{\theta_M D} \sum_{m=1}^M \pi_m^{\text{ag}}$ ;
-



## Résumé du manuscrit

L'évolution microstructurale des matériaux nucléaires est déterminée par l'agglomération ou la recombinaison de défauts créés sous irradiation neutronique. Ces défauts sont souvent des lacunes, des atomes interstitiels, des dislocations, rassemblés en petits ou grand amas de défauts. Il est donc essentiel de prédire la cinétique des défauts d'irradiation pour comprendre comment les propriétés mécaniques des matériaux évoluent dans le temps. De nombreuses études théoriques permettent de décrire la cinétique de vieillissement des matériaux et les conséquences qui en découlent sur les propriétés.

Dans cette thèse, nous discutons de la cinétique de vieillissement des matériaux à l'aide d'une approche numérique. Pour cela, nous prenons en compte les fréquences de sauts élémentaire des défauts ponctuels à l'échelle atomique et nous faisons intervenir une équation maîtresse régissant l'évolution temporelle d'un vecteur de probabilité d'état à partir d'un état initial donné. Nous avons utilisé la théorie des états de transition et la théorie de l'élasticité pour calculer les fréquences de saut et construire la matrice des taux de transition, qui est l'ingrédient crucial de l'équation maîtresse.

Dans cette thèse, des techniques numériques non-stochastiques sont proposées pour caractériser le mouvement de défauts ponctuels individuels migrant sur de longues distances avant de s'agglomérer avec d'autres défauts mobiles ou d'être absorbés par un puits, typiquement un défaut stationnaire étendu. L'approche est basée sur la théorie des chaînes de Markov absorbantes dans lesquelles les états absorbants correspondent aux recombinaisons de défauts ou aux absorptions de défauts mobiles par des puits fixes. Les mouvements des défauts sont alors entièrement déterminés par la distribution des temps de premier passage vers des sites distants, la distribution des non-passages et les flux de probabilité vers les états absorbants. Ces quantités sont dérivées directement des propriétés spectrales de la matrice des taux de transition. Elles définissent également les lois probabilistes pour les événements non locaux qui peuvent ensuite être simulés par l'algorithme de Monte Carlo cinétique de premier passage. En outre, nous présentons également comment les temps de premier passage permettent de calculer

---

les forces de puits ou les efficacités d'absorption, qui sont les paramètres d'entrée cruciaux des équations de cinétique chimique considérées dans les simulations de dynamique d'amas.

En supposant que les défauts migrent selon un processus de diffusion réversible, nous montrons que la matrice de taux de transition d'absorption est diagonalement similaire à une matrice définie positive symétrique. Cette caractéristique facilite considérablement l'extraction de ses propriétés spectrales par des solveurs itératifs à faible densité. Dans un premier temps, nous testons l'efficacité des différents solveurs itératifs. Ensuite, nous démontrons l'efficacité de l'approche numérique en calculant directement les propriétés d'élasto-diffusion d'une lacune autour d'une cavité dans l'aluminium et en mesurant la diffusivité de petits amas de solutés dans des aciers alliés à faible teneur en manganèse. Par ailleurs, nous évaluons également l'efficacité de divers schémas mathématiques pour caractériser les lois d'évolution d'un défaut ponctuel près d'un puits. En particulier, nous développons un algorithme combinant la projection sur des sous-espaces de Krylov et la déflation des modes propres. Pour ce cas, nous choisissons le système modèle qui décrit l'absorption d'une lacune par une cavité dans l'aluminium. Nous montrons alors qu'un petit sous-espace de Krylov déflaté par l'unique mode propre correspondant à la distribution quasi-stationnaire est capable de capturer fidèlement la cinétique d'absorption du défaut.

Enfin, nous présentons de deux approches rigoureuses pour caractériser les événements rares essentiels qui régissent l'évolution microstructurale à long terme des alliages, telles que les mobilités des amas, les forces d'absorption et les distributions de premier passage associées. La première approche est basée sur l'algorithme cinétique de Monte Carlo et la seconde sur les événements de premier passage, qui peuvent être mis en œuvre efficacement pour calculer les forces de puits de petits amas d'auto-interstitiels migrant rapidement le long d'une direction de glissement et tournant occasionnellement.



## Publications and Oral presentations

### Publications

1. S. Kaur, M. Athènes, J. Creuze, "Absorption kinetics of vacancies by cavities in aluminium: Numerical characterisation of sink strengths and first passage statistics through Krylov subspace projection eigenvalue deflation", *Journal of Computational Physics*, 2022 ([DOI](#))
2. M. Athènes, S. Kaur, G. Adjanor, T. Vanacker, & T. Jourdan, "Elastodiffusion and cluster mobilities using kinetic Monte Carlo simulations: Fast first-passage algorithms for reversible diffusion processes", *Physical Review Materials*, 2019 ([DOI](#))

### Presentations

1. Poster presentation: *Journée de l'école doctorale 2MIB*, France (2019) - S. Kaur, M. Athènes, J. Creuze
2. Oral and Poster presentation: *Paris International School on Advanced Computational Materials Science (PISACMS)*, Sorbonne Université, France (2019) - S. Kaur, M. Athènes, J. Creuze
3. Poster presentation: *MRS conference*, Boston (2019) - S. Kaur, M. Athènes, J. Creuze
4. Oral and poster presentation: *Modeling in Nuclear Science & Engineering seminar*, Bangor University, Wales, UK (2020) - S. Kaur, M. Athènes, J. Creuze
5. Oral presentation: *APS – Virtual March Meeting* (2021) - S. Kaur, M. Athènes, J. Creuze



# Bibliography

- [1] J. A. Brinkman. "On the nature of radiation damage in metals". In: *Journal of Applied Physics* 25.8 (1954), pp. 961–970.
- [2] G. Odette, B. Wirth, D. Bacon, and N. Ghoniem. "Multiscale-Multiphysics Modeling of Radiation-Damaged Materials: Embrittlement of Pressure-Vessel Steels". In: *MRS Bulletin* 26.3 (2001), pp. 176–181.
- [3] L. Malerba. "15 - Multi-scale modelling of irradiation effects in nuclear power plant materials". In: *Understanding and Mitigating Ageing in Nuclear Power Plants*. Ed. by P. G. Tipping. Woodhead Publishing Series in Energy. Woodhead Publishing, 2010, pp. 456–543.
- [4] A. Gentils and C. Cabet. "Investigating radiation damage in nuclear energy materials using JANNuS multiple ion beams". In: *Nuclear Instruments and Methods in Physics Research Section B: Beam Interactions with Materials and Atoms* 447 (2019), pp. 107–112.
- [5] C.-C. Fu and F. Willaime. "Ab initio study of helium in  $\alpha$ -Fe: Dissolution, migration, and clustering with vacancies". In: *Phys. Rev. B* 72 (6 2005), p. 064117.
- [6] M. Athènes and M.-C. Marinica. "Free energy reconstruction from steered dynamics without post-processing". In: *Journal of Computational Physics* 229.19 (Sept. 2010), pp. 7129–7146.
- [7] N.-V. Buchete and G. Hummer. "Coarse Master Equations for Peptide Folding Dynamics". In: *The Journal of Physical Chemistry B* 112.19 (May 2008). Publisher: American Chemical Society, pp. 6057–6069.
- [8] T. Opperstrup, V. V. Bulatov, A. Donev, M. H. Kalos, G. H. Gilmer, and B. Sadigh. "First-passage kinetic Monte Carlo method". In: *Physical Review E* 80.6 (Dec. 2009). Publisher: American Physical Society, p. 066701.
- [9] D. Iracane, P. Chaix, and A. Alamo. "Jules Horowitz Reactor: a high performance material testing reactor". en. In: *Comptes Rendus Physique. Materials subjected to fast neutron irradiation* 9.3 (Apr. 2008), pp. 445–456.

- [10] R. G. Carter, N. Soneda, K. Dohi, J. M. Hyde, C. A. English, and W. L. Server. "Microstructural characterization of irradiation-induced Cu-enriched clusters in reactor pressure vessel steels". en. In: *Journal of Nuclear Materials* 298.3 (Oct. 2001), pp. 211–224.
- [11] W. J. Phythian and C. A. English. "Microstructural evolution in reactor pressure vessel steels". In: *Journal of Nuclear Materials* 205 (1993), pp. 162–177.
- [12] J. T. Buswell, W. J. Phythian, R. J. McElroy, S. Dumbill, P. H. N. Ray, J. Mace, and R. N. Sinclair. "Irradiation-induced microstructural changes, and hardening mechanisms, in model PWR reactor pressure vessel steels". en. In: *Journal of Nuclear Materials* 225 (Aug. 1995), pp. 196–214.
- [13] T. J. Frankcombe and S. C. Smith. "Numerical solution methods for large, difficult kinetic master equations". en. In: *Theoretical Chemistry Accounts* 124.5 (Aug. 2009), p. 303.
- [14] D. Carpentier, T. Jourdan, Y. Le Bouar, and M. -C. Marinica. "Effect of saddle point anisotropy of point defects on their absorption by dislocations and cavities". In: *Acta Materialia* 136 (Sept. 2017), pp. 323–334.
- [15] Y.-S. Kim, S.-W. Bae, S. Cho, K.-H. Kang, and H.-S. Park. "Application of direct passive residual heat removal system to the SMART reactor". In: *Annals of Nuclear Energy* 89 (2016), pp. 56–62.
- [16] K. Farrell. "5.07 - Performance of Aluminum in Research Reactors". In: *Comprehensive Nuclear Materials*. Ed. by R. J. Konings. Oxford: Elsevier, 2012, pp. 143–175.
- [17] J. Zelenty. "Understanding thermally induced embrittlement in low copper RPV steels utilising atom probe tomography". In: *Materials Science and Technology* 31 (May 2015), pp. 981–988.
- [18] M. Bickell and C. Ruiz. *Pressure Vessel Design and Analysis*. Macmillan, 1967.
- [19] S. Jumel. "RPV-1 : A First virtual reactor to simulate irradiation effects in light water reactor pressure vessel steels". PhD thesis. L'Université des Sciences et Technologies de Lille, 2005.
- [20] K. Farrell, T. Byun, and N. Hashimoto. "Deformation mode maps for tensile deformation of neutron-irradiated structural alloys". In: *Journal of Nuclear Materials* 335.3 (2004), pp. 471–486.
- [21] M. Hernández-Mayoral and M. Caturla. "8 - Microstructure evolution of irradiated structural materials in nuclear power plants". In: *Understanding and Mitigating Ageing in Nuclear Power Plants*. Ed. by P. G. Tipping. Woodhead Publishing Series in Energy. Woodhead Publishing, 2010, pp. 189–235.
- [22] M. Norgett, M. Robinson, and I. Torrens. "A proposed method of calculating displacement dose rates". In: *Nuclear Engineering and Design* 33.1 (1975), pp. 50–54.
- [23] G. Odette and G. Lucas. "Embrittlement of nuclear reactor pressure vessels". In: *Jom* 53.7 (2001), pp. 18–22.

- [24] V. Jansson. "Radiation-induced nanostructure evolution models for Fe alloys". PhD thesis. University of Helsinki, 2013.
- [25] M. Tomimatsu, T. Hirota, T. Hardin, and P. Todeschini. "4 - Embrittlement of reactor pressure vessels (RPVs) in pressurized water reactors (PWRs)". In: *Irradiation Embrittlement of Reactor Pressure Vessels (RPVs) in Nuclear Power Plants*. Ed. by N. Soneda. Woodhead Publishing Series in Energy. Woodhead Publishing, 2015, pp. 57–106.
- [26] *Guidelines for Application of the Master Curve Approach to Reactor Pressure Vessel Integrity in Nuclear Power Plants*. Technical Reports Series 429. Vienna: INTERNATIONAL ATOMIC ENERGY AGENCY, 2005.
- [27] E. D. Eason, J. E. Wright, and G. Odette. *Improved embrittlement correlations for reactor pressure vessel steels*. Division of Engineering Technology, Office of Nuclear Regulatory Research, U.S. Nuclear Regulatory Commission., 1998.
- [28] M. Akamatsu, C. Brillaud, R. Lloret, C. Rieg, and J.-C. Van Duysen. "L'irradiation de la cuve: un phénomène sous surveillance". In: *Revue générale nucléaire* 6 (1993), pp. 391–397.
- [29] C. Brillaud and F. Hedin. "In-service evaluation of french pressurized water reactor vessel steel". In: *Effects of radiation on materials: 15th international symposium*. ASTM International. 1992.
- [30] B. Pannier. "Towards the prediction of microstructure evolution under irradiation of model ferritic alloys with an hybrid AKMC-OKMC approach". 2017LIL10061. PhD thesis. L'Université des Sciences et Technologies de Lille, 2017.
- [31] P. G. Tipping. "18 - Plant life management (PLiM) practices for pressurized light water reactors (PWR)". In: *Understanding and Mitigating Ageing in Nuclear Power Plants*. Ed. by P. G. Tipping. Woodhead Publishing Series in Energy. Woodhead Publishing, 2010, pp. 609–632.
- [32] P. G. Tipping. *Understanding and mitigating ageing in nuclear power plants: materials and operational aspects of plant life management (PLiM)*. Elsevier, 2010.
- [33] F. Seitz. "Radiation effects in solids". In: *Physics Today* 5.6 (June 1952). Publisher: American Institute of Physics, pp. 6–9.
- [34] L. Greenwood. "Neutron interactions and atomic recoil spectra". In: *Journal of Nuclear Materials* 216 (1994), pp. 29–44.
- [35] C. Race. "A Radiation Damage Cascade". In: *The Modelling of Radiation Damage in Metals Using Ehrenfest Dynamics*. Berlin, Heidelberg: Springer Berlin Heidelberg, 2011, pp. 9–13.
- [36] G. Odette and B. Wirth. "A computational microscopy study of nanostructural evolution in irradiated pressure vessel steels". In: *Journal of Nuclear Materials* 251 (1997). Proceedings of the International Workshop on Defect Production, Accumulation and Materials Performance in an Irradiation Environment, pp. 157–171.
- [37] K. Nordlund, A. E. Sand, F. Granberg, S. J. Zinkle, R. Stoller, R. S. Averback, T. Suzudo, L. Malerba, F. Banhart, W. J. Weber, et al. "Primary Radiation Damage in Materials. Review of Current Understanding

- and Proposed New Standard Displacement Damage Model to Incorporate in Cascade Defect Production Efficiency and Mixing Effects". In: (2015).
- [38] M. Wellen. "2. Point Defect Relaxations". In: *Materials Science Forum*. Vol. 366. Trans Tech Publ. 2001, pp. 95–140.
- [39] R. Bullough and M. Wood. *Theory of microstructural evolution*. North Holland, Amsterdam, 1986.
- [40] A. Barashev, S. Golubov, and H. Trinkaus. "Reaction kinetics of glissile interstitial clusters in a crystal containing voids and dislocations". In: *Philosophical Magazine A* 81.10 (2001), pp. 2515–2532.
- [41] H. Trinkaus, B. Singh, and A. Foreman. "Glide of interstitial loops produced under cascade damage conditions: Possible effects on void formation". In: *Journal of Nuclear Materials* 199.1 (1992), pp. 1–5.
- [42] M. Lambrecht, E. Meslin, L. Malerba, M. Hernández-Mayoral, F. Bergner, P. Pareige, B. Radiguet, and A. Almazouzi. "On the correlation between irradiation-induced microstructural features and the hardening of reactor pressure vessel steels". In: *Journal of Nuclear Materials* 406.1 (2010). FP6 IP PERFECT Project: Prediction of Irradiation Damage Effects in Reactor Components, pp. 84–89.
- [43] E. Meslin, M. Lambrecht, M. Hernández-Mayoral, F. Bergner, L. Malerba, P. Pareige, B. Radiguet, A. Barbu, D. Gómez-Briceño, A. Ulbricht, et al. "Characterization of neutron-irradiated ferritic model alloys and a RPV steel from combined APT, SANS, TEM and PAS analyses". In: *Journal of Nuclear Materials* 406.1 (2010), pp. 73–83.
- [44] J. Du and J. M. Rimsza. "Atomistic computer simulations of water interactions and dissolution of inorganic glasses". In: *npj Materials Degradation* 1.1 (2017), pp. 1–12.
- [45] A. Schneider, C.-C. Fu, O. Waseda, C. Barreteau, and T. Hickel. "Ab initio based models for temperature-dependent magnetochemical interplay in bcc Fe-Mn alloys". In: *Phys. Rev. B* 103 (2 2021), p. 024421.
- [46] C. Becquart, C. Domain, A. Legris, and J. Van Duysen. "Influence of the interatomic potentials on molecular dynamics simulations of displacement cascades". In: *Journal of Nuclear Materials* 280.1 (2000), pp. 73–85.
- [47] D. G. Doran. "Computer simulation of displacement spike annealing". In: *Radiation Effects* 2.4 (1970). Cited By :46, pp. 249–267.
- [48] M. J. Caturla. "Object kinetic Monte Carlo methods applied to modeling radiation effects in materials". In: *Computational Materials Science* 156 (2019), pp. 452–459.
- [49] D. Frenkel and B. Smit. *Understanding molecular simulation: from algorithms to applications*. Vol. 1. Elsevier, 2001.
- [50] K. Reuter. "First-Principles Kinetic Monte Carlo Simulations for Heterogeneous Catalysis: Concepts, Status, and Frontiers". In: *ChemInform* 43.36 (2012), no.
- [51] M. Andersen, C. Panosetti, and K. Reuter. "A Practical Guide to Surface Kinetic Monte Carlo Simulations". In: *Frontiers in Chemistry* 7 (2019), p. 202.

- [52] J. L. Doob. "What is a Stochastic Process?" In: *The American Mathematical Monthly* 49.10 (1942), pp. 648–653.
- [53] J. Karush. "On the chapman-kolmogorov equation". In: *The Annals of Mathematical Statistics* 32.4 (1961), pp. 1333–1337.
- [54] D. R. Cox and H. D. Miller. *The theory of stochastic processes*. Vol. 134. CRC press, 1977.
- [55] K. Sigman. *Foundations for Category Theory*. <http://www.columbia.edu/~ks20/stochastic-I/stochastic-I-CTMC.pdf>. 2009.
- [56] S. M. Ross. "6 - Continuous-Time Markov Chains". In: *Introduction to Probability Models (Twelfth Edition)*. Ed. by S. M. Ross. Twelfth Edition. Academic Press, 2019, pp. 375–429.
- [57] M. A. Novotny. "Monte Carlo Algorithms with Absorbing Markov Chains: Fast Local Algorithms for Slow Dynamics". In: *Physical Review Letters* 74.1 (Jan. 1995). Publisher: American Physical Society, pp. 1–5.
- [58] M. A. Novotny. "A tutorial on advanced dynamic Monte Carlo methods for systems with discrete state spaces". In: *Annual Reviews Of Computational Physics IX* (), pp. 153–210.
- [59] M. Athènes, S. Kaur, G. Adjanor, T. Vanacker, and T. Jourdan. "Elastodiffusion and cluster mobilities using kinetic Monte Carlo simulations: Fast first-passage algorithms for reversible diffusion processes". In: *Physical Review Materials* 3.10 (Oct. 2019), p. 103802.
- [60] J.-M. Lanore. "Simulation de l'évolution des défauts dans un réseau par le méthode de Monte-Carlo". In: *Radiation Effects* 22.3 (1974), pp. 153–162.
- [61] G. A. Whitmore. "First-Passage-Time Models for Duration Data: Regression Structures and Competing Risks". In: *Journal of the Royal Statistical Society: Series D (The Statistician)* 35.2 (1986), pp. 207–219.
- [62] M.-L. T. Lee and G. A. Whitmore. "Threshold Regression for Survival Analysis: Modeling Event Times by a Stochastic Process Reaching a Boundary". In: *Statistical Science* 21.4 (2006), pp. 501–513.
- [63] M.-L. T. Lee and G. A. Whitmore. "First Hitting Time Models for Lifetime Data". In: *Handbook of Statistics* 23 (2003), pp. 537–543.
- [64] J. Rocca. *Introduction to Markov chains*. <https://towardsdatascience.com/brief-introduction-to-markov-chains-2c8cab9c98ab>. 2019.
- [65] A. Bortz, M. Kalos, and J. Lebowitz. "A new algorithm for Monte Carlo simulation of Ising spin systems". In: *Journal of Computational Physics* 17.1 (1975), pp. 10–18.
- [66] R. Ngayam-Happy, C. S. Becquart, C. Domain, and L. Malerba. "Formation and evolution of MnNi clusters in neutron irradiated dilute Fe alloys modelled by a first principle-based AKMC method". en. In: *Journal of Nuclear Materials* 426.1 (July 2012), pp. 198–207.
- [67] E. Martinez, P. R. Monasterio, and J. Marian. "Billion-atom Synchronous Parallel Kinetic Monte Carlo Simulations of Critical 3D Ising Systems". In: *Journal of Computational Physics* 230.4 (Feb. 2011). arXiv: 1005.4713, pp. 1359–1369.

- [68] G. Nandipati, A. Kara, S. I. Shah, and T. S. Rahman. "Off-lattice pattern recognition scheme for kinetic Monte Carlo simulations". In: *Journal of Computational Physics* 231.9 (2012), pp. 3548–3560.
- [69] M. Trochet, N. Mousseau, L. K. Béland, and G. Henkelman. "Off-lattice kinetic Monte Carlo methods". In: *Handbook of Materials Modeling: Methods: Theory and Modeling* (2020), pp. 715–743.
- [70] F. Soisson, C. Becquart, N. Castin, C. Domain, L. Malerba, and E. Vincent. "Atomistic Kinetic Monte Carlo studies of microchemical evolutions driven by diffusion processes under irradiation". In: *Journal of Nuclear Materials* 406.1 (2010), pp. 55–67.
- [71] C. Domain and C. S. Becquart. "Object Kinetic Monte Carlo (OKMC): A Coarse-Grained Approach to Radiation Damage". In: *Handbook of Materials Modeling: Methods: Theory and Modeling* (2020), pp. 1287–1312.
- [72] C. Domain, C. Becquart, and L. Malerba. "Simulation of radiation damage in Fe alloys: an object kinetic Monte Carlo approach". In: *Journal of Nuclear Materials* 335.1 (2004), pp. 121–145.
- [73] J. Dalla Torre, J.-L. Bocquet, N. Doan, E. Adam, and A. Barbu. "JERK, an event-based Kinetic Monte Carlo model to predict microstructure evolution of materials under irradiation". In: *Philosophical Magazine* 85.4-7 (2005), pp. 549–558.
- [74] T. L. Hoang, J. Marian, V. V. Bulatov, and P. Hosemann. "Computationally-efficient stochastic cluster dynamics method for modeling damage accumulation in irradiated materials". In: *Journal of Computational Physics* 300 (2015), pp. 254–268.
- [75] T. Opperstrup, V. V. Bulatov, G. H. Gilmer, M. H. Kalos, and B. Sadigh. "First-Passage Monte Carlo Algorithm: Diffusion without All the Hops". In: *Physical Review Letters* 97.23 (Dec. 2006), p. 230602.
- [76] A. Donev, V. V. Bulatov, T. Opperstrup, G. H. Gilmer, B. Sadigh, and M. H. Kalos. "A First-Passage Kinetic Monte Carlo algorithm for complex diffusion–reaction systems". In: *Journal of Computational Physics* 229.9 (2010), pp. 3214–3236.
- [77] D. Carpentier. "Simulation de la cinétique d'absorption des défauts ponctuels par les dislocations et amas de défauts". Theses. Université Paris-Saclay, Oct. 2018.
- [78] D. T. Gillespie. "A general method for numerically simulating the stochastic time evolution of coupled chemical reactions". In: *Journal of computational physics* 22.4 (1976), pp. 403–434.
- [79] S. A. Serebrinsky. "Physical time scale in kinetic Monte Carlo simulations of continuous-time Markov chains". In: *Phys. Rev. E* 83 (3 2011), p. 037701.
- [80] S. Redner. *A guide to first-passage processes*. Cambridge University Press, 2001.
- [81] A. Donev. "Asynchronous Event-Driven Particle Algorithms". In: *Simulation* 85.4 (2009), pp. 229–242.
- [82] A. F. Voter. "Introduction to the kinetic Monte Carlo method". In: *Radiation effects in solids*. Springer, 2007, pp. 1–23.

- [83] C. Daniels and P. Bellon. "Hybrid kinetic Monte Carlo algorithm for strongly trapping alloy systems". In: *Computational Materials Science* 173 (2020), p. 109386.
- [84] B. Puchala, M. L. Falk, and K. Garikipati. "An energy basin finding algorithm for kinetic Monte Carlo acceleration". In: *The Journal of Chemical Physics* 132.13 (Apr. 2010), p. 134104.
- [85] M. Athènes and V. V. Bulatov. "Path Factorization Approach to Stochastic Simulations". In: *Physical Review Letters* 113.23 (Dec. 2014). Publisher: American Physical Society, p. 230601.
- [86] G. Nandipati, Y. Shim, and J. G. Amar. "First-passage time approach to kinetic Monte Carlo simulations of metal (100) growth". In: *Physical Review B* 81.23 (June 2010), p. 235415.
- [87] T. D. Swinburne, D. Kannan, D. J. Sharpe, and D. J. Wales. "Rare events and first passage time statistics from the energy landscape". In: *The Journal of Chemical Physics* 153.13 (Oct. 2020). Publisher: American Institute of Physics, p. 134115.
- [88] C. Wert. "Diffusion coefficient of C in  $\alpha$ -iron". In: *Physical Review* 79.4 (1950), p. 601.
- [89] G. H. Vineyard. "Frequency factors and isotope effects in solid state rate processes". In: *Journal of Physics and Chemistry of Solids* 3.1-2 (1957), pp. 121–127.
- [90] K. J. Laidler and M. C. King. "Development of transition-state theory". In: *The Journal of Physical Chemistry* 87.15 (1983), pp. 2657–2664.
- [91] K. J. Laidler. *Transition state theory*. <https://www.britannica.com/science/transition-state-theory>.
- [92] C. Domain and C. Becquart. "Ab initio calculations of defects in Fe and dilute Fe-Cu alloys". In: *Physical Review B* 65.2 (2001), p. 024103.
- [93] E. Clouet, C. Varvenne, and T. Jourdan. "Elastic modeling of point-defects and their interaction". In: *Computational Materials Science* 147 (2018), pp. 49–63.
- [94] C. V. B. D.Sc. "XVIII. A theory concerning the constitution of matter". In: *The London, Edinburgh, and Dublin Philosophical Magazine and Journal of Science* 33.201 (1892), pp. 191–204.
- [95] J. Eshelby. "The Continuum Theory of Lattice Defects". In: ed. by F. Seitz and D. Turnbull. Vol. 3. *Solid State Physics*. Academic Press, 1956, pp. 79–144.
- [96] L. D. Landau and E. M. Lifshitz. *Theory of Elasticity, 2nd Edition Vol. 7 of Course of Theoretical Physics*. Pergamon Press, 1970.
- [97] J. F. Nye et al. *Physical properties of crystals: their representation by tensors and matrices*. Oxford university press, 1985.
- [98] R. Siems. "Mechanical interactions of point defects". In: *physica status solidi (b)* 30.2 (1968), pp. 645–658.
- [99] A. M. Stoneham. *Theory of Defects in Solids*. Oxford university press, 1975.
- [100] R. Nazarov, J. S. Majevadia, M. Patel, M. R. Wenman, D. S. Balint, J. Neugebauer, and A. P. Sutton. "First-principles calculation of the

- elastic dipole tensor of a point defect: Application to hydrogen in  $\alpha$ -zirconium". In: *Phys. Rev. B* 94 (24 2016), p. 241112.
- [101] L. Huang. "Micromechanical simulation and experimental investigation of the creep damage of stainless austenitic steels". Theses. Université Pierre et Marie Curie - Paris VI, Dec. 2017.
- [102] M. Gillan. "The elastic dipole tensor for point defects in ionic crystals". In: *Journal of Physics C: Solid State Physics* 17.9 (1984), p. 1473.
- [103] D. Mason, T. Hudson, and A. Sutton. "Fast recall of state-history in kinetic Monte Carlo simulations utilizing the Zobrist key". In: *Computer Physics Communications* 165.1 (2005), pp. 37–48.
- [104] O. Trushin, A. Karim, A. Kara, and T. S. Rahman. "Self-learning kinetic Monte Carlo method: Application to Cu(111)". In: *Phys. Rev. B* 72 (11 2005), p. 115401.
- [105] F. El-Mellouhi, N. Mousseau, and L. J. Lewis. "Kinetic activation-relaxation technique: An off-lattice self-learning kinetic Monte Carlo algorithm". In: *Physical Review B* 78.15 (2008), p. 153202.
- [106] A. Kara, O. Trushin, H. Yildirim, and T. S. Rahman. "Off-lattice self-learning kinetic Monte Carlo: application to 2D cluster diffusion on the fcc (111) surface". In: *Journal of Physics: Condensed Matter* 21.8 (2009), p. 084213.
- [107] L. K. Béland, P. Brommer, F. El-Mellouhi, J.-F. Joly, and N. Mousseau. "Kinetic activation-relaxation technique". In: *Physical Review E* 84.4 (2011), p. 046704.
- [108] S. I. Shah, G. Nandipati, A. Kara, and T. S. Rahman. "Extended pattern recognition scheme for self-learning kinetic Monte Carlo simulations". In: *Journal of Physics: Condensed Matter* 24.35 (2012), p. 354004.
- [109] G. Nandipati, N. Govind, A. Andersen, and A. Rohatgi. "Self-learning kinetic Monte Carlo simulations of Al diffusion in Mg". In: *Journal of Physics: Condensed Matter* 28.15 (2016), p. 155001.
- [110] M. Trochet, A. Sauvé-Lacoursière, and N. Mousseau. "Algorithmic developments of the kinetic activation-relaxation technique: accessing long-time kinetics of larger and more complex systems". In: *The Journal of chemical physics* 147.15 (2017), p. 152712.
- [111] M. Trochet, N. Mousseau, L. K. Béland, and G. Henkelman. "Off-lattice kinetic Monte Carlo methods". In: *Handbook of Materials Modeling: Methods: Theory and Modeling* (2019), pp. 1–29.
- [112] M. Athenes, P. Bellon, and G. Martin. "Identification of novel diffusion cycles in B2 ordered phases by Monte Carlo simulation". In: *Philosophical Magazine A* 76.3 (1997), pp. 565–585.
- [113] S. A. Trygubenko and D. J. Wales. "Graph transformation method for calculating waiting times in Markov chains". In: *The Journal of chemical physics* 124.23 (2006), p. 234110.
- [114] D. J. Wales. "Calculating rate constants and committor probabilities for transition networks by graph transformation". In: *The Journal of chemical physics* 130.20 (2009), p. 204111.
- [115] J. G. Mullen. "Effect of Bardeen-Herring correlation on vacancy diffusion in anisotropic crystals". In: *Physical Review* 124.6 (1961), p. 1723.

- [116] J. R. Manning. "Correlation factors for impurity diffusion. bcc, diamond, and fcc structures". In: *Physical Review* 136.6A (1964), A1758.
- [117] J. Bocquet. "Correlation factor for diffusion in cubic crystals with solute–vacancy interactions of arbitrary range". In: *Philosophical Magazine* 94.31 (2014), pp. 3603–3631.
- [118] D. R. Trinkle. "Automatic numerical evaluation of vacancy-mediated transport for arbitrary crystals: Onsager coefficients in the dilute limit using a Green function approach". In: *Philosophical Magazine* 97.28 (2017), pp. 2514–2563.
- [119] D. R. Trinkle. "Variational principle for mass transport". In: *Physical review letters* 121.23 (2018), p. 235901.
- [120] D. T. Gillespie. *Markov processes: an introduction for physical scientists*. Elsevier, 1991.
- [121] R. Zia and B. Schmittmann. "Probability currents as principal characteristics in the statistical mechanics of non-equilibrium steady states". In: *Journal of Statistical Mechanics: Theory and Experiment* 2007.07 (2007), P07012.
- [122] Y. Shim and J. G. Amar. "Rigorous synchronous relaxation algorithm for parallel kinetic Monte Carlo simulations of thin film growth". In: *Physical Review B* 71.11 (2005), p. 115436.
- [123] J. D. Stevenson and D. J. Wales. "Communication: Analysing kinetic transition networks for rare events". In: *The Journal of chemical physics* 141.4 (2014), p. 041104.
- [124] G. Di Gesù, T. Lelièvre, D. Le Peutrec, and B. Nectoux. "Jump Markov models and transition state theory: the quasi-stationary distribution approach". In: *Faraday Discussions* 195 (2016), pp. 469–495.
- [125] M. Picciani, M. Athenes, J. Kurchan, and J. Tailleur. "Simulating structural transitions by direct transition current sampling: The example of LJ38". In: *The Journal of chemical physics* 135.3 (2011), p. 034108.
- [126] P. R. Amestoy, I. S. Duff, J.-Y. L'Excellent, and J. Koster. "A Fully Asynchronous Multifrontal Solver Using Distributed Dynamic Scheduling". In: *SIAM Journal on Matrix Analysis and Applications* 23.1 (Jan. 2001). Publisher: Society for Industrial and Applied Mathematics, pp. 15–41.
- [127] P. R. Amestoy, A. Guermouche, J.-Y. L'Excellent, and S. Pralet. "Hybrid scheduling for the parallel solution of linear systems". In: *Parallel computing* 32.2 (2006), pp. 136–156.
- [128] Y. Saad. *Iterative methods for sparse linear systems*. SIAM, 2003.
- [129] S. Balay et al. *PETSc Users Manual*. Tech. rep. ANL-95/11 - Revision 3.11. Argonne National Laboratory, 2019.
- [130] Y. Saad. *Numerical methods for large eigenvalue problems: revised edition*. SIAM, 2011.
- [131] P. Arbenz. *Lecture Notes on Solving Large Scale Eigenvalue Problems*. Tech. rep. Computer Science Department, ETH Zürich, 2016.
- [132] V. Hernandez, J. E. Roman, and V. Vidal. "SLEPc: A Scalable and Flexible Toolkit for the Solution of Eigenvalue Problems". In: *ACM Trans. Math. Software* 31.3 (2005), pp. 351–362.

- [133] J. E. Roman, C. Campos, E. Romero, and A. Tomas. *SLEPc Users Manual*. Tech. rep. DSIC-II/24/02 - Revision 3.11. D. Sistemes Informàtics i Computació, Universitat Politècnica de València, 2019.
- [134] M. Eiermann and O. G. Ernst. “A Restarted Krylov Subspace Method for the Evaluation of Matrix Functions”. In: *SIAM Journal on Numerical Analysis* 44.6 (Jan. 2006). Publisher: Society for Industrial and Applied Mathematics, pp. 2481–2504.
- [135] M. Athenes, P. Bellon, and G. Martin. “Effects of atomic mobilities on phase separation kinetics: a Monte-Carlo study”. In: *Acta Materialia* 48.10 (2000), pp. 2675–2688.
- [136] S. Pogatscher, H. Antrekowitsch, M. Werinos, F. Moszner, S. S. Gerstl, M. Francis, W. Curtin, J. F. Löffler, and P. J. Uggowitzer. “Diffusion on demand to control precipitation aging: application to Al-Mg-Si alloys”. In: *Physical review letters* 112.22 (2014), p. 225701.
- [137] L. Messina, M. Nastar, T. Garnier, C. Domain, and P. Olsson. “Exact ab initio transport coefficients in bcc Fe- X (X= Cr, Cu, Mn, Ni, P, Si) dilute alloys”. In: *Physical Review B* 90.10 (2014), p. 104203.
- [138] L. Messina, L. Malerba, and P. Olsson. “Stability and mobility of small vacancy–solute complexes in Fe–MnNi and dilute Fe–X alloys: A kinetic Monte Carlo study”. In: *Nuclear Instruments and Methods in Physics Research Section B: Beam Interactions with Materials and Atoms* 352 (2015), pp. 61–66.
- [139] M. Athènes. “Conditioning and enhanced sampling schemes for simulating thermodynamic and kinetic properties of condensed matter”. Habilitation à diriger des recherches. Université Paris Saclay ; Université paris sud, Jan. 2018.
- [140] F. Soisson and C.-C. Fu. “Cu-precipitation kinetics in  $\alpha$ -fe from atomistic simulations: Vacancy-trapping effects and cu-cluster mobility”. In: *Physical Review B* 76.21 (2007), p. 214102.
- [141] T. Vanacker. “Improvement of an advance Kinetic Monte Carlo algorithm through sorting and recycling factorized transition matrices”. MA thesis. Ecole Centrale Paris and KTH, 2017.
- [142] M. R. Hestenes, E. Stiefel, et al. *Methods of conjugate gradients for solving linear systems*. Vol. 49. NBS Washington, DC, 1952.
- [143] S.-C. T. Choi, C. C. Paige, and M. A. Saunders. “MINRES-QLP: A Krylov Subspace Method for Indefinite or Singular Symmetric Systems”. In: *SIAM Journal on Scientific Computing* 33.4 (Jan. 2011). Publisher: Society for Industrial and Applied Mathematics, pp. 1810–1836.
- [144] A. Amritkar, E. de Sturler, K. Świrydowicz, D. Tafti, and K. Ahuja. “Recycling Krylov subspaces for CFD applications and a new hybrid recycling solver”. en. In: *Journal of Computational Physics* 303 (Dec. 2015), pp. 222–237.
- [145] G. W. Stewart. “A Krylov–Schur Algorithm for Large Eigenproblems”. In: *SIAM Journal on Matrix Analysis and Applications* 23.3 (2002), pp. 601–614.

- [146] C. L. Bris, T. Lelièvre, M. Luskin, and D. Perez. “A mathematical formalization of the parallel replica dynamics”. In: 18.2 (2012), pp. 119–146.
- [147] S. Balay et al. *PETSc Web page*. <https://www.mcs.anl.gov/petsc>. 2019.
- [148] I. C. F. Ipsen and C. D. Meyer. “The Idea Behind Krylov Methods”. In: *The American Mathematical Monthly* 105.10 (1998), pp. 889–899.
- [149] A. C. Antoulas. *Approximation of large-scale dynamical systems*. SIAM, 2005.
- [150] N. J. Higham and A. H. Al-Mohy. “Computing matrix functions”. en. In: *Acta Numerica* 19 (May 2010). Publisher: Cambridge University Press, pp. 159–208.
- [151] O. Coulaud, L. Giraud, P. Ramet, and X. Vasseur. “Deflation and augmentation techniques in Krylov subspace methods for the solution of linear systems”. In: *arXiv:1303.5692 [math]* (Mar. 2013). arXiv: 1303.5692.
- [152] M. Gutknecht. “Spectral deflation in Krylov solvers: A theory of coordinate space based methods”. In: *ETNA. Electronic Transactions on Numerical Analysis [electronic only]* 39 (Jan. 2012).
- [153] A. Gaul, M. H. Gutknecht, J. Liesen, and R. Nabben. “A Framework for Deflated and Augmented Krylov Subspace Methods”. In: *SIAM Journal on Matrix Analysis and Applications* 34.2 (Jan. 2013). Publisher: Society for Industrial and Applied Mathematics, pp. 495–518.
- [154] V. Hernandez, J. E. Roman, A. Tomas, and V. Vidal. *A survey of software for sparse eigenvalue problems*. Tech. rep. STR-6. Available at <https://slepc.upv.es>. Universitat Politècnica de València, 2009.
- [155] S. Balay, W. D. Gropp, L. C. McInnes, and B. F. Smith. “Efficient Management of Parallelism in Object Oriented Numerical Software Libraries”. In: *Modern Software Tools in Scientific Computing*. Ed. by E. Arge, A. M. Bruaset, and H. P. Langtangen. Birkhäuser Press, 1997, pp. 163–202.
- [156] C. N. Haddad. “Cholesky factorization”. In: *Encyclopedia of Optimization*. Springer Science & Business Media, 2009, pp. 374–377.
- [157] C. A. Floudas and P. M. Pardalos. *Encyclopedia of optimization*. Springer Science & Business Media, 2008.
- [158] T. Jourdan, G. Bencteux, and G. Adjanor. “Efficient simulation of kinetics of radiation induced defects: A cluster dynamics approach”. In: *Journal of Nuclear Materials* 444.1 (2014), pp. 298–313.
- [159] U. M. Gösele. “Reaction kinetics and diffusion in condensed matter”. In: *Progress in reaction kinetics* 13.2 (1984).
- [160] A. Brailsford and R. Bullough. “The rate theory of swelling due to void growth in irradiated metals”. In: *Journal of Nuclear Materials* 44.2 (1972), pp. 121–135.
- [161] N. V. Doan and G. Martin. “Elimination of irradiation point defects in crystalline solids: Sink strengths”. In: *Phys. Rev. B* 67 (13 2003), p. 134107.

- [162] T. R. Waite. "Theoretical Treatment of the Kinetics of Diffusion-Limited Reactions". In: *Phys. Rev.* 107 (2 1957), pp. 463–470.
- [163] G. Greenwood, A. Foreman, and D. Rimmer. "The role of vacancies and dislocations in the nucleation and growth of gas bubbles in irradiated fissile material". In: *Journal of Nuclear Materials* 1.4 (1959), pp. 305–324.
- [164] F. Nichols. "On the estimation of sink-absorption terms in reaction-rate-theory analysis of radiation damage". In: *Journal of Nuclear Materials* 75.1 (1978), pp. 32–41.
- [165] H. Wiedersich. "On the theory of void formation during irradiation". In: *Radiation Effects* 12.1-2 (1972), pp. 111–125.
- [166] A. Brailsford and R. Bullough. "The theory of sink strengths". In: *Philosophical Transactions of the Royal Society of London. Series A, Mathematical and Physical Sciences* 302.1465 (1981), pp. 87–137.
- [167] H. Rouchette, L. Thuinet, A. Legris, A. Ambard, and C. Domain. "Numerical evaluation of dislocation loop sink strengths: A phase-field approach". In: *Nuclear Instruments and Methods in Physics Research Section B: Beam Interactions with Materials and Atoms* 352 (2015), pp. 31–35.
- [168] C. Tomé, H. Cecatto, and E. Savino. "Point-defect diffusion in a strained crystal". In: *Physical Review B* 25.12 (1982), p. 7428.
- [169] V. Dubinko, A. Abyzov, and A. Turkin. "Numerical evaluation of the dislocation loop bias". In: *Journal of nuclear materials* 336.1 (2005), pp. 11–21.
- [170] Z. Chang, P. Olsson, D. Terentyev, and N. Sandberg. "Dislocation bias factors in fcc copper derived from atomistic calculations". In: *Journal of nuclear materials* 441.1-3 (2013), pp. 357–363.
- [171] Z. Chang, N. Sandberg, D. Terentyev, K. Samuelsson, G. Bonny, and P. Olsson. "Assessment of the dislocation bias in fcc metals and extrapolation to austenitic steels". In: *Journal of Nuclear Materials* 465 (2015), pp. 13–19.
- [172] T. Jourdan. "Influence of dislocation and dislocation loop biases on microstructures simulated by rate equation cluster dynamics". In: *Journal of Nuclear Materials* 467 (2015), pp. 286–301.
- [173] G. Adjanor. *Complete characterization of sink-strengths for 1D to 3D mobilities of defect clusters I. Extension to diffusion anisotropy analog cases.* 2020.
- [174] H. L. Heinisch, B. Singh, and S. Golubov. "The effects of one-dimensional glide on the reaction kinetics of interstitial clusters". In: *Journal of nuclear materials* 283 (2000), pp. 737–740.
- [175] L. Malerba, C. S. Becquart, and C. Domain. "Object kinetic Monte Carlo study of sink strengths". In: *Journal of Nuclear Materials* 360.2 (Feb. 2007), pp. 159–169.
- [176] A. Vattré, T. Jourdan, H. Ding, M.-C. Marinica, and M. Demkowicz. "Non-random walk diffusion enhances the sink strength of semicoherent interfaces". In: *Nature communications* 7.1 (2016), pp. 1–10.

- 
- [177] D. Carpentier, T. Jourdan, P. Terrier, M. Athènes, and Y. Le Bouar. “Effect of sink strength dispersion on cluster size distributions simulated by cluster dynamics”. en. In: *Journal of Nuclear Materials* 533 (May 2020), p. 152068.
- [178] P. Terrier, M. Athènes, T. Jourdan, G. Adjanor, and G. Stoltz. “Cluster dynamics modelling of materials: A new hybrid deterministic/stochastic coupling approach”. In: *Journal of Computational Physics* 350 (Dec. 2017), pp. 280–295.
- [179] U. Gösele and A. Seeger. “Theory of bimolecular reaction rates limited by anisotropic diffusion”. In: *Philosophical Magazine* 34.2 (1976), pp. 177–193.
- [180] G. Adjanor. *Complete characterization of sink-strengths for 1D to 3D mobilities of defect clusters.II. Bridging between limiting cases with effective sink-strengths calculations*. 2020.
- [181] D. Mason, R. Rudd, and A. Sutton. “Stochastic kinetic Monte Carlo algorithms for long-range Hamiltonians”. In: *Computer Physics Communications* 160.2 (2004), pp. 140–157.
- [182] M. Afanasjew, M. Eiermann, O. G. Ernst, and S. Güttel. “Implementation of a restarted Krylov subspace method for the evaluation of matrix functions”. en. In: *Linear Algebra and its Applications*. Special Issue in honor of Richard S. Varga 429.10 (Nov. 2008), pp. 2293–2314.

